D I S S E R T A T I O N

submitted to the
Combined Faculties for Natural Sciences and Mathematics
of the Ruperto-Carola University of Heidelberg, Germany

for obtaining the degree of
DOCTOR OF NATURAL SCIENCES

presented by
Dipl.-Chem. Zoe Cournia
born in Athens, Greece

oral examination: 21 December, 2006

Structure and Dynamics of Biomembranes containing Cholesterol and other Biologically-Important Sterols. A computational perspective.

Referees:

Prof. Dr. Jeremy C. Smith

Prof. Dr. Michael Grunze

Structure and Dynamics of Biomembranes containing Cholesterol and other Biologically-Important Sterols. A computational perspective.

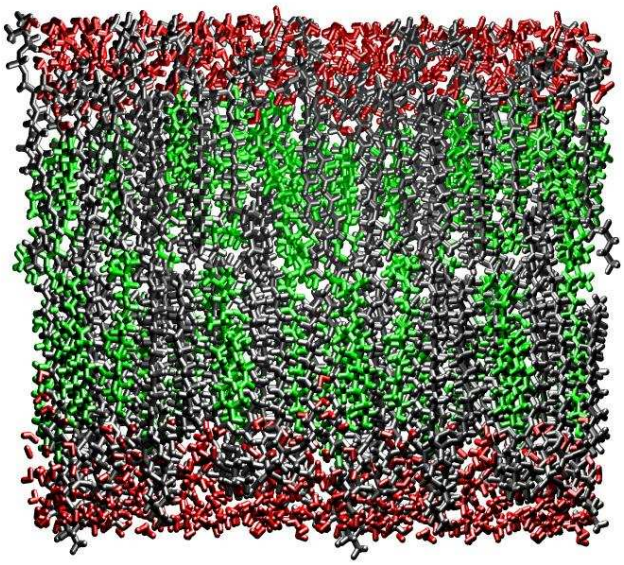

Zoe Cournia

ABSTRACT

Cholesterol plays a significant role in the function and dynamics of plasma membranes in the cells. A problem of longstanding interest has been to determine how cholesterol and other biologically-important sterols influence the structure and dynamics of lipid bilayers, as the results presented are often contradictory. In this thesis, the differential effects of three closely-related sterols: ergosterol, cholesterol and lanosterol on the structural and dynamical properties of a model dipalmitoyl phosphatidylcholine (DPPC) membrane were examined using Molecular Dynamics (MD) simulations and Neutron Scattering (NS) calculations.

As a necessary step towards realistic sterol:biomembrane simulations, molecular mechanics force field parameters for cholesterol, ergosterol and lanosterol, for the program package CHARMM are derived. For the parametrization an automated refinement method that involves fitting the molecular mechanics potential to both vibrational frequencies and eigenvector projections derived from quantum chemical calculations was used. This method is particularly useful for deriving parameters for rigid molecules, for which the flexibility is determined principally by vibrations, as is the case for sterols. The results show good agreement between CHARMM and quantum chemical normal modes. Final, refined parameters are tested against independent experimental data.

Subsequently, MD simulations of hydrated sterol:DPPC lipid systems are performed at a biologically-relevant concentration (40% mol.) at 309K and 323K. The simulations are compared with control simulations of the gel and liquid DPPC phases. All three sterols are found to order and condense the lipids relative to the liquid phase, but to markedly different degrees. Ergosterol is enhancing the packing of the lipids with each other and has a higher condensing effect on the membrane than the other two sterols. Moreover, ergosterol induces a higher proportion of *trans* lipid conformers, a thicker membrane and higher lipid order parameters, and is aligned more closely with the membrane normal. Ergosterol also positions itself closer to the bilayer:water interface. In contrast, lanosterol orders, straightens and packs the lipids less well, and is less closely aligned with the membrane normal. Furthermore, lanosterol lies closer to the relatively-disordered membrane center than do the other sterols. The behaviour of cholesterol in all the above respects is intermediate between that of lanosterol and ergosterol. The origins of the different membrane behavior upon addition of each sterol are discussed with respect to the sterol chemical differences.

Finally, in order to study the dynamics of the sterols, NS calculations using the MD coordinate trajectories were also performed. These confirmed the high anisotropical motion of cholesterol in the xy-plane observed in the NS experiments. Ergosterol was found to diffuse the slowest and cholesterol the fastest both in the xy-plane and the z-axis of the membrane among the three sterols studied.

The findings here may explain why ergosterol is the most efficient of the three sterols at promoting the liquid-ordered phase and lipid domain formation, and may also furnish part of the explanation as to why cholesterol is evolutionarily preferred over lanosterol in higher-vertebrate plasma membranes.

ZUSAMMENFASSUNG

Cholesterol spielt eine entscheidende Rolle in der Funktionsweise und Dynamik der Plasmamembranen von Zellen. Seit längerer Zeit besteht ein großes Interesse am Einfluss des Cholesterols und anderen biologisch wichtigen Sterolen auf die Struktur und Dynamik von Lipid-Doppelschichten; die veröffentlichten Ergebnisse zu diesem Thema sind häufig widersprüchlich. In dieser Doktorarbeit werden die unterschiedlichen Effekte von drei nahverwandten Sterolen - nämlich das Ergosterol, das Cholesterol und das Lanosterol - auf die strukturellen und dynamischen Eigenschaften einer Dipalmitoyl-phosphatidylcholine (DPPC) Modellmembran unter Verwendung von "molekular-dynamischen" (MD) Simulationen und Neutronen-Streuungs (NS) Berechnungen untersucht.

Ein notwendiger Schritt zu einer realistischen Simulation des Sterol:Biomembembran-Systems ist die Bestimmung von Kraftfeldparametern der molekulare Mechanik von Cholesterol, Ergosterol und Lanosterol für das Programmpaket CHARMM entwickelt worden. Für die Parametrisierung wird eine automatische Bestimmungsmethode verwendet, welche das Potential der molekularen Mechanik sowohl an die Vibrationsfrequenzen als auch an die Eigenvektorprojektionen, die quantenchemisch bestimmt werden, anpasst. Diese Methode ist insbesondere hilfreich, um Parameter für rigide Moleküle, wie zum Beispiel Sterole, für welche die Flexibilität prinzipiell durch Vibrationen bestimmt wird, abzuleiten. Die Ergebnisse zeigen eine gute Übereinstimmung zwischen CHARMM und quantenchemischen Normalmoden. Die bestimmten Parameter werden am Ende gegen unabhängige, experimentelle Daten getestet.

Danach werden MD Simulationen von hydrierten Sterol:DPPC Lipidsystemen mit einer biologisch relevanten Konzentration (40% mol.) bei 309K und 323K durchgeführt. Die Simulationen werden mit Kontrollsimulationen der Gel- und flüssigen DPPC-Phasen verglichen. Man stellt fest, dass alle drei Sterole die Lipide relativ zur flüssigen Phase anordnen und kondensieren, dies aber zu bemerkenswert verschiedenen Graden tun. Ergosterol induziert eine dichtere Ansammlung der Lipide und hat eine höhere kondensierende Wirkung auf die Membran als die anderen beiden Sterole. Desweiteren induziert das Ergosterol einen höheren Anteil von *trans*-Lipidkonformeren, eine dickere Membran, höhere Lipidanordnungparameter, und es ist näher zur Membrannormalen angeordnet. Ergosterol positioniert sich auch näher an die Doppelschicht:Wasser-Grenze. Ganz im Gegensatz ordnet, streckt und packt das Lanos-

terol die Lipide weniger gut und ist auch nicht so nah an die Membrannormale angeordnet. Es liegt näher als die beiden anderen Sterole am Membranzentrum, welches relativ ungeordnet ist. Das Verhalten von Cholesterol ist in jeglicher Hinsicht zwischen dem des Lanosterols und Ergosterols anzuordnen. Die Ursachen der unterschiedlichen Membraneigenschaften unter dem Einfluss eines Sterols werden im Hinblick auf die unterschiedlichen chemischen Eigenschaften charakterisiert.

Um schließlich die Dynamik der Sterole zu untersuchen werden NS Berechnungen auf der MD Koordinaten-Trajektorien durchgeführt. Diese bestätigen die hohen anisotropischen Bewegungen des Cholesterols in der xy-Ebene, die in den NS Experimenten beobachtet wurde. Es zeigt sich, dass sowohl in der xy-Ebene als auch entlang der z-Achse der Membran Ergosterol am langsamsten und Cholesterol am schnellsten diffundieren.

Die Ergebnisse können eine Erklärung geben, warum Ergosterol das effizienteste der drei Sterole ist, um die flüssig-geordnete Phase (liquid-ordered phase) und die Formation von Lipiddomänen zu fördern. Des Weiteren geben diese Ergebnisse Aufschlußdarüber, warum das Cholesterol gegenüber dem Lanosterol als Bestandteil von Plasmamembranen höherer Vertebraten in der Evolution begünstigt wurde.

To my parents

“The unexamined life is not worth living . . .
Wisdom begins in wonder . . .
There is only one good, knowledge,
and one evil, ignorance.”

Socrates, 469 - 399 B.C.

“Look and you will find it - what is unsought
will go undetected.”

Sophocles, 496 - 406 B.C.

CONTENTS

ACKNOWLEDGMENTS

Words will probably fail to convey my gratitude to my supervisor, Professor Jeremy Smith. His great scientific insights were a source of inspiration for this work. Without his guidance, this thesis would not have taken its present form. He has been very supportive during my studies, both when things were promising but also, more importantly, at the difficult moments. I am grateful to him for the academic freedom he provided me, which helped me develop my independent thinking. And of course, I have to thank him for being such great company during fun times in the lab.

Professor Matthias Ullmann helped me in the initial learning-stages of my doctoral research and gave me direction when I thought I was in a dead-end. His suggestions, ideas and motivation have helped me bring this project to a successful conclusion. He has greatly contributed to the development of my scientific thinking and I am grateful to him for that.

I am much obliged to Professor Michael Grunze for being a referee of this thesis. I would also like to thank Professor Irmgard Sinning and Professor Horst Köppel for participating in my doctoral examination committee.

There are a number of my colleagues whom I would like to thank wholeheartedly for their help and advice during my time in Heidelberg. In chronological order, I would like to thank Ms. Ellen Vogel who helped me a lot with administrative matters and for the numerous corrections to my German. I had a great collaboration with Dr. Andrea Vaiana on applying AFMM to 'my sterols'. I also have to thank him for long scientific and not-so-scientific discussions and for being a very good friend. Bogdan Costescu has been a 'dream' system administrator and I would like to thank him for always taking the time to answer all of my computing questions and for developing AFMM into an independent program. I am grateful to Dr. Alexander Tournier for being there in the ups and downs of my data analysis and for introducing me to Python, which has been an excellent tool for analyzing all those gigabytes of data. Sven Lammers has supported and motivated me throughout my stay in Heidelberg. I would like to thank him for his patience and for all the good times.

I must express my indebtedness to my friend and colleague Dr. Vandana Kurkal-Siebert, with whom I have discussed almost all aspects of this work. She has patiently answered my scientific questions and has especially contributed to my understanding of neutron scattering. I also have to thank her for her wise career advice and the numerous corrections to my English.

I would also like to thank Dr. Torsten Becker for helping me out with the neutron scattering theory, Dr. Stefan Fischer for valuable suggestions during my parameterization times, Dr. Lars Meinhold for all the CHARMM tricks of the trade, Dr. Isabella Daidone for nice discussions, Dr. Nicoleta Bondar for useful literature, Jens Keienburg for proofreading this thesis and making useful suggestions, Dr. Emil Endreß for providing me with the raw data from the QENS experiments and for informative neutron scattering discussions and Stefan Friedel of the Helics supercomputer team for his assistance during the last stages of my doctoral studies. Thanks to all the members of the Biocomputing group for creating such a unique, pleasant working as well as partying environment.

Many thanks to my sister, Eleni Cournia, for long, encouraging discussions. Finally, very special thanks go to my parents, Effie and John Cournias. They have instilled in me their fondness for learning and supported me throughout my long studies. I know that they will always trust and support me by any means they can.

Finally, I gratefully acknowledge the Bundesministerium für Bildung und Forschung and the Deutsche Forschungsgemeinschaft, which financially supported a large part of this research.

Z.C., Heidelberg, 28 September 2006

PUBLICATIONS ARISING FROM THIS THESIS

[1] COURNIA, Z., ULLMANN, G. M., AND SMITH, J. C. Differential Effects of Cholesterol, Ergosterol and Lanosterol on a Dipalmitoyl Phosphatidylcholine (DPPC) membrane: A Molecular Dynamics Simulation Study. *submitted*, 2006.

[2] DE HATTEN, X., COURNIA, Z., SMITH, J., AND METZLER-NOLTE, N. Towards Synthetic Hydrogenase Mimicry: Force-Field Development and Molecular Dynamics Simulations of Novel Ferrocene-Bearing Peptides. *manuscript in preparation*, 2006.

[3] COURNIA, Z., ULLMANN, G. M., AND SMITH, J. C. *Development and Validation of a Force-Feild for Biologically-Important Sterol in Biomembranes. In:* Lecture Series on Computer and Computational Sciences, Vol. 4, Brill Academic Publishers, Leiden, 2005, pp. 949–953.

[4] COURNIA, Z., SMITH, J. C., AND ULLMANN, G. M. A molecular mechanics force-field for biologically important sterols. *J. Comp. Chem.*, 2005, **26**, 1383–1399.

[5] VAIANA, A. C., COURNIA, Z., COSTESCU, I. B., AND SMITH, J. C. AFMM: A Molecular Mechanics Force-Field Vibrational Parametrization Program. *Computer Physics Communications*, 2005, **167**, 34–42.

[6] COURNIA, Z., ULLMANN, G. M., AND SMITH, J. C. *Molecular Dynamics of Cholesterol in Biomembranes. In:* Lecture Series on Computer and Computational Sciences, Vol. 1, VSP International Science Publishers, Zeist, 2004, pp. 131–135.

[7] COURNIA, Z., VAIANA, A. C., SMITH, J. C., AND ULLMANN, G. M. Derivation of a molecular mechanics force field for cholesterol. *Pure Appl. Chem.*, 2004, **76**, 189–196.

[8] SMITH, J. C., COURNIA, Z., TALY, A., L.TOURNIER, A., MIHAILESCU, D., AND ULLMANN, G. M. *Conformational Changes in Proteins and Membranes. In:* Novel Approaches to the Structure and Dynamics of Liquids: Experiments, Theories and Simulations, Kluwer Academic Publishers, Dordrecht, 2004, pp. 485–502.

CHAPTER 1

INTRODUCTION

1.1 THE PLASMA MEMBRANE AND THE LIPID BILAYER

Biological membranes are crucial to cell life and perform a variety of functions in the cell. The plasma membrane, which is the outer cell membrane, encloses the cell, defines its boundaries, senses external signals, is a selective barrier for water and ions, and plays an important role in signal transduction of membrane proteins. The intracellular membranes separate the cell into different compartments, increasing thus the organization of the cell and allowing each organelle, such as Golgi apparatus, mitochondria, endoplasmatic reticulum, etc., to execute a characteristic function.[1]

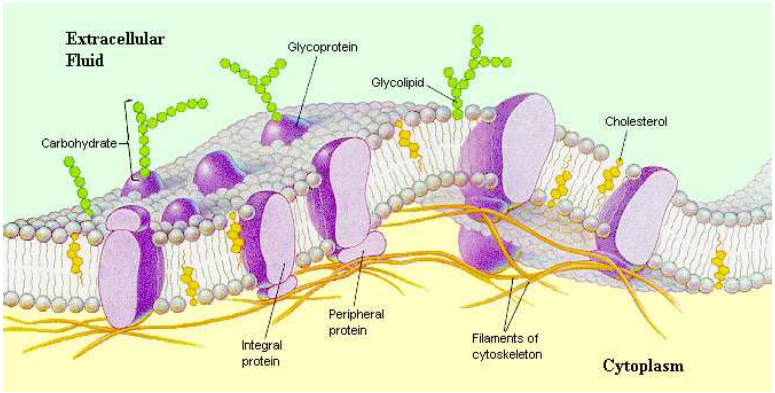

Figure 1.1: A schematic representation of a biomembrane. Membranes consist of different lipids, (depicted in grey) which have a polar headgroup and two hydrophobic hydrocarbon tails, cholesterol (yellow) and membrane proteins (lilac). The aqueous layer surrounding the membrane is not depicted for clarity.

Despite their differing functions, all biological membranes have a common basic structure: the lipid bilayer (Fig. 1.1). Biological membranes contain most commonly phospholipids, but also glycolipids and sphingolipids. The occurrence of phospho-

lipids as an essential membrane component is attributable to their ability to form bilayer vesicles spontaneously upon dispersion in water. This property of bilayer self-organization arises from the amphiphilic structure of the phospholipids. The phospholipid molecule consists of a phosphate-containing polar headgroup attached to two hydrophobic hydrocarbon chains (see Figure 1.2a). Differences in the length and saturation of the fatty acid tails are important because they influence the ability of phospholipid molecules to pack in the bilayer, a factor that influences the fluidity of the bilayer (see Section 1.3).

Cell membranes are dynamic, fluid structures where the molecules are able to diffuse rapidly in the plane of the membrane. Membranes of eukaryotic cells have a complex composition consisting of hundreds of different lipids and proteins, plus cholesterol or closely-related sterols (Figure 1.1). In particular, in higher vertebrate cells the plasma membranes have an especially high concentration of cholesterol, of about 40 mol. %[1]

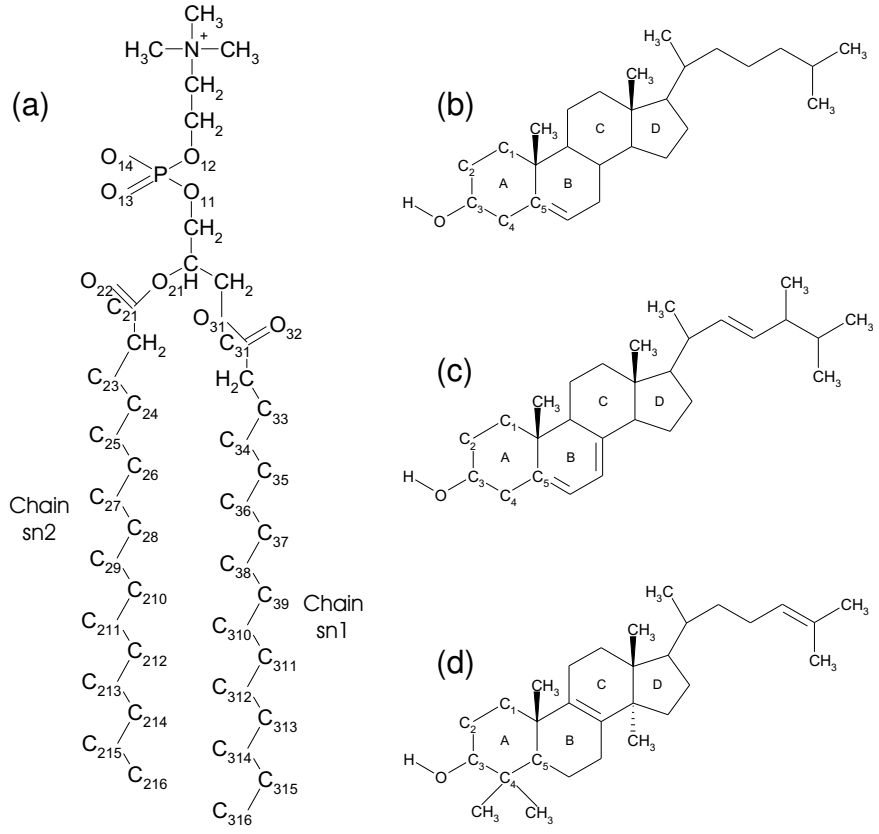

Figure 1.2: Chemical structure and atom numbering schemes of (a) DPPC, (b) cholesterol, (c) ergosterol, (d) lanosterol

1.2 DISTRIBUTION AND ROLE OF STEROLS IN CELL MEMBRANES

Sterols are required for cell growth but their exact role in the functioning of membranes is a yet unanswered question in cell biology and biochemistry. Although sterols are classified chemically as lipids, they are synthesized by complex pathways independent of the pathways for the synthesis of other common lipids. Their biosynthetic pathways are long, complicated and energetically expensive. As an example, in order to synthesize cholesterol from acetyl-CoA about 30 enzymatically catalyzed steps are required. Along the biosynthetic path of cholesterol, a large number of sterols are synthesized as intermediates.[2] The first sterol to be produced from squalene is lanosterol and from that point another 18 sterols will be made until cholesterol is synthesized. Thus, considerable cellular energy is spent on producing the specific structure of cholesterol. Cholesterol must therefore fulfill some important functions in higher vertebrate cells that cannot be fulfilled by any other sterol structure.

Among the sterols, cholesterol is particularly abundant in higher vertebrates. Within a cell, cholesterol is found exclusively in the cell membranes and as much as 90% of the total cellular cholesterol is found in the plasma membrane.[3] The remaining 10% of cholesterol in mammals is found in small concentrations in inner cell membranes or is bound to the circulating lipoproteins, for example to the low-density lipoprotein (LDL) which carries cholesterol in the serum. Cholesterol has been found to account for up to 50% of the lipid concentration in the plasma membrane, being an essential component of the higher vertebrate plasma membrane.

Cholesterol performs a wide range of roles in human cells. It is the precursor for the synthesis of hormones and numerous other biologically-important molecules.[4–6] It has also been shown to influence the physical properties of membranes, such as their fluidity,[7,8] and may also play other membrane-associated roles, such as in signal transduction[9] and ion permeation.[10]

The effect of cholesterol and other biologically-important sterols, such as lanosterol and ergosterol, on functional, structural and dynamical membrane properties has received considerable attention in the past decades.[4] Ergosterol (provitamin D_2) is found in the membranes of fungi, yeasts and protozoans. Lanosterol, the evolutionary and biosynthetic precursor of cholesterol[2] is the major constituent of prokaryotic cell membranes. Other examples of biologically-important sterols are sitosterol and stigmasterol, which are common plant sterols.

Mammalian cells die in the absence of cholesterol or if substituted with a plant

sterol or with lanosterol or ergosterol. Cholesterol also cannot substitute for ergosterol in yeast and fungi. This observation leads to the conclusion that sterols are important for cell survival and also that only a particular sterol structure is suited for a particular cell type.

1.3 LIPID PHASE TRANSITION

One of the very important features of phospholipid bilayers is their thermotropic phase behavior. Fully hydrated bilayers composed of a single phospholipid species undergo a well-defined phase transition in which the lipid chains change from an ordered or gel state to a fluid or liquid crystalline state. Each lipid has a characteristic transition temperature, T_t. Studies of the changes taking place at the phase transition provide a very valuable method of characterizing the properties of the fluid state, which is probably the most relevant to biological membranes. The fluid state is relevant to biological membranes because at body temperature a big proportion of the membrane lipids are above their main phase transition, *i.e.* in the fluid phase. The fluid phase is conventionally designated L_α or *ld* (liquid-disordered) phase and the gel phase is designated L'_β or *so* (solid-ordered) phase. In addition, an intermediate phase $P_{\beta'}$, in which the bilayer is rippled, is found in the gel phase of certain phospholipids. The phase diagram for dimyristoyl phosphatidylcholine (DMPC) is shown in Figure 1.3.

The transition temperature T_t and phase behavior differ among the various lipid types, but all depend strongly on water content. With increasing water content, the transition temperature decreases progressively, reaching a limiting value at 25-30 wt % water. At this point the water-binding capacity of the lipid has almost reached its saturation, and it is only beyond this water content that a transition is observed which corresponds to the freezing of free water. When the lipid reaches its water-binding capacity then exactly this water concentration is referred to as 'full hydration'. The water molecules that are hydrating the phospholipid are prevented from participating in the cooperative interactions found in bulk water. The hydration characteristics can be summarized in a lipid phase diagram (Fig. 1.3). The near anhydrous phospholipid forms bilayer crystals that undergo a chain-melting transition ($L'_\beta - L_\alpha$) at a relatively high temperature. Both the main transition and the pretransition temperatures decrease as water is taken up by the bilayer. Water molecules bind to the phospholipid headgroups and depress the transition temperature by approximately 4°C per water molecule. The gel phase achieves maximum hydration at approximately 30 % wt water, at which point there is no further decrease in transition temperature. Hydration continues further in the fluid phase, a free water phase not appearing until above 40%

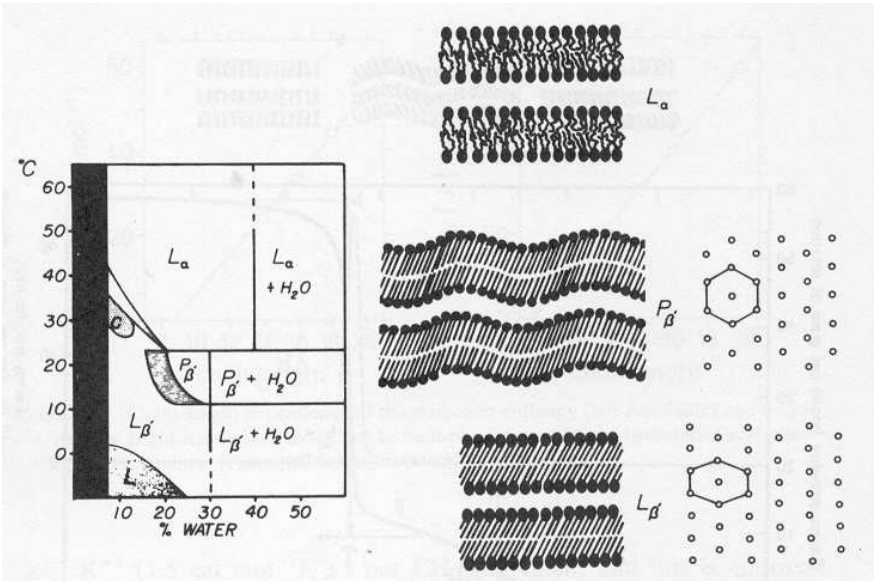

Figure 1.3: Phase diagram of hydrated dimyristoyl phosphatidylcholine (DMPC) bilayers, together with representations of the L_α, $P_{\beta'}$ and L'_β phases. The hydrocarbon chain packing is a hexagonal array for the $P_{\beta'}$ phase and a 'distorted' hexagonal lattice of the L'_β phase. [Adapted from Ref.11]

wt water. This increased water content has little effect on the thermodynamics of the phase transition, but can be observed by X-ray diffraction as an increase in the water space between the lipid bilayers.

The temperature at which the phase transition occurs in phospholipids depends on the hydrophobic tail structure of the specific lipid. A long tail length increases the tendency of the hydrocarbon tails to interact with each other and this in turn increases the transition temperature. If the hydrocarbon chain is unsaturated, *i.e.* contains one or more double bonds, then this produces a kink in the chain that makes it more difficult to pack with the rest of the lipid acyl chains. This results to lowering the transition temperature. As an example, DMPC is a saturated lipid with two 14-carbon tails, which has a transition temperature of 24°C. If we add two carbons more in each of the DMPC carbon chains, the resulting structure is Dipalmitoyl Phosphatidylcholine (DPPC), which has a transition temperature of 41°C. The introduction of a double bond in DPPC (to get the Dipalmitoleic Phosphatidylcholine lipid structure) results in a dramatic drop in the transition temperature, which decreases to -20°C.

The precise fluidity of cell membranes is biologically important. Certain membrane-transport processes as well as enzyme activity have been shown to cease upon making the membrane too fluid or too rigid. The fluidity of a lipid bilayer depends on its temperature (as described above) but also on its composition.

The next section describes the influence of cholesterol and other biologically-important sterols on bilayer fluidity.

1.4 LIPID RAFTS AND THE LIQUID-ORDERED PHASE

Upon addition of cholesterol in a concentration above 25 mol % in a pure lipid bilayer there is a dramatic influence on the lipid phase transition. With the addition of cholesterol the gel-liquid phase transition is inhibited and a new thermodynamically-stable region of coexistence between the liquid-disordered (*ld*) and solid-ordered (*so*) phase is introduced: the liquid-ordered (*lo*) phase (see Fig.1.4a).[12–17] This new phase is characterized by a fluidity intermediate between those of the gel and the fluid phases formed by the pure lipids.

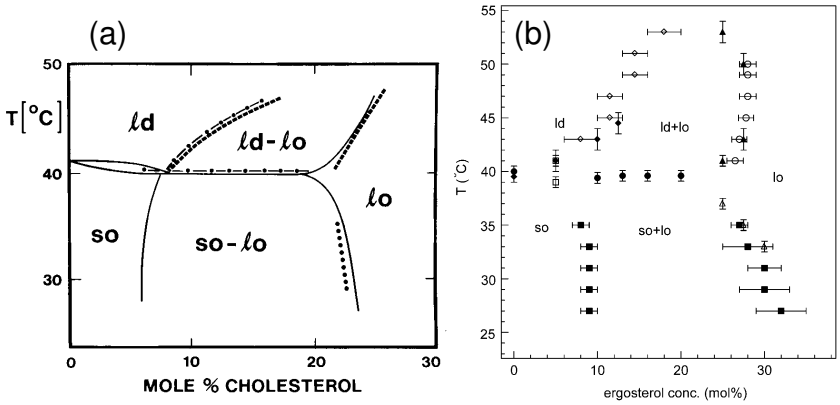

Figure 1.4: (a) Experimental phase diagram for the DPPC-cholesterol system as determined by ^{2}H NMR spectroscopy and differential scanning calorimetry.[13] Above 25 mol % cholesterol a new thermodynamically stable phase is introduced: the *lo* phase. [Adapted from Ref.4] (b) Experimental phase diagram of the DPPC/ergosterol system as determined by by ^{2}H NMR spectroscopy and differential scanning calorimetry.[18] The various phases are denoted by *so* (solid-ordered), *ld* (liquid-disordered) and *lo* (liquid-ordered). [Adapted from Ref. 18]

Recently, it has been proposed that the *lo* phase is formed in model membranes when cholesterol associates with saturated, high-melting lipids, such as DPPC and sphingomyelin, to create dynamic complexes, so-called 'lipid rafts'.[19–22] In this manner cholesterol promotes a phase separation where cholesterol-rich and cholesterol-poor microdomains are formed (see Fig. 1.5).[23–27] The cholesterol-rich domains contain saturated lipids (e.g. sphingomyelin or DPPC), with which cholesterol associates particularly strongly and these domains are in the *lo* phase. The cholesterol-poor domains contain unsaturated lipids found in the liquid phase. A schematic representation

of a lipid raft is shown in Figure 1.6. The lipid rafts are dynamic assemblies of proteins and lipids that float freely within the liquid-disordered bilayer of cellular membranes. These assemblies have still a degree of fluidity but are more ordered and tightly packed than the surrounding liquid bilayer. The difference in the packing within the lipid rafts arises from the saturation of the hydrocarbon chains found in rafts as compared to the unsaturated lipids found in the rest of the membrane (liquid-disordered phase).[19] The saturated lipids are able to pack their chains more effectively than the unsaturated lipids (see Fig. 1.6).

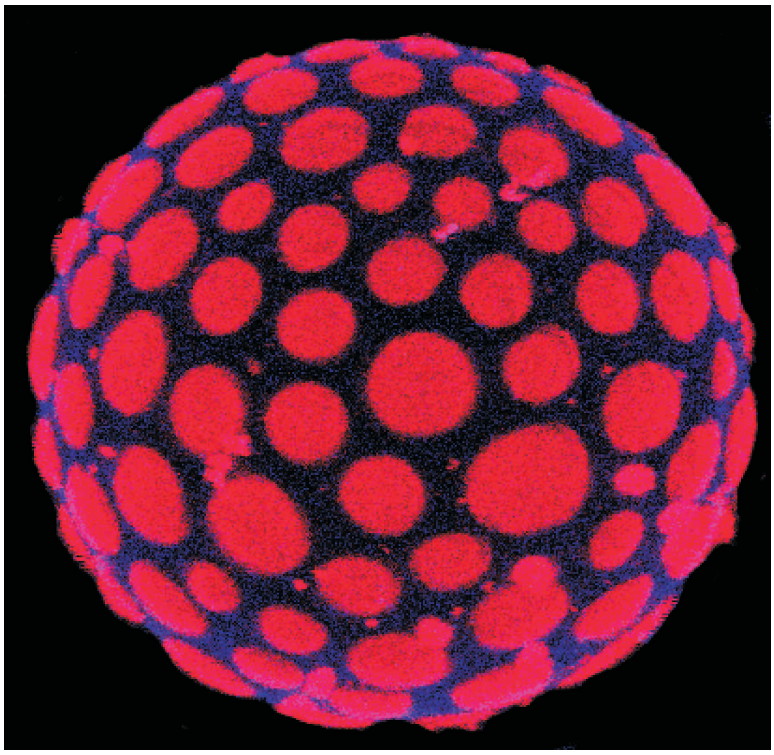

Figure 1.5: A giant unilamellar vesicle (GUV) designed to mimic rafts of lipid segregation in cell plasma membranes, when examined under multiphoton fluorescence microscopy. The separation of cholesterol-saturated phospholipid domains in the *lo* phase (labeled in red) and of unsaturated phospholipids *ld* phase (marked in blue) is evident. The GUV, made of sphingomyelin, cholesterol and another unsaturated phospholipid, is approximately 30 micrometers in diameter. [Adapted from Ref. 20].

The presence of liquid-ordered microdomains in cells has transformed the classical membrane fluid mosaic model proposed by Singer and Nicholson in 1972[28] into a more complex system, where proteins and lipid rafts diffuse laterally within a two-dimensional liquid.[29]

Evidence that ergosterol is also able to promote the formation of the *lo* phase was very recently published.[18, 30] A fluorescence study[31] showed that ergosterol promotes

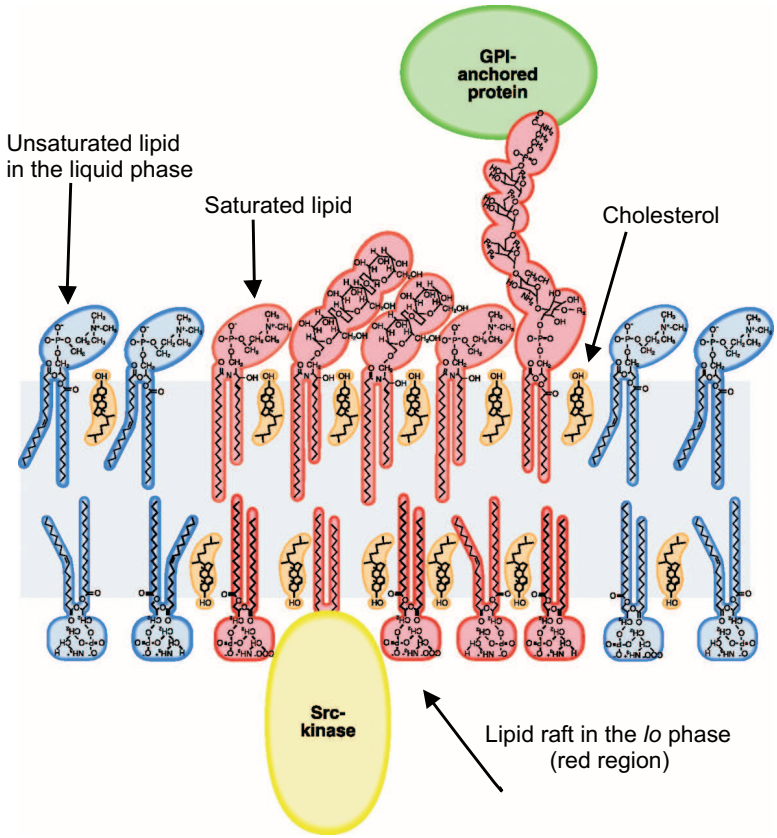

Figure 1.6: A schematic representation of a lipid raft. Cholesterol associates with saturated lipids to form cholesterol-rich domains (rafts) in the liquid-ordered phase (red region). These lipid rafts float freely in a pool of unsaturated lipids found in the liquid phase (blue region).

domain formation stronger than cholesterol. The DPPC-ergosterol phase diagram is very similar to the one obtained for DPPC-cholesterol, but to achieve the formation of the *lo* phase in the ergosterol-DPPC membrane, a concentration of ergosterol above 30 mol % is needed (see Fig. 1.4).[18]

Lanosterol is shown to be less prone to induce the *lo* phase compared to ergosterol or cholesterol and to have little effect on domain formation.[32, 33] A NMR/calorimetry study combined with computer modelling[15] also showed that lanosterol is not stabilizing the *lo* phase as effectively as cholesterol. In other words, in cholesterol-containing membranes the *lo* phase is a well-defined thermodynamic phase, clearly separated from the *ld* phase. On the contrary, in lanosterol-containing membranes, as calculated and experimental phase diagrams show, the *lo* and *ld* phases are no longer thermodynamically distinguishable (see Fig. 1.7).[15, 32]

Lipid rafts in mammalian plasma membranes (*i.e.* cholesterol-rich lipid domains) have received considerable attention in the past few years. They have not only changed

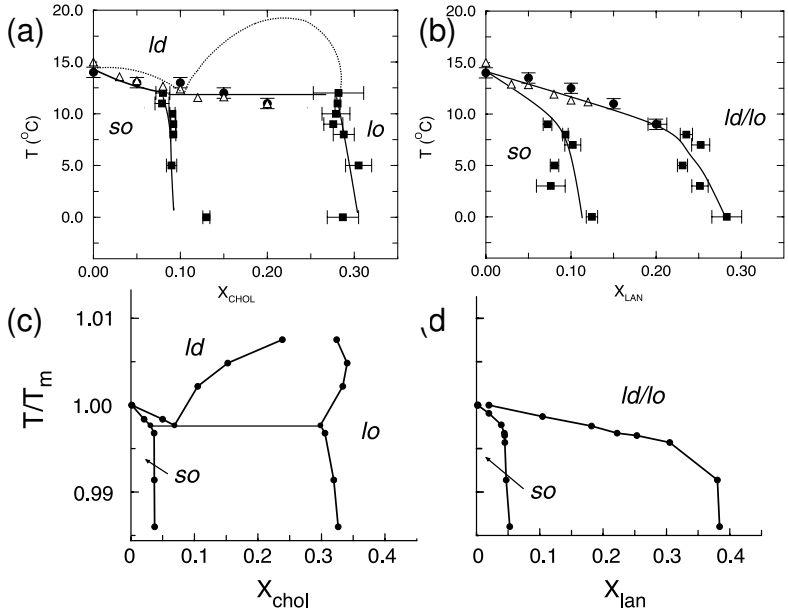

Figure 1.7: Top panel: Experimental phase diagrams as determined by DSC (open triangles) and by NMR spectroscopy (solid squares and solid circles). (a) PPetPC-cholesterol systems (b) PPetPC-lanosterol systems. The phase boundaries indicated by the dashed lines in (a) are not derived experimentally and are shown to illustrate the qualitative structure of the phase diagram, which is consistent with the thermodynamic phase rules. Lower panel: Theoretical phase diagrams determined from Monte Carlo simulations (c) lipid-cholesterol membranes, (d) lipid-lanosterol membranes. [Adapted from Ref. 15.]

our view for membrane architecture, but they might also play a role in a huge range of processes such as signal transduction, molecular trafficking, diseases such as HIV, Alzheimer and malaria, as well as being involved in the immune, vascular, digestive and reproductive systems. In particular, the possibility of modulating lipid raft properties using statins and sterol/synthetic sphingolipid analogues opens up new approaches for therapeutic interventions in such raft-associated diseases.[34–36]

The way in which cholesterol and ergosterol strongly promote raft formation, while lanosterol has limited capacity, must lie in the specific sterol:saturated lipid interactions in the membrane. Since cholesterol or ergosterol are key components for the formation of functional lipid rafts and are present in many eukaryotic plasma membranes, the way these sterols modulate the physical properties of membranes requires a more detailed description of the specific sterol-lipid interactions. In particular, the specific chemical structures of these molecules, also in comparison to lanosterol, will be the cause of the effects that are observed in sterol-containing lipid membranes, such as lipid ordering and the *lo* phase formation.

A possible argument for the evolutionary preference for cholesterol might lie in cholesterol's ability to promote the lipid raft formation better than lanosterol. Al-

though the definition of the *lo* phase is now established,[4] a number of questions associated with the characteristics of this phase are still being debated. For example there is little information on the position of cholesterol/ergosterol in the membrane, the role of hydrogen bonding, population of *gauche* conformers, the dynamics of the sterols in the rafts, and the origin of the inequivalence of the interaction between the sterols and the lipid acyl *sn1* and the *sn2* chains. The above considerations raise the intriguing question as to which are the particular chemical characteristics of cholesterol that have led to its evolutionary selection for higher vertebrate plasma membranes, given its structural similarity with its precursors.

1.5 CHEMICAL STRUCTURE OF CHOLESTEROL *vs.* ERGOSTEROL AND LANOSTEROL

Although cholesterol, ergosterol and lanosterol have very similar chemical structures (see Figures 1.2b, 1.2c, and 1.2d, respectively), they have significantly different effects on membrane properties.[8, 37] The main structural difference between lanosterol and the other two sterols is the presence of three extra methyl groups (two at position C_4 and one at C_{14}) that protrude from its otherwise flat α-surface. In the steroid ring system cholesterol has a double bond between carbons C_5 and C_6, in contrast to lanosterol's double bond between C_8 and C_9. Ergosterol, on the other hand, has a conjugated π-system in its second steroid ring, which has two *cis* hydrogens bound to C_6 and C_7. In the acyl side chain slight chemical differences are also present. Cholesterol has a saturated side chain, while ergosterol has a *trans* double bond at position C_{22} and is methylated at position C_{24}; lanosterol has a double bond between carbons C_{24} and C_{25}. Although these differences seem to be subtle, only cholesterol was evolutionarily selected to be a major constituent of the higher vertebrate plasma membranes. Moreover, the process of conversion of lanosterol to cholesterol in vertebrate cells is laborious, requiring eighteen enzymatic steps.[2] Depletion of cholesterol, or its substitution with ergosterol or lanosterol is lethal to all mammalian cells.

There has been much interest in studying the differences on structure and dynamics between biologically-important sterols (e.g. cholesterol, ergosterol, lanosterol).[18, 33, 38–41] Among them, the relevant questions are whether the different sterol molecules interact differently with the same lipid and whether the different sterols have different dynamics in the membrane. A variety of experimental and MD studies have attempted to investigate the diffusion of sterols in phospholipid model membranes.[42–49]

1.6 THE PROBLEM TO BE ADDRESSED

Physical properties of mammalian plasma membranes can be reproduced and studied with model biological membranes.[4] Both experimental and computational studies of model systems have shed light on the nature of phospholipid-sterol interactions. Experimental studies aimed at determining how cholesterol influences membrane properties are valuable but very often lack sufficient resolution for investigating the detailed underlying molecular interactions involved. In contrast, using molecular dynamics (MD) simulation it is possible to interpret experimental results on complex membrane systems in detail and to gain insight into the relevant interactions at the atomic level. The field of lipid bilayer simulations is growing rapidly and with it, the level of complexity of the systems with explicit inclusion of membrane proteins[50–53] and cholesterol[37, 54–56] in the simulated systems. Although several MD simulations of lipid/cholesterol systems have been published over the past decade,[37, 54–56] only two have investigated the different effect of sterols in the membrane.[37, 57]

The main aim of this thesis is to study the different structural and dynamical effects arising from three different biologically-important sterols, namely cholesterol, ergosterol and lanosterol in a model membrane with the MD simulation technique. This study provides insights as to why cholesterol was evolutionary chosen to be incorporated into the higher-vertebrate plasma membranes. The following questions are addressed:

- What differences exist in the phospholipid conformations within the membrane between the three sterol systems and as compared to the pure phospholipid systems?
- What is the effect of temperature on sterol-containing membranes (*e.g.* below and above the phospholipid phase transition) ?
- How are the micromechanical properties of the sterol/lipid membrane correlated to the sterol chemical structures?
- What are the differences in the structural characteristics of the sterol-membrane systems?
- What differences exist in the membrane dynamics between the three sterol systems?
- Is there an anisotropy of the molecular motions of cholesterol, ergosterol and lanosterol in membranes in the ns-ps regime?

To achieve these goals, three major milestones were needed:

1. *Development of the necessary parameters for the three sterols for performing reliable MD simulations.*

   The functional form of the potential used in MD simulations contains a set of empirical parameters, which are molecule dependent and have to be optimized prior to performing simulations. This optimization procedure is referred to as parameterization of the force field. The reliability of a molecular mechanics calculation is dependent on the numerical values of these parameters. In Chapter 3 the derivation of the intramolecular parameters and the partial atomic charges for cholesterol, ergosterol and lanosterol, associated with the CHARMM force field is being presented.

2. *Production of MD trajectories from sterol-containing membranes and 'control' neat DPPC systems. Analysis of the structural properties of these systems and comparison.*

   The step following the parameterization of the force field is to perform MD simulations in order to gain insights on the structure and dynamics of the biomolecules under study. In Chapter 4, a pure DPPC phospholipid bilayer is simulated as 'control' simulation in two phases (above and below the phase transition): the gel and the liquid phase. In Chapter 5, cholesterol-, ergosterol- and lanosterol- DPPC membranes are being simulated at the same temperatures as the pure DPPC bilayer. The effect of each sterol on the membrane structural properties is examined at atomic detail. The structural properties of the pure DPPC systems are also analyzed and compared to the sterol-containing membranes. Some important conclusions on the structure-function relationships of the sterols under study are presented in Section 5.3.

3. *Dynamical analysis of the systems with MD and neutron scattering calculations.*

   Although structural aspects of cholesterol in membranes have been investigated in detail by both experimental and theoretical studies, our knowledge of sterol dynamics is quite limited. In particular, there are barely any studies of ergosterol and lanosterol dynamics in membranes. In order to gain insights into the dynamical aspects that govern these sterols, the MD trajectories were analyzed in order to study the diffusion of the three sterols in the membranes. Incoherent quasielastic neutron scattering (QENS) calculations were performed to validate the MD simulation and to further study molecular motional processes in membranes. The high anisotropical motion of cholesterol observed in previous

quasielastic neutron scattering experiments is confirmed from the MD simulations. These results are presented in Chapter 6.

SYSTEMS STUDIED

The cholesterol-, ergosterol-, and lanosterol- DPPC membranes were studied at two temperatures, chosen such that one is below (T=309K) and one is above (T=323K) the DPPC gel-liquid transition, which occurs at T=315K for the neat DPPC system.[58] Pure DPPC membranes in the gel (309K) and the liquid (323K) phase were also performed as control simulations.

BIBLIOGRAPHY

[1] ALBERTS, B., BRAY, D., LEWIS, J., RAFF, M., ROBERTS, K., AND WATSON, J. *Molecular Biology of the Cell*. Garland Publishing Inc., New York and London, 1994.

[2] RISLEY, J. M. Cholesterol Biosynthesis: Lanosterol to Cholesterol. *J. Chem. Ed.*, 2002, **79**, 377–384.

[3] LANGE, Y., AND RAMOS, B. V. Analysis of the distribution of cholesterol in the intact cell. *J. Biol. Chem.*, 1983, **258**, 15130–15134.

[4] FINEGOLD, L. *Cholesterol in Membrane Models*. CRC Press, Boca Barton, FL, 1985.

[5] RUSSELL, D. W., AND SETSCHELL, K. D. Bile acid biosynthesis. *Biochemistry*, 1992, **31**, 4737–4749.

[6] SCHOONJANS, K., BRENDEL, C., MANGELSDORF, D., AND ANXWERX, J. Sterols and gene expression: Control of affluence. *Biochim. Biophys. Acta*, 2000, **1529**, 114–125.

[7] KUSUMI, A., TSUDA, M., AKINO, T., OHNISHI, O., AND TERAYAMA, Y. Protein-phospholipid-cholesterol interaction in the photolysis of invertebrate rhodopsin. *Biochemistry*, 1983, **22**, 1165–1170.

[8] BLOCH, K. *Cholesterol, evolution of structure and function. In:* Biochemistry of Lipids and Membranes, Eds. J. E. Vance and D. E. Vance, Benjamin/Cummins Pub. Co. Inc., New York, 1985, pp. 1–24.

[9] SIMONS, K., AND TOOMRE, D. Lipid rafts and signal transduction. *Nature Rev. Mol. Cell Biol.*, 2000, **1**, 31–39.

[10] HAINES, T. H. Do sterols reduce proton and sodium leaks through lipid bilayers? *Prog. Lipid Res.*, 2001, **40**, 299–324.

[11] CEVC, G., AND MARSH, D. *Phopsholipid bilayers: Physical principles and models*. Wiley, New York, 1987.

[12] POLOZOV, I. V., AND GAWRISCH, K. Characterization of the Liquid-Ordered State by Proton MAS NMR. *Biophys. J.*, 2006, **90**, 2051–2061.

[13] VIST, M. R., AND DAVIS, J. H. Phase equilibria of cholesterol/dipalmitoylphosphatidylcholine mixtures: ^{2}H nuclear magnetic resonance and differential scanning calorimetry. *Biochemistry*, 1990, **29**, 451–464.

[14] ZUCKERMANN, M. J., IPSEN, J. H., AND MOURITSEN, O. G. *Theoretical studies of the phase behavior of lipid bilayers containing cholesterol*. *In:* Cholesterol in Membrane Models, CRC Press, Boca Barton, FL, 1993, pp. 223–256.

[15] MIAO, L., NIELSEN, M., THEWALT, J., IPSEN, J., BLOOM, M., ZUCKERMANN, M. J., AND MOURITSEN, O. G. From lanosterol to cholesterol: structural evolution and differential effects on lipid bilayers. *Biophys. J.*, 2002, **82**, 1429–1444.

[16] MOURITSEN, J. H. I. O. G., AND ZUCKERMANN, M. J. Theory of thermal anomalies of the specific heat of lipid bilayers containing cholesterol. *Biophys. J.*, 1989, **56**, 661–667.

[17] IPSEN, J. H., KARLSTROEM, G., MOURITSEN, O. G., WENNERSTROEM, H., AND ZUCKERMANN, M. J. Phase equilibria in the phosphatidylcholine-cholesterol system. *Biochim. Biophys. Acta*, 1987, **905**, 162–172.

[18] HSUEH, Y.-W., GILBERT, K., TRANDUM, C., ZUCKERMANN, M., AND THEWALT, J. The effect of ergosterol on dipalmitoylphosphatidylcholine bilayers: A deuterium NMR and calorimetric study. *Biophys. J.*, 2005, **88**, 1799–1808.

[19] BROWN, D. A., AND LONDON, D. Functions of lipid rafts in biological membranes. *Annu. Rev. Cell Dev. Biol.*, 1998, **14**, 111–136.

[20] BAUMGART, T., HESS, S. T., AND WEBB, W. W. Imaging coexisting fluid domains in biomembrane models coupling curvature and line tension. *Nature*, 2003, **425**, 821–824.

[21] SILVIUS, J. R. Role of choleserol in lipid raft formation: lessons from lipid model systems. *Biochim. Biophys. Acta*, 2003, **1610**, 174–183.

[22] SIMONS, K., AND IKONEN, E. Functional rafts in cell membranes. *Nature*, 1997, **387**, 569–572.

[23] MCCONELL, H. M., AND RADHAKRISHNAN, A. Condensed complexes of cholesterol and phospholipids. *Biochim. Biophys. Acta*, 2003, **1610**, 159–173.

[24] KELLER, S. L., III, W. H. P., HUESTIS, W. H., AND MCCONNELL, H. M. Red blood cell lipids form immiscible liquids. *Phys. Rev. Lett*, 1998, **81**, 5019–5022.

[25] RIETVELD, A., AND SIMONS, K. The differential miscibility of lipids as the basis for the formation of functional membrane rafts. *Biophys. J.*, 1998, **1376**, 467–479.

[26] RADHAKRISHNAN, A., ANDERSON, T. G., AND MCCONNELL, H. M. Condensed complexes, rafts, and the chemical activity of cholesterol in membranes. *Proc. Natl. Acad. Sci. USA*, 2000, **97**, 12422–12427.

[27] ANDERSON, T. G., AND MCCONNELL, H. M. Condensed complexes and the calorimetry of cholesterol-phospholipid bilayers. *Biophys. J.*, 2001, **81**, 2774–2785.

[28] SINGER, S. J., AND NICHOLSON, G. L. The fluid mosaic model of the structure of cell membranes. *Science*, 1972, **175**, 720–731.

[29] ENGELMAN, D. Membranes are more mosaic than fluid. *Nature*, 2005, **438**, 578–580.

[30] CLARKE, J. A., HERON, A. J., SEDDON, J. M., AND LAW, R. V. The diversity of the liquid ordered phase (L_o) phase of phosphatidylcholine/cholesterol membranes: a variable temperature multinuclear solid-state NMR and X-Ray diffraction study. *Biophys. J.*, 2006, **90**, 2383–2393.

[31] XU, X., BITTMAN, R., DUPORTAIL, G., HEISSLER, D., VILCHEZE, C., AND LONDON, E. Effect of the structure of natural sterols and sphingolipids on the formation of ordered sphingolipid/sterol domains (rafts). *J. Biol. Chem.*, 2001, **276**, 33540–33546.

[32] XU, X., AND LONDON, E. The effect of sterol structure on membrane lipid domains reveals how cholesterol can induce lipid domain formation. *Biochemistry*, 2000, **39**, 843–849.

[33] BACIA, K., SCHWILLE, P., AND KURZCHALIA, T. Sterol structure determines the separation of pahses and the curvature of the liquid-ordered phase in model membranes. *Proc. Natl. Acad. Sci. USA*, 2005, **102**, 3272–3277.

[34] FANTINI, J., GARMY, N., MAHFOUD, R., AND YAHI, N. Lipid rafts: structure, function and role in HIV, Alzheimer s and prion diseases. *Exp. Rev. Mol. Med.*, 2002, **1**, 1–22.

[35] BARON, G. S., WEHRLY, K., DORWARD, D. W., CHESEBRO, B., AND CAUGHEY, B. Conversion of raft associated prion protein to the protease-resistant state requires insertion of PrP-res (PrP(Sc)) into contiguous membranes. *EMBO J.*, 2002, **21**, 1031–1040.

[36] SIMONS, K., AND EHEHALT, R. Cholesterol, lipid rafts and disease. *J. Clin. Invest.*, 2002, **110**, 597–603.

[37] SMONDYREV, A., AND BERKOWITZ, M. L. MD Simulation of the structure of DMPC bilayers with Cholesterol, Ergosterol, and Lanosterol. *Biophys. J.*, 2001, **80**, 1649–1658.

[38] TIERNEY, K. J., BOCK, D. E., AND LONGO, M. L. Elasticity and phase behavior of DPPC membrane modulated by cholesterol, ergosterol and ethanol. *Biophys. J.*, 2005, **89**, 2481–2493.

[39] ARORA, A., RAGHURAMAN, H., AND CHATTOPADHYAY, A. Influence of cholesterol and ergosterol on membrane dynamics: a fluorescence approach. *Biochim. Biophys. Acta*, 2004, **318**, 920–926.

[40] BEATTIE, M. E., VEATCH, S. L., STOTTRUP, B. L., AND KELLER, S. L. Sterol structure determines miscibility versus melting transitions in lipid vesicles. *Biophys. J.*, 2005, **89**, 1760–1768.

[41] SOUBIAS, O., JOLIBOIS, F., MASSOU, S., MILON, A., AND REAT, V. Determination of the orientation and dynamics of ergosterol in model membranes using uniform 13C and dynamically averaged 13C chemical shift anisotropies as experimental restraints. *Biophys. J.*, 2005, **89**, 1120–1131.

[42] ORÄDD, G., LINDBLOM, G., AND WESTERMAN, P. W. Lateral Diffusion of Cholesterol and Dimyristoylphosphatidylcholine in a Lipid Bilayer Measured by Pulsed Field Gradient NMR Spectroscopy. *Biophys. J.*, 2002, **83**, 2702–2704.

[43] A.SCHEIDT, H., HUSTER, D., AND GAWRISCH, K. Diffusion of Cholesterol and its Precursors in Lipid Membranes Studied by ^{1}H Pulsed Field Gradient Magic Angle Spinning NMR. *Biophys. J.*, 2005, **89**, 2504–2512.

[44] MARTINEZ, G. V., DYKSTRA, E. M., LOPE-PIEDRAFITA, S., AND BROWN, M. F. Lanosterol and cholesterol-induced variations in bilayer elasticity probed by H-2 NMR relaxation. *Langmuir*, 2004, **20**, 1043–1046.

[45] ENDRESS, E., BAYERL, S., PRECHTEL, K., MAIER, C., MERKEL, R., AND BAYERL, T. M. The effect of cholesterol, lanosterol, and ergosterol on lecithin bilayer mechanical properties at molecular and microscopic dimensions: A solid-state NMR and micropipet study. *Langmuir*, 2002, **18**, 3292–3299.

[46] DOXASTAKIS, M., SUM, A. K., AND DE PABLO, J. J. Modulating Membrane Properties: The Effect of Trehalose and Cholesterol on a Phospholipid Bilayer. *J. Phys. Chem. B*, 2005, **109**, 24173–24181.

[47] HOFSÄSS, C., LINDAHL, E., AND EDHOLM, O. Molecular dynamics simulations of phospholipid bilayers with cholesterol. *Biophys. J.*, 2003, **84**, 2192–2206.

[48] FILIPPOV, A., ORÄDD, G., AND LINDBLOM, G. The effect of cholesterol on the lateral diffusion of phospholipids in oriented bilayers. *Biophys. J.*, 2003, **84**, 3079–3086.

[49] ALMEIDA, P. F. F., VAZ, W. L. C., AND THOMPSON, T. E. Lateral diffusion in the liquid phases of dimyristoylphosphatidylcholine/cholesterol lipid bilayers: A free volume analysis. *Biochemistry*, 1992, **31**, 6739–6747.

[50] BAUDRY, J., TAJKHORSHID, E., MOLNAR, F., PHILLIPS, J., AND SCHULTEN, K. Molecular Dynamics Study of Bacteriorhodopsin and the Purple Membrane. *J. Phys. Chem. B*, 2001, **105**, 905–918.

[51] MIHAILESCU, D., AND SMITH, J. C. Atomic detail peptide-membrane interactions: Molecular Dynamics of gramicidine S in a DMPC bilayer. *Biophys. J.*, 2000, **79**, 1718–1730.

[52] BERNECHE, S., NINA, M., AND ROUX, B. Molecular Dynamics simulation of melittin in a dimyristoyl phosphatidylcholine bilayer membrane. *Biophys. J.*, 1998, **75**, 1603–1618.

[53] FORREST, L., KUKOL, A., ARKIN, I., TIELMAN, A., AND SANSOM, M. Exploring the models of Influenza M2 channel - MD Simulations in a phospholipid bilayer. *Biophys. J.*, 2000, **78**, 55–69.

[54] SMONDYREV, A. M., AND BERKOWITZ, M. L. Structure of DPPC/Cholesterol bilayer at low and high cholesterol concentrations: molecular dynamics simulation. *Biophys. J.*, 1999, **77**, 2075–2089.

[55] CHIU, S. W., JACOBSSON, E., AND SCOTT, H. L. Combined MC and MD simulation of hydrated lipid-cholesterol lipid bilayers at low Cholesterol concentration. *Biophys. J.*, 2001, **80**, 1104–1114.

[56] TU, K., KLEIN, M. L., AND TOBIAS, D. J. Constant-Pressure MD investigation of Cholesterol effects in a DPPC bilayer. *Biophys. J.*, 1998, **75**, 2147–2156.

[57] CZUB, J., AND M.BAGINSKI. Comparative molecular dynamics study of lipid membranes containing cholesterol and ergosterol. *Biophys. J.*, 2006, **90**, 2368–2382.

[58] KOYNOVA, R., AND CAFFREY, M. Phases and phase transitions of the phosphatidylcholines. *Biochim. Biophys. Acta*, 1998, **1376**, 91–145.

CHAPTER 2

METHODS AND THEORY

This chapter presents the theoretical foundations of the present work. First, an introduction to density functional theory (DFT) is presented, which is the method that is used for the quantum chemical calculations performed in this study. Next, a molecular modelling introduction is given, including energy minimization methods, normal mode analysis and a description of the molecular dynamics simulation technique and the potential energy function used (force field). The automated frequency matching method (AFMM) for the optimization of the intra-molecular force field parameters is then presented, as well as the CHELPG method for calculating the partial atomic charges. Finally, a brief introduction to neutron scattering is given.

2.1 QUANTUM CHEMICAL CALCULATIONS

2.1.1 DENSITY FUNCTIONAL THEORY

The basis for the Density Functional Theory (DFT) is the proof by Hohenberg, Kohn and Sham[1, 2] that the ground-state electronic energy is determined completely by the electron density ρ. In other words, for the ground state there is a one-to-one correspondence between the electron density and the nuclear potential, and thereby also with the Hamilton operator and the energy. That means that the energy is a unique functional of the electron density, $E[\rho]$. The significance of this observation is pointed out if compared to the wavefunction approach. A wavefunction for an N-electron system contains $3N$ coordinates, three for each electron (or four, if the spin is included). On the contrary, the electron density is the square of the wavefunction, integrated over $N-1$ electron coordinates, which depends only on *three* coordinates and is independent of the number of electrons. Therefore, DFT is primarily a theory of electronic ground state structures based on the electron density, $\rho(\mathbf{r})$, and three variables as op-

posed to the many-electron wavefunction $\Psi(\mathbf{r}_1, \ldots, \mathbf{r}_N)$, requiring $3N$ variables.[3]

However, although it is proven that each different density yields a different ground-state energy, the functional that connect these two quantities is not known. The goal of DFT methods is to design functionals connecting the electron density with the energy.[4] A wavefunction and the electron density are functions, because they produce numbers from a set of coordinates, while the energy, which depends on a wavefunction or an electron density, is a functional. The energy functional can be divided into three parts, kinetic energy, $T[\rho(\mathbf{r})]$, attraction between nuclei and electrons, $E_{att}[\rho(\mathbf{r})]$, and the repulsion between electrons, $E_{rep}[\rho(\mathbf{r})]$. The electron repulsion term can be divided into a Coulomb and an Exchange part, $E_c[\rho(\mathbf{r})]$, and $E_{xc}[\rho(\mathbf{r})]$, which implicitly include correlation energies in all terms. Therefore, within the KS formalism, the unknown Hohenberg-Kohn functional, $E[\rho(\mathbf{r})]$, is partitioned in the following manner:[5, 6]

$$E[\rho(\mathbf{r})] = T + E_{att} + E_c + E_{xc} \tag{2.1}$$

where T is the kinetic energy, E_{att} is the electron-nuclear interaction energy, E_c is the Coulomb self-interaction of the electron density $\rho(\mathbf{r})$, and E_{xc} is the exchange-correlation energy.

However, difficulties arise when the kinetic and exchange energy functionals are constructed, and the kinetic energy is thus poorly represented. The foundation for the use of DFT methods further, was the introduction of orbitals by Kohn and Sham (KS).[2] The basic idea behind the Kohn and Sham (KS) formalism splits the kinetic energy functional into two parts, one of which can be calculated exactly, and one small correction term. With the introduction of orbitals the exact kinetic energy can be calculated from the natural orbitals (eigenvectors of the exact density matrix).

Since the exact electron density is not known, the (approximate) density is written in terms of a set of auxiliary one-electron orbitals. Therefore, the key to Kohn-Sham theory is the calculation of the kinetic energy under the assumption of non-interacting electrons. In reality, the electrons are interacting, so the remaining kinetic energy is implicitly included in an exchange-correlation (XC) term.

Following the KS formalism, $\rho(\mathbf{r})$ of an N-electron system (with N^α spin up electrons and N^β spin down electrons) is expressed as the sum of the square moduli of singly occupied orthonormal KS molecular orbitals,

$$\rho(\mathbf{r}) = \rho^\alpha(\mathbf{r}) + \rho^\beta(\mathbf{r}) = \sum_i^{N^\alpha} |\psi_i^\alpha(\mathbf{r})|^2 + \sum_i^{N^\beta} |\psi_i^\beta(\mathbf{r})|^2 \tag{2.2}$$

Having done this, $T[\rho(\mathbf{r})]$ can now be defined as:

$$T[\rho(\mathbf{r})] = \sum_{\sigma=\alpha,\beta} \sum_{i}^{N^\sigma} \int \psi_i^\sigma(\mathbf{r}) \frac{-\nabla^2}{2} \psi_i^\sigma(\mathbf{r}) d\mathbf{r} \tag{2.3}$$

One should note that $T[\rho(\mathbf{r})]$ is not a true density functional, because the KS orbitals are required. Finally, recalling the fact that the energy functional is minimized by the true ground state density, $\rho(\mathbf{r})$, the energy functional, $E[\rho(\mathbf{r})]$, must be stationary with respect to any arbitrary variation in either of the spin densities, *i.e.*,

$$\frac{\delta E[\rho(\mathbf{r})]}{\delta \rho^\alpha(\mathbf{r})} = \frac{\delta E[\rho(\mathbf{r})]}{\delta \rho^\beta(\mathbf{r})} = 0 \tag{2.4}$$

This condition yields the one-electron KS equations,

$$\left\{ \frac{-\nabla^2}{2} - \left(\sum_A \frac{Z_A}{|\mathbf{r} - \mathbf{R}_A|} \right) + \int \frac{\rho(\mathbf{r}')}{|\mathbf{r} - \mathbf{r}'|} d\mathbf{r}' + \frac{\delta E_{xc}[\rho(\mathbf{r})]}{\delta \rho^\sigma(\mathbf{r})} \right\} \psi_i^\sigma(\mathbf{r}) = \epsilon_i \psi_i^\sigma(\mathbf{r}) \tag{2.5}$$

with $\sigma = \alpha, \beta$. A scheme for performing practical DFT calculations thus emerges. With an initial guess at the total spin densities, $\rho^\alpha(\mathbf{r})$ and $\rho^\beta(\mathbf{r})$, the KS equations are constructed and solved, and the resulting set of KS spin-orbitals, $\{\psi_i^\sigma(\mathbf{r})\}$, are then used to generate new guesses at $\rho^\alpha(\mathbf{r})$ and $\rho^\beta(\mathbf{r})$. This procedure is repeated until self-consistency is achieved so that the same densities and KS orbitals are regenerated.

In the preceding discussion the precise nature of the XC energy functional, $E_{xc}[\rho(\mathbf{r})]$, and the XC potentials, which are the functional derivatives of $E_{xc}[\rho(\mathbf{r})]$ with respect to $\rho^\alpha(\mathbf{r})$ and $\rho^\beta(\mathbf{r})$ was not discussed; $\nu_{xc}^\alpha(\mathbf{r})$ and $\nu_{xc}^\beta(\mathbf{r})$ are formally given by

$$\nu_{xc}^\sigma(\mathbf{r}) = \frac{\delta E_{xc}[\rho(\mathbf{r})]}{\delta \rho^\sigma(\mathbf{r})} \tag{2.6}$$

If the true XC energy functional, $E_{xc}[\rho(\mathbf{r})]$, were known, this scheme would yield the true ground state density, and in turn, exact values for all ground state properties. Unfortunately, the precise form of $E_{xc}[\rho(\mathbf{r})]$ is not known. However, very simple approximations to $E_{xc}[\rho(\mathbf{r})]$ can yield fairly accurate results. The KS approach is therefore of great practical importance and has become the cornerstone of all modern DFT applications.

DFT has been recently very popular among computational chemists, the reasons being its relatively cheap computational expense together with its proven chemical accuracy. The major problem in DFT is deriving suitable functionals for the

exchange-correlation term. The drawback of DFT is that one has to carefully choose the exchange-correlation functional because the energy functionals are parameterized. Therefore the choice of the functional depends on the question asked and the system studied.

2.1.2 EXCHANGE-CORRELATION FUNCTIONALS

There is an increasing number of exchange and correlation functionals as well as hybrid DFT methods. In short, there are two basic types of functionals: those based on the local spin density approximation (LSDA) and those based on generalized gradient approximations (GCA). Hybrid exchange-correlation functionals linearly combine several different exchange and correlation functionals to form a new functional have also proven to be successful. The most commonly-used hybrid functionals are B-LYP and B3LYP.

2.2 MOLECULAR MODELLING

2.2.1 ENERGY MINIMIZATION

Function optimization is a calculation that requires much of numerical analysis. In the context of biomolecules, the function to be optimized (minimized) is the potential energy. The potential energy of biological systems is a complicated, multidimensional function of the $3N$ Cartesian coordinates of the system. The energy landscape of a biomolecule possesses an enormous number of minima, or conformational substates. The goal of energy minimization is to find the local energy minimum, *i.e.*, the bottom of the energy well occupied by the initial conformation (see Fig.2.1). The energy at this local minimum may be much higher than the energy of the global minimum. Physically, energy minimization corresponds to an instantaneous freezing of the system. A static structure in which no atom feels a net force that corresponds to a temperature of 0 K. To identify those geometries of the system that correspond to minimum points on the energy surface minimization algorithms are used. Minimization algorithms are very important for MD simulations in order to calculate to start from a structure that corresponds to the local minimum and avoid unwanted high energy interactions.

Given a function f which depends on the variables $x_1, x_2, \ldots, x_n$, a minimum of f is defined as a point where the first derivative of the function with respect to each of

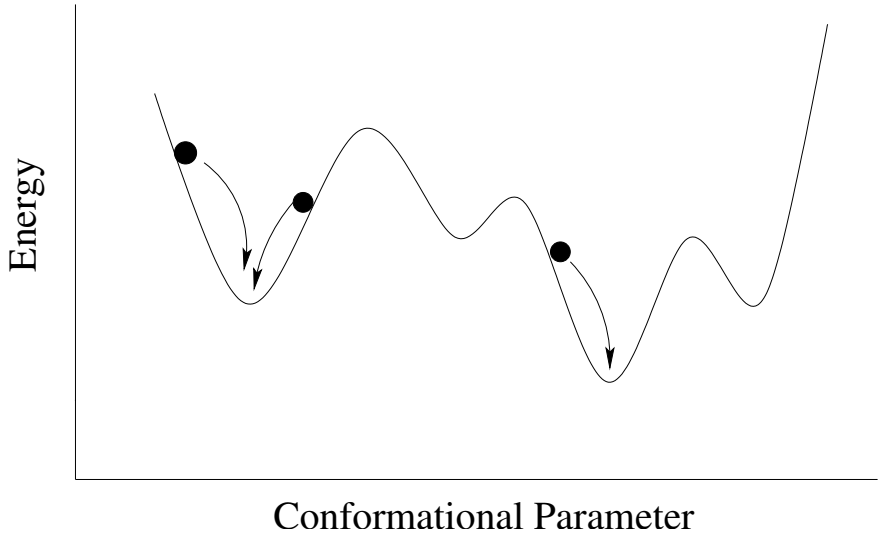

Figure 2.1: A schematic one-dimensional potential energy surface. Minimization methods move downhill to the nearest minimum.

the variables is zero and the second derivatives are all positive:

$$\frac{\partial f}{\partial x_i} = 0; \frac{\partial^2 f}{\partial x_i^2} > 0 \tag{2.7}$$

For analytical functions, minima can be found using standard calculus methods. However, for biomolecular systems this is not possible, since the shape of the potential energy landscape (PES) cannot be expressed by an analytical function. Therefore, for these systems, the minima can be calculated by using numerical methods that gradually change the coordinates to produce configurations with decreasing energies until a convergence criterion is achieved.

Most common minimization algorithms use derivatives of the energy with respect to the coordinates to predict the location of the closest minimum. There are two factors that need to be taken into consideration for a minimization algorithm: speed of convergence and memory requirements. Since no single method has yet been proved to be the best for all problems, a combination of different algorithms for the minimization of biological molecules is commonly used. Most minimization algorithms can go only downhill on the energy surface. Therefore, they can only locate the minimum that is nearest to the starting point (see Fig. 2.1). To be able to locate more minima on a PES, different starting points are required.

The energy minimization procedures used in this work are a combination of three derivative minimization methods: the Steepest Descent (SD), the Conjugate Gradients (CG) and the Newton-Raphson (NR) methods.

When discussing derivative methods it is useful to write the potential energy function V as a Taylor series expansion about the point $\mathbf{r}_0$:

$$V(\mathbf{r}) = V(\mathbf{r}_0) + V'(\mathbf{r}_0)(r - r_0) + \frac{V''(\mathbf{r}_0)(r - r_0)^2}{2} + \dots \tag{2.8}$$

where $V(\mathbf{r})$ is the potential energy of the system with respect to the coordinates. The vector $\mathbf{r}$ has $3N$-dimensional components and $\mathbf{r}_0$ corresponds to the current configuration of the system. In the vicinity of a minimum, $V(\mathbf{r})$ can be described by truncating the series at the second order.

The direction of the first derivative of the energy indicates the direction to a minimum and the magnitude of the gradient indicates the steepness of the local slope. By moving each atom in response to the force (negative gradient) acting on it, the energy of the system is lowered. The second derivatives of the potential energy indicate the curvature of the function, and this information can be used to predict where the function will change its direction.

The minimization algorithms can be divided into two categories: those which use the derivatives of the energy with respect to the coordinates and those which do not. Derivative methods can be classified according to the highest order derivative used. First-order methods use the first derivatives whereas second-order methods use both first and second derivatives.

The SD and the CG are both first-order minimization methods. They gradually change the coordinates of the atoms from an initial configuration provided by the user as they move the system closer and closer to the minimum point.

STEEPEST DESCENTS

The SD method moves in the direction parallel to the net force, *i.e.* downhill. For $3N$ Cartesian coordinates this direction is most conveniently represented by a $3N$-dimensional unit vector, $\mathbf{s}_k$.

$$\mathbf{s}_k = -\mathbf{g}_k / |\mathbf{g}_k| \tag{2.9}$$

where $\mathbf{g}_k$ is the gradient at one given point. The minimum is located iteratively by using a line search algorithm. A line search is used to locate the minimum in the function on the direction opposite to the gradient. The search starts at an arbitrary point and then slides down the gradient, until it is close enough to the solution. The SD method is very robust, meaning that the minimum is found even when the starting structure is far away from the minimum. The SD is a good method for relieving unwanted high energies in an initial configuration. However, if the minimum lies in

a long, narrow valley then the SD method will perform many small steps. Due to the inflexible determination of the search direction the path oscillates and continually overcorrects itself. Later steps might reintroduce then errors that were corrected by earlier moves.

CONJUGATE GRADIENTS

The CG method produces a set of directions which does not show the oscillatory behavior of the SD method in narrow valleys. In the SD method both the gradients and the direction of successive steps are orthogonal. In conjugate gradients, the gradients at each point are orthogonal but the directions are conjugate. A set of conjugate directions has the property that for a quadratic function of M variables, the minimum will be reached in M steps. The CG method moves in a direction $\mathbf{v}_k$ from point $\mathbf{x}_k$, where $\mathbf{v}_k$ is computed from the gradient at the current point and the previous direction vector $\mathbf{v}_{k-1}$:

$$\mathbf{v}_k = -\mathbf{g}_k + \gamma_k \mathbf{v}_{k-1} \tag{2.10}$$

where γ_k is a scalar factor given by

$$\gamma_k = \frac{\mathbf{g}_k \cdot \mathbf{g}_k}{\mathbf{g}_{k-1} \cdot \mathbf{g}_{k-1}} \tag{2.11}$$

In the conjugate gradients method all of the directions and gradients satisfy the following relationships:

$$\mathbf{g}_i \cdot \mathbf{g}_i = 0 \tag{2.12}$$

$$\mathbf{v}_i \cdot \ V''_{ij}(\mathbf{r}) \cdot \mathbf{v}_i = 0 \tag{2.13}$$

$$\mathbf{g}_i \cdot \mathbf{v}_j = 0 \tag{2.14}$$

where V is the potential energy of the system as a function of the coordinates.

NEWTON-RAPHSON METHOD

The NR method is a second-derivative method. This method uses the inverted matrix of the second derivatives of the energy with respect to the coordinates, which is referred to as the "Hessian matrix". This can be computationally demanding for systems with many atoms and can also require a significant amount of storage. It is therefore used after one has used the SD and CG methods for a small number of steps in the study of biological systems.

For a purely harmonic function the method finds the minimum in only one step from any point of the PES. As the PES contains anharmonic terms, an iterative cy-

cle has to be used, in which the Hessian matrix is calculated and inverted. In the NR method, the eigenvalues of the Hessian matrix must be positive. When the eigenvalues are negative, then the NR method moves to saddle points where the energy increases. Far away from the minimum the harmonic approximation is not valid and the minimization can become unstable. One solution to this problem is to use a more robust method (such as SD or CG) to approach the minimum and then apply the NR method.

Energy minimization is of special interest for both quantum mechanics and molecular mechanics calculations. It can be used to prepare a system for other types of calculations (e.g. MD simulations) or it can aid in conformational search procedures. Moreover, one of the most important applications of potential energy minimizations is normal mode analysis.

2.2.2 NORMAL MODE ANALYSIS

In both QM and MM calculations, normal modes are useful because they provide an orthonormal basis of the configurational space of a system in which collective motions of the atoms can be represented. That is, in a coupled system the normal modes describe independent motions of the whole system that can be individually excited. A non-linear molecule with N atoms has $3N - 6$ vibrational modes and 6 global translational and rotational modes. The frequencies of the normal modes as well as the displacements of the individual atoms when a particular normal mode is excited, can be calculated from a MM force field or from the QM wavefunction. To calculate the normal modes, the Hessian matrix is used in a minimum of the PES. The normal mode analysis is based on the assumption that the energy surface is harmonic in the vicinity of the energy minimum.

The starting point of the calculation is Newton's equations of motion for a system of coupled harmonic oscillators. These can be written in a matrix form as:

$$\mathbf{M}\frac{d^2}{dt^2}(\Delta\mathbf{r}) = -V''(\mathbf{r}_0)\Delta\mathbf{r} \tag{2.15}$$

where $\mathbf{r}$ is a $3N$ diagonal matrix containing the masses of the nuclei and $\Delta\mathbf{r} = \mathbf{r} - \mathbf{r}_0$ is the vector of the displacements of the nuclear coordinates. The solution of this differential equation is of the form:

$$\Delta\mathbf{r} = \mathbf{Y}e^{i(\omega t+\phi)}, \tag{2.16}$$

where ϕ is an arbitrary phase shift, $\mathbf{Y}$ is a vector and ω is a scalar. From the two previous equations it follows that:

$$[\mathbf{M}\omega^2 - V''(\mathbf{r}_0)]\mathbf{Y} = 0. \tag{2.17}$$

This is a homogeneous system of linear equations that must be solved for $\mathbf{M}$. In order to get non-zero solutions $det[\mathbf{M}\omega^2 - V''(\mathbf{r}_0)]$ must be zero. We can re-write this expression as:

$$det[\mathbf{M}\omega^2 - V''(\mathbf{r}_0)] = det[\omega^2 - \mathbf{M}^{-1/2}V''(\mathbf{r}_0)\mathbf{M}^{-1/2}]det(\mathbf{M}) = 0 \tag{2.18}$$

$$-det[\mathbf{M}^{-1/2}V''(\mathbf{r}_0)\mathbf{M}^{-1/2} - \omega^2 \cdot I]det(\mathbf{M}) = 0 \tag{2.19}$$

where I is the identity matrix. Since $det(\mathbf{M}) \neq 0$, $-det[\mathbf{M}^{-1/2}V''(\mathbf{r}_0)\mathbf{M}^{-1/2} - \omega^2 \cdot I] = 0$, which is the characteristic polynomial associated with the eigenvalue problem. The solution of this equation will result in the eigenvalues, ω^2 (the frequencies of the normal modes squared) and the respective eigenvectors $\mathbf{u}$.

The main limit of the normal mode analysis is that it is based upon the assumption that the PES is harmonic in the vicinity of the energy minimum. Deviations from the harmonic model can require corrections to calculated thermodynamic properties. One way to estimate anharmonic corrections is to calculate a force constant matrix using the atomic motions obtained from a molecular dynamics simulation. In other words, MD calculations allow exploration of the full potential energy landscape, by implicitly including anharmonic motions. In spite of the neglect of anharmonic contributions to the potential, however, normal mode descriptions of biological-system dynamics have proved to provide useful results concerning the internal motions of these systems.[7,8]

2.2.3 MOLECULAR DYNAMICS SIMULATIONS

This section covers the theoretical background to Molecular Dynamics (MD) pertinent to the present work. For an in-depth introduction to molecular dynamics the reader is referred to the books by A. Leach[9] and by Allen and Tildesey.[10] In the following, the scope of MD is highlighted, as well as how we perform simulations, how we obtain force fields and how we can calculate macroscopic properties for the systems under study from the MD simulations.

Molecular modelling is dedicated to the study of the properties of molecular systems with the aid of computer models. Very commonly molecular modelling is used to study the properties of biological molecules. The size of biological systems, as well as the time scales in which interesting phenomena occur, is prohibitive for their study

with QM. QM describe the electrons of a system, and this results in a huge number of particles that have to be considered in the study of a biological system (see Fig. 2.2) Since it is not computationally feasible to treat such systems with QM, approximate methods, such as Molecular Dynamics, have been developed. MD uses an empirical potential to calculate the energy of a system based on the nuclear positions only. To describe the dynamics of the system, MD simulations numerically integrate Newton's equations of motion to generate information about the system on the microscopic level. Then the microscopic information is linked to the macroscopic observables *via* statistical mechanics.

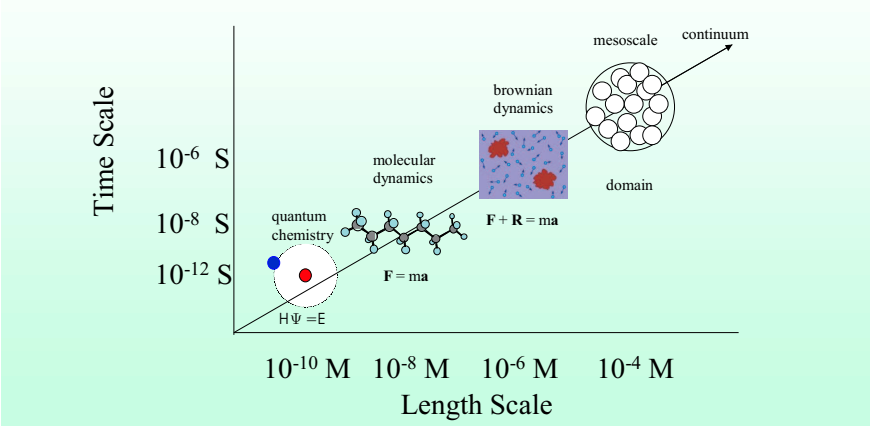

Figure 2.2: Graphical representation of the different time and length scales achieved by different methods in molecular modelling.

MD is nowadays an established modelling method for the study of biomolecular systems and it has proved to provide accurate results in many cases. The success of MD is lying in the validity of different approximations that are assumed in this method. First of all, the Born-Oppenheimer approximation, which states that the electronic motion and the nuclear motion in molecules can be separated and that the nuclear motion is so much slower than electron motion that they can be considered to be fixed. The empirical potential energy function is also a physical model employed to describe the intra- and inter-molecular interactions that occur between the nuclei. Even when simple functions, such as Hooke's law are used to describe these contribution to the energy function, the description of the properties of the system is quite accurate. These simple functions that come together to describe the total energy of the system are called the 'force field' and will be described in the following section.

2.2.4 FORCE FIELD: THE EMPIRICAL POTENTIAL ENERGY FUNCTION

The functional form adopted for the potential energy is designed to allow efficient computation of the energy of a system as a function of the coordinates. The potential energy, $V(\mathbf{r})$, can be described as the sum over the bonded and non-bonded energy terms in the system:

$$V(\mathbf{r}) = V_{bonded} + V_{nonbonded} \tag{2.20}$$

BONDED INTERACTIONS

The bonded terms describe simple covalent binding as well as implicitly taking into account more complex hybridization. Simple harmonic terms describe bond stretching and angle bending. Rotation about single bonds (torsions) is described by sinusoidal energies. The planarity of groups (e.g., the planarity of the double bond) can be enforced by harmonic potentials known as improper torsions. These terms are schematically drawn in figure 2.3.

$$V_{bonded} = V_{bonds} + V_{angles} + V_{dihedrals} + V_{impropers} \tag{2.21}$$

BOND STRETCHING

The bond stretching term describes the forces acting between two covalently bonded atoms. The potential is assumed to be approximately harmonic:

$$V_b = k_b(b - b_0)^2 \tag{2.22}$$

where b is the distance between the two atoms. Two parameters characterize each bonded interaction: the equilibrium distance between them, b_0 and a force constant of the spring, k_b. Values for force constants and bond lengths can be evaluated from experimental data, such as infrared stretching frequencies, high-resolution crystal structures, microwave spectroscopy data or theoretically from quantum chemical calculations.

ANGLE BENDING

The angle bending terms describe the force originating from the deformation of the valence angles between three covalently bonded atoms. The deviation of angles from

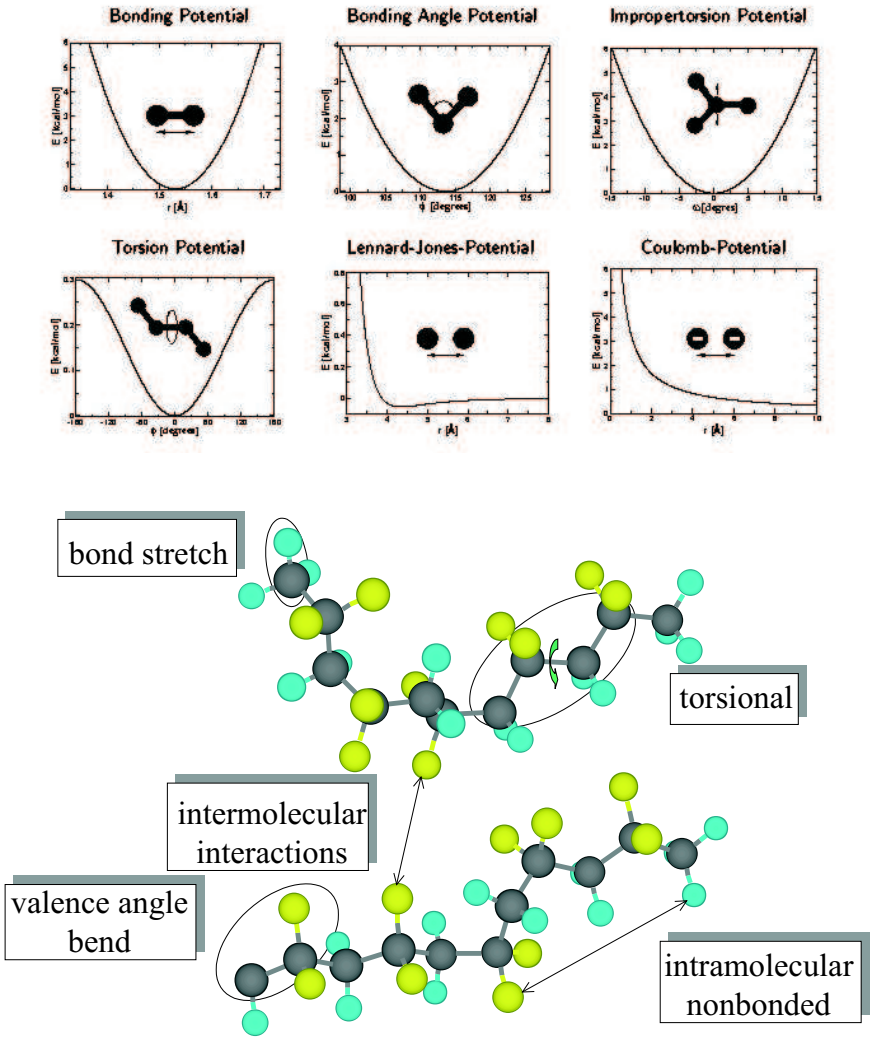

Figure 2.3: Schematic representation of the bonded interaction terms contributing to the force field: bond stretching, angle bending, proper and improper dihedrals.

their equilibrium values is also described using a harmonic potential:

$$V_\theta = k_\theta(\theta - \theta_0)^2, \tag{2.23}$$

where θ is the angle between three atoms. Two parameters characterize also each angle in the system: the equilibrium angle, θ_0 and a force constant, k_θ. Vibrational motions involving angle bending normally occur at lower frequencies than those of typical bond vibrations and therefore less energy is needed to distort an angle from its equilibrium value than to stretch a bond. Therefore, the angle force constants are expected to be much lower than the bond force constants.

UREY-BRADLEY TERM

The Urey-Bradley (UB) term is an interaction term based on the distance between atoms separated by two bonds (1,3 interaction):

$$V_{ub} = k_{ub}(s - s_0)^2 \tag{2.24}$$

where s is the Urey-Bradley 1-3 distance. Again two parameters characterize each UB term in the system: the equilibrium UB term, θ_0 and a force constant, k_{ub}. This term represents a spring connecting 1-3 atoms and is used only in special cases.

TORSIONAL TERMS

The torsional terms are weaker than the bond stretching and angle bending terms. They describe the rotational barriers existing between four bonded atoms. There are two type of torsional terms: proper and improper dihedrals. Proper torsional potentials are described by a cosine function:

$$V_\phi = k_\phi[1 + \cos(n\phi - \delta)], \qquad n = 1, 2, 3, 4, 6 \tag{2.25}$$

where ϕ is the angle between the planes formed by the first and the last three of the four atoms. Three parameters characterize this interaction: δ sets the minimum energy angle, k_ϕ is a force constant, and n is the periodicity.

The improper dihedral term is designed both to maintain chirality about a tetrahedral heavy atom and to maintain planarity about certain atoms. The potential is described by a harmonic function:

$$V_\omega = k_\omega(\omega - \omega_0)^2 \tag{2.26}$$

where ω is the angle between the plane formed by the central atom and two peripheral atoms and the plane formed by the peripheral atoms (see Fig. 2.3).

NON-BONDED INTERACTIONS

The contribution of non-bonded interactions has two components in the energy function: the van der Waals interaction energy and the electrostatic interaction energy:

$$V_{non-bonded} = V_{vdW} + V_{elec} \tag{2.27}$$

The calculation of these interactions is the most time-consuming part, because they contain long-range interactions of the atoms in the system.

VAN DER WAALS INTERACTIONS

The van der Waals force acts on atoms in close proximity (short-range interactions). At short range it is strongly repulsive and at medium range it is weakly attractive. The van der Waals interactions are most commonly modeled by a Lennard-Jones potential:

$$V_{VdW} = 4\epsilon \left[\left(\frac{\sigma}{r}\right)^{12} - \left(\frac{\sigma}{r}\right)^{6} \right] \tag{2.28}$$

where r is the distance between two atoms. The Lennard-Jones (LJ) potential is parametrized by σ, the collision parameter (the separation for which the energy is zero), and ϵ, the depth of the potential well. The LJ model has an attractive part that varies with r^{-6} and a repulsive part that varies with r^{-12}.

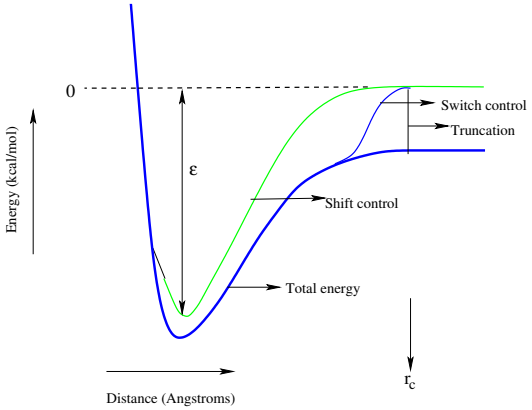

Figure 2.4: A schematic representation of the Lennard-Jones potential. A shifted (green line) or a switched (blue line) or simply a truncation of the potential (black line) can be used to realize a cutoff criterion: beyond the cutoff distance r_c, the potential is zero. The well depth, ϵ is also shown.

In order to reduce the number of interaction terms and thus the calculation time, the LJ potential is often truncated. This is done by defining an appropriate cutoff distance and calculating the pair-wise interactions only for the atoms lying within this distance. All van der Waals interactions of atoms beyond this cutoff are set to zero. Several methods have been developed for the truncation of the LJ term (see Fig. 2.4). One way is to abruptly set the potential to zero at the cutoff distance. However, this causes discontinuities in the force at the cutoff distance. An alternative method is to shift the whole potential to higher values so as to achieve a zero value exactly at the cutoff distance. This method leads to an artificially-induced overestimation of the LJ potential. Another method is to use a switching function to taper the interaction potential over a predefined range of distances. The potential takes its usual value up to the first cutoff and is then switched to zero smoothly between the first and the second cutoff. This model suffers from strong interaction forces in the switching region. The

Lennard-Jones potential and the cutoff methods are schematically represented in 2.4.

ELECTROSTATIC INTERACTIONS

Electronegative elements attract electrons more than less electronegative elements, giving rise to an unequal distribution of charge in a molecule. This charge distribution can be represented in a number of ways, one common approach being an arrangement of fractional point charges throughout the molecule. The charges are designed to reproduce the electrostatic properties of the molecule. Charges restricted to the nuclear centers they are called partial atomic charges.

The long-range electrostatic interaction between two atoms bearing net or partial atomic charges is described by Coulomb's law:

$$V_{Elec} = \frac{q_i q_j}{D r_{ij}} \tag{2.29}$$

where q_1 and q_2 are the charges of both atoms and r_{ij} the distance between them. $D = 4\pi\epsilon_0$, where ϵ_0 is the electric susceptibility in vacuum. The calculation of the partial atomic charges is described in section 2.3.2.

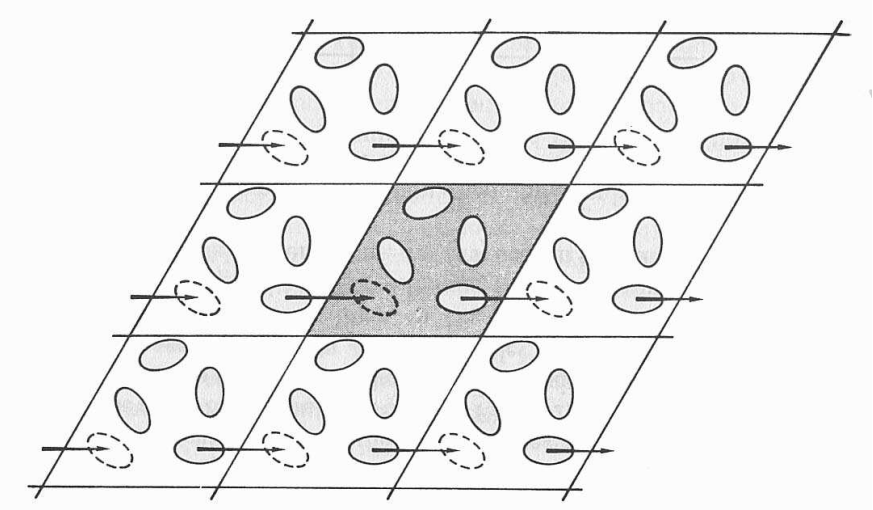

Figure 2.5: A two dimensional periodic system illustrating the periodic boundary conditions used in MD simulations.

In MD simulations the long-range interactions are the most time-consuming ones. The range of these forces is greater than half of the box length for a simulation of 500 molecules. In order to correctly account for the electrostatic interactions one could simply increase the size L of the central box length, so that the potential drops close to 0 at the boundary of the box. Even by using very modern computer systems this

solution is impracticable, since the time required to run such a simulation is proportional to N^2, *i.e.* the computational time is increased by a factor of 64, if one doubles the box length.[10] Many methods have been proposed to solve this problem. The most commonly used method in MD simulations is the Ewald sum, which includes the interaction of an ion or molecule with all its periodic images.[11, 12]

Periodic boundary conditions are very often used in MD simulations as an approximation of an infinite system. They are based on the assumption that the correlation length between two particles is smaller than the box length. We consider a central cubic box in our simulation, which is replicated through space to form an infinite system. During the simulation it is assumed that as a molecule leaves the central box, its periodic image will enter the central box in exactly the same way. There are no walls at the boundary of the central box and no surface molecules. This box forms an axis of the system which we use to measure the coordinates of N molecules. Thus, the number density in the central box is conserved. A two dimensional version of such a periodic system, which illustrates the periodic boundary conditions is shown in Fig. 2.5. Using this method, it is not necessary to store the coordinates of all the images in a simulation, but only the particles of the central box. At this point the question arises of whether the properties of a small, infinitely periodic system and the macroscopic system, which it represents, are the same. The accuracy of such an approximation depends on the range of the intermolecular potential and the phenomenon under investigation, but it is generally considered to be a very good approximation.

The Coulombic potential of such a periodic system can be written then as:

$$U_{ij} = \frac{1}{4\pi\varepsilon_0}\frac{1}{2}{\sum_{\mathbf{n}\neq 0}}' \sum_{i,j=1}^{N} \frac{q_i q_j}{r_{ij,\mathbf{n}}} \tag{2.30}$$

where the sum over $\mathbf{n}$ is the sum over all simple cubic lattice points, $\mathbf{n} = (n_x L, n_y L, n_z L)$, with n_x, n_y, n_z integers. This vector reflects the shape of the central box.

The problem in Eq. 2.30 is that the sum is conditionally convergent. The result of a conditionally convergent sum is dependent on the order in which we add up the terms, and so Eq. 2.30 cannot be handled as a convergent series. To overcome this problem a method developed by Ewald,[11] called the Ewald summation method, can be used. Ewald has originally developed this method for crystals, using their natural periodicity.

The Ewald sum is a technique for efficiently summing up the interaction between ions and all its periodic images. The principle of the Ewald summation method is that it introduces a Gaussian convergence factor, e^{-sn^2}, in the lattice sum by which

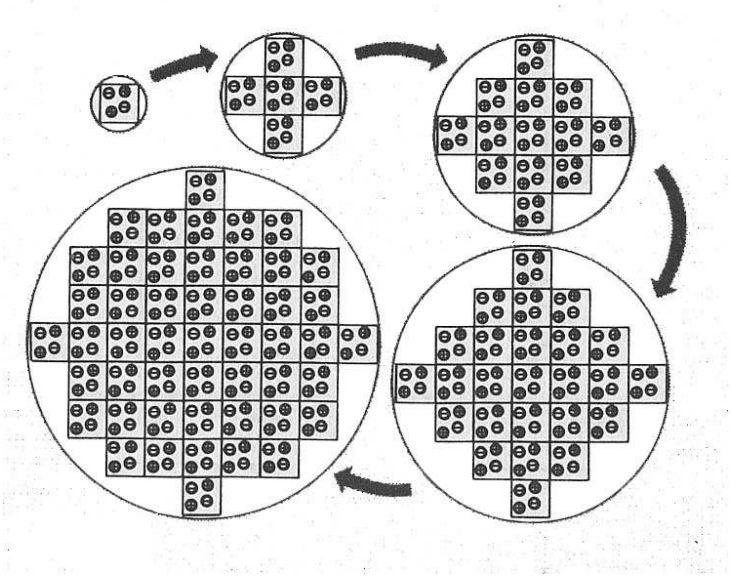

Figure 2.6: Building up the sphere of simulation boxes.

the conditionally convergent series is split into two rapidly convergent sums plus a constant term:

$$U = \frac{1}{2}\sum_{i,j=1}^{N}{\sum_{\mathbf{n}}}' e^{-sn^2}\frac{q_i q_j}{\mid r_i - r_j + \mathbf{n}L \mid} \tag{2.31}$$

At the end of the calculation one has to perform the limit $s \to 0$, *i.e.* $U = lim_{s\to 0}U(s)$. This procedure is done by adding the unit cells in spherical layers and building up an infinite system, as shown in Fig. 2.6. Following this approach, we must also specify the nature of the surrounding medium, that has a dielectric constant, ε. If we consider the surrounding material to be a conductor (*i.e.* tin foil), then the value of this surface term is zero. The equation that is finally obtained has the form:

$$U_{Ewald} = U^{real} + U^{recipr.} + U^{0} + U^{surf.} \tag{2.32}$$

where:

$$U^{real} = \frac{1}{4\pi\varepsilon_0}\frac{1}{2}\sum_{i,j=1}^{N}\left(\underbrace{\sum_{n=0}^{\infty}{}' q_i q_j \frac{erfc(\kappa|\mathbf{r}_{ij}+\mathbf{n}|)}{|\mathbf{r}_{ij}+\mathbf{n}|}}_{\text{real-space term}}\right) \tag{2.33}$$

$$U^{recipr.} = \frac{1}{4\pi\varepsilon_0}\frac{1}{2}\sum_{i,j=1}^{N}\left(\underbrace{(\frac{1}{\pi L^3})\sum_{\mathbf{k}\neq\mathbf{0}} q_i q_j \left(\frac{4\pi^2}{k^2}\right) e^{-k^2/4\kappa^2}\cos(\mathbf{k}\cdot\mathbf{r}_{ij})}_{\text{reciprocal-space term}}\right) \tag{2.34}$$

$$U^0 + U^{surf.} = \underbrace{\left(\frac{\kappa}{\pi^{1/2}}\right)\sum_{i=1}^{N} q_i^2}_{\text{self term}} \quad + \quad \underbrace{\left(\frac{2\pi}{3L^3}\right)\left|\sum_{i=1}^{N} q_i \mathbf{r}_i\right|}_{\text{surface term}} \tag{2.35}$$

Here the $erfc(x)$ is the complementary error function $\left(erfc(x) = \frac{2}{\pi^{1/2}} \times \int_x^\infty e^{-t^2}dt\right)$, which is approximated as:[13]

$$erfc(x) = \frac{1}{[1 + a_1 x + a_2 x^2 + a_3 x^3 + a_4 x^4]^4} + \epsilon(x) \tag{2.36}$$

where a_i are constants and the error is $\mid \varepsilon(x) \mid \leq 5 \cdot 10^{-4}$. The error function decreases monotonously as x increases. **k** = (l,j,k) is a reciprocal-space vector, and **n** was defined earlier.

COMPLETE FUNCTIONAL FORM OF THE FORCE FIELD

Finally, the equation for the potential energy describing the force field can be written (e.g. for the program CHARMM):

$$\begin{aligned} V(\mathbf{r}^N) \;=\; & \sum_{bonds} K_b(b-b_0)^2 + \sum_{ub} K_{ub}(s-s_0)^2 + \sum_{angles} K_\theta(\theta-\theta_0)^2 + \\ & \sum_{dihedrals} K_\chi(1+cos(n\chi-\chi_0)) + \sum_{impropers} K\psi(\psi-\psi_0)^2 + \\ & \sum_{nonbond} \epsilon_{ij}\left[\left(\frac{R_{ij}^{min}}{r_{ij}}\right)^{12} - \left(\frac{R_{ij}^{min}}{r_{ij}}\right)^{6}\right] + \frac{q_i q_j}{D r_{ij}} \end{aligned} \tag{2.37}$$

where K_b, K_{ub}, K_θ, K_χ, K_ϕ are, respectively, the bond, Urey-Bradley, angle, dihedral and improper dihedral constants, and b, s, θ, χ, and ϕ represent, respectively, bond lengths, Urey-Bradley 1-3 distances, bond angles, dihedral angles, and improper torsion angles (the subscript zero is used to represent the corresponding equilibrium value).

Nonbonded interactions between pairs of atoms (labeled i and j) at a relative distance r_{ij} are described by the Lennard-Jones 6-12 (LJ) term for the van der Waals

interactions and the Coulomb interaction term for the electrostatics. R_{ij}^{min} and ϵ_{ij} are, respectively, the distance between atoms i and j at which the LJ potential is minimum and the depth of the LJ potential well for the same pair of atoms. The calculated van der Waals energies mentioned throughout the thesis always correspond to energies calculated with the LJ potential. D is the effective dielectric constant and q_i the partial atomic charge on atom i.

2.2.5 EQUATIONS OF MOTION

NEWTONIAN EQUATIONS OF MOTION

Newton's equations of motion are as follows:

$$\begin{aligned} \dot{\mathbf{r}}_i &= \frac{\mathbf{p}_i}{m_i} \\ \dot{\mathbf{p}}_i &= \mathbf{F}_i(\mathbf{r}_1, ..., \mathbf{r}_N, t) \end{aligned} \tag{2.38}$$

where $\mathbf{r}_i$ and $\mathbf{P}_i$ are the position and momentum of atom i at a time t. $\mathbf{F}_i$ is the force acting on atom i: $\mathbf{F}_i = \nabla_i V$

Newtonian equations are the physically exact equations that describe the motion of atoms in the system. However, they have the disadvantage for molecular dynamics simulations that the temperature of the system has to be periodically reset so as to mimic biological conditions. To avoid this problem different sets of equations have been developed, which take care of the temperature as well as the pressure control of the system.[14]

2.2.6 SIMULATING IN DIFFERENT ENSEMBLES

MD simulations generate information on the microscopic level. The microscopic state of a system is defined in a $6N$-dimensional space, consisting of the momenta, **p**, and spatial coordinates **r** of the N particles. The thermodynamic state of a system is usually defined by a small set of parameters, for example the temperature T, the pressure, P, and the number of particles, N. Other thermodynamic properties can be derived from the equations of state and other fundamental thermodynamic equations.[15]

Statistical Mechanics relates the microscopic information to macroscopic properties (*i.e.* pressure, internal energy, etc.). This is achieved through the use of statistical ensembles. An ensemble is a collection of points in phase space satisfying the conditions of a particular thermodynamic state. Ensembles describe a collection of all possible systems that can have different microscopic states but are identical macro-

scopically (or thermodynamically) state. A summary of different statistical ensembles with different characteristics are given below.[16]

MICROCANONICAL ENSEMBLE

In the microcanonical ensemble the three constant parameters are N, V, E, *i.e.* number of particles, volume and energy of the system. This is the *natural* ensemble for MD simulations, where the Newtonian equations of motion can be applied unchanged to the system. To convert to other statistical ensembles one has to integrate other equations in place of Newton's equations in such a way that sampling is performed in another statistical ensemble.

CANONICAL ENSEMBLE

In the canonical ensemble the fixed parameters are N, V, T, *i.e.* number of particles, volume and temperature of the system. Since the temperature has to be kept constant in this ensemble, a thermostat has to be introduced and the Hamiltonian of the system becomes:

$$H = K + V + K_s + V_s \tag{2.39}$$

where K is the kinetic energy of the system, V is the potential energy of the system and K_s and V_s are the kinetic and potential energies coupled to the thermostat.

NOSÉ-HOOVER CONSTANT TEMPERATURE ALGORITHM

The equations of motion for constant temperature or Nosé-Hoover thermostat equations are the following:[17]

$$\begin{aligned} \dot{\mathbf{r}}_i &= \frac{\mathbf{p}_i}{m_i} \\ \dot{\mathbf{p}}_i &= \mathbf{F}_i - \frac{p_\eta}{Q}\mathbf{p}_i \\ \dot{\eta} &= \frac{p_\eta}{Q} \\ \dot{p_\eta} &= \sum_i \frac{\mathbf{p}_i^2}{m_i} - dNkT \end{aligned} \tag{2.40}$$

where η and p_η are the thermostat position and momentum and T is the temperature at which the system is to be regulated. N being the number of atoms in the system, k Boltzmann's constant and d the number of spatial dimensions. The parameter Q, given by $Q = dNkT\tau^2$, determines the time scale of the thermostat motion via the

time scale parameter τ, which should be chosen in correspondence to a characteristic time scale of the system, *e.g.*, a vibrational period.

The Nosé-Hoover scheme has the advantageous feature that it approximates the canonical distribution of temperature present in physical temperatures, *i.e.* the temperature of the system is not fixed at a given temperature but oscillates about it, as expected for small systems.

ISOBARIC-ISOTHERMAL ENSEMBLE

In this ensemble, pressure and temperature are kept constant in the system, *i.e.* the constant parameters are N, P, T. The Newtonian equations of motion become even more complicated in this ensemble because of the introduction of an additional barostat to the system.

CONSTANT TEMPERATURE AND PRESSURE

Simultaneous regulation of temperature and pressure can also be taken care of through the equations of motions: the isothermal-isobaric equations of motion:[14]

$$\begin{aligned}
\dot{\mathbf{r}}_i &= \frac{\mathbf{p}_i}{m_i} + \frac{p_\epsilon}{W}\mathbf{r}_i \\
\dot{\mathbf{p}}_i &= \mathbf{F}_i - \left(1 + \frac{1}{N}\right)\frac{P_\epsilon}{W}\mathbf{p}_i - \frac{P_\eta}{Q}\mathbf{p}_i \\
\dot{V} &= \frac{dVp_\epsilon}{W} \\
\dot{p_\epsilon} &= dV(P_{\text{int}} - P_{\text{ext}}) + \frac{1}{N}\sum_i \frac{\mathbf{p}_i^2}{m_i} - \frac{p_\eta}{Q}p_\epsilon \\
\dot{\eta} &= \frac{P_\eta}{Q} \\
\dot{p_\eta} &= \sum_i \frac{\mathbf{p}_i^2}{m_i} + \frac{p_\epsilon^2}{W} - (dN+1)kT
\end{aligned} \tag{2.41}$$

where p_ϵ is a momentum conjugate to the logarithm of the volume, W is its associated mass parameter, $\epsilon = \ln(V/v_0)$, P_{ext} is the externally applied pressure, and P_{int} is the instantaneous internal pressure of the system given by:

$$P_{\text{int}} = \frac{1}{\mathrm{d}V}\left[\sum_i \frac{\mathbf{p}_i^2}{m_i} + \sum_i \mathbf{r}_i\mathbf{F}_i - (\mathrm{d}V)\frac{\partial U}{\partial V}\right] \tag{2.42}$$

Thus, the variable p_ϵ acts as a 'barostat', which drives the system to the steady

state $\langle P_{\text{int}} \rangle = P_{\text{ext}}$. In this way, both temperature and pressure are regulated so as to reproduce exact canonical distributions.

Having gained an overview of the force field and of the equations of motion let us now turn to the methods by which these equations can be integrated over time.

2.2.7 METHODS FOR INTEGRATING THE EQUATIONS OF MOTION

SIMPLE INTEGRATION ALGORITHMS

Numeric integration of equations of motion is done step by step using Finite Difference methods. These methods are explicit and use the information available at time t to predict the system's coordinates and velocities at a time $t + \Delta t$, where Δt is a short time interval.

These integration schemes are based on a Taylor expansion of the position at time $t + \Delta t$, represented by the $n + 1$ subscript:

$$\mathbf{r}_{n+1} = \mathbf{r}_n + \Delta t\ \mathbf{v}_n + \frac{\Delta t^2}{2}\ \mathbf{a}_n + ... \tag{2.43}$$

where $\mathbf{v}_n$ is the first derivative of the position $\mathbf{r}_n$, $\mathbf{a}_n$ is the second derivative of the position etc. For Newtonian equations this simply yields:

$$\mathbf{r}_{n+1} = \mathbf{r}_n + \Delta t\ \mathbf{v}_n + \Delta t^2\ \frac{\mathbf{F}_n}{2m} + ... \tag{2.44}$$

The different simple integration algorithms vary in the way they implement this basic expansion.

The most basic and most common integration algorithm is the ***Verlet Integrator***. This integrator is based on two Taylor expansions, one forward and one backward:

$$\begin{aligned} \mathbf{r}_{n+1} &= \mathbf{r}_n + \Delta t\ \mathbf{v}_n + \Delta t^2\ \frac{\mathbf{F}_n}{2m} + ... \\ \mathbf{r}_{n-1} &= \mathbf{r}_n - \Delta t\ \mathbf{v}_n + \Delta t^2\ \frac{\mathbf{F}_n}{2m} - ... \end{aligned} \tag{2.45}$$

These two expansions are then added to give the basic Verlet integration formalism:

$$\mathbf{r}_{n+1} = 2\mathbf{r}_n - \mathbf{r}_{n-1} + \Delta t^2\ \frac{\mathbf{F}_n}{m} + \mathcal{O}(\Delta t^4)... \tag{2.46}$$

The simple Verlet approach has the advantage that it does not require the velocities, needs a single force calculation per cycle and is naturally reversible in time. It generates, however, relatively large errors.

The ***Leap Frog Integrator*** is a variation of the Verlet algorithm designed to improve the velocity evaluations. Its name comes from the fact that the velocities are evaluated at the mid-point of the position evaluation and vice versa. The algorithm is as follows:

$$\begin{aligned} \mathbf{v}_{n+1/2} &= \mathbf{v}_{n-1/2} + \Delta t \, \frac{\mathbf{F}_n}{m} \\ \mathbf{r}_{n+1} &= \mathbf{r}_n + \Delta t \, \mathbf{v}_{n+1/2} \end{aligned} \tag{2.47}$$

This scheme has the advantage of providing a direct handle on the velocities, which can be useful for temperature regulation. It has less error that the simple Verlet scheme.

2.2.8 PAIR RADIAL DISTRIBUTION FUNCTION

The structure of soft matter can be characterized by a set of distribution functions for the atomic positions, the simplest of which is the pair distribution function, $g(r)$. This function gives the probability of finding a pair of atoms a distance r apart, relative to the probability expected for a completely random distribution at the same density.[10] To define $g(r)$, we integrate the configurational distribution function over the positions of all atoms except two, incorporating the appropriate normalization factors.[15] In the canonical ensemble:

$$g(\mathbf{r}_1, \mathbf{r}_2) = \frac{N(N-1)}{\rho^2 Z_{NVT}} \int d\mathbf{r}_3 d\mathbf{r}_4 \cdots d\mathbf{r}_N exp(-\beta V(\mathbf{r}_1, \mathbf{r}_2, \cdots, \mathbf{r}_N)) \tag{2.48}$$

The pair radial distribution functions, $g(r)$, were calculated in this thesis from the equation:

$$g(r) = \frac{V}{N} \left\langle \frac{n(r)}{4\pi r^2 dr} \right\rangle . \tag{2.49}$$

In this expression $g(r)$ describes the probability of finding a particle y at a distance $r + dr$ away from particle x in a simulation box of volume V containing N particles. $n(r)$ is the number of particles y in the sphere of radius r and width dr around particle x. The distances between the atoms on different molecules are binned and the resulting $g(r)$ was normalized by dividing by $4\pi r^2 dr$ in which r is the distance in the middle of the bin and dr in the bin width, set at 0.07 Å. The volume around each particle is divided into concentric spherical shells, and the number of particles in each shell is counted and divided by the shell volume (given by the difference between two spherical volumes), to obtain the local density. The densities at each distance are then averaged over all particles, and normalised with the overall density to obtain $g(r)$.

2.3 FORCE FIELD PARAMETERIZATION

2.3.1 THE AUTOMATED FREQUENCY MATCHING METHOD (AFMM)

AFMM (Automated Frequency Matching Method) provides an efficient, automated way to generate intra-molecular force field parameters using normal modes. The method can be, in principle, used with any atom-based molecular mechanics program, which has the facility of calculating normal modes and the corresponding eigenvectors.

The basic principle behind the AFMM method is to iteratively tune an initial MM (e.g. CHARMM[7]) parameter set in order to reproduce the normal modes generated from a quantum mechanical (QM) calculation. The program refines an initial parameter set, which can either be a pre-existing set or using chemically-reasonable estimation. For parametrization of new molecules, the starting parameters should be based on analogy to other similar existing molecular mechanics parameters and on chemical intuition. Equilibrium values and hybridization of the atoms involved should be carefully taken into account when designing a set of initial parameters. Another way to ensure a good choice of the initial parameter set is checking by visual inspection the motions involved in exchanged eigenvector modes (*e.g.* using the Molden program[18]). After identifying problematic parameters one can manually adjust the parameters concerned. This approach is particularly useful for critical torsion parameters. In some cases it is necessary to derive initial parameters from rotational potential energy profiles (single point calculations from QM programs) before achieving good optimization. Equilibrium values for bonds b_0, angles, θ_0, and dihedrals χ_0 can be derived from the quantum chemical ground state structure or from experimental X-ray or NMR structures. A set of partial atomic charges can be computed from the QM packages using various methods as well.

Use of AFMM for optimizing van der Waals parameters is not recommended. The van der Waals constants ϵ_{ij} and R_{ij}^{min} depend mostly on atomic properties and are relatively insensitive to changes in the molecular environment. Therefore, they can often be transferred from existing values and should not be modified during refinement.

The reference quantum mechanical normal modes can be calculated with any QM programs (e.g. Gaussian 94/98,[19, 20] NWChem,[21] ADF[22]) and using any levels of theory (e.g. Hartree-Fock, DFT). Frequencies resulting from the quantum calculations often need to be scaled by an "empirical scaling factor" to compensate for approximations in the electronic structure calculations.[23] The choice of reference data upon

which the MM parametrization is based, is a critical step in the parametrization procedure. The reliability and accuracy of the new parameters in reproducing various properties of the molecule depend on the quality of the reference data.

DESCRIPTION OF THE METHOD, THE MERIT FUNCTION

Here the principles of the parametrization method implemented in the program are briefly sketched. For a more detailed theoretical treatment and applications, see Refs. 24 and 25. Automated refinement methods are mostly based on optimizing a "merit function", which usually corresponds to minimizing a weighted sum of square deviations from a set of reference values. One of the major problems of parametrization methods that fit to vibrational frequencies is identifying a calculated mode with the corresponding reference mode. Incorrect mode matching can lead to an unfaithful reproduction of the correct distribution of energy among the intra-molecular modes, and consequently of the dynamical properties of the molecule. It is therefore important to use a merit function which requires that both the reference frequencies and eigenvectors should coincide with those resulting from the new parameter set. Since the eigenvectors are orthonormal, the dot product (or the projection) of the corresponding quantum mechanical and molecular mechanical eigenvectors will be 1. The dot product between all other eigenvectors should be zero.

To check for this condition, AFMM projects each of the MM eigenvectors, $\{\overline{\chi_i^M}\}$ (where the subscript *i* indicates the normal mode number and the superscript *M* indicates that the modes are calculated with MM), onto the reference set of eigenvectors $\{\overline{\chi_i^Q}\}$ (the superscript *Q* indicates that these modes are calculated with a QM program) to find the frequency ν_j^{max} corresponding to the highest projection ($j : \overline{\chi_i^M} \cdot \overline{\chi_i^Q}$=max) and compares this frequency with the corresponding frequency, ν_i. In the ideal case $\nu_i = \nu_j^{max}$ and $\overline{\chi_i^M} \cdot \overline{\chi_i^Q} = \delta_{ij}$, where δ_{ij} is the Kroenecker delta. Frequencies ν_i that deviate from this ideal situation may indicate exchanged eigenvectors or mismatched frequencies. AFMM is based on minimizing the merit function, Y^2, which in this case, is the deviation from the ideal situation:

$$Y^2 = \sum_{3N-6} \Omega_i^2 (\nu_i - \nu_j^{max})^2 \tag{2.50}$$

$$\Omega_i^{(1)} = \frac{1}{max_j(\overline{\chi_i^M} \cdot \overline{\chi_i^Q})} \tag{2.51}$$

$$\Omega_i^{(2)} = \frac{1}{\omega_i^M} \tag{2.52}$$

where ω_i are the frequencies, N is the number of atoms in the molecule and there are $3N$-6 independent vibrational frequencies. The program allows three possibilities to weigh the merit function:

1. The weights Ω_i are chosen to be the inverse of the highest eigenvector projection. This biases the merit function, even in the case of a good frequency assignment, such that minimization of Y^2 leads to an improved eigenvector projection distribution (Eq.2.51).

2. The weights Ω_i are chosen to be the inverse of the MD frequency. This biases the merit function towards better fitting of the lowest, biologically more relevant frequencies. (Eq.2.52).

3. No weights. ($\Omega_i = 1$)

PARAMETER REFINEMENT

For the automatic optimization of the chosen subset of parameters a standard Monte Carlo (MC) scheme is used to minimize Y^2. Although the subset of parameters to be optimized can be chosen at wish by the user, it is advisable to perform optimizations separately on bond, angle, and torsion constants. At each step i all chosen parameters are iteratively varied in the MC algorithm with a uniform distribution within a fixed range, Y_i^2 is evaluated, and, if $Y_i^2 < Y_{i-1}^2$, the new parameter set is used in the next step, i+1. The optimization algorithm is illustrated in Fig.2.7.

When comparing results for different molecules, normalization of Y^2 can be rather tedious due to the different weights Ω_i. For comparison purposes after minimization of Y^2, the root-mean-square deviation σ from the reference case is calculated:

$$\sigma = \sqrt{\frac{\sum_{3N-6}(\nu_i - \nu_j^{max})^2}{3N-6}} \tag{2.53}$$

For comparison between different molecules or optimizations with different weights, the non-weighted σ should be used.

DESCRIPTION OF THE PROGRAM

The present version of the program is interfaced with the Gaussian 94/98, NWChem 4.5 and older and Molden format[18] output files as input for reading the QM normal modes set and optimizes parameters for the CHARMM program.[7] The program is written in Python and requires Python version 2 or newer; however, it does not require any non-standard Python modules. The program is composed of only one source code

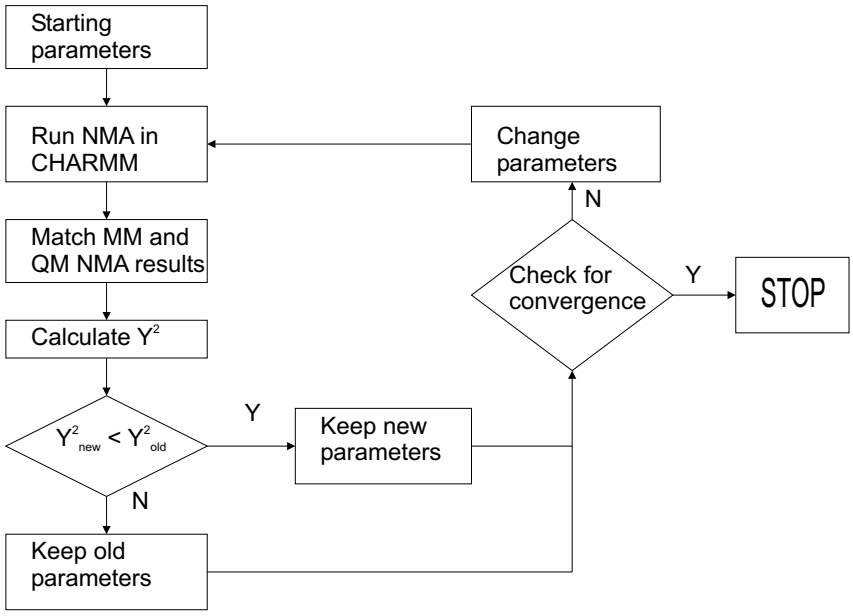

Figure 2.7: Schematic representation of the optimization algorithm used in the AFMM method. The method iteratively changes the parameters and matches both frequencies and eigenvector projections from the molecular mechanics (CHARMM in this case) normal mode analysis (NMA) with reference QM NMA.

file (afmm.py) which contains definitions of two classes and the normal modes import functions.

The `param` class contains information about the parameter set to be optimized and a Monte Carlo-like method to generate new random values of the parameters that are different from both the starting and the current values.

The names of the normal modes import-functions are composed of `read_` followed by the program name. For the QM output files, there are also functions that identify the type of file, their name being composed of `is_` followed by the program name. All the normal modes import-functions, return lists of non-zero frequencies and corresponding eigenvectors.

The `afmm` class is the core of the program and contains the following methods:

- `ReadConfig` - read the configuration file
- `WriteNewParams` - write new parameters in the CHARMM stream file
- `WriteStreamedInput` - write a new CHARMM input file
- `RunMD` - run CHARMM, checking for normal termination
- `DotProduct` - calculates the dot product between the eigenvectors

- `TooLow` - checks if a value is too close to zero (before division)
- `Compute` - matches the modes and computes the merit function
- `Optimize` - main routine that iteratively assigns new values to parameters and minimizes the merit function
- `OutputResults` - writes out the minimum weighted σ (Eq.3.2), the corresponding non-weighted σ, the optimized parameters and the frequency matching file

The main program consists of only 3 calls: reading the configuration file, calling `Optimize` for computation, then calling `OutputResults`. The program can be run as follows:

```
python afmm.py
```

Before running the program the user must verify that the order of the atoms and the orientation of the molecule in the MM and QM files are the same when matching the normal modes. While running, the program will print on standard output the values of the weighted σ that result during the optimization. The program will stop in either of two cases: when the maximum number of steps for which σ remains constant is reached (convergence criterion) or when the maximum number of optimization steps is reached. Upon program completion, the minimum weighted σ, the corresponding non-weighted σ and the final parameter set are printed on standard output and the frequency matching file is created. The frequency matching file contains 2 columns, the first containing the scaled QM frequencies (if a scaling factor was given to the program) and the second containing corresponding MM frequency values.

2.3.2 CALCULATING PARTIAL ATOMIC CHARGES

The electrostatic properties of a molecule are a consequence of the electron and the nuclei distribution. Thus, it is reasonable to assume that one should be able to obtain a set of partial atomic charges using quantum mechanics. However, the partial atomic charge is not an experimentally observable quantity and cannot be unambiguously calculated from the wavefunction. Many methods have been proposed for calculating the partial atomic charges from quantum mechanics. In this thesis, the CHELPG method, which is described below, has been used to derive the partial atomic charges for cholesterol, ergosterol and lanosterol.

The electrostatic potential at a point is the force acting on a positive unit charge placed at that point. The electrostatic potential is an observable quantity that can be determined from a wavefunction:

$$\phi_{qm}(\mathbf{r}) = \phi_{nucl}(\mathbf{r}) + \phi_{elec}(\mathbf{r}) = \sum_{j=1}^{N} \frac{Z_j}{|\mathbf{r} - \mathbf{R}_j|} - \int \frac{d\mathbf{r}'\rho(\mathbf{r})}{|\mathbf{r}' - \mathbf{r}|}. \tag{2.54}$$

Classically it is defined as:

$$\phi_{class}(\mathbf{r}) = \sum_{j=1}^{N} \frac{q_j}{|\mathbf{r} - \mathbf{R}_j|} \tag{2.55}$$

The electrostatic potential is a continuous property, and is not easily represented by an analytical function. Therefore, it is necessary to derive a discrete representation for use in numerical analysis. The objective is to derive the set of partial atomic charges that best reproduces the quantum mechanical electrostatic potential at a series of points surrounding the molecule. The electrostatic potential at chosen points can be calculated from the wavefunction. A least-squared fitting procedure is then employed to determine the set of partial atomic charges that best reproduces the electrostatic potential at the points, subject to the constraint that the sum of the charges should be equal to the net charge of the molecule[26] (see Fig. 2.8 for a schematic representation). Symmetry conditions can be also imposed to ensure that the charges on symmetrically equivalent atoms are equal (*e.g.* in a methyl group all hydrogens should have identical charges and their sum should be opposite to that of the carbon). It is also possible to require the atomic charges to reproduce other electrostatic properties of the molecules such as the dipole moment. The fitting procedure minimizes the sum of squares of the differences in the electrostatic potential. Thus, if the quantum mechanical electrostatic potential at a point is ϕ_{qm} (see Eq. 2.54) and the value from the charge model is ϕ_{class} (see Eq. 2.55) then the objective is to minimize the following function:

$$R = \sum_{i=1}^{N_{points}} (\phi_{qm} - \phi_{class})^2 \tag{2.56}$$

with the respect to q_j.

At a minimum value of the error function, R, the first derivative is equal to zero with respect to all charges q_k:

$$\frac{\partial R}{\partial q_k} = -2 \sum_{i=1}^{N_{points}} (\phi_{qm} - \phi_{class}) \left(\frac{\partial \phi_{class}}{\partial q_k} \right) = 0 \tag{2.57}$$

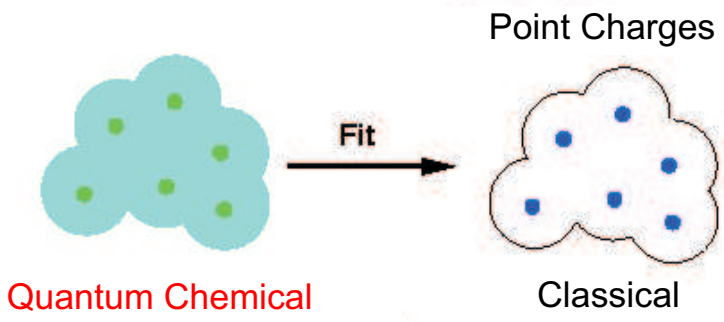

Figure 2.8: A schematic representation of fitting the quantum chemical potential with partial atomic point charges. [from Matthias Ullmann]

or

$$-2\sum_{i=1}^{N_{points}}\left(\phi_{qm}(\mathbf{r}_i)-\sum_{j=1}^{N_{atoms}}\frac{q_j}{|\mathbf{r}_i-\mathbf{R}_j|}\right)\left(\frac{1}{|\mathbf{r}_i-\mathbf{R}_k|}\right)=0 \qquad (2.58)$$

The system of equations for all q_j has the form $\mathbf{A}q-\mathbf{a}=0$. The charges, q, can then be determined using standard matrix methods via $q=\mathbf{A}^{-1}\mathbf{a}$.

The points $i=(1,2,\cdots,N_{points})$ where the potential is fitted can be chosen in a variety of ways, but should be taken from the region where it is most important to correctly model intermolecular interactions. This region is just beyond the van der Waals radii of the atoms involved. In the CHELPG procedure[27] the points are selected from spherical shells, 1 Å apart, centered on each atom with points symmetrically distributed on the surface. Any points within the van der Waals radius of any atom in the system are discarded and the shells extend to 3 Å from the van der Waals surface of the molecule. The CHELPG method employs a Lagrange multiplier method to find the atomic charges, rather than an iterative least-squares procedure. This method minimizes the error function R subject to the constraint that the charges sum to the total molecular charge. The CHELPG algorithm of Breneman and Wiberg[28] is an improved version from that proposed by Chirlian and Francl.[27] A cubic grid of points (spaced 0.3-0.8 Å apart) is used and all grid points that lie within the van der Waals radius of any atom are discarded, together with all points that lie further than 2.8 Å away from any atom.

2.4 NEUTRON SCATTERING AS A TOOL TO PROBE STEROL-CONTAINING MEMBRANES

Neutron scattering is a unique tool for studying the structure and dynamics of lipid membranes. Thermal neutron wavelengths (≈Å) and energies (≈meV) correspond to interatomic distances and the energy of thermal excitations, respectively, so that neutrons are sensitive to both the amplitudes and frequencies of molecular motions. The fact that thermal neutron scattering is sensitive to time and space correlations of atomic positions on the ps timescale and the Å length scale, makes it directly comparable to MD simulations. Another advantage of neutron scattering is that neutrons, being electrostatically neutral, only interact with the nuclei of the system and electrostatics do not need to be taken into consideration. Neutrons are especially sensitive to hydrogen nuclei (a single proton), for which they have a very large scattering cross section, 10 times greater than for any other nuclei that can be found in a biological sample. Thus, using selective deuteration allows to focus on the interesting parts of the system, for example the sterol in a membrane.

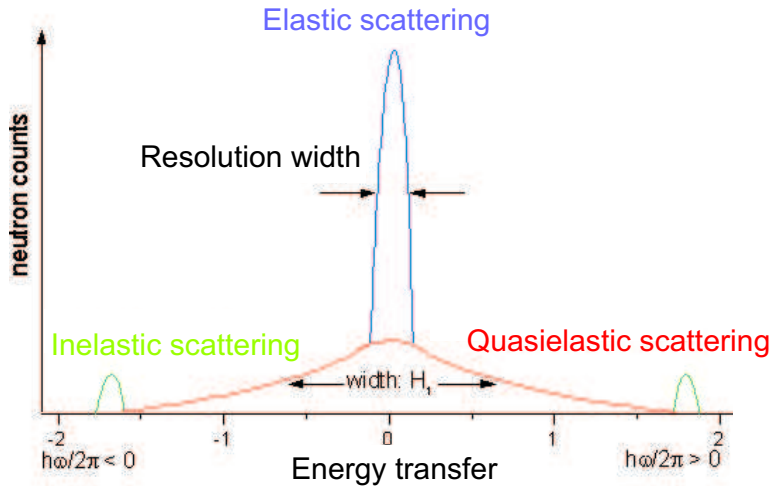

Figure 2.9: A schematic representation of the neutron scattering dynamic structure factor $S(\mathbf{q}, E)$. There are three regions in the spectrum: the elastic peak, which arises from motions which are too slow for the resolution of the experiment, the quasielastic broadening arising from diffusional motions within the system studied and the inelastic region which is due to vibrational motions.

From the atomic trajectories it is possible to calculate the scattering intensity of the sample and compare it to the neutron experiment performed. The scattering of neutrons arising from individual atoms is calculated and averaged out over the time period of the simulation and the different atoms present in the system (although hy-

drogen atoms dominate the signal). Section 2.4.2 will present the equations which describe neutron scattering.

In calculating neutron scattering intensities and comparing them with the experimental ones, one is in a unique position to validate the model used to perform the simulation. Neutron scattering yields critical information about the frequencies of the motion present in the system, which gives a good measure of the accuracy of the model.

Neutrons can be used in either of two ways: for spectroscopic measurements, using elastic and inelastic scattering to give dynamical information. They can also be used in crystallographic measurements, using elastic scattering on protein crystals to get structural information. In the present work, incoherent quasielastic neutron scattering (QENS) calculations were performed to validate the MD simulation and to further study molecular motional processes in membranes. A schematic representation of the neutron scattering spectrum can be found in Fig. 2.9.

2.4.1 BASIC CONCEPTS OF NEUTRON SCATTERING

Thermal neutrons from a nuclear reactor or a spallation source are moderated to be at thermal equilibrium close to room temperature with a typical energy of ≈25meV. Cold neutrons are obtained by equilibration at very low temperatures of ≈20 K and have typical energies of ≈2.5meV. The corresponding wavelength of a neutron, λ, is ≈1 Å. Neutrons are characterized by their energy

$$E = \hbar\omega \tag{2.59}$$

and their momentum

$$\mathbf{p} = m\mathbf{v} = \hbar\mathbf{k} \tag{2.60}$$

where $\mathbf{k}$ is the wave vector and $|\mathbf{k}| = 2\pi/\lambda$.

If we neglect electromagnetic interactions, an incident neutron has three possibilities of interactions when it encounters a sample. (1) The neutron passes through the sample without changing its physical characteristics. (2) It is absorbed in a nuclear process and its energy is dissipated. (3) The neutron is scattered by a nucleus, exchanging energy and momentum (inelastic scattering, $\Delta E \neq 0$) or exchanging just momentum and conserving energy (elastic scattering, $\Delta E = 0$) with the sample:

$$\Delta E = \hbar(\omega' - \omega) \tag{2.61}$$

$$\Delta\mathbf{p} = \hbar(\mathbf{k}' - \mathbf{k}) = \hbar\mathbf{q} \tag{2.62}$$

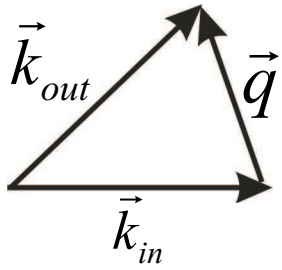

Figure 2.10: Schematic depiction of the scattering triangle.

where primed and unprimed quantities are after and before the scattering event, respectively and **q** is the momentum transfer. The scattering triangle, which depicts the momentum transfer as calculated from the incident and the scattered wave vector is seen in Figure 2.10.

Information on the sample structure and dynamics is obtained by analyzing the scattered beam as a function of momentum and energy transfer. Scattered neutrons are captured by the detectors surrounding the sample in an angle θ (see Fig. 2.11). The neutron detectors are not capable of resolving the energy of the scattered neutron but only detect neutrons in a 'yes' or 'no' event. The energy of the scattered neutron must be therefore analyzed either by determining the wavelength by Bragg reflection from a crystal or by determining its velocity in a time-of-flight experiment before it is counted by the detector.

The probability of a neutron being scattered in a unit solid angle is expressed in terms of the double differential cross section:

$$\frac{d\sigma}{d\Omega} = \frac{I'}{I} = b^2 \tag{2.63}$$

The differential cross section is defined as the average number of neutrons I', which are scattered per unit time into the solid angle interval $[\Omega, \Omega + d\Omega]$ and per unit incident neutron flux I (neutrons per area per unit time). b is the scattering length, representing an effective linear dimension of the scattered. Units of b are in 10^{-15}m, much smaller than the neutron wavelength, so that the nucleus can be considered as a point and the scattering as isotropic. The total scattering cross section (unit: 1 barn=10^{-24}cm^2) is the integral of the differential scattering cross section in all directions (solid angle 4π):[29, 30]

$$\sigma_t = \int_{4\pi} \frac{d\sigma}{d\Omega} = 4\pi b^2 \tag{2.64}$$

Since neutron scattering is also dependent on the energy exchange occurring during the scattering event, the differential cross section can be extended to the double dif-

ferential cross section. The double differential cross section is defined as the number of neutrons which are scattered per unit time into the solid angle interval $[\Omega, \Omega + d\Omega]$ and into the energy interval $[\omega, \omega + d\omega]$.[31, 32]

$$\int \frac{\partial^2\sigma}{\partial\Omega\partial\omega} d\omega = \frac{d\sigma}{d\Omega}. \tag{2.65}$$

2.4.2 THE DYNAMIC STRUCTURE FACTOR

The quantity of interest in neutron scattering experiments with thermal neutrons is the dynamic structure factor, $S(\mathbf{q}, \omega)$, which is closely related to the double differential cross-section, $\partial^2\sigma/\partial\Omega\partial\omega$. It is normalized to $d\Omega, dE$, and the flux of incoming neutrons,

$$\frac{\partial^2\sigma}{\partial\Omega\partial\omega} = N \cdot \frac{k'}{k} S(\mathbf{q}, \omega) \tag{2.66}$$

where N is the number of atoms, and $k' \equiv |\mathbf{k}'|$ and $k \equiv |\mathbf{k}|$ are the wave vectors of scattered and incident neutrons, respectively. They are related to the corresponding neutron energies by $E' = \hbar^2 k'^2/2m$ and $E = \hbar^2 k^2/2m$, where m is the neutron mass. $\mathbf{q}$ and ω are the momentum and energy transfer in units of $\hbar$, respectively:

$$\mathbf{q} = \mathbf{k} - \mathbf{k}' \tag{2.67}$$

$$\omega = \frac{E - E'}{\hbar} \tag{2.68}$$

The modulus of the momentum transfer can be expressed in terms of the scattering angle θ (also detector angle), the energy transfer, and the energy of the incident neutrons:

$$|\mathbf{q}| = \sqrt{2|\mathbf{k}_i|^2 - 2\frac{m_N\omega}{\hbar} - 2cos\theta|\mathbf{k}_i|\sqrt{|\mathbf{k}_i|^2 - \frac{2m_N\omega}{\hbar}}} \tag{2.69}$$

If scattering is elastic then Eq. 2.69 becomes:

$$|\mathbf{q}| = 2|\mathbf{k}_i| sin\frac{\theta}{2} \tag{2.70}$$

The dynamic structure factor contains information about the structure and dynamics of the scattering of the system:

$$S(\mathbf{q}, \omega) = \frac{1}{2\pi}\int_{-\infty}^{+\infty} exp[-i\omega t] F(\mathbf{q}, t) dt. \tag{2.71}$$

$F(\mathbf{q}, t)$ is called the intermediate scattering function and is defined as:

$$F(\mathbf{q},t) = \sum_{\alpha,\beta} \Gamma_{\alpha\beta} \langle exp[-i\mathbf{q}\cdot\widehat{\mathbf{R}_\alpha}(0)] exp[-i\mathbf{q}\cdot\widehat{\mathbf{R}_\beta}(t)]\rangle \tag{2.72}$$

$$\Gamma_{\alpha\beta} = \frac{1}{N}[\bar{b_\alpha}\bar{b_\beta} + \delta_{\alpha\beta}(\bar{b_\alpha^2} - \bar{b_\alpha}^2)] \tag{2.73}$$

The operators $\widehat{\mathbf{R}_\alpha}(t)$ are the position operators of the nuclei in the sample. The quantities b_α are the scattering lengths of the nuclei which depend on the isotope and the relative orientation of the spin of the neutron and the spin of the scattering nucleus.

It is possible to split the intermediate scattering function and the dynamic structure factor into two parts: (1) an autocorrelation function describing the trajectory of single nuclei and giving rise to incoherent scattering, (2) a correlation function describing different nuclei and giving rise to coherent scattering. The intermediate scattering function can be therefore written as:

$$F_{coh}(\mathbf{q},t) = \frac{1}{N}\sum_{\alpha,\beta} \bar{b_\alpha}\bar{b_\beta} \langle exp[-i\mathbf{q}\cdot\widehat{\mathbf{R}_\alpha}(0)] exp[-i\mathbf{q}\cdot\widehat{\mathbf{R}_\beta}(t)]\rangle \tag{2.74}$$

$$F_{inc}(\mathbf{q},t) = \frac{1}{N}\sum_{\alpha} (\bar{b_\alpha^2} - \bar{b_\alpha}^2) \langle exp[-i\mathbf{q}\cdot\widehat{\mathbf{R}_\alpha}(0)] exp[-i\mathbf{q}\cdot\widehat{\mathbf{R}_\alpha}(t)]\rangle \tag{2.75}$$

It is evident from Eq. 2.75 that the intermediate scattering function can be readily computed by MD simulations as an autocorrelation function of the positions. The corresponding dynamic structure factors are obtained by performing the Fourier transformation defined in Eq.2.71.

Incoherent scattering can be understood as waves scattered independently by individual atoms and interfering with themselves during a time-course defined by the instrumental resolution. The origin of the incoherent scattering is the spin dependence of the neutron-nucleus interaction. The hydrogen atom, H, has one of the largest incoherent cross sections, 10 times greater than for any other nuclei that can be found in a biological sample. Neutron scattering from a biological sample is therefore dominated by the incoherent scattering of the hydrogen nucleus. In the time and space window of neutron scattering experiments, the incoherent scattering by H atoms reflect the motions of the larger groups to which they are bound.[33]

2.4.3 THE ELASTIC INCOHERENT STRUCTURE FACTOR

The total elastic intensity as a function of the scattering vector contains information on the geometry of the motions integrated over the time corresponding to the instrumental resolution. For example, if H-atom motions can be described by an ellipse in 100ps,

this motion will then correspond to the elastic incoherent structure factor (EISF) that can be reproduced by an ellipse (the instrumental resolution has to correspond to a time of 100ps or longer - 10μeV or better). The EISF is defined as the fraction of the elastically scattered intensity over the total intensity.

As the positions of the nuclei after infinite time, $\mathbf{R}_\alpha(\infty)$, are uncorrelated to the initial positions, $\mathbf{R}_\alpha(0)$, for infinitely good resolution $\Delta E = 0$, the total elastic intensity is described by the time-independent part of the intermediate scattering function:

$$EISF(\mathbf{q}) \doteq \lim_{t\to\infty} F_{inc}(\mathbf{q}, t). \tag{2.76}$$

Using the above definition one can decompose the incoherent intermediate scattering function as follows:

$$F_{inc}(\mathbf{q}, t) = EISF(\mathbf{q}) + F'_{inc}(\mathbf{q}, t) \tag{2.77}$$

where $F'_{inc}(\mathbf{q}, t)$ decays to zero for infinite time. Taking now the Fourier transform of this expression:

$$S_{inc}(\mathbf{q}, t) = EISF(\mathbf{q})\delta(\omega) + S'_{inc}(\mathbf{q}, t). \tag{2.78}$$

The EISF appears as the amplitude of the elastic line in the neutron scattering spectrum. The EISF gives the sampling distribution of the points in space in the limit of infinite time. In a real experiment this means times longer than the time observable with a given instrument. The EISF therefore vanishes for all systems that can access infinite volume, as is the case for liquids and gases. The existence of an elastic component in the scattered intensity clearly indicates the presence in the sample of a scatterer, the motion of which is essentially located in space. The EISF can be also defined as:

$$EISF(\mathbf{q}) = \frac{1}{N}\sum_\alpha (\bar{b_\alpha^2} - \bar{b_\alpha}^2)\langle|exp[-i\mathbf{q}\cdot\widehat{\mathbf{R}_\alpha}]|^2\rangle \tag{2.79}$$

from Equation 2.75, if we assume that for infinite time the following expression holds:

$$\langle exp[-i\mathbf{q}\cdot\widehat{\mathbf{R}_\alpha}(0)]exp[-i\mathbf{q}\cdot\widehat{\mathbf{R}_\alpha}(t)]\rangle = \langle|exp[-i\mathbf{q}\cdot\widehat{\mathbf{R}_\alpha}]|^2\rangle \tag{2.80}$$

$$F_{inc}(\mathbf{q}, \infty) = \frac{1}{N}\sum_k |< exp(i\mathbf{q}\cdot\mathbf{R}_\alpha) >|^2. \tag{2.81}$$

In order to get an estimate of the EISF from MD simulation and with using the above definition (Eq. 2.79) one needs a long enough trajectory to allow for representative sampling of the conformational space.

By integrating the incoherent scattering law over the energy transfer ω at constant

q we get from the definition (Eq. 2.71):

$$\int_{-\infty}^{\infty} S_{inc}(\mathbf{q},\omega)d\omega = \int_{-\infty}^{\infty} F_{inc}(\mathbf{q},t)dt = F_{inc}(\mathbf{q},0) = 1. \tag{2.82}$$

Therefore, the EISF is the fraction of the total quasielastic intensity contained in the purely elastic peak. The direct important consequence is that the separation between the sharp, purely elastic component and the wider, quasielastic contribution can be performed, evaluated from the ratio:

$$A_0(\vec{q}) \doteq \frac{\mathcal{S}^{el}_{inc}(\mathbf{q})}{\mathcal{S}^{el}_{inc}(\mathbf{q}) + \mathcal{S}^{qe}_{inc}(\mathbf{q})} \tag{2.83}$$

of the integrated intensities $\mathcal{S}^{el}_{inc}(\mathbf{q})$ and $\mathcal{S}^{qe}_{inc}(\mathbf{q})$ corresponding to the elastic and the quasielastic part of the spectra, respectively. The EISF is experimentally accessible as the ratio of the elastically scattered intensity to the sum of elastically and quasielastically scattered intensity. The above definition neglects inelastic scattering.

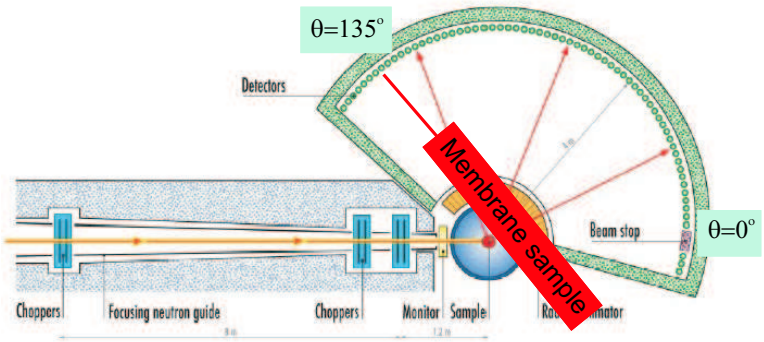

Figure 2.11: Schematic depiction of the IN5 spectrometer in ILL. A specific scattering geometry is used for orientation-dependent measurements. The scattering angle between the incident neutron beam and the sample normal is in the picture 135° resulting in a momentum transfer directed predominantly parallel to the sample plane.

2.4.4 QUASIELASTIC NEUTRON SCATTERING (QENS)

The quasielastic broadening of the elastic peak appears due to diffusional motions of the atoms within the system. In quasielastic experiments, the scattered intensity is interpreted in the form of a Debye-Waller factor, the EISF, and the (close to zero) energy-transfer scattering from which information on the evolution of different motions can be obtained.

One can split up the intermediate scattering function to the EISF, A_0 and a time-dependent part

$$F\mathbf{q},t) = A_0(\mathbf{q}) + [1 - A_0(\mathbf{q})]\Phi(\mathbf{q},t) \tag{2.84}$$

Convoluting with the instrumental resolution, results in the structure factor:

$$S(\mathbf{q},\omega) = R(\mathbf{q}) \otimes \left\{exp[- < x^2 > q^2] \cdot (A_0(\mathbf{q})\delta(\omega) + [1 - A_0(\mathbf{q})]S_{QE}(\mathbf{q},\omega))\right\} \tag{2.85}$$

where $R(\mathbf{q})$ is the resolution function of the instrument, $exp[- < x^2 > q^2]$ is the Debye-Waller factor, which accounts for vibrational modes (x^2 is the mean squared amplitude of the vibration), $A_0(\mathbf{q})\delta(\omega)$ is the EISF and S_{QE} is the quasielastic scattering centered on $\omega = 0$. The $[1 - A_0(\mathbf{q})]S_{QE}(\mathbf{q},\omega)$ part of the equation is referred to as quasielastic incoherent structure factor (QISF).

The QISF can be described by a sum of Lorentzian functions, thus transforming Eq. 2.85 into:

$$S(\mathbf{q},\omega) = R(\mathbf{q}) \otimes \left\{exp[- < x^2 > q^2] \cdot (A_0(\mathbf{q})\delta(\omega) + \sum_i A_i L(\Gamma_i,\omega))\right\} \tag{2.86}$$

where A_i is the amplitude of the Lorentzian function, $L(\Gamma_i,\omega)$ is the Lorentzian line shape function, centered at $\omega = 0$ and with line width Γ_i (half width at half maximum):

$$L_i(\Gamma(\mathbf{q}),\omega) = \frac{1}{\pi}\left(\frac{\Gamma_i(\mathbf{q})}{\Gamma_i(\mathbf{q})^2 + \omega^2}\right) \tag{2.87}$$

To study molecular diffusion with quasielastic neutron scattering, one is able to fit the neutron scattering spectra with a Gaussian function for the elastic peak and a sum of Lorentzian functions for the quasielastic broadening. For the case of Fickian diffusion it is typical to fit the QENS spectra with only one Lorentzian line. For the full width at half maximum (FWHM) of the Lorentzian, $\Gamma(\mathbf{q})$, the Fickian theory predicts a linear dependence of $\Gamma(\mathbf{q})$ vs q^2 with the slope D (long-range diffusion coefficient) in the limit of small q (*i.e.* large distances).

Furthermore, the $\mathbf{q}$ and ω dependencies of the above-mentioned spectral parameters are commonly fitted to dynamic models for which analytical expressions for $S_{inc}(\mathbf{q},\omega)$ have been derived, which can describe diffusion constants, jump lengths, residence times, etc. that characterize the motion with models.[29]

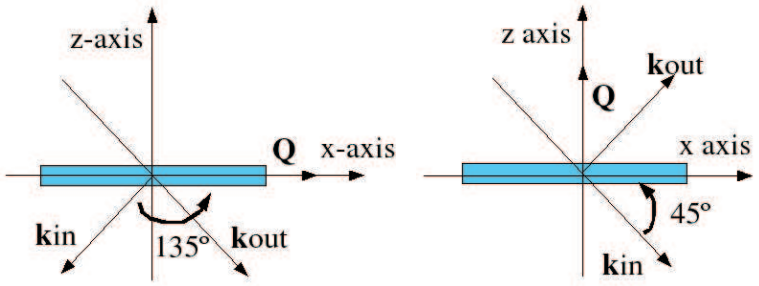

Figure 2.12: The elastic momentum transfer vector **q** is parallel (left picture) and perpendicular (right picture) to the membrane plane, if scattered neutrons (wave vector $\mathbf{k}_{out}$ are detected at $\phi = 90°$ with respect to the incident wave vector $\mathbf{k}_{in}$.

2.4.5 NEUTRON SCATTERING FROM ORIENTED SAMPLES

Although the incoherent scattering law does not involve any selection rule in the reciprocal space, it still depends on the scattering vector. One can take advantage of this geometrical experimental parameter in order to get more information on the problem under study. Powder samples average the relevant signal over all the **q**-directions in space and leave only the dependence on the modulus for **q**. In two dimensional compounds, such as a membrane, the orientation of the sample plays an important role in determining motions in the two directions of the compound, *i.e.* the xy-plane and the z-axis of the membrane. The scattering geometry is depicted in Figure 2.11.

At an orientation of 135° between the incident and neutron beam and the membrane normal, the momentum transfer is mainly directed perpendicular to the membrane normal, *i.e.* parallel to the bilayer plane ($x - y$ plane). In this case, the in-plane (lateral) motion of the sterol under study will dominate the incoherent scattering. On the other hand, at an orientation of 45° the momentum transfer is mainly parallel to the membrane normal, and thus the incoherent scattering is dominated by out-of plain motion of the sterol along the z-direction (membrane normal). The two scattering geometries is schematically depicted in Figure 2.12. To measure the anisotropy of the sterol motion and take full advantage of the use of oriented multilayer samples, QENS experiments took place in two specific orientations of the sample with respect to the incident neutron beam.

2.4.6 CALCULATING NEUTRON SCATTERING SPECTRA FROM MD TRAJECTORIES

In calculating the quasielastic scattering from an MD trajectory in order to compare it with the experimental pattern, it is essential to follow exactly the same procedure as

used by the experimentalists. That is, for the comparison to be meaningful, it is essential to compute spectra from the MD trajectory that are broadened by the resolution of the experiment.

Moreover, the calculations have to be performed for a specific orientation of **q**. The intermediate scattering function needs to be calculated only for the qx, qy, qz components of this **q** and not to be averaged as in the case of isotropic media.

For the 45° orientation, if we consider the incident beam to have coordinates $\mathbf{k}_{in} = k(cos45°, 0, -cos45°)$. where $k = 2\pi/\lambda$. Under the assumption that scattering is elastic, the moduli of $\mathbf{k}_{in}$ and $\mathbf{k}_{out}$ will be the same: $|\mathbf{k}_{in}| = |\mathbf{k}_{out}|$. The direction of $\mathbf{k}_{out}$ is given by the scattering angle, θ, as is schematically depicted in Fig. 2.11. Therefore, to get the coordinates of the scattered wave vector, $\mathbf{k}_{out}$, $\mathbf{k}_{in}$ has to be rotated anticlockwise with the scattering angle θ. $\mathbf{q} = (q_x, q_y, q_z)$ can be then calculated according to the relation $\mathbf{q} = \mathbf{k}_{out} - \mathbf{k}_{in}$ for all detector angles, θ.

For the 135° orientation, if we consider the incident beam to have coordinates $\mathbf{k}_{in} = \frac{2\pi}{\lambda}(sin45°, 0, cos45°)$, then the coordinates of $\mathbf{k}_{out}$ can also be calculated by anticlockwise rotation of $\mathbf{k}_{in}$ with respect to the scattering angle.

BIBLIOGRAPHY

[1] HOHENBERG, P., AND KOHN, W. Inhomogeneous Electron Gas. *Phys. Rev.*, 1964, **136**, B864–B871.

[2] KOHN, W., AND SHAM, L. Self-consistent equations including exchange and correlation effects. *Phys. Rev.*, 1965, **136**, A1133.

[3] BARTOLOTTI, L. J., AND FLURCHICK, K. An Introduction to Density Functional Theory. *Rev. Comp. Chem.*, 1996, **7**, 187–216.

[4] JENSEN, F. *Introduction to Computational Chemistry*. Wiley, USA, 1999.

[5] ST-AMANT, A. Density Functional Methods in Biomolecular Modeling. *Rev. Comp. Chem.*, 1996, **7**, 217–259.

[6] APPEL, H., AND GROSS, E. K. U. *Static and Time-Dependent Many-Body Effects via Density-Functional Theory*. *In:* Quantum Simulations of Complex Many-Body Systems: From Theory to Algorithms, NIC-Directors, 2002, pp. 255–268.

[7] BROOKS, B. R., BRUCCOLERI, R., OLAFSON, B. D., STATES, D. J., SWAMINATHAN, S., AND KARPLUS, M. CHARMM: A Program for Macromolecular Energy, Minimization and Dynamics Calculations. *J. Comp. Chem.*, 1983, **4**, 187–217.

[8] KURKAL, V., AND SMITH, J. C. Low temperature protein dynamics: A simulation analysis of inter-protein vibrations and the Boson peak at 150K. *J. Am. Chem. Soc.*, 2006, **128**, 2356–2363.

[9] LEACH, A. R. *Molecular Modelling. Principles and Applications*. Longman, Essex, England, 1999.

[10] ALLEN, M. P., AND TILDESLEY, D. J. *Computer Simulation of Liquids*. Oxford University Press Inc., New York, USA, 2001.

[11] EWALD, P. Die Berechnung optischer und elektrostatischer Gitterpotentiale. *Ann. Phys.*, 1921, **64**, 253–287.

[12] COURNIA, Z. *The ewald summation method: Calculating long-range interactions*. *In:* Beiträge zum Wissenschaftlichen Rechnen Ergebnisse des Gaststudentenprogramms 2000 des John von Neumann-Instituts für Computing, Zentralinstitut für Angewandte Mathematik, 2000, pp. 27–38.

[13] ABRAMOWITZ, M., AND STEGUN, I. *Handbook of mathematical functions*. Dover Publications, Inc., New York, USA, 1972.

[14] TUCKERMAN, M. E., AND MARTYNA, G. J. Understanding modern molecular dynamics: techniques and applications. *J. Phys. Chem. B*, 2000, **104**, 159–178.

[15] MCQUARRIE, D. *Statistical Mechanics*. Harper & Row, Harper & Row, New York, 1976.

[16] SUTMANN, G. *Classical Molecular Dynamics*. *In:* Quantum Simulations of Complex Many-Body Systems: From Theory to Algorithms, NIC-Directors, 2002, pp. 211–235.

[17] HOOVER, W. G. Canonical dynamics: Equilibrium phase-space distributions. *Phys. Rev. A*, 1985, **31**, 1695–1697.

[18] SCHAFTENAAR, G., AND NOORDIK, J. H. Molden: a pre- and post-processing program for molecular and electronic structures. *J. Comput.-Aided Mol. Design*, 2000, **14**, 123–134.

[19] FRISCH, M. J., TRUCKS, G. W., SCHLEGEL, H. B., GILL, P. M. W., JOHNSON, B. G., ROBB, M. A., CHEESEMAN, J. R., KEITH, T., PETERSSON, G. A., MONTGOMERY, J. A., RAGHAVACHARI, K., AL-LAHAM, M. A., ZAKRZEWSKI, V. G., ORTIZ, J. V., FORESMAN, J. B., CIOSLOWSKI, J., STEFANOV, B. B., NANAYAKKARA, A., CHALLACOMBE, M., PENG, C. Y., AYALA, P. Y., CHEN, W., WONG, M. W., ANDRES, J. L., REPLOGLE, E. S., GOMPERTS, R., MARTIN, R. L., FOX, D. J., BINKLEY, J. S., DEFREES, D. J., BAKER, J., STEWART, J. P., HEAD-GORDON, M., GONZALEZ, C., AND POPLE, J. A. Gaussian 94, Revision E.1. *Gaussian, Inc., Pittsburgh PA*, 1995.

[20] FRISCH, M. J., TRUCKS, G. W., SCHLEGEL, H. B., SCUSERIA, G. E., ROBB, M. A., CHEESEMAN, J. R., ZAKRZEWSKI, V. G., J. A. MONTGOMERY, J., STRATMANN, R. E., BURANT, J. C., DAPPRICH, S., MILLAM, J. M., DANIELS, A. D., KUDIN, K. N., STRAIN, M. C., FARKAS, O., TOMASI, J., BARONE, V., COSSI, M., CAMMI, R., MENNUCCI, B., POMELLI, C., ADAMO, C., CLIFFORD, S., OCHTERSKI, J., PETERSSON, G. A., AYALA, P. Y., CUI, Q., MOROKUMA, K., MALICK, D. K., RABUCK, A. D., RAGHAVACHARI, K., FORESMAN, J. B., CIOSLOWSKI, J., ORTIZ, J. V., BABOUL, A. G., STEFANOV, B. B., LIU, G., LIASHENKO, A., PISKORZ, P., KOMAROMI, I., GOMPERTS, R., MARTIN, R. L., FOX, D. J., KEITH, T., AL-LAHAM, M. A., PENG, C. Y., NANAYAKKARA, A., CHALLACOMBE, M., GILL, P. M. W., JOHNSON, B., CHEN, W., WONG, M. W., ANDRES, J. L., GONZALEZ, C., HEAD-GORDON, M., REPLOGLE, E. S., AND POPLE, J. A. Gaussian 98, Revision A.9. *Gaussian, Inc., Pittsburgh PA*, 1998.

[21] HARRISON, R. J., NICHOLS, J. A., STRAATSMA, T. P., DUPUIS, M., BYLASKA, E. J., FANN, G. I., WINDUS, T. L., APRA, E., ANCHELL, J., BERNHOLDT, D., BOROWSKI, P., CLARK, T., CLERC, D., DACHSEL, H., DE JONG, B., DEEGAN, M., DYALL, K., ELWOOD, D., FRUCHTL, H., GLENDENNING, E., GUTOWSKI, M., HESS, A., JAFFE, J., JOHNSON, B., JU, J., KENDALL, R., KOBAYASHI, R., KUTTEH, R., Z.LIN, LITTLEFIELD, R., LONG, X., MENG, B., NIEPLOCHA, J., NIU, S., ROSING, M., SANDRONE, G., STAVE, M., TAYLOR, H., THOMAS, G., VAN LENTHE, J., WOLINSKI, K., WONG, A., AND ZHANG, Z. NWChem, A Computational Chemistry Package for Parallel Computers, Version 4.0.1. *Pacific Northwest National Laboratory, Richland, Washington, USA*, 2001.

[22] TE VELDE, G., BICKELHAUPT, F. M., BAERENDS, E. J., GUERRA, C. F., VAN GISBERGEN, S. J. A., SNIJDERS, J. G., AND ZIEGLER, T. Chemistry with ADF. *J. Comp. Chem.*, 2001, **22**, 931.

[23] FORESMAN, J. B., AND FRISCH, A. E. Exploring Chemistry with Electronic Structure Methods. *Gaussian, Inc., Pittsburgh PA*, 1993, 2nd ed.

[24] VAIANA, A. C., SCHULZ, A., WORFRUM, J., M.SAUER, AND SMITH, J. C. Molecular mechanics force field parametrization of the fluorescent probe rhodamine 6G using automated frequency matching. *J. Comp. Chem.*, 2003, **24**, 632–639.

[25] COURNIA, Z., VAIANA, A. C., SMITH, J. C., AND ULLMANN, G. M. Derivation of a molecular mechanics force field for cholesterol. *Pure Appl. Chem.*, 2004, **76**, 189–196.

[26] COX, S. R., AND WILLIAMS, D. E. Representation of the Molecular Electrostatic Potential by a New Atomic Charge Model. *J. Comp. Chem.*, 1981, **2**, 304–323.

[27] CHIRLIAN, L. E., AND FRANCL, M. M. Atomic Charges Derived from Electrostatic Potentials: A Detailed Study. *J. Comp. Chem.*, 1987, **8**, 894–905.

[28] BRENEMAN, C. N., AND WIBERG, K. B. Determining atom-centered monopoles from molecular electrostatic potentials. The need for high sampling density in formamide conformational analysis. *J. Comp. Chem.*, 1990, **11**, 361–373.

[29] BEE, M. *Quasielastic Neutron Scattering*. Adam Hilger, Bristol and Philadephia, 1988.

[30] GABEL, F., BICOUT, D., TEHEI, U. L. M., WEIK, M., AND ZACCAI, G. Protein dynamics studied by neutron scattering. *Q. Rev. Biophys.*, 2002, **91**, 327–367.

[31] LOVESEY, S. W. *Theory of Neutron Scattering from Condensed Matter*. Clarendon Press, Oxford, 1984.

[32] KNELLER, G. R., KEINER, V., KNELLER, M., AND SCHILLER, M. nMOLDYN: A program package for a neutron scattering oriented analysis of molecular dynamics simulations. *Comp. Phys. Commun.*, 1995, **91**, 191–214.

[33] SMITH, J. C. Comparison of simulations with inelastic neutron scattering experiments. *Q. Rev. Biophys.*, 1991, **24**, 227.

CHAPTER 3

MOLECULAR MECHANICS FORCE FIELD PARAMETERIZATION OF CHOLESTEROL, ERGOSTEROL AND LANOSTEROL

The functional form of the force field used in a MD simulation must be used in conjunction with a set of empirical parameters, which are molecule dependent and must be optimized prior to performing simulations. This optimization step is generally referred to as parameterization of the force field. The reliability of a molecular mechanics (MM) calculation is dependent on both the functional form of the force field and the numerical values of the associated parameters. Thus, the first necessary step towards a reliable MD simulation is the parameterization procedure. Most "all-atom" empirical force fields used in common MD packages (such as CHARMM[1]) are equipped with parameter sets for modelling basic building blocks of biomolecules, which can then be combined for more complex molecular systems. However, for more exotic molecules such as steroids or sterols a force field is not available.

In the literature two force-field studies on cholesterol have appeared, for the CFF93[2] and CVFF[3] force fields[4] and for GROMOS96.[5, 6] The first study reproduces quite accurately the crystal structures of anhydrous cholesterol[7] and cholesterol acetate[8] and examines further the rigidity of the tetracyclic ring of cholesterol and cholesterol-cholesterol interactions. The latter study tested the existing GROMOS 96 force field against the cholesterol hemiethanolate crystal.[9] Although the poor quality of the crystal is a limiting factor for the results, the force field adequately reproduces the crystal properties; problems observed in this study with the conformation of the alkyl chain might arise from the 'united atom' approximation used. Most of the recently-reported cholesterol:membrane simulations have used united atom mod-

els.[10–12] Although united-atom force fields are rapid to calculate, all-atom force-fields may be required for the accurate modelling of some cholesterol:lipid interactions or the simulation of experimental techniques that probe hydrogen-atom dynamics, such as nuclear magnetic resonance (NMR) or incoherent neutron scattering.

In the present study, we present a new parameter set for cholesterol, ergosterol and lanosterol for the CHARMM force field. The work involved the refinement of a preliminary parameter set for cholesterol[13] and the developing from scratch sets for ergosterol and lanosterol. The parameters are obtained using the Automated Frequency Matching Method (AFMM),[14, 15] described in Chapter 2. Furthermore, care has been taken to reproduce the results for important rotational energy barriers. The final refined set for cholesterol is tested against the available crystal structure.[7]

3.1 COMPUTATIONAL DETAILS

All quantum chemical calculations were performed with the NWChem 4.5 package.[16] Geometry optimizations and normal mode analyses were performed at the DFT/B3LYP level of theory and with the SBKJC: Stevens-Basch-Krauss-Jasien-Cundari[17] basis set for the isolated molecules. To reduce computational time the effective core potential (ECP) of SBKJC was used for the carbons and the oxygen. ECPs replace the core electrons with an effective potential, thus eliminating the need for calculating the core basis functions, which usually require a large set of Gaussians to describe them. Geometry optimizations were performed to a maximum gradient of 0.00045 a.u. and a root mean square gradient of 0.0003 a.u. in the Cartesian coordinates. The frequencies were calculated numerically. A frequency scaling factor of 0.9614 was used to compensate for the use of the harmonic approximation to the potential energy surface.[18, 19] For the calculation of partial atomic charges, all the structures were first optimized at the DFT/6-31G(d) level of theory and then the CHELPG method[20] in NWChem was used to derive them. The grid on which the partial atomic charges were calculated as described in Section 2.3.2 was extended to 3 Å from any of the atomic centers and the grid spacing was set to 0.1 Å. In this study, all grid points lying within a distance less than 2 Å from any of the atomic centers were discarded.

The Hartree-Fock (HF) method was not preferred for the calculation of the charges, as it has been shown that HF/6-31G* RESP charges systematically overestimate dipole moments.[21] This overestimation may be tolerable when the system studied is solvated in a polar solvent, as the overestimated charges implicitly incorporate polarization effects on the molecular charge distribution. However, in an apolar environment such as a lipid bilayer, overestimation of the partial charges is not desired.

All molecular mechanics calculations were performed using the CHARMM27 package.[1] Except for the new parameters which are derived here, the existing CHARMM atom-type parameters were used.[22–25] The molecular mechanics minimizations were carried out using the Steepest Descent algorithm for initial minimization, followed by Newton-Raphson minimization with a convergence criterion for the energy gradient of 10^{-6} kcal/mol/Å. Non-bonded interactions were cut off at 12 Å using the CHARMM shifted potential.[1] In CHARMM the empirical potential energy function is given by Equation 2.37 (see also Section 2.2.4).

The MD simulation on the cholesterol crystal structure was performed at constant pressure-temperature with periodic boundary conditions and an integration time step of 0.001 ps. The starting configuration was taken from the experimental coordinates. After minimization the system was heated up to 500 K with 10 K temperature steps. Subsequently, the system was equilibrated for 10 ps using velocity rescaling followed by a second phase of equilibration without velocity rescaling for 10 ps at 298 K (the experimental temperature). Finally, production dynamics followed for 2 ns at 298 K.

3.1.1 PARAMETER REFINEMENT

The values of the various parameters in Eq. 2.37 must be determined. These parameters cannot be directly determined from experiments. The experimental data that pertain to force field calculations, such as infrared frequencies or crystal lattice constants are not a simple function of the force field parameters. Force-field parameters are more directly connected to quantities that are well-defined theoretically, such as the second derivatives of the energy with respect to coordinates (*i.e.* the Hessian matrix elements). These quantities can therefore be obtained via quantum chemical calculations.

Before refinement, an initial set of parameters must be determined. The LJ parameters ϵ_{ij} and R_{ij} depend mostly on atomic properties and are relatively insensitive to changes in the molecular environment. Here, these were directly transferred from original CHARMM values and were not modified during refinement.

Equilibrium values for bonds b_0, angles q_0 and dihedrals χ_0 that were not existing in the original CHARMM force field parameter file[22–25] were derived from the optimized quantum chemical structure and were not further optimized. An initial guess, based on analogy to similar existing CHARMM parameters and on chemical intuition, was made for all other missing parameters.

Equilibrium values and hybridization of the atoms involved should be carefully considered when deriving a set of initial parameters. In some cases it is necessary to

derive initial parameters from rotational potential energy profiles (single point QM energy calculations) before achieving good optimization. This approach is particularly useful for critical torsion parameters. After designing the initial parameter set, one can match the MM normal modes with reference normal modes and by visual inspection to check the motions involved in any exchanged eigenvector modes, using the Molden program[26] for example. This procedure can give a first hint as to which parameters were not appropriately designed or should be manually adjusted. The H-O-C_3-C_2 dihedral (see Figure 3.1a) was optimized by fitting the rotational energy barrier to the potential derived by quantum mechanical single-point calculations. These parameters were determined before the optimization and remained fixed during the rest of the optimization procedure.

The initial parameter set was used for minimization and calculation of normal modes (eigenvalues and eigenvectors) with CHARMM. The parameters were optimized by matching the obtained MM normal modes with reference normal modes calculated with the quantum chemistry methods employing the AFMM method.[14] AFMM uses an iterative procedure to refine the parameters in order to reproduce the quantum-chemical reference set of normal modes (both eigenvalues and eigenvectors).

An efficient way to check simultaneously for both orthonormality and frequency matching is to project each of the CHARMM eigenvectors onto the reference set of eigenvectors and to find the frequency ν_j^{max} corresponding to the highest projection (also discussed in Section 2.3.1). Plotting this frequency against the corresponding frequency, ν_i, would in the ideal case, give a one-to-one relationship: $\nu_i = \nu_j^{max}$. Points that deviate from the ideal plot may indicate exchanged or mismatched frequencies. AFMM is based on iteratively minimizing the sum-of-squares, Y^2 of the deviations from the ideal situation as follows:

$$Y^2 = \sum_{3N-6} (\nu_i - \nu_j^{max})^2 \tag{3.1}$$

where N is the number of atoms in the molecule; there are $3N - 6$ independent vibrational frequencies.

The range over which parameters were allowed to vary was ± 300 kcal/mol/Å^2, ± 100 kcal/mol/rad^2, ± 5 kcal/mol and ± 20 kcal/mol/rad^2 for the bond, angle, dihedral and improper force constants, respectively. To check for convergence of the function Y^2, the optimizations were allowed to run until the value of Y^2 remained constant for at least 6000 steps. The root-mean-square deviation, σ, from the reference case is also

calculated:

$$\sigma = \sqrt{\frac{\sum_{3N-6} (\nu_i - \nu_j^{max})^2}{3N-6}} \tag{3.2}$$

A desirable property of MM force fields is the transferability of the parameter set, *i.e.* the possibility to transfer parameters from one molecule to another. In this respect, when designing a new parameter set addition of new atom types to the force field should be limited only to those specific cases in which existing types cannot be used. For the parameterization of cholesterol and lanosterol, it was not necessary to define any new atom types for CHARMM and the parameterization was based on existing lipid atom types. For the sp^3 atoms the atom types used were CTL1, CTL2 and CTL3 with one/no (HAL1), two (HAL2), or three (HAL3) hydrogens, respectively. For the sp^2 lipid atoms, the atom type CEL1 was used with one hydrogen (HEL1). For the parameterization of ergosterol, it was necessary to introduce a new atom type (CAL1) for the atoms participating in the conjugated cis system of the steroid nucleus. The atom type CEL1, that is normally used to represent the sp^2 lipid atoms, is biased towards the *trans* isomer in the CHARMM27 force field. This results in the normal modes associated with the conjugated system highly deviating from the QM modes, which makes the introduction of a new atom type necessary. For the new atom type CAL1, LJ parameters of the sp^2 carbon atom type CEL1 were used. For all other parameters of ergosterol existing atom types were used.

3.2 RESULTS OF THE PARAMETERIZATION

DERIVATION OF THE PARAMETERS

3.2.1 PARAMETERIZATION OF CHOLESTEROL

Parameters for cholesterol were developed in a four step procedure. Initially, the charges were calculated on the QM-optimized structure with the CHELPG method. The AFMM method was then used to obtain a first complete set of parameters. In the third step parameters for the hydroxyl group rotation were further refined using single-point QM energy calculations performed on hexanol. Finally, all remaining parameters were re-refined using AFMM. Atom type assignments and partial atomic charges for cholesterol are listed in Table I of the Appendix. Final (refined) values for the new parameters for cholesterol can be found in Tables II to V of the Appendix.

The atom numbering scheme is shown in Figure 3.1a. The v_j^{max} vs. v_i plot for the refined cholesterol parameters is shown in Figure 3.2a. The corresponding value of

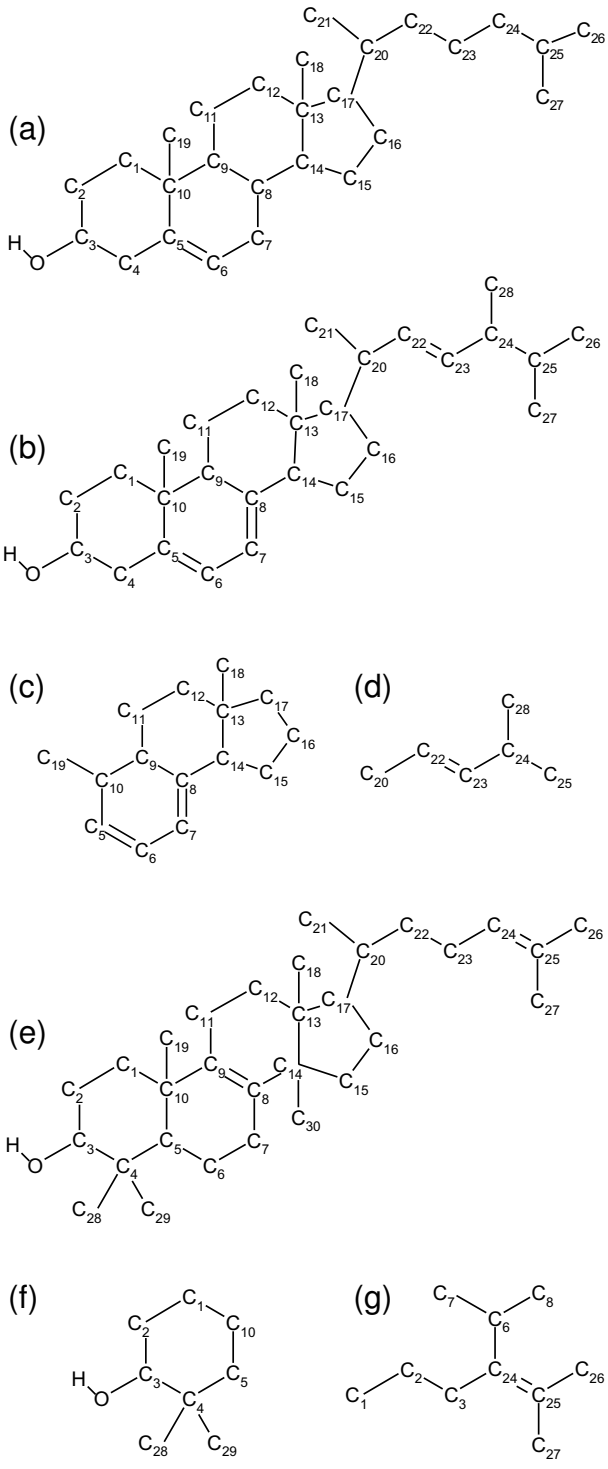

Figure 3.1: The atom numbering scheme of (a) cholesterol, (b) ergosterol, (c) NP, (d) 4-methyl-pent-2-ene, (e) lanosterol, (f) 2,2-dimethyl cyclohexanol, (g) 3-isopropyl-2-methylhex-2-ene.

σ= 40 cm^{-1} is lower than obtained in previous parameterization studies on molecules of similar size.[14]

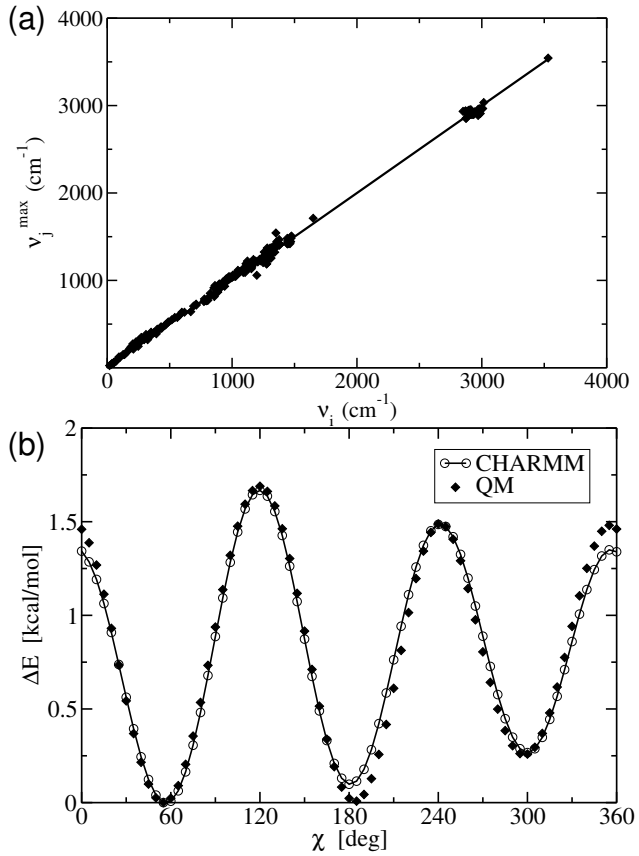

Figure 3.2: (a) Frequency matching plot (v_j^{max} vs. v_i) for cholesterol. The line is the ideal case of perfectly matched frequencies and eigenvector projections. Points refer to the optimized parameter set. σ= 40.0 cm^{-1}, (b) Rotational energy barrier along the C_2–C_3–O–H dihedral angle for cyclohexanol. The filled diamonds are the QM points calculated with NWChem. The open circles and the line are the fitted CHARMM potential.

Special care was taken to reproduce correctly the torsional potential of the hydroxyl group region. The rotation around this dihedral is very important because it can influence the residence time and stability of the hydrogen bonds between cholesterol and water and lipid head groups in a membrane simulation. The cholesterol hydroxyl hydrogen atom can adopt three conformations with minimum energy (*i.e.*, gauche$^+$, anti and gauche$^-$) with respect to C_2. To check the accuracy of the parameter set in this region we calculated the rotational energy barrier of the H-O-C_3-C_2 dihedral, using both molecular mechanics and quantum chemistry. To reduce computational time, these calculations were performed using hexanol as a model of the first sterol ring.

The torsional force constants [K_χ in Eq. 2.37] were derived from the energy barrier for rotation of the above-mentioned dihedral at the DFT/SBJKC level of theory

using single-point calculations of the geometry-optimized structures. The remaining missing CHARMM parameters were re-optimized using AFMM. The rotational energy barrier of the H-O-C_3-C_2 dihedral after the final parameterization is shown in Figure 3.2b. In CHARMM, the dihedral potential energy term has the functional form: $K_\chi(1 + cos(n\chi - \chi_0)$. To obtain an improved fit to the rotational barrier, the H-O-C_3-C_2 dihedral potential is represented as a combination of two terms (see Table V of the Appendix).

3.2.2 PARAMETERIZATION OF ERGOSTEROL

Most of the CHARMM parameters for ergosterol are the same as those for cholesterol, and thus they were directly transferred from the optimized cholesterol parameters, given the similarity of the two molecules. To derive parameters which were still missing and to save computational time, calculations were performed on the ergosterol molecule truncated to the steroid ring part *i.e.* 2,3,3a,4,5,5a,6,9b-octahydro-3a,6-dimethyl-1*H*-cyclopenta[*a*]napthalene (NP), and to the alkyl tail part (4-methyl pent-2-ene), see Figures 3.1c and 3.1d, respectively.

As mentioned in the "Parameter Refinement" section, the ergosterol molecule has a conjugated π-system in its second steroid ring with two *cis* hydrogens on C_6 and C_7. Initial parameterization of the ergosterol molecule, using the CHARMM atom type CEL1 for all the double bonds in the system, showed high deviation of certain normal modes from the QM reference vibrations. After visual inspection of the motions involved in the exchanged modes with the Molden program, we attributed this mismatch to vibrations located in the conjugated π system. The current implementation of the CEL1 atom type is biased towards accurate representation of the *trans* isomer. Therefore, modeling a system containing both *cis* and *trans* bonds required the introduction of a new atom type, CAL1, which corresponds to the conjugated π-system. For all other atoms existing atom types were used. Due to the similarity of cholesterol and ergosterol in C_3, C_4, C_5, and C_6, the parameters optimized for these carbons for the cholesterol molecule were directly transferred to ergosterol. Atom type assignments and partial atomic charges for lanosterol are listed in Table VI of the Appendix. Final (refined) values for the new parameters for lanosterol can be found in Tables III to V of the Appendix.

The resulting v_j^{max} vs. v_i plots after the parameter optimization of NP and of 4-methyl pent-2-ene are shown in Figures 3.3a and 3.3b, respectively. The corresponding values of σ= 38.7 cm^{-1} and of σ= 58.5 cm^{-1} are within the σ-values obtained in previous parameterization studies of similarly-sized molecules.[14]

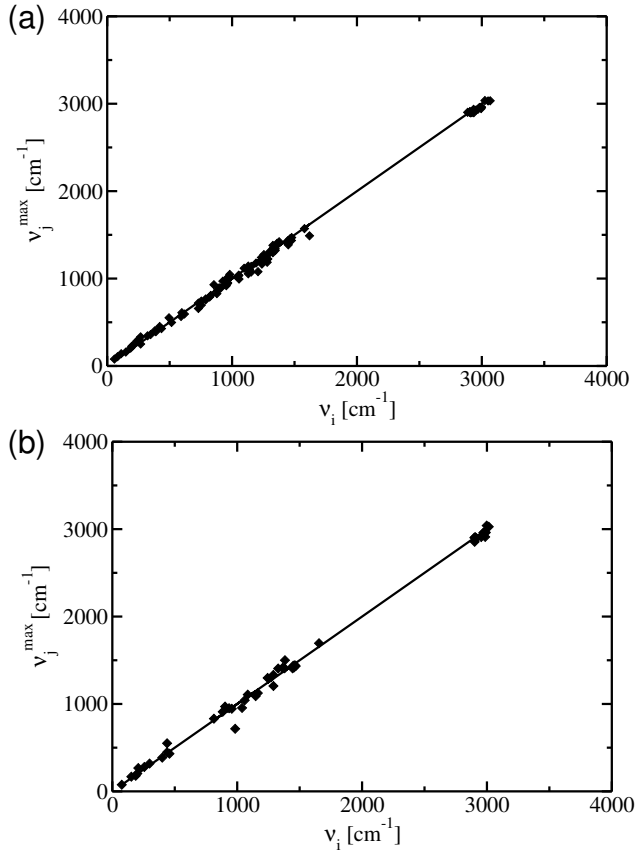

Figure 3.3: Frequency matching plot (v_j^{max} vs. v_i) for (a) NP (σ= 38.7 cm^{-1}) and for (b) 4-methyl pent-2-ene (σ= 58.5 cm^{-1}). The line is the ideal case of perfectly matched frequencies and eigenvector projections. Points refer to the optimized parameter set.

3.2.3 PARAMETERIZATION OF LANOSTEROL

For the parameterization of lanosterol, parameters developed for both cholesterol and ergosterol were transferred and only parameters that did not previously exist were optimized. For computational efficiency lanosterol was parameterized using two smaller molecules: 2,2 dimethyl cyclohexanol and 2 methyl 3 isopropyl hex-2-ene (Figures 3.1f and 3.1g, respectively). The resulting v_j^{max} vs. v_i plots for the two molecules are shown in Figures 3.4a (σ= 41.2 cm^{-1}) and 3.4b (σ= 61.2 cm^{-1}), respectively.

The first steroid ring of lanosterol is bulkier than that of cholesterol, containing two extra methyl groups on C_4. As in the case of cholesterol, we calculated the rotational energy barrier of the HO–O–C_3–C_2 dihedral, using both molecular mechanics and quantum chemistry. To reduce computational time, this calculation was performed using 2,2 dimethyl hexanol to model the first sterol ring. The torsional force constants [K_χ in Eq. 2.37] were derived from the energy barrier for rotation of the above-mentioned dihedral at the DFT/SBJKC level of theory using single point calculations

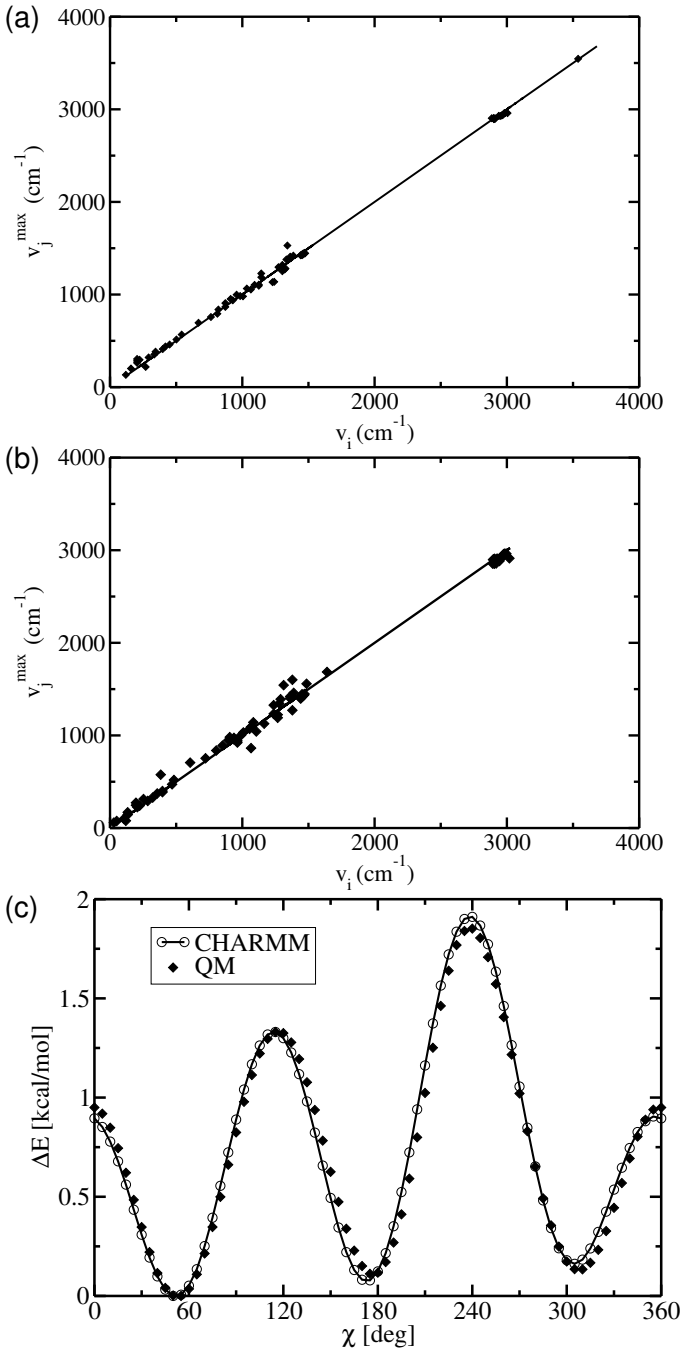

Figure 3.4: Frequency matching plot (v_j^{max} vs. v_i) for (a) 2,2 dimethyl hexanol (σ= 41.2 cm^{-1}) and for (b) 3-isopropyl-2-methylhex-2-ene (σ= 61.2 cm^{-1}). The line is the ideal case of perfectly matched frequencies and eigenvector projections. Points refer to the optimized parameter set. (c) Rotational energy barrier along the C_2–C_3–O–H dihedral angle of 2,2 dimethyl cyclohexanol. The filled diamonds are the quantum chemically calculated energies. The open circles and the line are the fitted CHARMM potential.

to scan the potential energy profile.

In the case of lanosterol, two two-fold and two one-fold dihedral terms were added to the already existing three-fold term of the potential to obtain a better fit for the barrier (see Table V of the Appendix). The rotational energy barrier of the H–O–C_3–C_2 dihedral after the final parameterization can be seen in Figure 3.4c. The 2 kcal/mol barrier arises from the unfavorable interaction between the two methyl groups on C_4 and with the hydroxyl hydrogen. The parameters adjusted to reproduce this rotational barrier were subsequently fixed and the remaining parameters optimized in CHARMM using AFMM. Atom type assignments and partial atomic charges for lanosterol are listed in Table VII of the Appendix. Final (refined) values for the new parameters for lanosterol can be found in Tables III to V of the Appendix.

3.3 TESTING OF THE PARAMETERS

3.3.1 CHOLESTEROL CRYSTAL SIMULATION

Final testing of a parameter set should be performed against independent experimental and/or theoretical data. Here, the refined potential was tested by performing an energy minimization and MD simulation of cholesterol in its crystalline state and comparing the results with the X-ray experimental results.[7] The experimental unit cell contains eight cholesterol molecules (A-H) and is triclinic with no symmetry (space group P_1) as seen in Figure 3.5a.

In all structures of cholesterol and its solvates, the molecules adopt a bilayer arrangement generally similar to that of cholesterol in biological membranes with alternating hydrophilic and hydrophobic layers. In the hydrophilic layer of the triclinic unit cell there are four hydrogen-bonded chains parallel to the c-axis, with all eight hydrogen atoms of each hydroxyl group pointing towards the positive c direction. The molecules are hydrogen-bonded in two separate chains: ...-BHAG-BHAG-... and ...-DFCE-DFCE-... (see Figure 3.5b).

Another interesting feature of the cholesterol crystal is the presence of local pseudosymmetry, i. e., non-crystallographic symmetry.[27] Each molecule in one chain is related to a molecule in the other chain by a series of parallel axes of local twofold symmetry. Thus, molecule A is related to molecule E, H to D, B to F, and G to C. The pseudosymmetry operation, which applies to complete molecules, involves a rotation of 180° and a translation of about 2.8 Å parallel to the c-axis. This operation brings molecules A, B, C and D into close superposition with molecules E, F, G and H. This complex packing arrangement allows an infinite hydrogen-bonded network

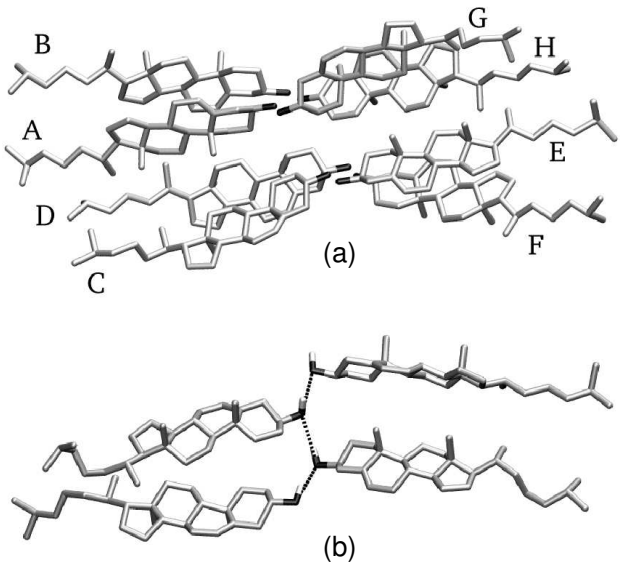

Figure 3.5: (a) Experimental unit cell of the crystal structure of cholesterol projected on the a, b plane. The crystal structure is that of ref. 7. The letters A, B, C, D, E, F, G, H mark the crystallographically resolved molecules. (b) Hydrogen bonding scheme for molecules D, F, C, E (top to bottom) in the crystal structure of cholesterol.

to be formed, with an average O...O distance of 2.9 Å. In the monohydrate structure of cholesterol[28] the cholesterol molecules exhibit a more regular packing due to the presence of the water molecules, which assist the hydrogen-bonded bridges.

The MD calculations were performed for the whole crystal using periodic boundary conditions. The unit cell dimensions were allowed to vary both during the energy minimization and the MD simulation. Hydrogens were constructed using idealized geometric parameters form the HBUILD module in CHARMM.

The energy-minimized cell vectors are reported in Table 3.1 along with the experimental values. After minimization the cell volume was computed to be 5056.8 Å^3, within 0.5 % of the experimental volume of 5032.8 Å^3.

Cell Dimension	Experimental Values	Energy Minimization	Molecular Dynamics
a	14.172 Å	13.94 Å	(14.26 ±0.21) Å
b	34.209 Å	35.03 Å	(34.24 ±0.49) Å
c	10.481 Å	10.39 Å	(10.73 ±0.14) Å
α	94.64°	93.70°	(94.61 ±1.83)°
β	90.67°	91.46°	(90.99 ±1.63)°
γ	96.32°	91.38°	(97.03 ±1.85)°

Table 3.1: Cell Vectors for the cholesterol X-ray diffraction at room temperature and after energy minimization and MD using the new CHARMM force field.

The calculated cell vectors and the volume obtained during the MD simulation are shown in Table 3.1. The MD simulation reproduces the hydrogen-bonded network in the cholesterol crystal. The hydrogen-bond distances are shown in Table 3.2.

HBond Pair	X-Ray	Molecular Dynamics
A-G	2.97	3.01±0.18
B-H	2.82	2.93±0.16
C-E	2.76	2.91±0.15
D-F	2.90	2.97±0.17
F-C	2.88	2.93±0.16
H-A	2.79	2.88±0.14

Table 3.2: O$\cdots$O distances between hydrogen bonded pairs in Angstroms. Experimental values, values after energy minimization and mean values and standard deviations from the molecular dynamics simulation.

The MD H-bonds were slightly longer (0.1 Å on average) than those reported experimentally. However, we observed that the H-bonding pattern remains stable throughout the simulation. (Time-series of the O...O distances between the hydrogen-bonded pairs D-F, F-C, C-E from the first chain and B-H, H-A, A-G from the second chain can be seen in Figure 3.6).

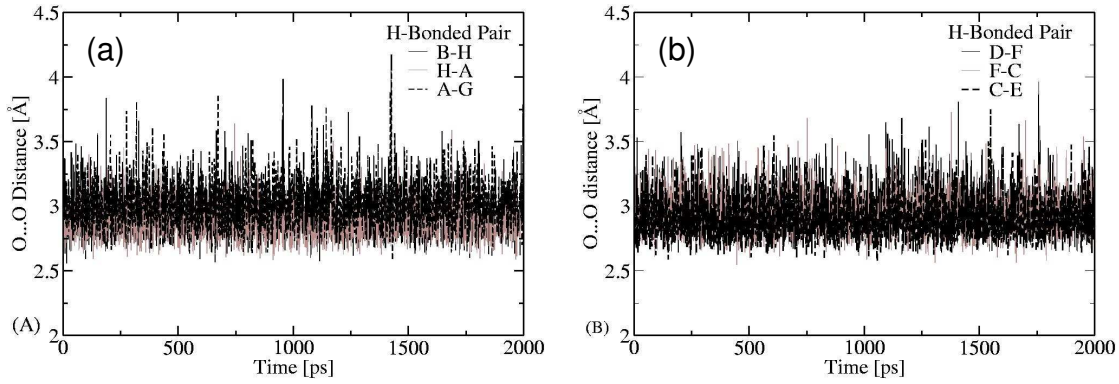

Figure 3.6: Time series of the hydrogen bond distances between two oxygen atoms that form a hydrogen-bonded pair (a) in the first chain between molecules B-H, H-A, A-G and (b) in the second chain between molecules D-F, F-C, C-E.

The average H-bonding distance is 2.9 Å for the six hydrogen bonds formed. The experimental ordering of the hydrogen-bonded distances within each of the two hydrogen-bonded chains is also preserved, e.g. $d_{DF} > d_{FC} > d_{CE}$. The angle between the donor hydroxyl group and the acceptor oxygen atom was found to be on average 160.3° for the six hydrogen bonds formed in the primary unit cell, which is close to linearity (see Table 3.3).

HBond Pair	Molecular Dynamics
A-G	163.8±9.1
B-H	156.4±10.8
C-E	164.7±8.3
D-F	151.8±11.3
F-C	160.8±9.3
H-A	164.4±8.5

Table 3.3: O-H...O angles between hydrogen bonded pairs in degrees. Mean values and standard deviations from the molecular dynamics simulation.

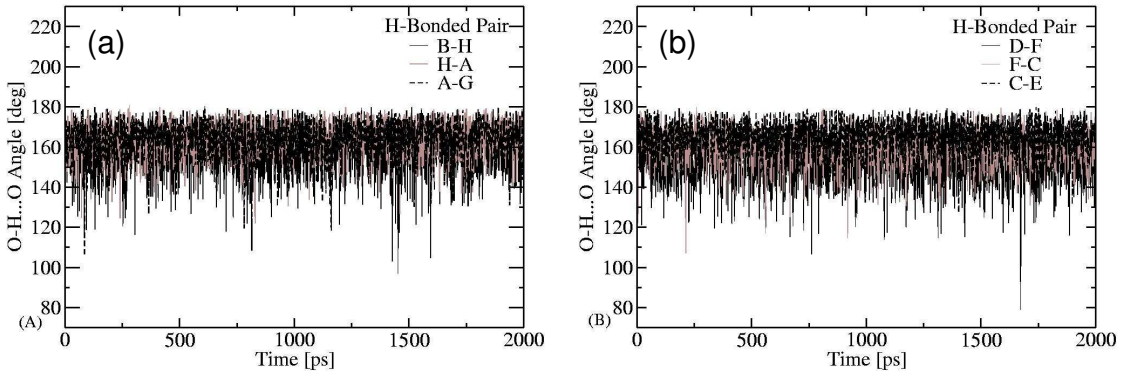

Figure 3.7: Time series of the hydrogen bond angles O-H...O between atoms that form a hydrogen-bonded pair (A) in the first chain between molecules B-H, H-A, A-G and (B) in the second chain between molecules D-F, F-C, C-E.

Figure 3.7 shows the time series of these angles. Further evidence that the hydrogen bonds remain stable during the simulation comes from the observation that the dihedral C_1-C_2-C_3-O remains almost constant for all eight molecules, with a value of 175.1±3.7° (see Table 3.4).

Hydrogen bonds link the molecules into chains along the c-axis and all eight hydrogen atoms of each hydroxyl group point towards the positive c direction. The mean value of the angle between the a axis of the unit cell and the O-H vector (Table 3.5) is 91.1°, indicating that the preferred position of the hydrogens is indeed aligned with the c-axis of the unit cell.

The distribution of the interaction energies between two hydrogen-bonded hydroxyl groups is plotted in Figure 3.8. for the hydrogen bonded pairs H-A, A-G, B-H from the first chain and E-C, C-F, F-D from the second. The mean value of the hydrogen-bond strength, -4.2 kcal/mol, lies well within the typical hydrogen bond range (-1 to -5 kcal/mol depending on donor and acceptor atom as well as their environment).

To examine the rigidity of the steroid rings the average values and standard devia-

Molecule	Experimental	Minimization	Molecular Dynamics
D	179.4	179.6	175.7±3.3
F	177.5	177.8	175.5±3.4
C	178.7	176.1	174.8±3.9
E	179.8	177.6	174.7±3.9
H	176.5	179.0	175.5±3.4
B	179.3	177.8	175.5±3.4
G	177.2	176.6	174.9±3.8
A	179.9	178.0	174.7±3.9

Table 3.4: C_1-C_2-C_3-O dihedral angle value in degrees. Experimental values, and mean values and standard deviations from the molecular dynamics simulation.

Molecule	θ
A	88.0±10.9
B	111.0±16.9
C	102.3±11.0
D	89.1±13.4
E	86.7±10.4
F	83.8±20.0
G	80.4±10.5
H	87.5±13.3

Table 3.5: Angles between hydrogen atoms of the hydroxyl group with respect to the *a*-axis, in degrees. Mean values and standard deviations from the molecular dynamics simulation.

tions of the torsional angles of the steroid ring system were calculated. The low values of the deviations show that the eight steroid units are similar and do not undergo major variability. The results, shown in Table 3.6, are in good agreement with those obtained in the crystal structure study.[7]

The hydrocarbon tail of cholesterol is expected to be flexible at room temperature and to undergo several conformational transitions. Table 3.7 shows the percentage of the *trans* conformation for the alkyl tail dihedrals of cholesterol. It is clear that, compared to the simulation of a single molecule in vacuum (see below), the crystal environment inhibits the *trans* to *gauche* transitions of the individual molecules due to steric hindrance arising from the packing in the crystal. The adjacent crystal molecules 'lock' the conformation, for example the pseudosymmetrically-related molecules C and G adopt a *gauche*$^-$-*trans*-*gauche*$^-$ conformation in the crystal and do not change it throughout the simulation. The atoms of the hydrocarbon tail of cholesterol are more flexible than the steroid-ring atoms. Therefore they are expected to exhibit more freedom of movement, corresponding to spreading of the probability distribution of

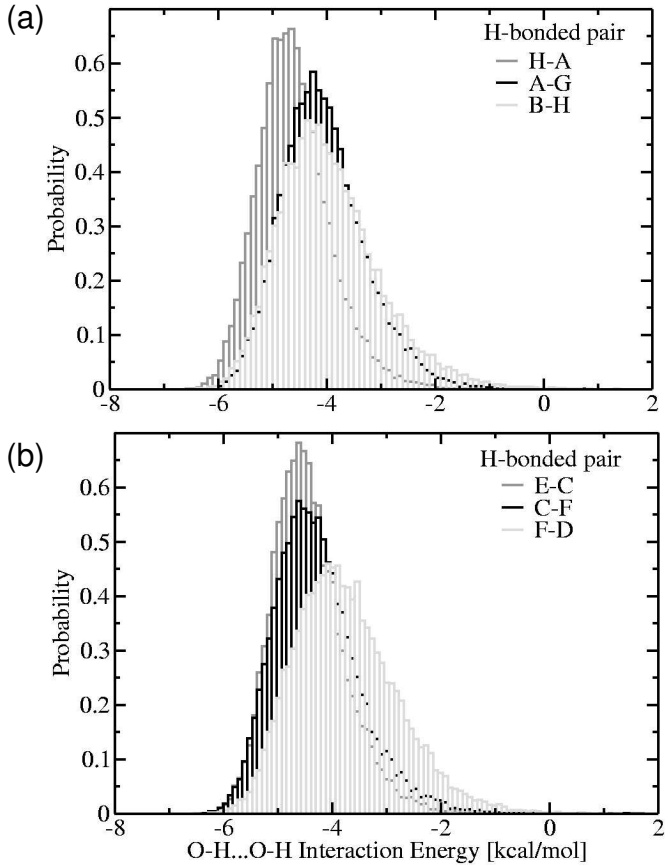

Figure 3.8: Probabilities of interaction energies for the hydrogen-bonded hydroxyl pairs in the primary unit cell (a) between molecules H-A (-4.6±0.7 kcal/mol), A-G (-4.1±0.8 kcal/mol), B-H (-4.0±0.9 kcal/mol) and (b) in the second chain between molecules E-C (-4.4±0.7 kcal/mol), C-F (-4.3±0.8 kcal/mol), F-D (-3.7±0.9 kcal/mol). The values in the parentheses correspond to mean values and standard deviations.

each atom over a small region of space. Diffraction is affected by this spreading out of the atomic positions, as manifested by temperature factors (B-factors), assigned to each atom. Assuming isotropic, harmonic dynamics, the B-factor is given by:

$$B_{eq} = \frac{8\pi^2}{3}\langle u^2 \rangle \tag{3.3}$$

where $\langle u^2 \rangle$ is the mean-square fluctuation of the position of an atom.

In Figure 3.9a the average experimental and calculated isotropic B-factors for the oxygen and the carbon atoms of cholesterol are shown. Figure 3.9b shows the unit cell colored by the B-factor: red indicates high values of B_{eq} and blue low values of B_{eq}. Both representations indicate parts of the molecule that are particularly flexible and parts, which are particularly rigid. The side-chain B-factors are larger and more varied (10 to 45 Å^2) than those of the rigid steroid ring atoms (3 to 9 Å^2). The B-

torsion angle	Experiment	MD of crystal	MD of single molecule
C_1-C_2-C_3-C_4	58±2	55.9±5.2	56.6±5.7
C_2-C_3-C_4-C_5	-56±2	-54.7±5.6	-54.6±6.3
C_3-C_4-C_5-C_{10}	53±1	53.0±5.3	51.0±6.3
C_4-C_5-C_{10}-C_1	-48±3	-47.6±4.6	-45.5±5.6
C_5-C_{10}-C_1-C_2	49±4	48.7±5.4	47.8±6.2
C_5-C_6-C_7-C_8	13±1	15.7±5.3	12.6±6.5
C_6-C_7-C_8-C_9	-43±2	-44.0±5.5	-39.9±7.0
C_7-C_8-C_9-C_{10}	62±1	60.8±4.5	58.9±5.0
C_8-C_9-C_{10}-C_5	-47±2	-45.8±4.9	-47.4±5.7
C_8-C_{14}-C_{13}-C_{12}	-61±1	-59.4±4.3	-59.5±4.4
C_9-C_8-C_{14}-C_{13}	57±1	55.2±4.7	56.1±4.8
C_9-C_{10}-C_5-C_6	16±2	16.7±4.8	19.4±5.9
C_{10}-C_1-C_2-C_3	-56±2	-55.3±5.7	-55.6±6.1
C_{10}-C_5-C_6-C_7	1±2	-1.9±3.5	-2.2±3.7
C_{11}-C_9-C_8-C_{14}	-49±1	-46.5±5.0	-48.1±5.3
C_{12}-C_{11}-C_9-C_8	50±2	47.1±6.0	48.4±6.1
C_{13}-C_{12}-C_{11}-C_9	-55±1	-51.3±5.7	-51.5±5.7
C_{13}-C_{14}-C_{15}-C_{13}	-34±1	-30.3±5.7	-30.5±5.9
C_{14}-C_{13}-C_{12}-C_{11}	56±1	54.9±4.6	54.4±4.8
C_{14}-C_{15}-C_{16}-C_{17}	8±2	5.2±6.8	5.9±7.1
C_{15}-C_{16}-C_{17}-C_{13}	21±2	20.8±6.5	20.0±7.0
C_{16}-C_{17}-C_{13}-C_{14}	-41±2	-37.5±4.3	-37.0±4.8
C_{17}-C_{13}-C_{14}-C_{15}	47±1	42.3±3.8	42.1±4.0

Table 3.6: Torsional angles (°) in the rings of the steroid ring system, averaged over the eight molecules. Experimental values and mean values from the molecular dynamics simulations of the crystal and of the single molecule.

factors obtained from MD are somewhat larger than those derived experimentally for the ends of the flexible tails. These differences may arise from the use of isotropic, harmonic approximation in the experimental refinement; this approximation is invalid for barrier-crossing dynamics (e.g. *trans-gauche* dynamics).

The root mean square deviation (RMSD):

$$RMSD = \sqrt{\frac{1}{N}\sum_{i=1}^{N}(x_i - \overline{x})^2} \tag{3.4}$$

between the experimental and calculated average structure and experimental non-hydrogen atom positions in the unit cell was found to be 0.45 Å, but after comparison only to atoms with experimental $B_{eq} < 10$ Å^2 the RMSD becomes 0.22 Å. After removing the rotation and translation of the individual molecules in the unit cell, the RMSD was 0.33 Å including all heavy atoms and 0.13 Å when including only atoms

Carbon Atoms	single molecule	A	B	C	D	E	F	G	H
C_{17}-C_{20}-C_{22}-C_{23}	96.2	100.0	100.0	0.0	100.0	100.0	100.0	0.0	100.0
C_{20}-C_{22}-C_{23}-C_{24}	68.0	84.4	99.6	100.0	92.0	83.6	100.0	100.0	100.0
C_{22}-C_{23}-C_{24}-C_{25}	84.6	93.5	92.8	0.0	96.4	98.5	22.1	0.0	100.0
C_{23}-C_{24}-C_{25}-C_{26}	33.0	51.9	59.5	0.0	16.7	21.8	13.2	0.0	1.0

Table 3.7: Percentages (%) of *trans* conformations for the alkyl tail of cholesterol. The A-H columns refer to the molecules from the molecular dynamics simulation of the crystal.

with $B_{eq} < 15$ Å^2. Averaging the coordinates of the eight cholesterol molecules over all the trajectory, and calculating the RMSD with respect to the average experimental coordinates of one cholesterol molecule (including all non-hydrogen atoms with $B_{eq} < 15$ Å) the RMSD reduces significantly, to 0.07 Å.

Molecular crystals are held together due to attractive non-bonded energies between the molecules (electrostatic, van der Waals forces). Since the cholesterol crystal has a high melting point (around 140 °C), these energies must be relatively strong. The average interaction energy between a cholesterol molecule and the rest of the crystal was found to be -53.7±0.6 kcal/mol, from which 85 % arises from van der Waals interactions and 15 % from electrostatics.

To further examine the nature of the non-bonded interactions in the cholesterol crystal, interaction energies between the different cholesterol molecules were calculated. Adjacent molecules along the positive c-axis (*i.e.* on top of each other) form four chains: ...ABAB...(I), ...CDCD...(II), ...EFEF...(III) and ...HGHG...(IV) and each cholesterol pair in these chains has negative van der Waals energies. In chains I and III, the cholesterol molecules interact as seen in Figure 3.10d and in chains II and IV as seen in Figure 3.10b. The molecules in these two groups of chains contain molecules which are pseudosymmetrically related between them. The time series of the interaction energy between molecules A and B, E and F (of chains I and III) and between molecules C and D, H and G (of chains II and IV) in the primary unit cell are shown in Figures 3.10c and 3.10a, respectively. The interaction energy is averaged over the two pseudosymmetrically-related pairs. Adjacent image molecules that contribute to the interaction energy were included in the calculation. Further decomposition of the interaction energy of these pairs into the van der Waals and electrostatic contributions shows that the electrostatic interaction energy is small and the main stabilizing energetic contribution arises from the van der Waals energy. In addition, the main van der Waals contribution to the interaction energy was found to arise from the ring-ring interaction between molecules that are on top of each other. The van der Waals interaction energies between two adjacent molecules in chains I and III, and chains II

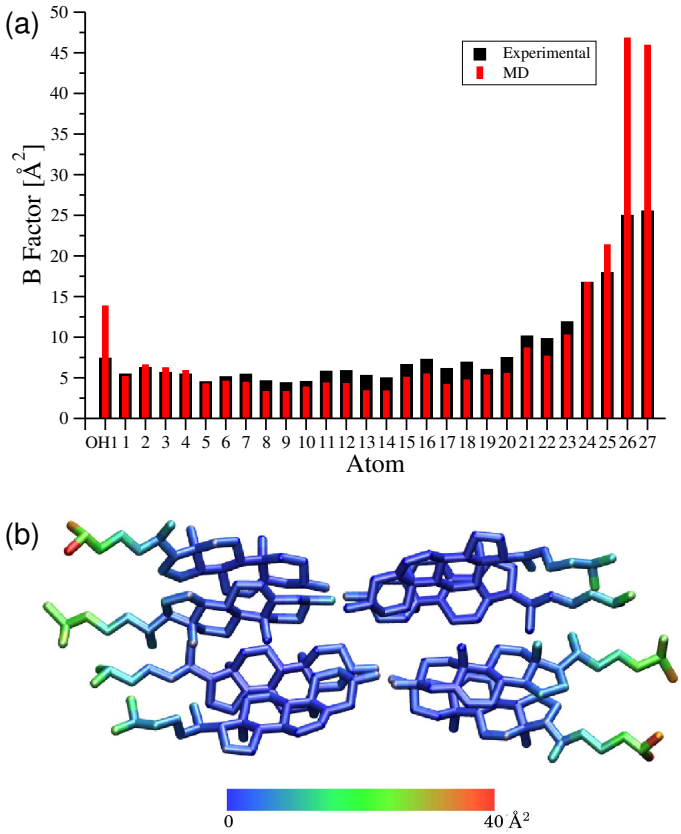

Figure 3.9: (a) Experimental versus the calculated average B-factors for the oxygen and the carbon atoms. (b) The experimental unit cell colored according to the experimentally determined B-factors (Å^2). Red ("hot") corresponds to high values of B-factors and blue ("cold") corresponds to low values of B-factor. The color scale is given at the bottom.

and IV have mean values of -10 kcal/mol and -8.5 kcal/mol, respectively. This interaction energy is more than double the mean hydrogen-bond energy between cholesterol molecules in the crystal.

The interaction energy between molecules that are hydrogen-bonded along the c-axis is mainly electrostatic. The average interaction energy of all eight hydrogen-bonded pairs is -4.1$\pm$0.1 kcal/mol. The electrostatic contribution to the average interaction energy of all hydrogen-bonded pairs is -4.9$\pm$0.3 kcal/mol, while the van der Waals contribution accounts for 0.8$\pm$0.2 kcal/mol. As an example, the distribution of the total interaction energy of the hydrogen bonded pair B and H along with the electrostatic and van der Waals contributions can be seen in Figure 3.11. Along the c-axis the favorable forces in the cholesterol crystal are the hydrogen-bonded network and the van der Waals interactions between the rings of adjacent molecules. Figure 3.12a shows three unit cells projected on the (c, b) plane. Hydrogens have been omitted from

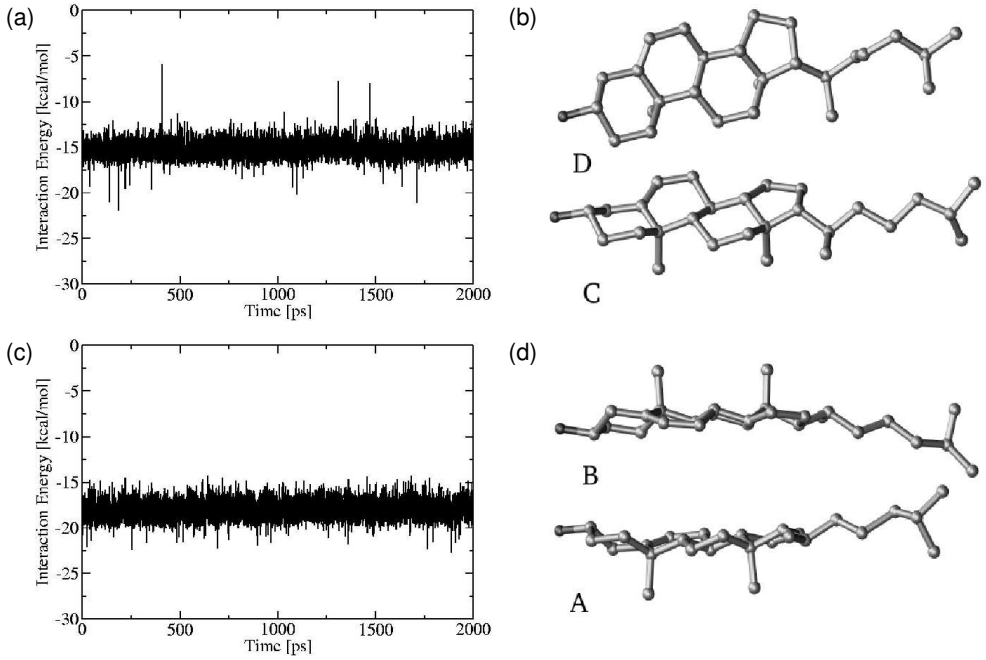

Figure 3.10: (a) Time series of the interaction energy between molecules C and D and between molecules H and G (averaged). (b) Adjacent molecules C and D projected on the (c, b) plane. (c) Time series of the interaction energy between the molecules A and B and between molecules E and F (averaged). (d) Adjacent molecules A and B projected on the (c, b) plane The cholesterol pairs shown, form chains along the c-axis in the crystal, *i.e.* ...ABAB... and ...CDCD... The molecules in these chains have favorable interaction energies that arise mainly from the ring-ring interaction of adjacent molecules.

the representation for clarity.

Along the a axis in the primary unit cell, molecules B and D, F and H, C and A, E and G are adjacent (see Figure 3.5a). The interaction energy between adjacent along the a-axis cholesterol molecules arises mainly from van der Waals contributions. For example, the van der Waals interaction energy between adjacent molecules B and D is on average -4.2±0.6 kcal/mol and the electrostatic interaction energy 0.4±0.1 kcal/mol (see Figure 3.3.1). When constructing the crystal lattice, the corresponding transformations following the geometry of the unit cell place the ring of molecule C next to the hydrogen-bonded molecules A and G of the next unit cell, as well as placing the ring of molecule A next to the hydrogen bond between molecules C and E of the neighboring unit cell (see Figure 3.12b). The interaction energy between these pairs was also calculated and it was found that again the van der Waals interactions dominate. The van der Waals interaction energy between molecule C of the primary unit cell and molecule G of the image unit cell was found to be on average -5.0±0.6 kcal/mol and the electrostatic interaction energy just 0.3±0.1 kcal/mol (see Figure 3.3.1). It is interesting to note that, in both cases, the van der Waals contribution

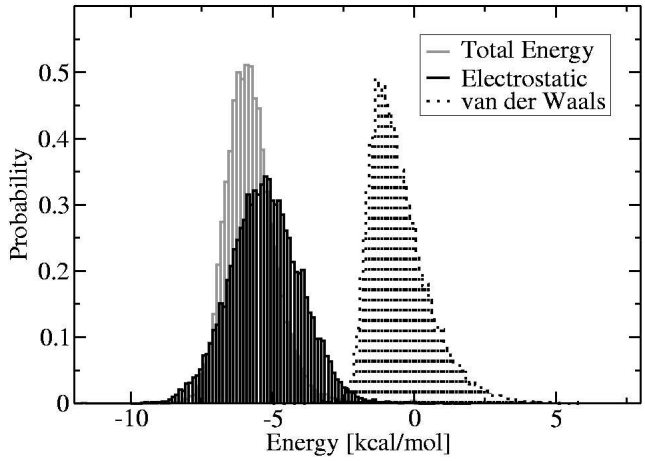

Figure 3.11: The total, van der Waals and electrostatic energy probability distributions for the hydrogen-bonded pair B–H. The main contribution to the interaction energy of a hydrogen bond arises from electrostatics.

to the interaction energy has the approximate strength of a hydrogen bond.

Along the *b*-axis (*i.e.* the long axis of the unit cell) the crystal forms an alternating network of hydrophobic and hydrophilic layers (Figure 3.12c). The hydrocarbon chains are staggered, resulting to significant interdigitation in the hydrophobic layer. Specifically, the tails of the molecules B and F from the primary unit cell come in to close contact with the tails of the image molecules F and B, respectively (see Figure 3.12c). The tail of molecule F comes near the tail of molecule A, the one of molecule H to molecule A, molecule D to E, A to E, B to G and B to E. The interaction energy between the tails of the molecules is also found to be favorable and to arise mainly from van der Waals forces.

The above observations allow us to conclude that the dominating energy contribution to the total interaction energy in the cholesterol crystal is the negative van der Waals interaction between neighboring molecules. Electrostatics contribute $\approx$15% to the total interaction energy, arising from the hydrogen-bonded network.

3.3.2 800K MD *in vacuo* OF CHOLESTEROL, ERGOSTEROL AND LANOSTEROL

It has been shown that the chiral conformation of biologically-important sterols is essential for their *in vivo* function.[29] Therefore, it is important that the sterols should preserve their stereochemistry during an MD simulation. In previous MD simulation studies of cholesterol in bilayers with other force fields, an inversion of the asymmetrical centers were observed.[30] To ensure that the chirality of the molecule is maintained

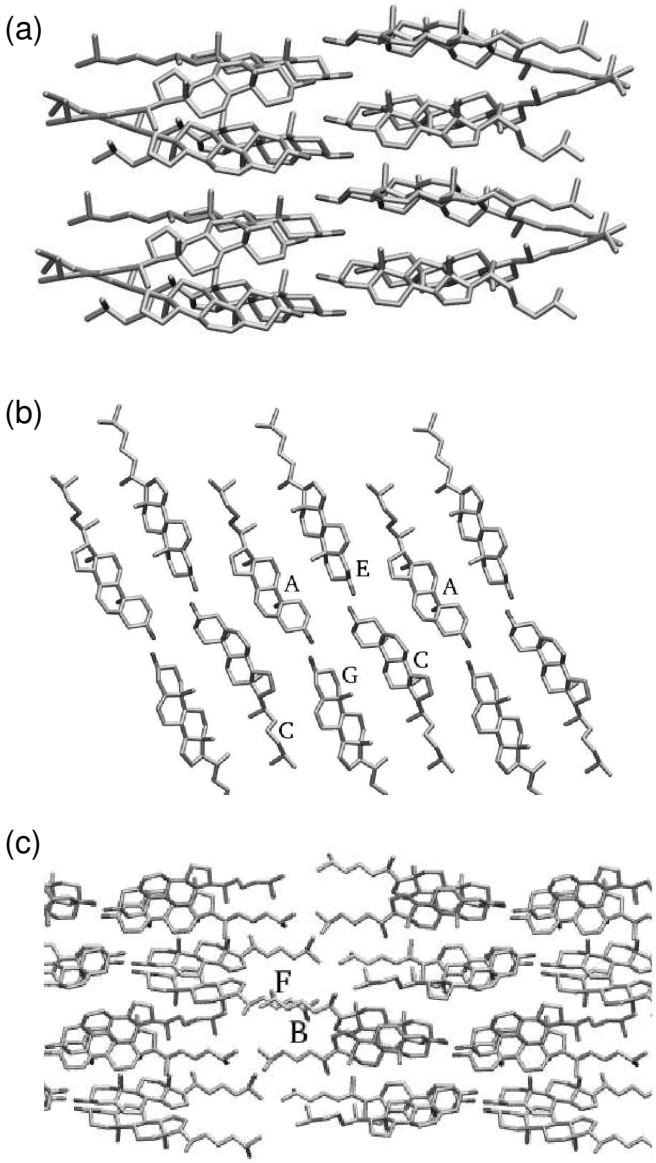

Figure 3.12: (a) Two unit cells, projected on the (c, b) plane. The interactions that dominate in this direction is the hydrogen-bonded network and the van der Waals interactions between molecules on top of each other. (b) Three unit cells, projected on the (b, a) plane. For clarity only one of the layers of the crystal is presented. When constructing the crystal lattice, the corresponding transformations place the ring of molecule C next to the hydrogen-bonded molecules A and G of the next unit cell. The ring of molecule A is then placed next to the hydrogen-bonded molecules C and E of the neighboring unit cell. The van der Waals interactions between these molecules are favorable. (c) Part of the cholesterol crystal,projected on the (a, b) plane. The hydrocarbon chains of molecules B and F from neighboring unit cells come into close contact.

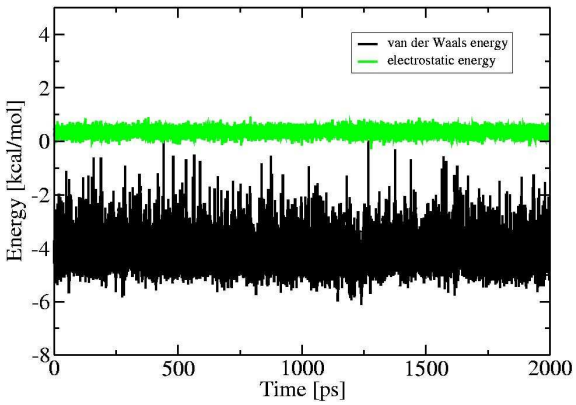

Figure 3.13: Time series of the van der Waals and electrostatic contributions to the total interaction energy between adjacent, along the a-axis, molecules B and D in the primary unit cell.

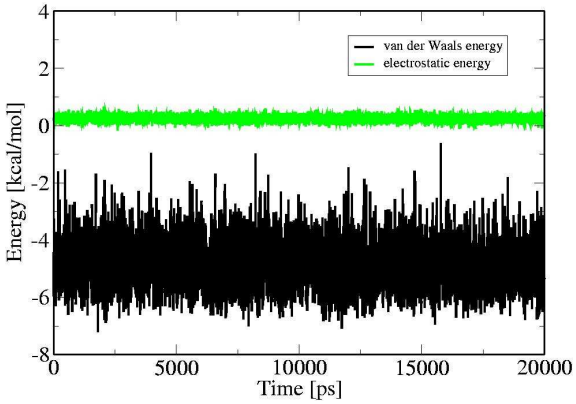

Figure 3.14: Time series of the van der Waals and electrostatic contributions to the total interaction energy between adjacent, along the a-axis, molecules C of the primary unit cell and molecule G of the neighboring cell.

and to test the new parameter set, we performed 2 ns MD simulations of the isolated cholesterol, ergosterol and lanosterol molecules at 800 K, following the same protocol as in the crystal MD simulation. Although the temperature was elevated during the simulation, the stereochemistry of all the seven asymmetrical centers was preserved in all three sterols. To assess the stability of the steroid ring *in vacuo* and to estimate the role of the crystal environment in confering rigidity to the steroid nucleus, the torsional angles of the steroid ring from this simulation were monitored. The values and the standard deviations of these torsional angles (summarized in Table 3.6) are slightly larger than the ones obtained from the crystal simulation. However they remain small, indicating that the rigidity is indeed inherent to the steroid ring and is not conferred by

the crystal environment. In contrast to the steroid ring, and as expected, the flexible hydrocarbon tails underwent numerous *trans-gauche* transitions.

3.4 CONCLUSION

In this chapter, a parameter set for cholesterol, ergosterol and lanosterol for the all-atom CHARMM27 molecular mechanics force field is presented. The method used here for force-field determination is particularly useful for deriving parameters for rigid molecules, for which the flexibility is determined principally by vibrations, as is the case for these sterols. Furthermore, special care was taken to reproduce the rotational barrier of the hydroxyl around the O-C_3 bond. Fitting of the molecular mechanics potential onto that derived by quantum chemistry produced a good match both for cholesterol/ergosterol and lanosterol. Energy minimization and molecular dynamics of the X-ray structure of cholesterol lead to cell dimensions being reproduced within 2.4 % of experimental values. The characteristic structural features of the crystal, such as the rigidity of the sterol ring and the hydrogen-bonded network of the crystal, were also reproduced. The nature of the non-bonded interactions in the cholesterol crystal were investigated by calculating the interaction energies between cholesterol molecules in the crystal. The favourable energy contributions arise mainly from van der Waals interactions between neighboring molecules, with a smaller contribution from the dynamically stable hydrogen-bonded network. A simulation of the three sterols at 800K in vacuo, showed that the stereochemistry of all asymmetrical centers was preserved.

Sterols represent essential constituents of the lipid systems of all organisms. These 3β-hydroxy steroids, with different types of side chains, different numbers and positions of C=C-double bonds, and varying stereochemical characteristics, are crystalline, neutral, unsaponifiable alcohols with high melting points, and exhibit very similar physical and chemical properties. The force field presented herein may also be useful for the simulation of other sterols or steroids, such as the phytosterols sigmasterol and sitosterol and many classes of steroids.

Deriving force field parameters for cholesterol is an essential step towards reliable and realistic simulations of sterol-containing membranes. Subsequent use of MD simulation will provide insights into the dynamical effects of sterols in membranes and help to derive biologically-relevant structure-function relationships from a dynamical standpoint.

BIBLIOGRAPHY

[1] BROOKS, B. R., BRUCCOLERI, R., OLAFSON, B. D., STATES, D. J., SWAMINATHAN, S., AND KARPLUS, M. CHARMM: A Program for Macromolecular Energy, Minimization and Dynamics Calculations. *J. Comp. Chem.*, 1983, **4**, 187–217.

[2] MAPLE, J. R., HWANG, M. J., STOCKFISCH, T. P., DINUR, U., WALDMAN, M., EWIG, C. S., AND HAGLER, A. T. Derivation of Class II Force Fields. I. Methodology and Quantum Force Field for the Alkyl Functional Group and Alkane Molecules. *J. Comp. Chem.*, 1994, **15**, 162–182.

[3] HAGLER, A. T., E.HULER, AND LIFSON, S. Energy functions for peptides and proteins. I. Derivation of a consistent force field including the hydrogen bond from amide cystals. *J. Am. Chem. Soc.*, 1974, **96**, 5319–5327.

[4] LIANG, C., YAN, L., HILL, J. R., EWIG, C. S., STOUCH, T. R., AND HAGLER, A. T. Force Field studies of cholesterol and cholesteryl acetate crystals and cholesterol-cholesterol intermolecular interactions. *J. Comp. Chem.*, 1995, **16**, 883–897.

[5] VAN GUNSTEREN, W. F., BILLETER, S. R., EISING, A. A., HÜNENBERGER, P. H., KRÜGER, P., MARK, A. E., SCOTT, W. R. P., AND TIRONI, I. G. *Biomolecular Simulation: The GROMOS96 manual and user guide*. Hochschuleverlag AG an der ETH Zürich, Zürich, Switzerland, 1996.

[6] BARAN, M., AND MAZERSKI, J. Molecular modelling of membrane sterols with the use of the GROMOS 96 force field. *J. Comp. Chem.*, 2002, **16**, 883–897.

[7] SHIEH, H. S., HOARD, L. G., AND NORDMAN, C. E. The structure of cholesterol. *Acta Cryst.*, 1981, **B37**, 1538–1543.

[8] WEBER, H. P., CRAVEN, B. M., AND SAWZIK, P. Crystal structure and thermal vibrations of cholesteryl acetate from neutron diffraction at 123K and 20K. *Acta Cryst.*, 1991, **B47**, 116–127.

[9] SHIEH, H. S., HOARD, L. G., AND NORDMAN, C. E. Structures of triclinic and monoclinic cholesterol hemiethanolate. *Acta Cryst.*, 1982, **B38**, 2411–2419.

[10] SMONDYREV, A., AND BERKOWITZ, M. L. MD Simulation of the structure of DMPC bilayers with Cholesterol, Ergosterol, and Lanosterol. *Biophys. J.*, 2001, **80**, 1649–1658.

[11] SMONDYREV, A. M., AND BERKOWITZ, M. L. Structure of DPPC/Cholesterol bilayer at low and high cholesterol concentrations: molecular dynamics simulation. *Biophys. J.*, 1999, **77**, 2075–2089.

[12] PASENKIEWICZ-GIERULA, M., ROG, T., KITAMURA, K., AND KUSUMI, A. Cholesterol Effects on the PC Bilayer polar region: A MD study. *Biophys. J.*, 2000, **78**, 1376–1389.

[13] COURNIA, Z., VAIANA, A. C., SMITH, J. C., AND ULLMANN, G. M. Derivation of a molecular mechanics force field for cholesterol. *Pure Appl. Chem.*, 2004, **76**, 189–196.

[14] VAIANA, A. C., SCHULZ, A., WORFRUM, J., M.SAUER, AND SMITH, J. C. Molecular mechanics force field parametrization of the fluorescent probe rhodamine 6G using automated frequency matching. *J. Comp. Chem.*, 2003, **24**, 632–639.

[15] VAIANA, A. C., COURNIA, Z., COSTESCU, I. B., AND SMITH, J. C. AFMM: A Molecular Mechanics Force-Field Vibrational Parametrization Program. *Computer Physics Communications*, 2005, **167**, 34–42.

[16] HARRISON, R. J., NICHOLS, J. A., STRAATSMA, T. P., DUPUIS, M., BYLASKA, E. J., FANN, G. I., WINDUS, T. L., APRA, E., ANCHELL, J., BERNHOLDT, D., BOROWSKI, P., CLARK, T., CLERC, D., DACHSEL, H., DE JONG, B., DEEGAN, M., DYALL, K., ELWOOD, D., FRUCHTL, H., GLENDENNING, E., GUTOWSKI, M., HESS, A., JAFFE, J., JOHNSON, B., JU, J., KENDALL, R., KOBAYASHI, R., KUTTEH, R., Z.LIN, LITTLEFIELD, R., LONG, X., MENG, B., NIEPLOCHA, J., NIU, S., ROSING, M., SANDRONE, G., STAVE, M., TAYLOR, H., THOMAS, G., VAN LENTHE, J., WOLINSKI, K., WONG, A., AND ZHANG, Z. NWChem, A Computational Chemistry Package for Parallel Computers, Version 4.0.1. *Pacific Northwest National Laboratory, Richland, Washington, USA*, 2001.

[17] STEVENS, W. J., BASCH, H., AND KRAUSS, M. Compact effective potentials and efficient shared-exponent basis sets for the first- and second-row atoms. *J. Chem. Phys.*, 1984, **81**, 6026–6033.

[18] SCOTT, A. P., AND RADOM, L. Harmonic Vibrational Frequencies: An evaluation of Hartree-Fock, Moeller-Plesset, Quadratic Configuration Interaction, Density Functional Theory, and Semiempirical Scale Factors. *J. Phys. Chem.*, 1996, **100**, 16502–16513.

[19] http://srdata.nist.gov/cccbdb. *National Institute of Strandards and Technology, USA*, 2004.

[20] BRENEMAN, C. N., AND WIBERG, K. B. Determining atom-centered monopoles from molecular electrostatic potentials. The need for high sampling density in formamide conformational analysis. *J. Comp. Chem.*, 1990, **11**, 361–373.

[21] CIEPLAK, P., CALDWELL, J., AND KOLLMAN, P. Molecular Mechanics Models for organic and biological systems going beyond the atom centerd two body

additive approximation: Aqueous solution free energies of methanol and N-methyl acetamide, nucleic acid base and amide hydrogen bonding and chloroform/water partition coefficients of the nucleic acid bases. *J. Comp. Chem.*, 2001, **22**, 1048–1057.

[22] FELLER, S. E., GAWRISCH, G., AND A. D. MACKERELL, J. Polyunsaturated Fatty Acids in Lipid Bilayers: Intrinsic and Environmental Constributions to their Unique Physical Properties. *J. Am. Chem. Soc.*, 2002, **124(2)**, 318–326.

[23] FELLER, S. E., AND A. D. MACKERELL, J. An Improved Empirical Potential Energy Function for Molecular Simulations of Phospholipids. *J. Phys. Chem. B*, 2000, **104**, 7510–7515.

[24] YIN, D., AND A. D. MACKERELL, J. Combined Ab Initio/Empirical Approach for Optimization of Lennard-Jones Parameters. *J. Comp. Chem.*, 1998, **19**, 334–348.

[25] FELLER, S. E., YIN, D., PASTOR, R. W., AND A. D. MACKERELL, J. Molecular Dynamics Simulation of Unsaturated Lipid Bilayers at Low Hydration: Parametrization and Comparison with Diffraction Studies. *Biophys. J.*, 1997, **73**, 2269–2279.

[26] SCHAFTENAAR, G., AND NOORDIK, J. H. Molden: a pre- and post-processing program for molecular and electronic structures. *J. Comput.-Aided Mol. Design*, 2000, **14**, 123–134.

[27] SHIEH, H. S., HOARD, L. G., AND NORDMAN, C. E. Crystal structure of anhydrous cholesterol. *Nature*, 1977, **267**, 287–289.

[28] CRAVEN, B. M. Pseudosymmetry in Cholesterol Monohydrate. *Acta Cryst.*, 1979, **B35**, 1123–1128.

[29] CROWDER, C. M., WESTOVER, E. J., KUMAR, A. S., R. E OSTLUND, J., AND COVEY, D. F. Enantiospecificity of cholesterol function in vivo. *J. Biol. Chem.*, 2001, **276**, 44369–44372.

[30] ROG, T., AND PASENKIEWICZ-GIERULA, M. Cholesterol effects on the phospatidylcholine bilayer nonpolar region: a molecular simulation study. *Biophys. J.*, 2001, **81**, 2190–2202.

CHAPTER 4

MOLECULAR DYNAMICS SIMULATIONS OF PURE PHOSPHOLIPID BILAYERS: THE EFFECT OF SURFACE TENSION

In this chapter a single-component pure-phospholipidic bilayer, namely a DPPC bilayer, is studied in two phases: the gel and the liquid phase.

Physical properties of the plasma membrane can be reproduced and studied with model biological membranes.[1] Both experimental and computational studies of model membrane systems have shed light on the nature of interactions that occur in real membranes. The study of the liquid phase of the DPPC bilayer with Molecular Dynamics simulations has been the subject of much discussion in the literature. A large part of the argumentation for this system concerns the need for the application of external surface tension on the bilayer normal in order to reproduce most of the experimental bilayer properties in the simulation. The effect of the applied surface tension on the pure liquid bilayer with MD simulations is discussed in this chapter.

The simulations of the pure DPPC bilayer were performed as controls in order to compare the simulation results with different experimental results and also to study the effect of each sterol on the pure membrane.

4.1 COMPUTATIONAL DETAILS

The 'control' simulations of pure DPPC bilayers were performed at T=309K and T=323K. For all simulations the CHARMM package version 28b1[2] was used with the all-atom CHARMM 27 force field[2] for DPPC.

The Particle Mesh Ewald summation technique[3] was employed to calculate elec-

trostatic contributions. The van der Waals and electrostatic interactions were cut off at 14 Å using the CHARMM shifted potential. It has been shown that 'shift' (see Section 2.2.4) is an appropriate method of electrostatic truncation in lipid bilayer simulations.[4] Periodic boundary conditions of the orthorhombic cells were applied in all directions. The equation of motion was integrated using the Verlet algorithm with a time step of 1 fs. The simulations were carried out in the NPγT ensemble (constant number of molecules, pressure, surface tension and temperature), in which the surface tension and the normal pressure are specified. The surface tension, γ, is defined as:[5]

$$\gamma = \int_{-\infty}^{\infty} dz[P_n - P_l(z)] \tag{4.1}$$

where P_n is the normal component and P_l the lateral pressure of the pressure tensor. The box length in the z direction was allowed to vary independently of x and y and was coupled to the z component of the pressure tensor. The x and y dimensions of the unit cell vary while maintaining constant surface tension.[6] In the case that the lateral pressure and the normal pressure are equal, the average surface tension is zero. The values of the surface tension chosen for this study depend on the system being simulated: the test calculations for this are described in the Appendix.

A constant pressure of P=1atm was imposed using the Langevin piston method.[7] The collision frequency was set to 30 ps^{-1} for the heating and equilibration and to 10 ps^{-1} for production dynamics. Constant temperature conditions were maintained by a Hoover thermostat[8] using the extended system constant pressure and temperature algorithms implemented in CHARMM with a mass of 2000 kcal/ps.

Before analysis, all coordinate sets were superposed on a primary-box reference structure so as to remove global unit-cell rotation and translation. Analysis of the system properties was performed using a combination of CHARMM utilities and our own analysis code. The CPU time needed for the production runs of all systems was 11,360 hours on 16 Dual AMD Athlon 1.4 Ghz processors with Myrinet 2 Gbit network. The total time of the simulations presented in this and in the next chapter is over 150 ns.

4.1.1 GEL DPPC MEMBRANE

For the gel DPPC system, two simulations, one with 64 lipids and 762 water molecules and one with 256 lipids and 3048 water molecules (11.9 waters/lipid), were performed. The initial configuration of the 64-lipid system was taken from the final frame of the NPT simulation in Ref. 9. The initial dimensions of the box were x=42.79, y=33.73 and z=64.90 Å. The 256-lipid unit cell was constructed by replicating the initial 64-

lipid unit cell in the $x-$ and $y-$axis, resulting in initial dimensions for this system of x=85.58, y=67.46 and z=64.90 Å. These two sizes were chosen to check for system size effects.

For the simulation of DPPC in the gel phase, the protocol proposed in Ref. 9 was used. Given that simulation at constant area leads to a pleated structure,[9] which, according to experimental evidence[10] is an artefact, the NPγT ensemble with γ=0 was chosen. The two membranes were minimized first for 100 steps with the Steepest Descent (SD) algorithm. Next, another 100 steps of Conjugated Gradient (CG) minimization was applied, followed by 9400 steps of the Adopted Basis Newton Raphson (ABNR) minimization with an exit criterion of an energy change less than 10^{-4} kcal/mol. The systems were then heated up to 309K over 160ps in 2K increments. Equilibration followed for 50ps with a 10K window for rescaling the velocities. Further equilibration without velocity rescaling was required for 1ns. The production run was then carried out for 4ns for the 256-system and for 8ns for the 64-lipid system.

4.1.2 LIQUID DPPC MEMBRANE

For the liquid DPPC system, again two simulations, one with 72 lipids and 2094 water molecules and one with 200 lipids and 5814 water molecules (29 waters/lipid) were performed at T=323K. The initial configuration for the 72-lipid system was taken from the last frame of the 20ns DPPC simulation performed in Ref. 11. The initial dimensions of this system were x=47.58, y=47.58 and z=66.52 Å. The 200-lipid system was constructed by duplicating selected lipids in the $x-$ and $y-$axis so as to yield the same system size as used in the sterol-DPPC simulations. The initial dimensions for this system were x=67.50, y=93.20 and z=66.52 Å.

The two liquid DPPC systems were energy minimized with 10000 steps of the SD algorithm. Next, another 20000 steps of CG minimization were performed, followed by 10000 steps of ABNR minimization with an exit criteria of an energy change less than 10^{-6}kcal/mol. This energy tolerance was satisfied after 5000 steps. Subsequently, the systems were heated to 323K over 65ps in 5K increments. Equilibration followed for 50ps with a 10K window for rescaling the velocities. Additional equilibration for 1ns followed without rescaling the velocities. For the 72-DPPC system, the production runs were carried out for 2ns for each of the surface tension values chosen (*i.e.* 0, 10, 24.5, 25, 30 and 61 dyn/cm). For the optimal value found, γ=24.5 dyn/cm, the production run was continued up to 8 ns. The choice of this value is described in the Appendix. The production run for the 200-DPPC system was carried out for 4 ns also at γ=24.5 dyn/cm.

A separate simulation of a pure water box at T=309K and T=323K with the electrostatic treatment and simulation conditions as the lipid simulation with γ=0 dyn/cm was also performed so as to obtain an estimate of a water-molecule volume, V_W.

4.2 RESULTS AND DISCUSSION

4.2.1 CHOICE OF THE OPTIMAL SURFACE TENSION VALUE

The value of the surface tension, γ, that should be applied on a lipid bilayer so as to properly reproduce important bilayer properties, such as the area per lipid or the deuterium order parameters, is the subject of debate.[12–19] It has been suggested that the surface tension must be zero for an unstressed bilayer at its free energy minimum (*i.e.*, for a bilayer that is not subjected to osmotic stress).[18] On the other hand, it has been pointed out that the microscopic and macroscopic implications of the change in the free energy of a bilayer with surface area are not the same.[13] In Refs. 20 and 17 the CHARMM package was used with zero surface tension for simulating amphotericin B and cholesterol/ergosterol and gramicidin S, respectively, in a membrane environment using the CHARMM force field. Therefore, the question remains of what should be the correct value of the applied surface tension in lipid bilayer simulations.

The area per lipid is generally considered to be a reliable criterion for validating and comparing calculations. Once the area per lipid is correct, most of the other properties of the bilayer appear to be reasonable, consistent with the observation that the large number of DPPC simulations available in the literature using different force fields and simulation methods result in bilayers with similar properties.[4] It has been shown in previous simulations that the calculated surface area per lipid and the deuterium order parameters depend strongly on γ.[21]

Recently, a number of attempts have been made to simulate the liquid-crystalline state of a DPPC bilayer in CHARMM.[15, 16, 21, 22] In all of these studies, it is evident that the calculated area per lipid is sensitive to the used protocol and especially to the applied surface tension and the treatment of the electrostatics.[23] It has also been argued that the required applied surface tension is dependent on the system size.[24]

In Refs. 15 and 21 exactly the same system of 72 DPPC molecules at 323K was simulated with CHARMM. To achieve the observed experimental area per lipid of 62.9 Å^2, in Ref. 21 it was estimated that the surface tension applied on a bilayer should be in the range 35-45 dyn/cm, whereas a very different value of γ=61 dyn/cm was required to produce an area per lipid of 62.2 Å^2 in Ref. 15. One possible reason for this difference might be the fact that Ref. 21 used the PARM22b4b molecular

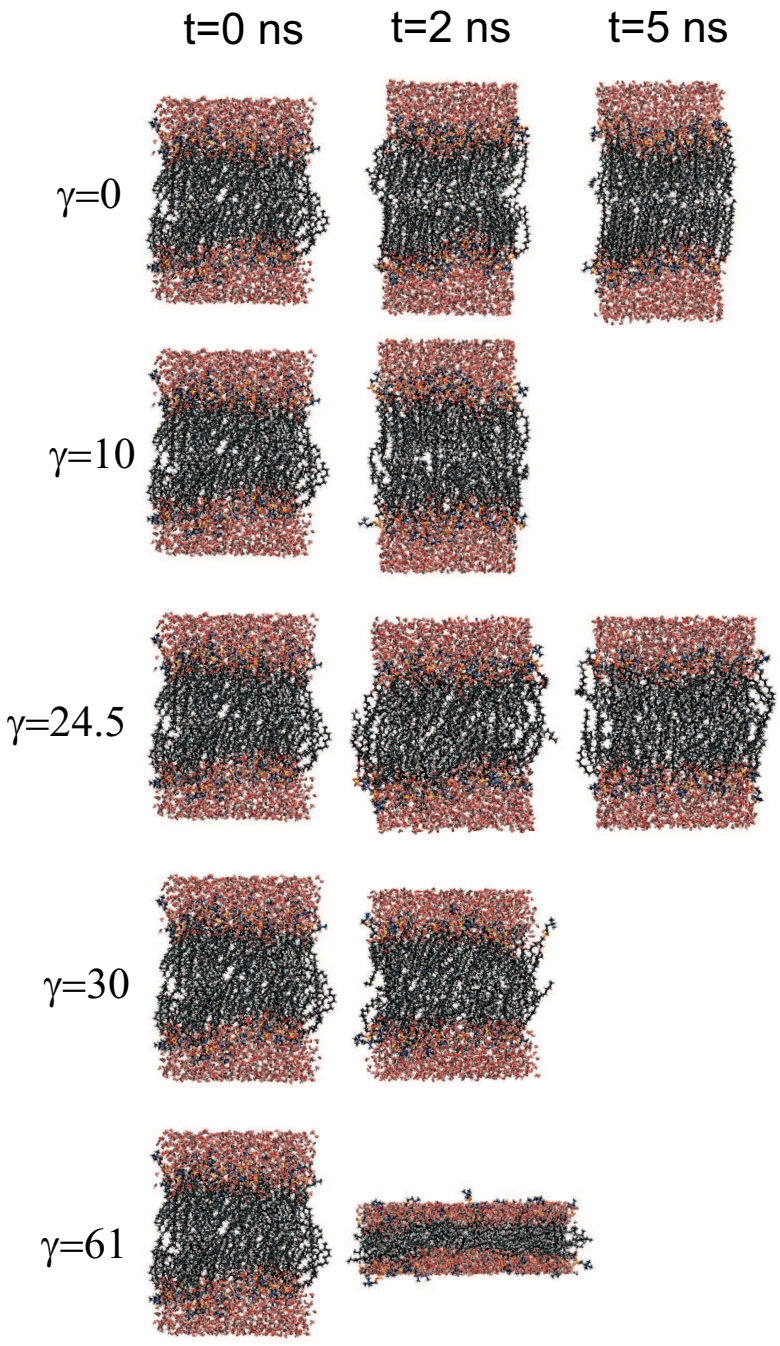

Figure 4.1: Snapshots of the liquid DPPC membrane (323K) taken at t=0ns, 2ns and 5ns (where available) simulated in the NPγT ensemble with γ=0, 10, 24.5, 30 and 61 dyn/cm. Oxygen atoms are shown in red, carbon atoms in black, nitrogen atoms in blue, phosphorus atoms in yellow and hydrogen atoms in grey. Pictures are in the (z, x) plane.

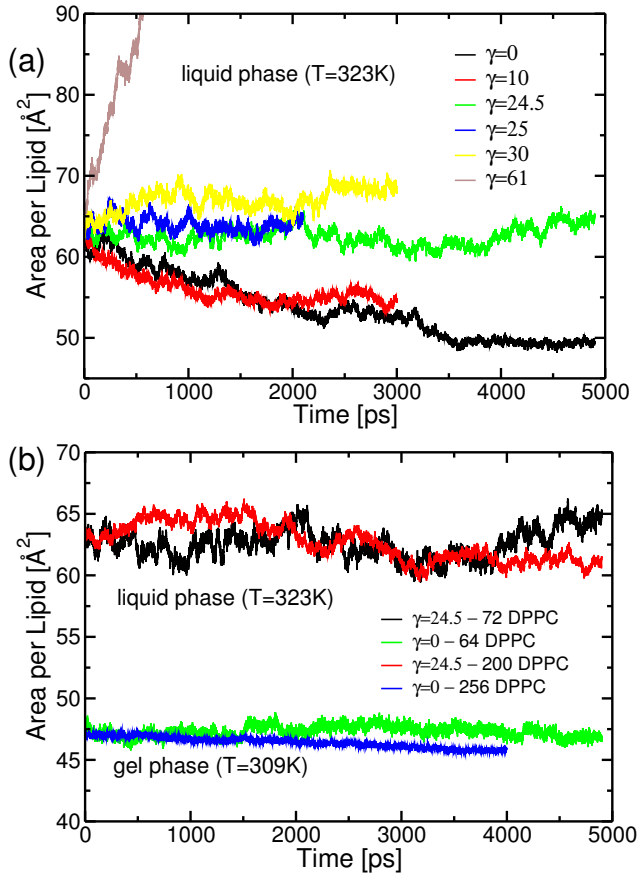

Figure 4.2: Areas per DPPC (a) for T=323K and for the 72-DPPC system, simulated with different values of γ. With γ=0 or γ=10 dyn/cm, the area per lipid did not converge after 5ns and is severely underestimated. γ=61 results in an over-stretching of the membrane (see also Figure 2 of the main text) and an extreme overestimation of the area per lipid. The surface tension values γ=24.5 and γ=25 seem to reasonably reproduce the experimental area per lipid. The mean values observed in these simulations are 62.6$\pm$1.2 and 63.7$\pm$0.8. (b) Time series of the area per lipid for T=323K and γ=24.5 for the 72- and 200-DPPC system and for T=309K for the 64- and 256-DPPC system. A system size dependence is found for the area per lipid of the liquid DPPC (T=323K, upper curves), while no system size dependence is observed for the gel phase (T=309K). The area per DPPC molecule was calculated from the NPγT trajectories of DPPC by diving the surface area of the bilayer ($x \times y$) by the number of lipids in one leaflet. All values of γ are in dyn/cm.

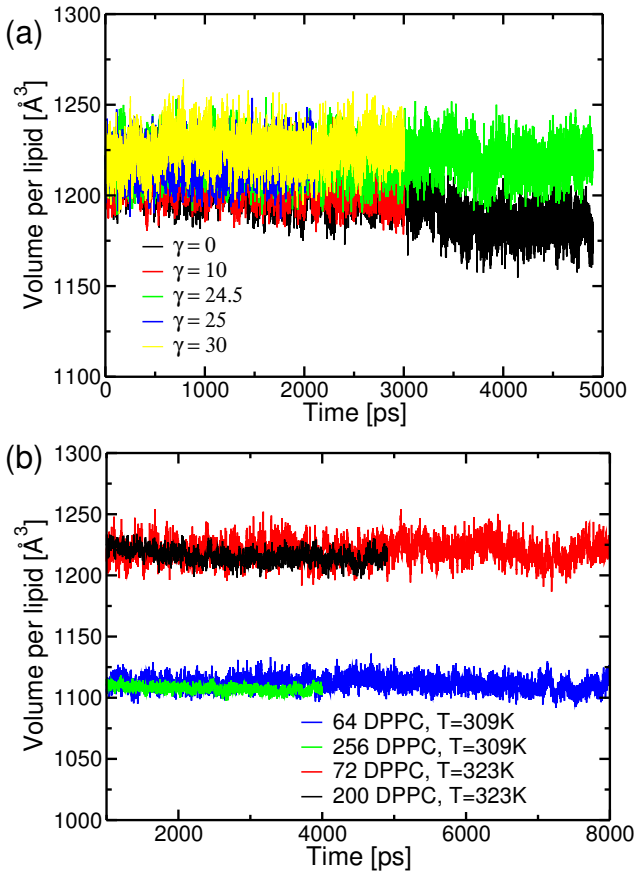

Figure 4.3: Volumes per DPPC (a) for T=323K and for the 72-DPPC system at different surface tensions and (b) for T=323K and γ=24.5 dyn/cm for the 72-DPPC (red) and 200-DPPC (black) systems and for T=309K for the 64-DPPC (blue) and 256-DPPC (green) systems (γ=0 dyn/cm). The volume per lipid does not exhibit any system size dependence and has considerably smaller fluctuation than the area per lipid.

mechanics force field parameter set, whereas Ref. 15 used CHARMM27. Different force fields might affect the surface tension required for a lipid bilayer.[14]

Recently, two further CHARMM simulations on lipid bilayers using the NPγT ensemble have been performed recently. In one simulation, a 80-DPPC bilayer patch was simulated,[16] requiring 17 dyn/cm to achieve an area per lipid of 67.0 Å^2. In the second simulation, a surface tension in the range of 25-30dyn/cm was required, for a 90-DMPC bilayer patch.[22]

The effect of surface tension in lipid bilayers was also recently studied with the GROMACS[25] force field. Refs. 4, 23, 24 used zero surface tension to simulate 128-DPPC bilayers. Ref. 26 studied the effect of surface tension on the 128-DPPC bilayer, and showed that to reproduce a surface area per lipid of 64Å^2, a surface tension between 20 and 30 dyn/cm was needed (depending on the system size).

To find the optimal value of γ that reproduces the correct area per lipid for the fluid

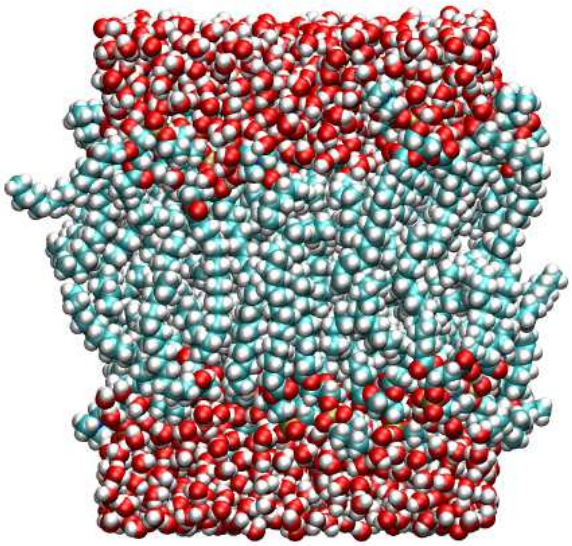

Figure 4.4: The final frame of the liquid DPPC membrane (323K) simulated at a constant surface tension of 24.5 dyn/cm.

phase, a number of simulations were performed on the liquid (*i.e.* T=323K) 72-DPPC bilayer with γ = 0, 10, 24.5, 25, 30 and 61 dyn/cm. In Figure 4.1 snapshots are shown, taken at t=0ns, t=2ns and t=5ns (where available) of the liquid membrane with the different applied surface tensions.

Figures 4.2 and 4.3 show the variation of the area and volume per DPPC molecule obtained for different surface tensions as a function of time. It is evident from Figures 4.1 and 4.2a that the value of γ=61dyn/cm proposed by Ref. 15 for a 72-DPPC bilayer over-suppresses the bilayer in the z-axis. Therefore, this simulation is not further analyzed.

At γ=0 dyn/cm the area per lipid in the liquid phase is severely underestimated and even at t=5ns is clearly not converged (Fig. 4.2a). Surface tension values of γ=24.5 and γ=25 dyn/cm reasonably reproduce the experimental area per lipid. The mean values for the area per lipid observed in these simulations are 62.6$\pm$1.2 and 63.7$\pm$0.8Å^2. Here, we find that, using the CHARMM27 parameter set for the same 72-lipid system used in both simulations of Refs. 21 and 15, a γ value of 24.5dyn/cm is required to reproduce an area per lipid of 62Å^2 and γ=25dyn/cm is required for an area per lipid of 64Å^2. Therefore, for the simulation of the neat bilayer at T=323K, an applied surface tension of 24.5 dyn/cm was chosen, which best reproduces the experimental area per lipid[27] (62.9$\pm$0.013Å^2). The final frame of the simulation of the DPPC liquid phase can be seen in Fig. 4.4.

Estimating the surface area per lipid in complex heterogeneous systems is difficult, and in these cases the choice of γ can be complicated.[22] The addition of compounds

to a pure phospholipid membrane is expected to influence the surface tension of the bilayer. From various simulation results, it has been suggested that the area per lipid in a cholesterol-DPPC bilayer is close to 50 Å^2.[28, 29] This area per lipid is closer to that of a gel state (47.9Å^2)[10] than to that of a liquid state (62.9Å^2).[10] Since the gel phase of a DPPC bilayer has been successfully simulated with γ=0dyn/cm, we have chosen to also perform the sterol-DPPC simulations at γ=0dyn/cm in order to reduce equilibration times.

4.2.2 AREA AND VOLUME PER LIPID VS. SURFACE TENSION IN THE LIQUID DPPC BILAYER

The volume of a lipid molecule, V_{DPPC}, was calculated as:

$$V_{DPPC} = \frac{V - N_W V_W}{N_{DPPC}} \tag{4.2}$$

where V_W is the volume of one water molecule, determined by a separate NPT simulation as described in the 'Methods' section. The volume of a water molecule was found to be V_W=29.6$\pm$0.2Å^3 for 323K and 29.2$\pm$0.2Å^3 for 309K.

The average DPPC volume is 1219.6$\pm$8.9Å^3, within two percent of the experimental values reported by Refs. 30 and 10. This value is remarkably stable, with a standard deviation of less than one percent. The volume per lipid does not exhibit any system-size dependence, being 1221.0$\pm$5.2Å^3 for the 200-lipid system and 1219.6$\pm$8.9Å^3 for the 64-lipid system.

The fluctuations in the area per lipid are considerably larger than the volume, and the equilibrium value exhibits a clear size dependence for the liquid DPPC membrane (see Figure 4.2b). The mean area per lipid for the 72-lipid system is 62.6Å^2 and for the 200-lipid system is 64.6Å^2 at γ=24.5 dyn/cm. These values are in good agreement with another MD study,[24] in which a similar dependence of the area per lipid on system size was also found (61.1Å^2 for a 64-lipid system and 63.0Å^2 for a 256-lipid system at T=323K).

4.2.3 AREA AND VOLUME PER LIPID IN THE GEL DPPC BILAYER

For the gel DPPC simulation, studied at γ=0 dyn/cm, no major fluctuations in the area or the volume per lipid were observed, contrary to the case of the liquid DPPC bilayer area fluctuations. System size effects are also much smaller in this system than in the liquid DPPC simulation (see Figure 4.2b). The area per lipid is 47.3$\pm$0.5Å^2 for the 64-lipid system and 46.8$\pm$0.2Å^2 for the 256-lipid system, both very close to the

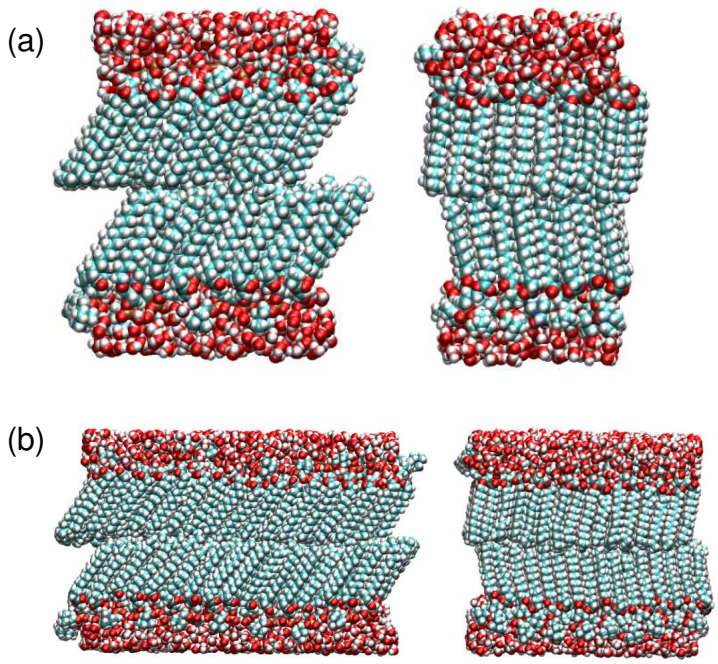

Figure 4.5: The final frames of the gel DPPC membrane (309K) (a) of 64 lipids taken at t=8ns and (b) of 256lipids at t=4ns. Oxygens are shown in red, hydrogens in white, carbons in turquoise, nitrogens in blue and phosphorus in yellow. The views are shown in the (x, z) plane (left) and in the (y, z) plane (right).

experimentally-reported value of 47.2$\pm$0.5Å^2.[31] The simulation study of a gel phase lipid bilayer carried out in Ref. 9, the simulation protocol of which was followed here, gave a somewhat smaller surface area per lipid of 45.4$\pm$0.5Å^2.

The volume per lipid in the gel phase, calculated from the present simulation, is 1110.4 $\pm$3.0Å^3 for the 256-lipid system and 1113.8$\pm$6.1Å^3 for the smaller 64-lipid system. These two values are the same within the statistical error and therefore there is no system size effect for the gel phase DPPC bilayer. The time evolution of the volume per DPPC can be seen in Figure 4.3b. This figure shows that there is no drift in the time evolution of the volume per lipid and also that different system sizes produce the same volume per lipid. A depiction of the final frame of the gel systems is shown in Figure 4.5. The characteristic tilt of the gel phase is seen in the (x, z) plane for both the 64- and the 256-lipid simulation.

4.2.4 STABILITY OF THE SIMULATIONS

The systems were allowed to adjust not only their volumes (density) but also their area-to-thickness ratios.

In Figure 4.6 the time evolution of the x, y, and z dimensions for the different

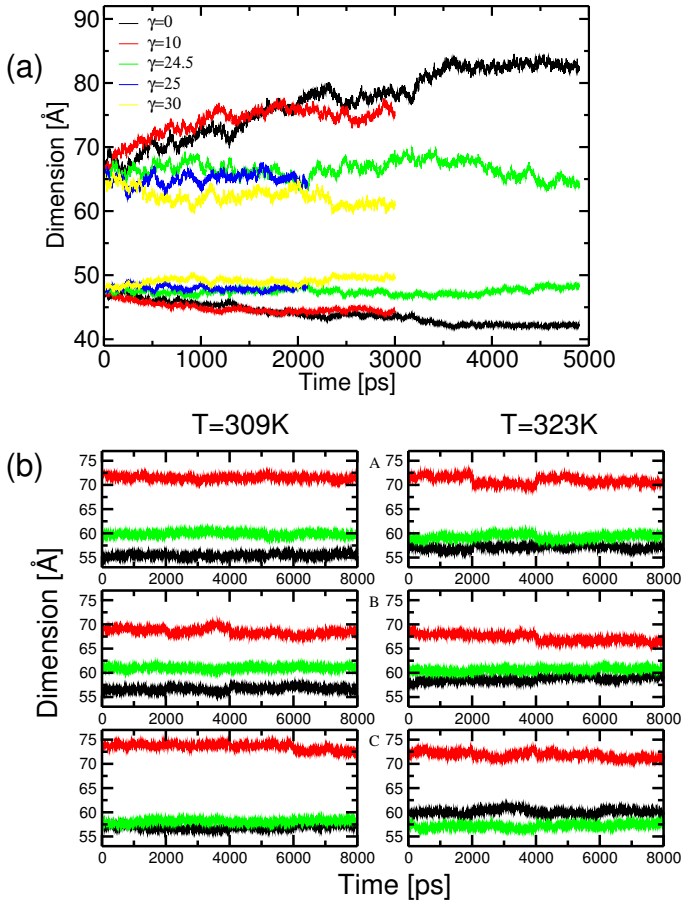

Figure 4.6: Time evolution of the unit cell dimensions for (a) the liquid 72-DPPC system (T=323K), simulated with different values of γ. The upper curves correspond to the z-coordinate and the lower curves to the x-coordinate (b) (A) cholesterol-DPPC, (B) ergosterol-DPPC, (C) lanosterol-DPPC at T=309K and at T=323K. The black line represents the x coordinate, the red line the y coordinate and the green line represents the z coordinate.

systems is plotted. For the neat liquid DPPC systems simulated with γ=0,10,30 or 61 dyn/cm (see Figure 4.6), the x and z dimensions drift in time, as does the area per lipid. Therefore, if the area per lipid drifts in time, other properties of the system may also not be converged.[4] The observed drift in the area per lipid indicates that the simulated systems with the above-mentioned surface tensions are not yet equilibrated. However, for γ=24.5 and γ=25 dyn/cm, the x and z dimensions and the area per lipid are stable, indicating that these systems are indeed equilibrated.

4.2.5 ELECTRON DENSITY PROFILES

Information on the average structure of the lipid bilayer:water interface can be obtained from the electron density distributions of different types of atoms along the

bilayer normal (z-axis). These profiles also provide information on the thickness and organisation of the molecules across the bilayer. Electron density profiles have been derived previously from X-ray diffraction of neat DPPC systems[10] and from simulation studies for the cholesterol and ergosterol systems.[32]

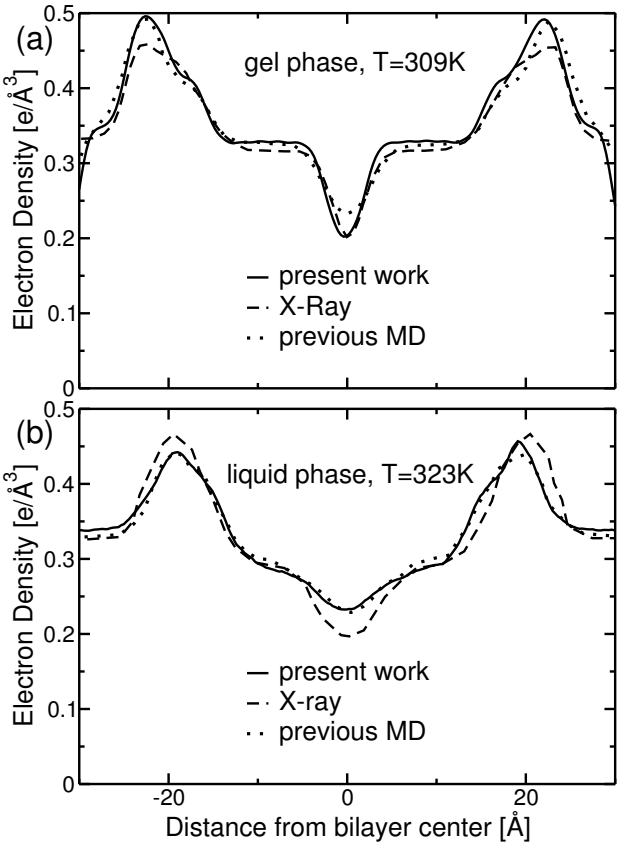

Figure 4.7: (a) Electron density profiles for the gel DPPC system at T=309K. The present simulation profile is the solid line and the experimental profile is taken from Ref. 33 and the profile from a previous simulation from Ref. 9. (b) Electron density profiles for the liquid DPPC system at T=323K. The present simulation profile is again the solid line. The experimental profile is taken from Ref. 27 and the profile from a previous simulation from Ref. 34. The electron density profiles were calculated from the trajectories by dividing the simulation cells into 0.3 Å slabs and determining the time-averaged number of electrons per slab, using the coordinates of the atoms from the trajectories and assigning the corresponding number of electrons to the atomic centers.

In Figure 4.7a electron density profiles for the neat gel DPPC system from low-angle X-ray diffraction[33] and a previous MD simulation[9] (which used the CHARMM22 parameter set) are compared to the present simulation results. The distance between the maxima (in the present simulation, 44.7$\pm$0.03 Å) agrees very well with the experimental value of 45.0$\pm$1 Å.[33] The flat methylene region and the terminal methyl trough are also well reproduced. However, the shoulder appearing

at the headgroup/glycerol region is less pronounced than in the X-ray data. In both the present simulation and the simulation of Ref. 9, the two high electron-density peaks also show higher electron density in the headgroup region than that derived experimentally. One possible explanation might be that the head group motion is more restricted in the simulation than in the experiment.[9] The electron density in the terminal methyl trough is improved with respect to the X-ray data in the present simulation relative to the previous simulation of Ref. 9.

The electron density profile for the liquid DPPC system is given in Fig. 4.7b together with those derived from an X-ray diffraction experiment[27] and a previous MD simulation with the CHARMM27 force field.[34] The electron density profile calculated from the present trajectory is in excellent agreement with the simulation profile calculated in Ref. 34. Both profiles are also in very good agreement with the X-ray results. The distance between the two peaks is 38.1 ± 0.2 Å, slightly smaller than the experimental distance of 39.8 Å.

4.2.6 FURTHER BILAYER PROPERTIES

In the next chapter, the properties of the pure bilayer in the gel and in the liquid phase are compared with the properties of the sterol-containing membranes.

BIBLIOGRAPHY

[1] FINEGOLD, L. *Cholesterol in Membrane Models*. CRC Press, Boca Barton, FL, 1985.

[2] BROOKS, B. R., BRUCCOLERI, R., OLAFSON, B. D., STATES, D. J., SWAMINATHAN, S., AND KARPLUS, M. CHARMM: A Program for Macromolecular Energy, Minimization and Dynamics Calculations. *J. Comp. Chem.*, 1983, **4**, 187–217.

[3] DARDEN, T., YORK, D., AND PEDERSEN, L. Particle mesh Ewald: An N.log(N) method for Ewald sums in large systems. *J. Chem. Phys.*, 1993, **98**, 10089–10092.

[4] ANÉZO, C., DE VRIES, A. H., HÖLTJE, H.-D., TIELEMAN, D. P., AND MARRINK, S. J. Methodological issues in lipid bilayer simulations. *J. Chem. Phys.B*, 2003, **107**, 9424–9433.

[5] HILL, T. L. *An Introduction to Statistical Thermodynamics*. Dover Publications Inc., New York, 1986.

[6] ZHANG, Y., FELLER, S. E., BROOKS, B. R., AND PASTOR, R. W. Computer simulation of liquid/liquid interfaces. I. Theory and application to octane/water. *J. Chem. Phys.*, 1995, **103**, 10252–10266.

[7] FELLER, S. E., ZHANG, Y., PASTOR, R. W., AND BROOKS, B. R. Constant pressure molecular dynamics simulation: The Langevin piston method. *J. Chem. Phys.*, 1995, **103**, 4613–4621.

[8] HOOVER, W. G. Canonical dynamics: Equilibrium phase-space distributions. *Phys. Rev. A*, 1985, **31**, 1695–1697.

[9] VENABLE, R. M., BROOKS, B. R., AND PASTOR, R. W. Molecular Dynamics Simulations of Gel ($L_{\beta I}$) Phase Lipid Bilayers in Constant Pressure and Constant Surface Area Ensembles. *J. Phys. Chem.*, 2000, **112**, 4822–2832.

[10] NAGLE, J. F., AND TRISTRAM-NAGLE, S. Structure of lipid bilayers. *Biochim. Biophys. Acta*, 2000, **1469**, 159–195.

[11] PASTOR, R. W., VENABLE, R. M., AND FELLER, S. E. Lipid Bilayers, NMR Relaxation, and Computer Simulations. *Acc. Chem. Res.*, 2002, **35**, 438–446.

[12] CHIU, S.-W., CLARK, M., BALAKI, V., SUBRAMANIAM, S., SCOTT, H. L., AND JAKOBSSON, E. Incorporation of surface tension into molecular dynamics simulation of an interface: A fluid phase lipid bilayer membrane. *Biophys. J.*, 1995, **69**, 1230–1245.

[13] FELLER, S. E., AND PASTOR, R. W. On simulating lipid bilayers with an applied surface tension:periodic boundary conditions and undulations. *Biophys. J.*, 1996, **71**, 1350–1355.

[14] MARRINK, S. J., AND MARK, A. E. Effect of undulations on surface tension in simulated bilayers. *J. Phys. Chem. B*, 2001, **105**, 6122–6127.

[15] JENSEN, M. O., MOURITSEN, O. G., AND PETERS, G. H. Simulations of a membrane-anchored peptide: structure, dynamics, and influence on bilayer properties. *Biophys. J.*, 2004, **86**, 3556–3575.

[16] SKIBINKSY, A., VENABLE, R. M., AND PASTOR, R. W. A molecular dynamics study of the response of lipid bilayers and trehalose. *Biophys. J.*, 2005, **89**, 4111–4121.

[17] BAGINSKI, M., RESAT, H., AND MCCAMMON, J. A. Molecular properties od Amphotericin B membrane channel: A molecular dynamics simulation. *Mol. Pharmacol.*, 1997, **52**, 560–570.

[18] JÄHNIG, F. What is the durface tension of a lipid bilayer membrane? *Biophys. J.*, 1996, **71**, 1348–1349.

[19] FELLER, S. E., ZHANG, Y., AND PASTOR, R. W. Computer simulation of liquid/liquid interfaces. II. Surface tension/area dependence of a bilayer and monolayer. *J. Chem. Phys.*, 1995, **103**, 10267–10276.

[20] MIHAILESCU, D., AND SMITH, J. C. Atomic detail peptide-membrane interactions: Molecular Dynamics of gramicidine S in a DMPC bilayer. *Biophys. J.*, 2000, **79**, 1718–1730.

[21] FELLER, S. E., AND PASTOR, R. W. Constant surface tension simulations of lipid bilayers: The sensitivity of surface areas and compressibilities. *J. Chem. Phys.*, 1999, **111**, 1281–1287.

[22] SANKARARAMAKRISHNAN, R., AND WEINSTEIN, H. Surface tension parameterization in molecular dynamics simulations of a phospholipid-bilayer membrane: calibration and effects. *J. Chem. Phys.B*, 2004, **108**, 11802–11811.

[23] PATRA, M., KARTTUNEN, M., HYVÖNEN, M. T., FALCK, E., LINDQVIST, P., AND VATTULAINEN, I. Molecular dynamics simulations of lipid bilayers: Major artifacts due to truncating electrostatics. *Biophys. J.*, 2003, **84**, 3636–3645.

[24] LINDAHL, E., AND EDHOLM, O. Mesoscopic undulations and thickness fluctuations in lipid bilayers from molecular dynamics simulations. *Biophys. J.*, 2000, **79**, 426–433.

[25] LINDAHL, E., HESS, B., AND VAN DER SPOEL, D. GROMACS: A package for molecular simulation and trajectory analysis. *J. Mol. Mod.*, 2001, **7**, 306–317.

[26] CHANDRASEKHAR, I., BAKOWIES, D., GLÄTTLI, A., HÜNENBERGER, P., PEREIRA, C., AND VAN GUNSTEREN, W. F. Molecular dynamics simulations of lipid bilayers with GROMOS96: Application of surface tension. *Mol. Simul.*, 2005, **31**, 543–548.

[27] NAGLE, J. F., ZHANG, R., TRISTRAM-NAGLE, S., SUN, W., PETRACHE, H. I., AND SUTER, R. M. X-ray structure determination of fully hydrated L alpha phase dipalmitoylphosphatidylcholine bilayers. *Biophys. J.*, 1996, **70**, 1419–1431.

[28] SMONDYREV, A. M., AND BERKOWITZ, M. L. Structure of DPPC/Cholesterol bilayer at low and high cholesterol concentrations: molecular dynamics simulation. *Biophys. J.*, 1999, **77**, 2075–2089.

[29] HOFSÄSS, C., LINDAHL, E., AND EDHOLM, O. Molecular dynamics simulations of phospholipid bilayers with cholesterol. *Biophys. J.*, 2003, **84**, 2192–2206.

[30] NAGLE, J. F., AND WIENER, M. C. Structure of fully hydrated bilayer dispersions. *Biochim. Biophys. Acta*, 1988, **942**, 1–10.

[31] TRISTRAM-NAGLE, S., ZHANG, R., SUTER, R. M., WORTHINGTON, C. R., SUN, W. J., AND NAGLE, J. F. Measurement of chain tilt angle in fully hydrated bilayers of gel phase lecithins. *Biophys. J.*, 1993, **64**, 1097.

[32] CZUB, J., AND M.BAGINSKI. Comparative molecular dynamics study of lipid membranes containing cholesterol and ergosterol. *Biophys. J.*, 2006, **90**, 2368–2382.

[33] WIENER, M. C., SUTER, R. M., AND NAGLE, J. F. Structure of the fully hydrated gel phase of dipalmitoylphosphatidylcholine. *Biophys. J.*, 1989, **55**, 315–325.

[34] FELLER, S. E., AND A. D. MACKERELL, J. An Improved Empirical Potential Energy Function for Molecular Simulations of Phospholipids. *J. Phys. Chem. B*, 2000, **104**, 7510–7515.

CHAPTER 5

MOLECULAR DYNAMICS SIMULATIONS OF STEROL-PHOSPHOLIPID BILAYERS: THE EFFECT OF STEROL STRUCTURE

In this chapter the effect of each sterol on the membrane properties is examined at atomic detail. First, the ordering effect on the lipids, lipid packing and the *gauche* populations on the DPPC acyl chains are discussed. The location of each sterol and its preferred orientation in the membrane is examined via electron density profiles and sterol tilt angles, respectively. The solvation of different groups in the sterol:DPPC systems is also studied. The chemical origins of the different membrane behavior upon addition of each sterol are discussed with respect to the sterol chemical structures. Figure 5.1 depicts the chemical structures of the molecules studied.

5.1 COMPUTATIONAL DETAILS

The simulations were performed at T=309K and T=323K on cholesterol/DPPC, ergosterol/DPPC and lanosterol/DPPC bilayers. For all simulations the CHARMM package version 28b1[1] was used with the all-atom CHARMM 27 force field[1] for DPPC. For cholesterol, ergosterol and lanosterol the force field derived in Ref. 2 was used.

The Particle Mesh Ewald summation technique[3] was employed to calculate electrostatic contributions. The van der Waals and electrostatic interactions were cut off at 14 Å using the CHARMM shifted potential. It has been shown that shift is an appropriate method of electrostatic truncation in lipid bilayer simulations.[4] Periodic boundary conditions of the orthorhombic cells were applied in all directions. The equation of motion was integrated using the Verlet algorithm with a timestep of 1 fs. The simula-

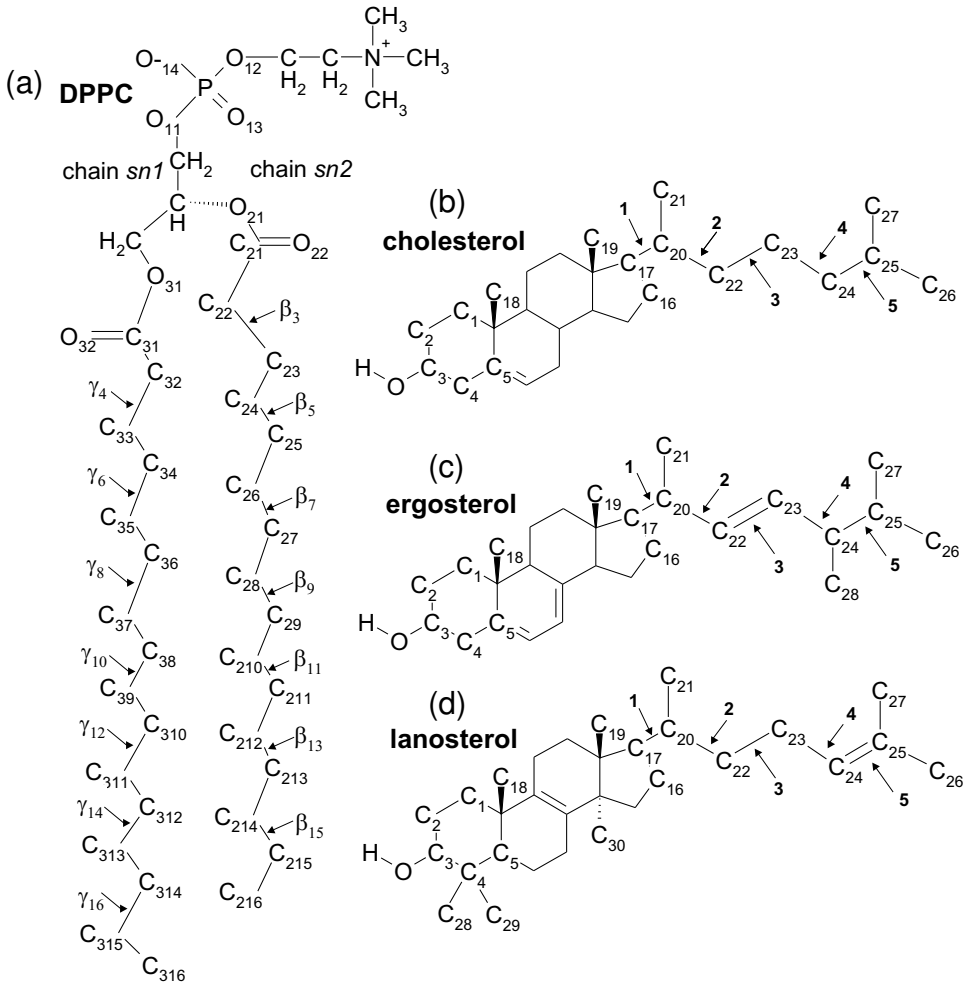

Figure 5.1: Chemical structure, atom numbering and dihedral angle schemes of (a) DPPC, (b) cholesterol, (c) ergosterol, (d) lanosterol.

tions were carried out in the NPT ensemble (constant number of molecules, pressure and temperature).

Constant temperature conditions were maintained by a Hoover thermostat[5] using the extended system constant pressure and temperature algorithms implemented in CHARMM with a mass of 2000 kcal/ps. A constant pressure of P=1atm was imposed using the Langevin piston method.[6] The collision frequency was set to 30 ps^{-1} for the heating and equilibration and to 10 ps^{-1} for production dynamics.

Before analysis, all coordinate sets were superposed on a primary-box reference structure to remove global unit-cell rotation and translation.

5.1.1 CREATING THE STEROL-DPPC BILAYER SYSTEMS

For the sterol-containing bilayer MD simulations, the membrane consisted of 120 DPPC and 80 sterol molecules, giving a biologically-relevant sterol concentration (40% mol.). Six simulations of the lipid bilayer were performed with the three different sterols (cholesterol, ergosterol and lanosterol) being simulated at two temperatures, namely 309K and 323K. Coordinates for DPPC were constructed within CHARMM.[1] Selected DPPC molecules were replaced with cholesterol molecules in order to obtain a 40% mol. sterol concentration, well within the *lo* phase. Coordinates for the cholesterol molecule were taken from its crystal structure.[7] Since there is no consensus for a specific organisation pattern of cholesterol in the membrane, in this simulation the cholesterol molecules were roughly uniformly placed in the bilayer patch, with the same number of sterol molecules in each bilayer leaflet. The cholesterol hydroxyl group was placed at the same depth as the carbonyl group of DPPC, as suggested by structural studies.[8] Ergosterol and lanosterol were constructed from the cholesterol molecule using the software package Insight II.[9] The lipid bilayer was surrounded by 1600 TIP3P[10] water molecules leading to a 20% wt. hydration.

Since there are no experimental measurements for the surface area per DPPC in a binary sterol/DPPC system, the cholesterol-containing membrane was constructed here so as to produce an initial mean value of the area per lipid of 50 Å^2, which is the average value from two previous cholesterol-DPPC MD simulations[11, 12] (45.6 Å^2 and 54.2 Å^2).

Thus, the initial dimensions of the primary cell chosen for the system were x = 56.0 Å, y = 72.0 Å, z = 60.0 Å using an orthorhombic box ($\alpha = \beta = \gamma = 90°$). The center of the unit cell was set at the origin of the coordinate system and the z-axis was chosen to coincide with the membrane normal. The NPT ensemble was chosen because a flexible simulation cell allows the lipid bilayer to expand or contract when sterol molecules are added so that the bilayer will adapt to its preferred state. Each system was allowed to relax into its preferred surface area per lipid with all three simulation box coordinates adjusting independently.

5.1.2 SIMULATION PROTOCOL

Initially, a 50-lipid system consisting of 30 DPPC, 20 cholesterol and 400 water molecules was constructed. This system was energy-minimized for 1000 steps with the CG method followed by 30000 steps of the ABNR minimization. Next, the system was heated up to 309 K or 323 K in 5K steps every 5000 timesteps. The system was equilibrated for 600 ps at constant pressure (1 atm) and temperature (309 K or

323 K) using the extended-system Hoover algorithm with periodic boundary conditions as implemented in CHARMM.[6] After 600 ps equilibration, a 200-lipid system was created by duplicating and translating the original slab of the pre-equilibrated 50 lipids in the x and y directions. To construct the ergosterol/lanosterol membrane systems, the cholesterol molecules were replaced accordingly and energy minimization and heating up to 309 K or 323 K was applied. Therefore, any differences arising in the structure and dynamics of the three sterol-containing membranes, are due to the differences in their molecular structures and do not arise from differences in their initial configurations.

Before production dynamics all the systems were subsequently equilibrated for 15ns. Long equilibration times are required for relaxing the molecules from their initial model-built configurations and for convergence of properties of these systems.[13, 14] The equilibration was checked by ensuring that the energy and volume distributions have a Gaussian shape. The time series of the total energy for each simulated system can be seen in Figure 5.2.

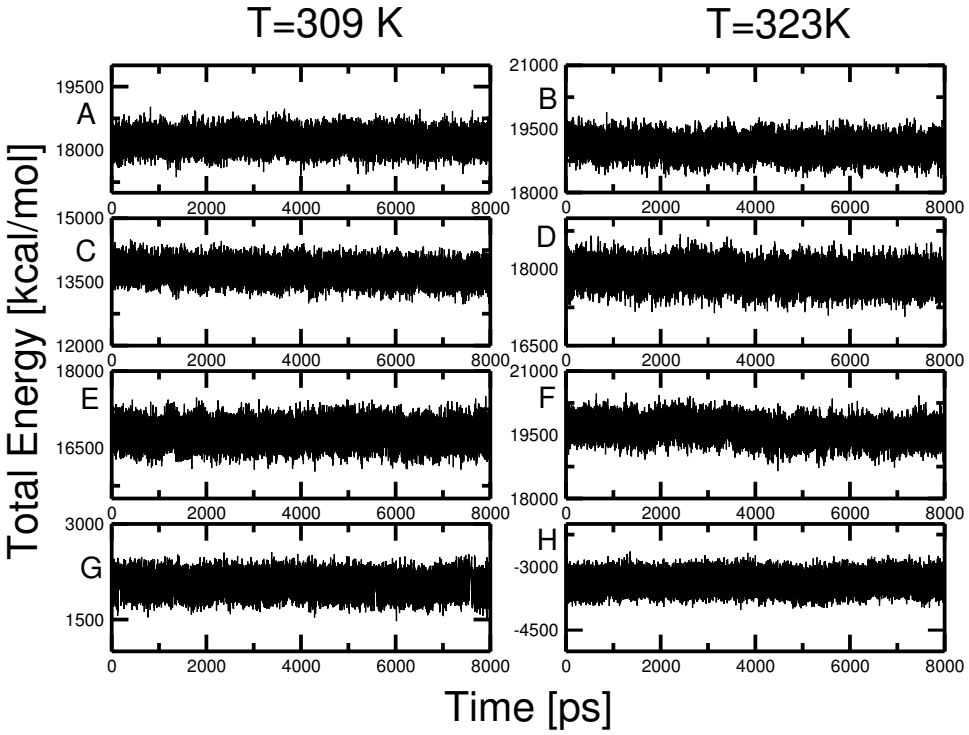

Figure 5.2: Time evolution of the total energy for the production run of the simulated systems. (A) and (B) chol-DPPC, (C) and (D) erg-DPPC, (E) and (F) lan-DPPC, (G) 64-DPPC in the gel phase and (H) 72-DPPC in the liquid phase.

A separate simulation of the isolated sterols in vacuum at T=309K and T=323K was also performed to assess their vacuum conformational flexibility.

5.1.3 THE QUESTION OF SURFACE TENSION

Estimating the surface area per lipid in complex heterogeneous systems is difficult, and in these cases the choice of γ can be complicated,[15] since the addition of compounds to a purely phopsholipidic membrane is expected to influence the surface tension of the bilayer.

Since there are no experimental measurements for the surface area per DPPC in a binary cholesterol/DPPC system, the cholesterol-containing membrane was constructed so as to produce an initial mean value of the area per lipid of 50 Å^2, averaged from two previous MD simulations[11] (45.6 Å^2) * and of 54.2 Å^2.[12] Thus, the initial dimensions of the primary cell chosen for the system were x=56.0 Å, y=72.0 Å, z=60.0 Å using an orthorhombic box ($\alpha = \beta = \gamma = 90°$). The center of the unit cell was set at the origin of the coordinate system and the z-axis was chosen to coincide with the membrane normal.

From various simulation results, it has been suggested that the area per lipid in a cholesterol-DPPC bilayer is close to 50 Å^2.[11, 12] This area per lipid is closer to that of a gel state (47.9Å^2)[16] than to that of a liquid state (62.9Å^2).[16] Since the gel phase of a DPPC bilayer has been successfully simulated with γ=0dyn/cm, we have chosen to perform also the sterol-DPPC simulations at γ=0dyn/cm so as to reduce equilibration times.

The NPT ensemble was chosen because a flexible simulation cell allows the lipid bilayer to expand or contract when sterol molecules are added so that the bilayer will adapt to its preferred state. Each system was allowed to relax into its preferred surface area per lipid with all three simulation box coordinates adjusting independently.

5.1.4 STABILITY OF THE SIMULATIONS

The systems were allowed to adjust not only their volumes (density) but also their area-to-thickness ratios. For the sterol-DPPC systems the dimensions of the unit cell and the total volume of the systems do not show a drift in time, indicating stable simulations (see Figures 4.6 and 5.3). The time series of the total energy for each system can be seen in Figure 5.2. The average cell dimensions x, y, z and the unit cell volumes for all systems are listed in Table 5.1.

*This simulation study was performed on two independent initial bilayer structures where cholesterol was arranged with a different pattern in the bilayer. These two simulations gave areas per lipid values of 46.5±0.6 and 44.7±0.6Å^2. The value of 45.6 Å^2 is the mean value between them.

	DPPC:Chol		DPPC:Erg	
	309K	323K	309K	323K
x	55.4±0.3	57.1±0.4	56.7±0.4	58.7±0.5
y	71.5±0.3	70.9±0.7	68.5±0.6	67.2±0.7
z	59.9±0.3	59.3±0.4	61.0±0.2	60.7±0.3
${V_{TOT}}^b$	237320±665	240130±790	236870±731	239300±684
V_{DPPC}	1175.3±5.5	1194.4±6.6	1163.7±6.0	1179.6±5.7
A_{DPPC}	48.3±0.2	49.6±0.3	47.1±0.2	47.9±0.2
h	48.7±0.5	48.2±0.3	49.4±0.3	49.2±0.2
	DPPC:Lan		pure DPPC[a]	
	309K	323K	309K	323K
x	56.9±0.4	60.1±0.5	89.3±0.6	65.4±0.9
y	73.6±0.5	71.8±0.6	66.3±0.2	94.5±0.9
z	58.1±0.3	57.1±0.4	62.9±0.4	67.1±1.0
${V_{TOT}}^b$	243470±692	246500±914	372630±747	414750±1071
V_{DPPC}	1188.4±5.8	1209.4±7.6	1110.4±3.0	1221.0±5.2
A_{DPPC}	49.8±0.2	50.8±0.3	46.8±0.2	64.6±0.3
h	47.7±0.9	47.6±0.8	44.7±0.03	38.1±0.2

Table 5.1: Average cell dimensions x, y, z (in Å), cell volume,V_{TOT} (in Å^3), volume per lipid, V_{DPPC} (in Å^3), area per lipid, A_{DPPC} in Å^2 and membrane thickness,h, (in Å) for the six systems and the two different temperatures. Results are given for the 256-DPPC simulation (T=309K) and for the 200-DPPC simulation (T=323K). Values for the initial dimensions and volume are given but cannot be compared directly to the sterol-containing simulations. The initial volume of the simulation cell was 241920 Å^3

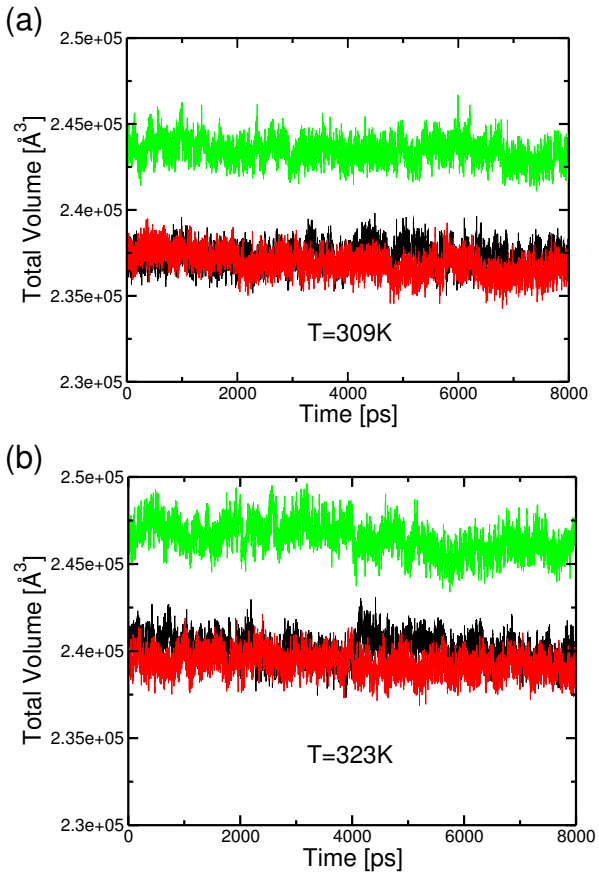

Figure 5.3: Total volume of the unit cell. Cholesterol-DPPC: black, ergosterol-DPPC: red and lanosterol-DPPC: green for (a) 309K and (b) 323K.

5.2 RESULTS AND DISCUSSION

5.2.1 ORDERING OF ACYL CHAINS

Many experimental and computational studies have been devoted to studying the effect of cholesterol on the acyl chain ordering. Here, we reexamine this and compare with ergosterol and lanosterol. A useful quantity for characterizing the order of the hydrocarbon chains in lipid bilayers is the deuterium NMR order parameter, S_{CD}. An order parameter may be defined for every CH_2 group in the chains as follows:

$$S^i_{CD} = \frac{1}{2}(3\langle cos^2\theta_{CD}\rangle - 1) \tag{5.1}$$

where θ_{CD} is the angle between a CD-bond (D is deuterium in the experiment) or a CH-bond (in the simulation) and the membrane normal (z-axis), and i is the number of the carbon atom in the lipid alkyl chain. The brackets indicate ensemble averaging over the two bonds in each CH_2 group, the lipid molecules, and time. S^i_{CD} thus relates

the geometry of the acyl chains to the orientational order parameter of the C-C bond. The order parameter profiles for the present simulations of the three sterols are given in Figure 5.4.

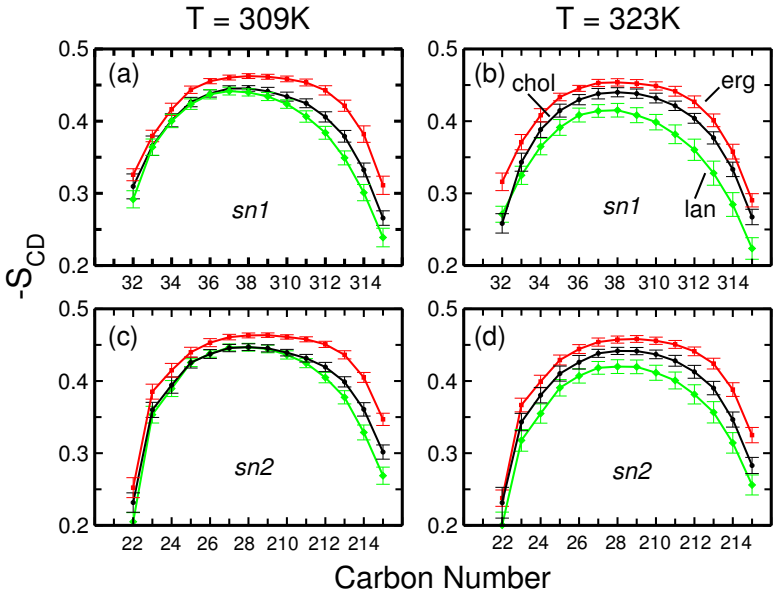

Figure 5.4: Order Parameter Profile for the DPPC in sterol-containing membranes. Cholesterol-DPPC: black line and circles, ergosterol-DPPC: red line and squares, lanosterol-DPPC: green line and diamonds. (a) T=309K, sn1 chain, (b) T=323K, sn1 chain, (c) T=309K, sn2 chain, (d) T=323K, sn2 chain. The error bars represent standard deviations calculated by dividing the 8ns trajectories into 100ps pieces and calculating order parameter profiles for each.

Figure 5.4 shows that the effect on the ordering of the alkyl chains is significantly different for the three sterols, especially towards the bilayer center. At both temperatures ergosterol induces the highest order in the bilayer and lanosterol has the smallest ordering effect. The temperature increase lowers significantly the order parameters of the lanosterol-DPPC membrane while there is just a slight decrease on the order parameters of the ergosterol- and cholesterol-DPPC membranes.

The changes in the order parameter profiles are different for the two lipid chains and depend on the position of the carbon atoms. Upon addition of the sterols, the $-S_{CD}$ profile is roughly constant along carbons C_6 to C_{8-11} (see Fig. 5.4), particularly for the ergosterol-DPPC membrane which takes values between 0.458 and 0.462 through carbons C_7 to C_{10} for T=309K and the DPPC *sn1* chain. Lanosterol does not exhibit as constant values for the middle-carbon S_{CD} .

As can be seen in Figure 5.5 the presence of sterol results in large increases relative to the pure DPPC bilayer in the $-S_{CD}$ profile of the hydrocarbon tails.[17,18] These increases are likely to arise from the rigid steroid body of the sterols associating with

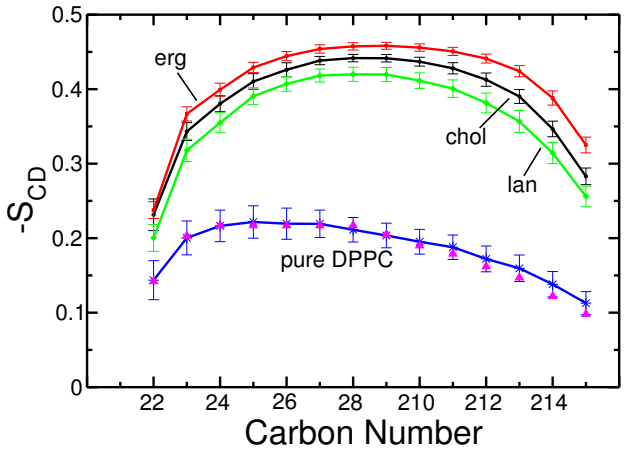

Figure 5.5: Order Parameter Profile for T=323K and the $sn2$ DPPC chain. Cholesterol-DPPC: black line and circles, ergosterol-DPPC: red line and squares, lanosterol-DPPC: green line and diamonds, neat 72-DPPC membrane: calculated from the present simulation in blue line and stars and NMR experimental results of Ref. 17 in magenta triangles. The error bars represent standard deviations calculated by dividing the 8ns trajectories into 100ps pieces and calculating order parameter profiles for each.

the saturated hydrocarbon tails of DPPC.[19, 20]

The addition of 50 mol% cholesterol increases the values of S_{CD} for a DPPC molecule by about a factor of 2 relative to a pure membrane.[11, 17, 18, 21, 22] The present simulation data for the pure DPPC $sn2$ chain are in excellent agreement with the corresponding NMR data in Ref. 17 (see Figure 5.5). The order parameter profile for cholesterol is also consistent with all previous simulation results obtained in similar conditions.[11, 12, 19] The results obtained here for cholesterol, ergosterol and lanosterol (Fig. 5.4) are also in good overall agreement with those obtained in an NMR study,[21] in which a similar ordering trend for cholesterol, ergosterol and lanosterol on DMPC bilayers was observed. Furthermore, other NMR studies of lanosterol and cholesterol, in a POPC bilayer,[23] indicated that lanosterol orders the acyl lipid chains but does not have such a big effect as cholesterol, again in agreement with our simulations. Moreover, two further NMR studies[24, 25] of cholesterol/ergosterol-DPPC bilayers concur with the present studies as they indicate that the chain ordering in ergosterol-containing membranes is stronger than in cholesterol-containing membranes. This stronger lipid chain ordering could arise from the fact that the ergosterol structure inhibits DPPC chain conformational freedom even more than does cholesterol (see later in text).

5.2.2 *Gauche* POPULATIONS OF THE ACYL CHAINS

A further important conformational property of phospholipid chains is the fraction of *gauche* dihedral angles in the acyl tails. The *trans-gauche* isomerisation is one of the fastest anharmonic motions experienced by the phospholipids (picosecond timescale) and it contributes to conformational disorder. Therefore, the *gauche* profiles can be viewed also as a measure of the order and organisation in the bilayer system, which will also affect other properties of the system. Here, the *gauche* fraction was determined by integrating each normalized torsion angle distribution for each lipid tail from -120° to 120°. The resulting values are plotted in Figure 5.6.

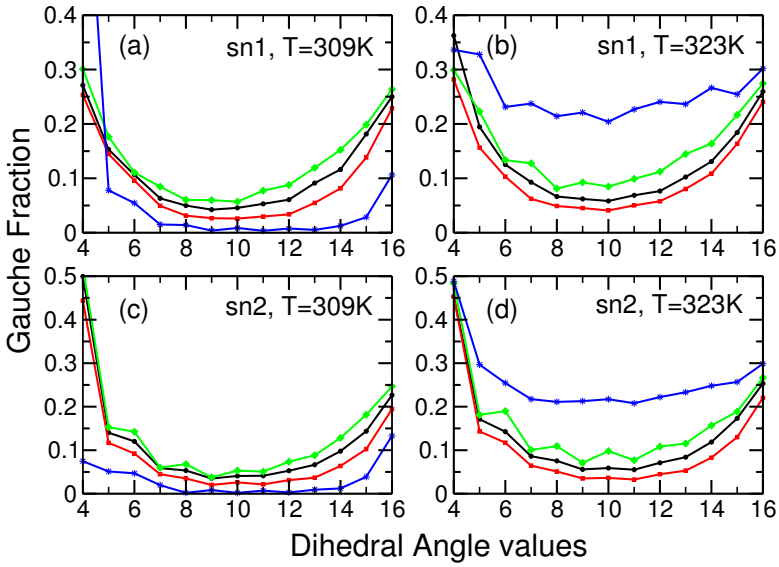

Figure 5.6: Order Parameter Profile for T=323K and the $sn2$ DPPC chain. Cholesterol-DPPC: black line and circles, ergosterol-DPPC: red line and squares, lanosterol-DPPC: green line and diamonds, neat 72-DPPC membrane: calculated from the present simulation in blue line and stars and NMR experimental results of Ref. 17 in magenta triangles. The error bars represent standard deviations calculated by dividing the 8ns trajectories into 100ps pieces and calculating order parameter profiles for each.

At T=309K the addition of any sterol increases to the gel DPPC system the *gauche* fraction thus disordering the gel phase. In contrast, presence of any of the three sterols to liquid DPPC (T=323K) clearly decreases the total number of *gauche* defects per DPPC molecule at all carbon positions, thus ordering the liquid phase. The increase in the *trans* percentage is particularly evident in the positions β6-β12 and γ6-γ12, where the rigid steroid nucleus is located. (The notation for the dihedral angles in the lipid tails follows that adopted in Ref. 26, which is commonly used.) The effect is

smaller at the terminus, where the methyl group has more freedom of movement and thus the last dihedral angle exhibits a significant number of *gauche* defects (three-fold symmetry). For the $sn2$ chain, the *gauche* fractions of $\beta 4$ torsions remain unchanged at T=323K and are close to those of liquid pure DPPC.

Infrared spectroscopic determination of the *gauche* fraction of gel/liquid and cholesterol-containing DPPC membranes[27] indicate that the gel phase of DPPC is characterized by high conformational order, with *gauche* percentage values of $\approx$2% for $\gamma 7$ and $\gamma 11$, similar to the percentages of 1.5% for $\gamma 7$ and 1% for $\gamma 11$ calculated from the present simulation data. Other infrared spectroscopic studies[28–30] have shown that, at 323K, the liquid DPPC bilayer features *gauche* fractions at γ5,7,11,14,15,16 are 0.21, 0.30, 0.20, 0.17, 0.40 and 0.40, respectively. Addition of 33 mol% cholesterol reduced the corresponding values to 0.04, 0.04, 0.13, and 0.11 by restricting the rotamer formation; no values were determined for positions 14 and 15. These values are again in general agreement with the present calculated *gauche* fraction. The 'odd-even' effect[17] for the *gauche* populations with $T > T_m$ and with respect to the carbon position, *i.e.* $P_{\gamma 6} < P_{\gamma 7}, P_{\gamma 8} < P_{\gamma 9}, P_{\gamma 10} < P_{\gamma 11}$, etc. ($P$: *gauche* population) is also observed (see Fig. 5.6b).

Gauche populations for ergosterol- or lanosterol-DPPC membranes have not been experimentally determined yet. Our simulation data show that the *gauche* concentration of the lipid tails follows the order: gel $<$ ergosterol-DPPC $<$ cholesterol-DPPC $<$ lanosterol-DPPC $<$ liquid. This suggests that the ergosterol-containing membrane features the most conformational order in acyl lipid chains while lanosterol the least among the three sterols studied.

An increase in the hydrocarbon chain order and decrease in the fraction of *gauche* dihedral angles is accompanied by the increase of the hydrocarbon chain lengths. The increase of the acyl chain length becomes less pronounced with the inclusion of lanosterol than with the inclusion of ergosterol or cholesterol. The hydrophobic thickness of each bilayer was calculated by taking the average distance C_{21}-C_{21} between lipids that are found in opposite monolayers. At T=323K the hydrophobic thickness is 38.6$\pm$0.2Å for lanosterol, 39.3$\pm$0.2Å for cholesterol and 39.9$\pm$0.2Å for ergosterol. At T=309K the corresponding values are 38.8$\pm$0.4Å for lanosterol, 39.9$\pm$0.2Å for cholesterol and 40.4$\pm$0.3Å for ergosterol. Thus, we expect that the membrane thickness is smaller for lanosterol and larger for ergosterol following the order of the *gauche* fractions. To evaluate the membrane thicknesses and compare it to available experimental data we have calculated the electron density profiles for all simulated systems.

5.2.3 ELECTRON DENSITY PROFILES

In Figure 5.7 the simulation-derived electron density profiles for the sterol-containing membranes at T=309K and T=323K are shown together with the pure DPPC profile. The peaks are relatively sharp, allowing the thickness of the bilayer to be estimated from the peak-to-peak separation. The results are listed in Table 1. It is evident that all the sterols tend to 'stretch' the bilayer increasing its thickness relative to both the gel and the liquid DPPC phases, as has also been experimentally inferred from volumetric studies of cholesterol, ergosterol and lanosterol in a DPPC bilayer.[31] This effect is, however, more noticeable in the case of liquid DPPC, where the sterol addition orders the membrane and as a result stretches the DPPC hydrocarbon tails (see also 'Ordering of Acyl Chains' section).

The membrane thickness of the gel-DPPC bilayer is close to that observed for the sterol-containing membranes. Addition of cholesterol, ergosterol or lanosterol to gel-phase DPPC again increases the bilayer thickness (see Figure 5.7b). This effect was also observed in two neutron diffraction experiments.[8, 32] The addition of these sterols to the pure lipid gel phase increases the *gauche* fraction of the phospholipid chains, decreasing the mean acyl chain ordering of the phospholipids[24, 33, 34] (see also '*Gauche* populations of the acyl chains' section). With increasing acyl chain order the membrane thickness increases due to the elongation of the lipid chains.[35] Reduction of the acyl chain order in the gel phase would thus lead to reduction of the membrane thickness. However, upon incorporation of sterols in the gel-phase the opposite is observed: an increased membrane thickness. This increase was found to be not a consequence of increased lipid order, as in the liquid phase, but rather of the decrease in the acyl chain tilt of the gel phase. Upon addition of the sterol, the gel-DPPC chain tilt (see Fig. 4.5) is lost, which leads to an increase in the bilayer thickness even though the acyl chain order is reduced. Experimental results show an increase in membrane thickness of about 3.5Å with the addition of 30mol% cholesterol to the gel phase of DMPC.[8] This increase is consistent with the present simulation results within the statistical error, where the gel phase membrane thickness increases 4.0$\pm$0.5Å from 44.7Å in the gel phase to 48.7$\pm$0.5Å upon addition of 40% cholesterol.

Figure 5.7 and Table 5.1 show that only small differences are observed between the density profiles of the sterol-containing membranes. In a recently-performed small-angle neutron scattering study on cholesterol-, ergosterol- and lanosterol-DMPC bilayers, it was also shown that only small differences occur in the influence of the sterols on membrane thickness occur.[32] Specifically, for a DMPC bilayer at 303K (liquid phase), the membrane thickness of an ergosterol-containing DMPC membrane

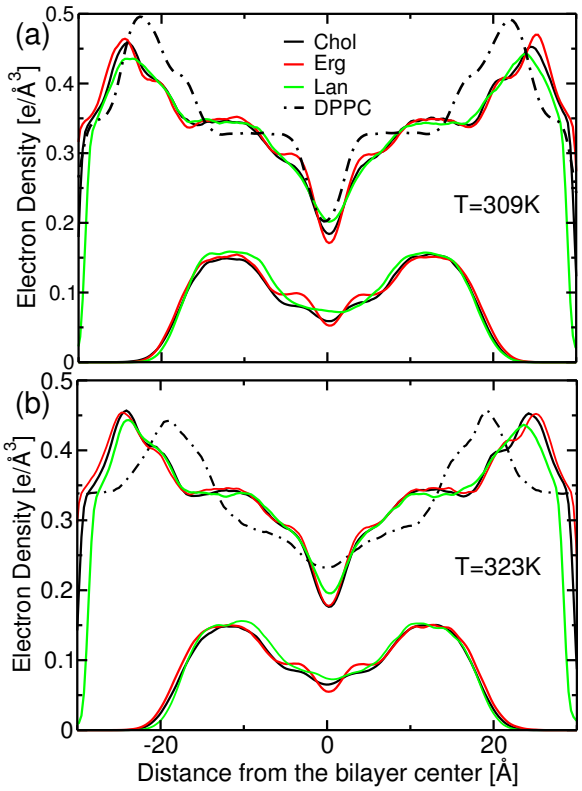

Figure 5.7: Electron density profiles for cholesterol-DPPC: black line, ergosterol-DPPC: red line and lanosterol-DPPC: green line for (a) 309K and (b) 323K in comparison with the neat DPPC membrane (dashed-dotted black line). The upper curves in the figures represent the total electron density of the system and the lower curves are the contributions of the three sterols. The electron density profiles were calculated from the trajectories by dividing the simulation cells into 0.3 Å slabs and determining the time-averaged number of electrons per slab, using the coordinates of the atoms from the trajectories and assigning the corresponding number of electrons to the atomic centers.

(47%mol. sterol) was 44.4Å and very close to the membrane thickness of the analogous cholesterol-containing DMPC membrane (44.2Å). The lanosterol system had a slightly smaller thickness of 43.6Å. The experimental membrane thickness, h, follows the order $h_{lan} < h_{chol} < h_{erg}$. This behaviour is also seen in the present MD simulations at both 309K and 323K, as the ergosterol membrane is thicker by $\approx$1Å than the cholesterol membrane and $\approx$2Å thicker than the lanosterol membrane (see Table 1). This result is in qualitative agreement with a recent MD study of cholesterol- and ergosterol-DMPC bilayers at 25%mol. sterol concentration and 300K, in which the ergosterol-DMPC bilayer had a thickness of 41.5Å and the cholesterol-DMPC 39.3Å.[19] However, the 25%mol. cholesterol concentration is on the border between the *lo* and the liquid phase[33, 36] and the 25%mol. ergosterol concentration is not in the

lo phase (a concentration of over 30% is required), as experimental studies show.[24]

The contribution of each sterol to the total electron density of the membrane is also shown in Figure 5.7. The electron density profiles arising from the sterols have two broad peaks. As the ergosterol side chain has one methyl group more than the other two sterols one should expect that its electron density near the bilayer center would be greater than the other two sterols. However, Fig. 5.7 indicates that in the center of the bilayer lanosterol exhibits a slightly higher electron density especially at T=309K (see Fig. 5.7a lower curve). Ergosterol, on the other hand, exhibits the lowest electron density in the bilayer midplane. Therefore, ergosterol is located closer to the water interface than the other two sterols.

To investigate further the z-positioning the electron density profiles were cal-

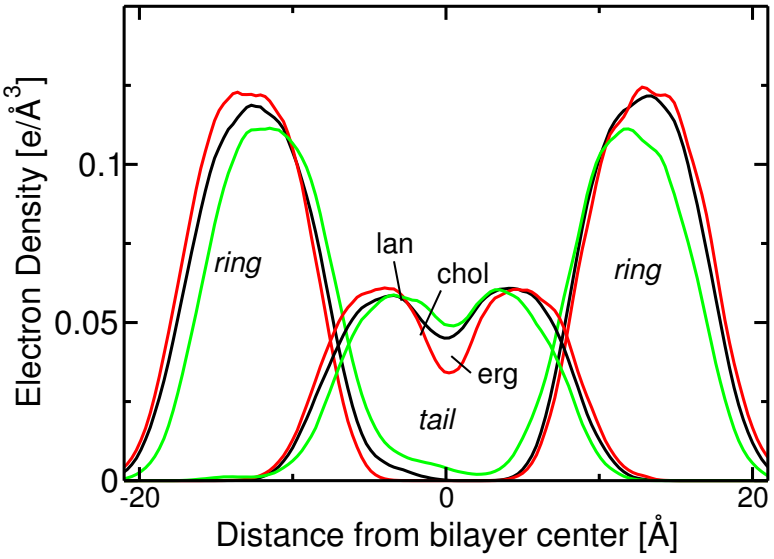

Figure 5.8: Electron density profiles for T=323K and for the common ring (C_1-C_{19}) and tail (C_{20}-C_{27}) atoms of the sterols. Cholesterol-DPPC: black line, ergosterol-DPPC: red line and lanosterol-DPPC: green line. The central profiles are the electron density of the tail and the outer profiles the electron density of each sterol ring systems.

culated solely from the common ring and side-chain atoms of the three sterols, *i.e.* C_1-C_{19} of the ring atoms and C_{20}-C_{27} of the sterol tail. In this manner, the positions of the three sterols in the bilayer can be directly compared. The results, shown in Fig. 5.8 unambiguously demonstrate that lanosterol is found closer to the bilayer core than cholesterol, by 2Å on average. Ergosterol is also slightly closer to the bilayer:water interface than cholesterol and thus occupies the bilayer center the least.

5.2.4 AREAS PER LIPID IN THE BINARY SYSTEMS

In the pure lipid simulations, the average area per lipid can be calculated by dividing the surface area of the simulation cell by the number of lipids per monolayer. However, in binary mixtures there is no unique way of obtaining the area per lipid. The problem of calculating the correct area per lipid in cholesterol-DPPC mixtures has been addressed in recent MD studies.[12, 37, 38] The procedure used here is that of Ref. 12, where the volume that a DPPC molecule occupies in a sterol-containing membrane in one frame of the trajectory is calculated as follows:

$$V_{DPPC} = \frac{V_T - N_W \times V_W - N_S \times V_S}{N_{DPPC}} \tag{5.2}$$

where V_T is the total volume of the system, N_{DPPC} (here, 120) the total number of the lipids, N_W (here, 1600) the number of water molecules, V_W (29.24Å^3) the volume of one water molecule at T = 309K and V_W (29.56Å^3) the volume of one water molecule at T = 323K derived from the bulk water simulation, and N_S (here, 80) the number of cholesterol molecules.

The volume of a cholesterol molecule, $V_S = 618.8\,\text{Å}^3$, was calculated as the average volume of one cholesterol molecule from the three published crystal structures.[39–41] To obtain the volumes of ergosterol and lanosterol, the cholesterol volume was scaled with respect to the ergosterol/lanosterol van der Waals volumes, as calculated with CHARMM using standard van der Waals radii. The volumes thus obtained for ergosterol and lanosterol are 630.6 Å^3 and 675.9 Å^3, respectively, *i.e.*, 2% and 8% larger than cholesterol. The increased volumes are due to the single additional methyl group of ergosterol and the three additional methyl groups of lanosterol. †

The area occupied by a DPPC molecule in a bilayer can be written as:

$$A_{DPPC}(x) = \frac{2V_{DPPC}(x)}{h(x)} \tag{5.3}$$

where V_{DPPC} is the volume of the lipid and $h(x)$ is the average thickness of the membrane, which corresponds to the average distance between two phosphorus atoms in opposite layers.

At T=323K for the cholesterol-DPPC system, the volume per DPPC is 1194.4 Å^3, very close to the value reported by another MD simulation (1189 Å^3)[12] for the same cholesterol concentration and temperature. For the same system from the present

†In the MD study of Ref. 19, the ratio of van der Waals volumes for ergosterol/cholesterol was calculated to be 0.87. Ergosterol has 5 hydrogens less than cholesterol but one additional methyl, and it is therefore expected to occupy a slightly larger volume than cholesterol.

simulation data using Eq. 5.3 the area per lipid is estimated to be 49.6±0.3 Å^2 (see also Table 5.1), being smaller than the value of 54.2 Å^2 reported from MD simulation results in Ref. 12, but very close to the value of 50.3 Å^2, reported again using MD simulations, by both Refs. 42 and 19.

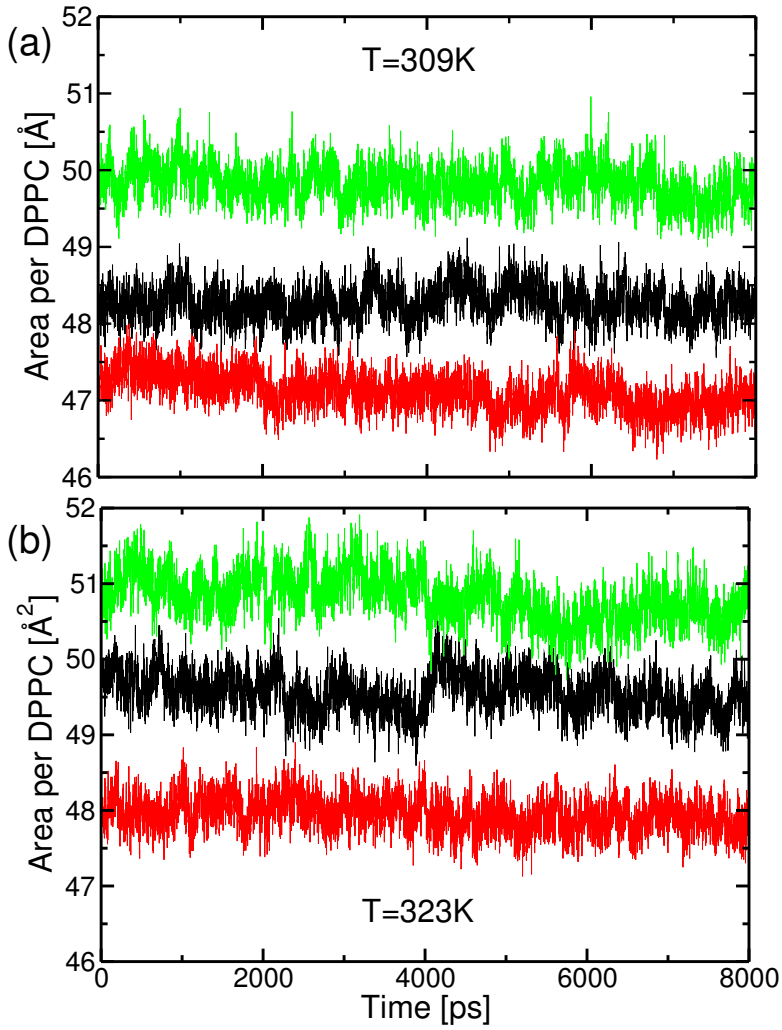

Figure 5.9: Time evolution of the area per DPPC in the sterol-containing membranes for (a) T=309K and (b) T=323K. Cholesterol-DPPC: black, ergosterol-DPPC: red, lanosterol-DPPC: green.

The area and volume per lipid for the ergosterol-DPPC and lanosterol-DPPC were also calculated and the results are listed in Table 5.1. The time evolution of the area per lipid for each system is plotted in Figure 5.9 and does not show a drift, also confirming the stability of these simulations. Ergosterol induces the smallest area and volume per DPPC, and lanosterol the largest. The area and volume per DPPC follow the order ergosterol $<$ cholesterol $<$ lanosterol for both temperatures studied. At the higher

temperature all values of the three areas per lipid are increased, but the above order is maintained. This effect was also observed in small angle neutron scattering (SANS) data that measured thermal area expansion coefficients for the three different sterol-containing vesicles.[32]

The above results imply that ergosterol has the largest condensing effect on the membrane and lanosterol the lowest. Since all three sterols are rigid, they all have an ordering influence on liquid DPPC, as is also observed from the order parameter profiles (see 'Ordering of the Acyl Chains' section). Therefore, acyl chain ordering not only reduces the number of *gauche* defects but also enhances the packing of the phospholipids, reducing cavity volumes between the molecules. All three sterols condense the bilayer (albeit to a different degree), decreasing the volume and area per DPPC molecule. Consequently, the total volume of the system is reduced relative to the pure liquid DPPC system, again in the order $V_{erg} < V_{chol} < V_{lan}$ (Table 5.1).

At T=309K the area per lipid in a cholesterol-DPPC membrane is found to be 47.9$\pm$0.2 Å^2, *i.e.*, very close to the value of 49.3Å^2 at 323K, thus indicating no significant change in the area per lipid with temperature as is observed in the pure lipid system simulation over this temperature range. For a pure DPPC bilayer, the lipid phase transition occurs at 315K and results in significantly different areas per lipid above and below the transition temperature. The area per lipid value in the sterol-containing membrane is in the range of the experimentally-measured values for the DPPC-gel phase at 309K (47.9-52.3 Å^2),[16] although at 309K with 40%mol. cholesterol concentration the lipids are still disordered (there is no specific packing of the phospholipids as in the gel state). These areas are significantly lower than the area per lipid for a pure DPPC bilayer in the liquid-crystalline state.[16, 43]

The differences in the amount of the area per lipid reduction among the different sterols arise from their individual chemical structures. Ergosterol is stiffer and more rigid than the other two sterols, having two double bonds more than cholesterol. The extra methyl group in the ergosterol tail at position C_{24} also restricts the rotational motion of the side chain due to steric hindrance arising in the bilayer core. As ergosterol is conformationally and dynamically more restricted than cholesterol, it is likely to be more effective in inducing order and condensation in the bilayer. In contrast, lanosterol is the bulkiest of all three sterols, with three more methyl groups than cholesterol, which are attached to C_4 and C_{14} and protrude from its otherwise flat α-surface. These three extra methyl groups are likely to disrupt close packing of lanosterol and DPPC, resulting in less effective condensation.

To test the above assumptions and to shed light on the intermolecular interactions that might govern the observed differences, in the following sections we have calcu-

lated the sterol tilt angles, van der Waals interaction energies and pair radial distribution functions of different groups in the sterol/DPPC systems.

5.2.5 STEROL TILT ANGLE

The distributions of the tilt angles of sterols in the bilayer with respect to the bilayer normal are shown in Figure 5.10.

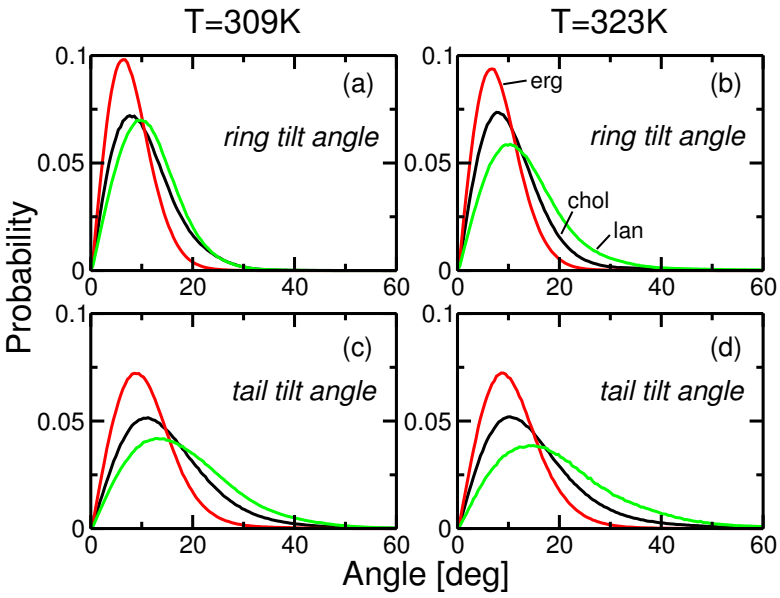

Figure 5.10: Tilt angle distributions between the bilayer normal and the vector connecting carbon atoms C_3 and C_{17} in the sterol ring system for (a) T=309K and (b) T=323K. Tilt angle between the bilayer normal and the vector connecting carbon atoms C_{17} and C_{25} for (c) T=309K and (d) T=323K. Cholesterol: black, ergosterol: red, and lanosterol: green.

The ring tilt angle is defined here as the angle between the bilayer normal and the vector connecting carbon atoms C_3 and C_{17} in the sterol ring system. Correspondingly, the tail tilt angle is defined as the angle between the bilayer normal and the vector connecting carbon atoms C_{17} and C_{25} (0° is parallel to the membrane normal).[19]

The mean values obtained for T=323K are 10.5°, 8.2° and 13.6° for the ring and 15.0°, 10.9° and 19.9° for the sterol tail, for cholesterol, ergosterol and lanosterol, respectively. Thus, for both the ring and tail tilt angles, cholesterol lies on average between ergosterol and lanosterol, with ergosterol the most closely aligned with the membrane normal and lanosterol the least. With the increase of temperature the tilt probabilities do not change significantly.

As ergosterol has an extra double bond in its steroid ring and a double bond in

the middle of the sterol tail (between C_{22} and C_{23}) it is stiffer than the other two sterols. This inherent stiffness causes the ergosterol molecule to be more aligned to the membrane normal than the other two sterols. The extra methyl in the alkyl ergosterol tail does not significantly impair its ability to align with the DPPC hydrocarbon tails.

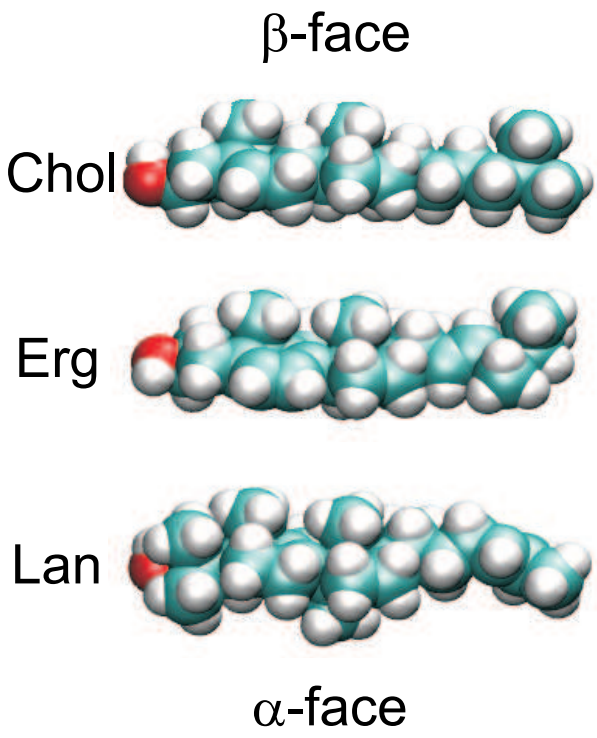

Figure 5.11: A space filling representation of cholesterol, ergosterol and lanosterol.

Although the lanosterol tail also contains a double bond, it is clearly the least aligned with the membrane normal. As this double bond is located towards the end of the sterol tail, and not in the middle as in the case of ergosterol, it has a smaller stiffening effect. Interestingly, the lanosterol tail is even more tilted than the saturated cholesterol tail. One possible explanation for this behavior is that lanosterol does not fit as well as ergosterol or cholesterol into the lipid bilayer (consistent with the observation that lanosterol induces the largest volume and the smallest order in the DPPC molecules). The poor fit of lanosterol is due to the rough α-face of the molecule (lanosterol has three methyls more protruding from the α-face than the other two sterols), which is evident in a schematic space-filling representation of the molecule (see Figure 5.11).

The width of lanosterol's tilt angle distributions imply that it is more dynamic than the other sterols. As shown previously in the text ('Area per lipid' section), lanosterol

creates the least-densely packed membrane. Furthermore, it is located, on average, closer to the bilayer center than do the other two sterols. Since the bilayer center is the least densely packed region of the bilayer (see electron density profile Fig. 5.7) more space is available there. The pronounced increase of rotational disorder (*i.e. gauche* rotational isomers) in lanosterol is energetically slightly unfavorable, but is favored on entropic grounds as a result of the available space in the bilayer midplane and in the loosely-packed lanosterol-DPPC membrane.

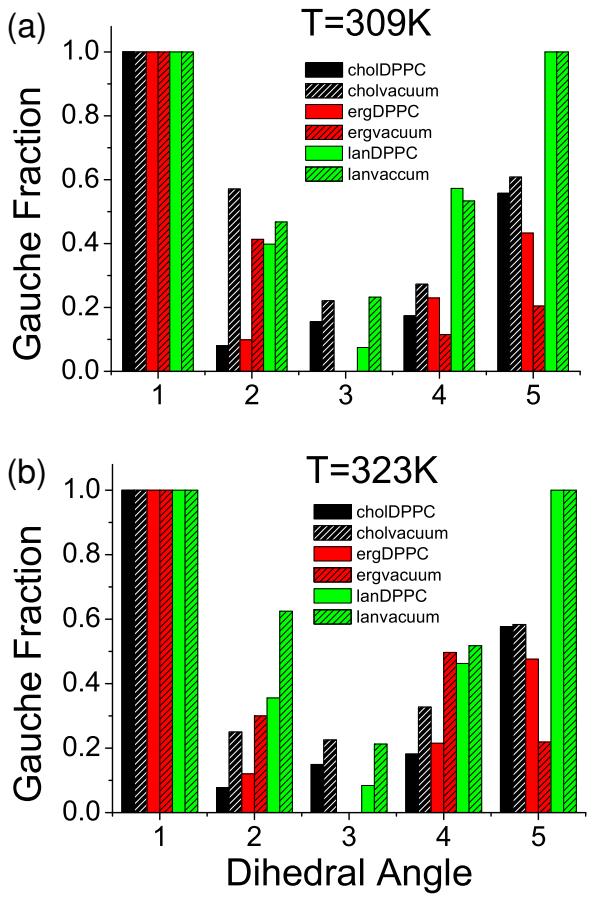

Figure 5.12: Positional dependence of *gauche* bond fraction in the sterol alkyl tail for (a) T=309K and (b) T=323K. cholesterol-DPPC: black, cholesterol in vacuum shaded black, ergosterol-DPPC: red, ergosterol in vacuum: shaded red, lanosterol-DPPC: green, lanosterol in vacuum: shaded green. The dihedral angles (**1-5**) are the sequential dihedral angles of the sterol tail: **1**:$C_{16}-C_{17}-C_{20}-C_{22}$, **2**:$C_{17}-C_{20}-C_{22}-C_{23}$, **3**:$C_{20}-C_{22}-C_{23}-C_{24}$, **4**:$C_{22}-C_{23}-C_{24}-C_{25}$, **5**:$C_{23}-C_{24}-C_{25}-C_{26}$ (see also Figure 5.1).

The angle distributions are such that, the more aligned a sterol is with the z-axis, the more order it induces in the DPPC acyl chains. Thus, ergosterol, which is more closely aligned with the membrane normal than the other sterols, induces more order in the hydrocarbon chains (as was also postulated in Ref. 19), as seen in Fig. 5.4.

Torsion Angle	DPPC:Chol		DPPC:Erg		DPPC:Lan	
	309K	323K	309K	323K	309K	323K
C_4-C_5-C_{10}-C_1	-45.9±5.5	-45.9±5.6	-44.8±5.4	-44.7±5.5	-47.3±4.8	-47.3±4.9
C_7-C_8-C_9-C_{10}	59.6±4.8	59.5±4.9	36.2±5.8	36.1±5.7	5.4±4.0	5.4±4.1
C_{17}-C_{13}-C_{14}-C_{15}	41.1±4.0	41.3±4.1	44.0±3.8	44.1±3.9	44.4±3.4	44.3±3.5
C_{10}-C_5-C_6-C_7	-2.1±3.7	-2.1±3.8	-10.3±5.9	-10.3±6.0	-56.2±6.5	-56.2±6.6
C_5-C_6-C_7-C_8	13.4±6.2	13.4±6.4	-0.5±5.0	-0.5±5.2	27.7±9.2	27.7±9.5
C_6-C_7-C_8-C_9	-41.2±6.7	-41.1±6.9	-13.5±5.4	-13.4±5.5	-2.4±8.0	-2.4±8.2
C_8-C_{14}-C_{13}-C_{12}		-60.2±4.5		-59.7±4.5		-61.8±3.8
C_{14}-C_{15}-C_{16}-C_{17}		5.4±7.4		8.5±7.1		12.0±6.5
C_{15}-C_{16}-C_{17}-C_{13}		20.0±7.1		18.1±7.1		15.3±6.3

Table 5.2: Selected torsional angles (in degrees) from the steroid rings, averaged over all sterol molecules.

In Figure 5.12 the *gauche* fractions of the sterol tail dihedral angles in the DPPC membrane are plotted. The angles calculated are **1**:$C_{16}-C_{17}-C_{20}-C_{22}$, **2**:$C_{17}-C_{20}-C_{22}-C_{23}$, **3**:$C_{20}-C_{22}-C_{23}-C_{24}$, **4**:$C_{22}-C_{23}-C_{24}-C_{25}$, **5**:$C_{23}-C_{24}-C_{25}-C_{26}$ (see Fig. 5.1). To investigate any conformational restrictions arising from the lipid environment on the sterol tail dihedral angles, we also performed a vacuum simulation of the three sterols at T=309K and T=323K.

For all three sterols the tail dihedral **1** is always *gauche*, due to the steric interaction of the C_{21} methyl and the C_{18} methyl, which hinders the rotation around this dihedral both in the membrane and in vacuum. In the membrane environment tail dihedrals **2** and **4** of cholesterol and ergosterol are constrained to be mostly in the *trans* conformation. In contrast, lanosterol has more freedom of movement in the tail and exhibits the *gauche* and *trans* conformations with almost equal probabilities for angles **2** and **4**. The membrane environment restricts the rotation around dihedrals **2** and **4** relative to vacuum. For these angles the sterols exhibit a significantly higher number of *gauche* defects in the vacuum simulation. Rotation around tail dihedral angle **3** is prohibited in the case of ergosterol due to the presence of the double bond. Although cholesterol and lanosterol have more freedom of movement, both show a preference for the *trans* conformation for dihedral **3**, both in the membrane and vacuum environments. The terminal lanosterol dihedral angle is restricted to the *trans* conformation due to its terminal double bond.

The above results indicate that the difference in the location of the double bond in the sterol ring system is important and results in conformational differences that affect the structural properties of the membrane.

Furthermore, the α-surface of lanosterol is less planar, which may weaken van der Waals interactions between lipid hydrocarbon chains and lanosterol.[44–46] To examine the rigidity of the steroid rings, the average values and standard deviations of some

	DPPC:Chol		DPPC:Erg		DPPC:Lan	
	1st shell	2nd shell	1st shell	2nd shell	1st shell	2nd shell
sterol hydroxyl H - O water[c]	1.5	2.9	1.4	2.7	1.3	2.5
sterol hydroxyl H - O_{22}	5.0	11.2	6.0	13.2	4.0	9.2
sterol hydroxyl H - O_{32}	4.1	15.9	2.7	14.7	4.3	13.9
sterol C_4 - DPPC C_{22}	11.1	16.7	11.0	17.6	7.5	14.8
sterol C_4 - DPPC C_{32}	10.0	16.0	11.8	17.7	10.0	16.6
sterol ring C - DPPC C_{24}:C_{210}	7.3	-	10.6	-	10.1	-
sterol ring C - DPPC C_{34}:C_{310}	6.2	-	10.1	-	8.9	-
sterol tail C - DPPC C_{216}	9.2	17.7	8.5	16.9	10.0	19.1
sterol tail C - DPPC C_{316}	9.3	18.8	9.4	17.9	9.5	19.4

Table 5.3: First and second average solvation shells for various groups in the simulation for T=323K. The first and second solvation shells were calculated by integrating the corresponding pair radial distribution function up to the first and second minima, respectively. H: Hydrogen atom, C: Carbon atom, O:Oxygen atom.

torsional angles of the steroid ring system were evaluated (see Table 5.2). Apart from the expected differences in torsional angles resulting from the difference in the position of the double bonds, no major differences between the three sterols are observed in the sterol ring. Temperature also has no effect.

5.2.6 MOLECULAR STRUCTURE OF THE STEROL:DPPC BILAYER

To further relate the differences in the chemical structure of the three sterols to their effects on the structure of the membrane, radial pair distribution functions, $g(r)$, for several types of interaction were calculated. The first and second solvation shell occupancies were calculated from the respective $g(r)$ functions by integrating up to the first and second minima, respectively (see Table 5.3).

5.2.7 HYDRATION OF THE STEROL HYDROXYL

Water in the polar lipid region hydrates the lipid head groups. The radial distribution functions for the sterol hydroxyl hydrogen to water oxygen are plotted in Fig. 5.13. The distributions for all three sterols exhibit a sharp first peak at 2 Å, corresponding to a first hydration shell around the hydroxyl group. The associated first hydration shell coordination numbers at T=309K are 1.6, 1.5 and 1.3 and at T=323K are 1.5, 1.4 and 1.3 for cholesterol, ergosterol and lanosterol, respectively. Thus, the fact that cholesterol and ergosterol are located closer to the lipid:water interface than lanosterol, means that they interact more often with water. Moreover, the two methyl groups attached to the C_4 of lanosterol make its hydroxyl region more hydrophobic (see also Fig. 5.11), which may also contribute to lanosterol being less hydrated.

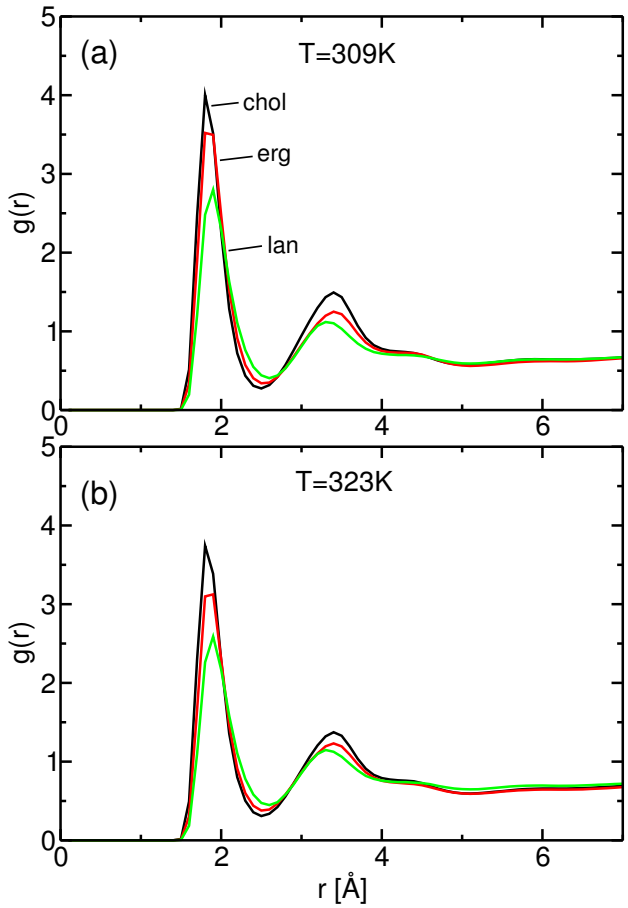

Figure 5.13: (a) Radial pair distribution functions of the sterol hydroxyl with water for (a) T=309K for cholesterol: black, ergosterol: red and lanosterol: green and (b) T=323K for cholesterol: black, ergosterol: red and lanosterol: green.

5.2.8 SOLVATION OF STEROLS BY DPPC MOLECULES IN THE BILAYER AT T=323K

The solvation of the sterol hydroxyl hydrogen by the carbonyl oxygen of both the $sn1$ and $sn2$ chains is shown in Figures 5.14a and b. It has been reported from previous MD simulations that cholesterol is hydrogen-bonded with the DPPC carbonyl atoms.[19, 42] Indeed, integration of up to the first minimum of the $g(r)$ shows that, here also, the sterol hydrogens are strongly solvated by the DPPC carbonyl oxygen. Cholesterol and ergosterol show a clear preference for the $sn2$ carbonyl over the $sn1$ carbonyl, again consistent with previous observations.[19, 42] Lanosterol, on the other hand, does not show such a preference. The reason for these differences is again that cholesterol and ergosterol are located more towards the bilayer:water interface, because the $sn2$ chain is closer to the bilayer:water interface than $sn1$, and therefore

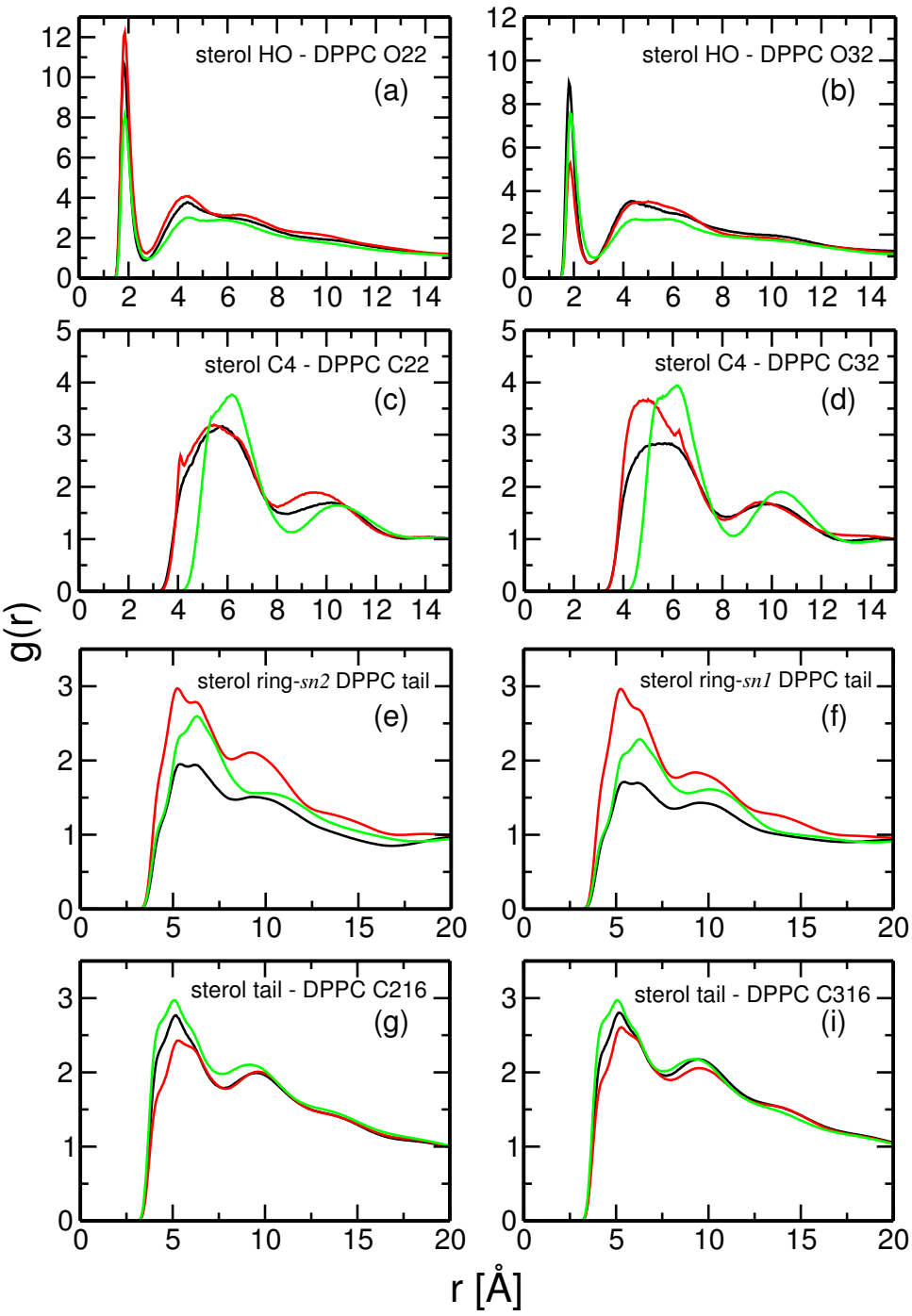

Figure 5.14: Radial pair distribution functions of (a) sterol hydroxyl hydrogen relative to $sn2$ DPPC carbonyl oxygen O_{22}, (b) sterol hydroxyl hydrogen relative to $sn1$ DPPC carbonyl oxygen O_{32}, (c) sterol C_4 relative to $sn2$ DPPC C_{22}, (d) sterol C_4 relative to $sn1$ DPPC C_{32}, (e) sterol ring carbon atoms $C_1 - C_{19}$ relative to $sn2$ DPPC carbon atoms $C_{24} - C_{210}$, (f) sterol ring carbon atoms $C_1 - C_{19}$ relative to $sn1$ DPPC carbon atoms $C_{34} - C_{210}$, (g) sterol side chain carbon atoms $C_{20} - C_{27}$ relative to $sn2$ DPPC terminal carbon atom C_{216}, (i) sterol side chain carbon atoms $C_{20} - C_{27}$ relative to $sn1$ DPPC terminal carbon atom C_{316}. Cholesterol: black, ergosterol: red, lanosterol: green.

these two sterols are preferentially solvated. That ergosterol is the most solvated sterol by the $sn2$ carbonyl and the least solvated by the $sn1$ carbonyl is again consistent with ergosterol being the closest to the water interface.

The atom packing around selected sterol ring atoms was also investigated. From the $g(r)$ functions plotted in Figure 5.14c it is clear that the C_4 of lanosterol interacts with the DPPC C_{22} or DPPC C_{32} carbons at a distance $\approx$ 1Å further away than the corresponding interaction of the other two sterols. This observation can be attributed to the 3 extra methyls of lanosterol *i.e.*, C_{28}, C_{29} and C_{30}, that protrude from its α-face and prevent closer interaction of the steroid nucleus with the DPPC chain.

The ergosterol steroid ring system ($C_1 - C_{19}$) is more highly solvated by both the $sn2$ and $sn1$ DPPC chains ($C_{24} - C_{210}$ and $C_{34} - C_{310}$), than the other two sterols (see Figures 5.14e and f). Due to the densely-packed membrane that ergosterol induces, the cavities inside the membrane are reduced. Therefore, it is expected that the ergosterol ring will have on average more DPPC-tail neighbours than the other two sterols.

Finally, the atom packing around the sterol tail was investigated. The $g(r)$ of the sterol side chain atoms $C_{20} - C_{27}$ with respect to the $sn2$ and $sn1$ DPPC terminal carbon atoms (C_{216} and C_{316}, respectively), are plotted in Figures 5.14g and i. There is no preference in the solvation of the sterol tails for the $sn1$ or the $sn2$ DPPC acyl chains. However, it is evident that the lanosterol side chain is surrounded on average more by the terminal DPPC carbons, with 10.0 C_{216} neighbours, as compared to 9.2 for cholesterol and 8.5 for ergosterol, again consistent with the fact that lanosterol is located more towards the bilayer midplane, as shown by the electron density profiles in Fig. 5.8.

5.2.9 INTERACTION ENERGIES

Van der Waals favourable interactions between the sterol and the phospholipid molecules could be one of the reasons for the sterol-condensing effect and the increase of the DPPC acyl chain order, as well as for the decrease in the DPPC diffusion as compared to the liquid phase.

In Figure 5.15, we plot the van der Waals contributions of the interaction energies for T=323K between the steroid ring and DPPC chains $sn1$ and $sn2$ (Fig. 5.15a,c) and between the sterol side chain and the DPPC chains (Fig. 5.15b,d). However, no significant differences are to be observed.

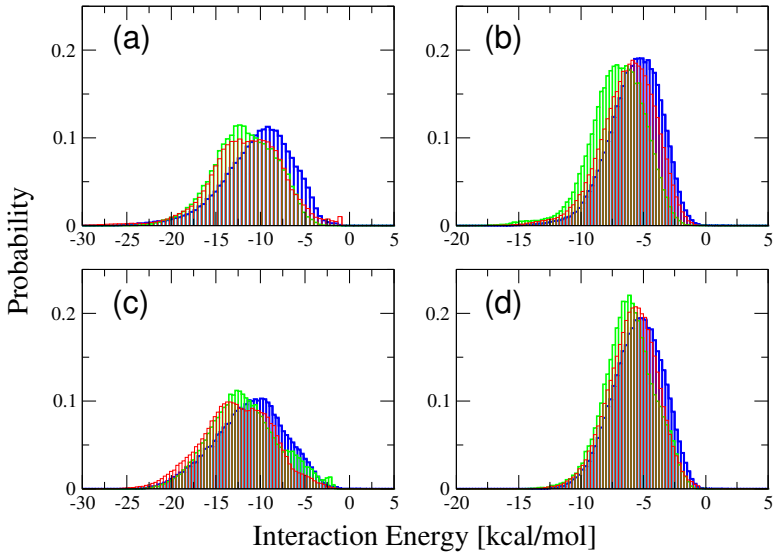

Figure 5.15: Distribution of interaction energies for T=323K and (a) sterol ring system and DPPC chain sn1, (b) sterol ring system and DPPC chain sn2, (c)sterol side chain and DPPC chain sn1, (b) sterol side chain and DPPC chain sn2. Cholesterol in black, ergosterol in red and lanosterol in green.

5.3 CONCLUSION

The results on sterol addition present a consistent picture of the effects of the sterols on the bilayer structure. At 323K the addition of any of the three sterols to the membrane orders the lipid chains relative to the pure-lipid liquid phase. The rigid sterol ring systems straighten the lipid chains, increase lipid order parameters and inhibit *trans-gauche* conformational transitions. In contrast, at T=309K the sterols disorder the gel DPPC phase and increase the *gauche* populations. The pure gel phase lipids are close to optimally packed, and intercalation of flat ring systems does not improve their packing. Consistent with the above picture, the area per lipid calculations indicate that the sterols condense the liquid bilayer and expand the gel system.

There is little difference in the physical properties of the sterol:lipid systems between 309K and 323K. Although the chemical differences between the sterols are relatively small, they lead to significant differences in membrane structure. The ordering and condensing effect of ergosterol is found to be the highest, with lanosterol the lowest, and cholesterol in between. Important differences in membrane properties are schematized in Fig. 5.16, in which the two extreme cases, ergosterol and lanosterol are sketched.

The three extra methyls of lanosterol (C_{28},C_{29},C_{30}) with respect to the other two sterols, protrude from its otherwise flat α-face and roughen its surface. In contrast, ergosterol has a smooth α-face (as does cholesterol), one double bond more than lanos-

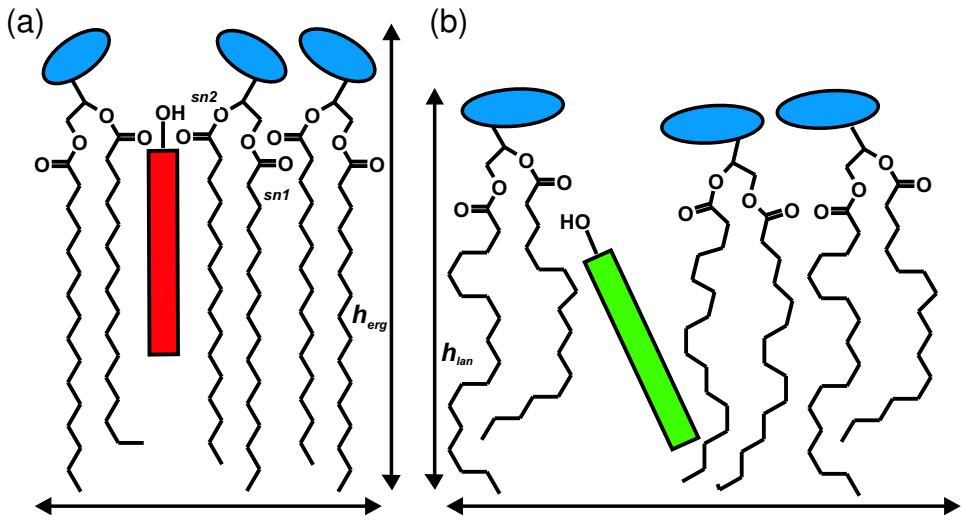

Figure 5.16: Schematic diagram depicting the following qualitative effects of (a) ergosterol and (b) lanosterol on the DPPC membrane. For the ergosterol system the chains are condensed (smaller area per lipid), straighter (more *trans*), and the membrane thicker. Ergosterol is closer to the headgroup region, interacts more closely with the *sn2* carbonyl than with the *sn1*, and is more closely aligned with the membrane normal. The behavior of cholesterol is intermediate between ergosterol and lanosterol.

terol and two more than cholesterol.

The result of the smoothness of ergosterol is that the ring packs closer to the lipid chains. This closer packing is seen in the relevant radial distribution functions (Fig. 5.14 c-f) but does not translate into more favourable interaction energies: for all three sterols the lipid:sterol interaction energies are strongly negative (Fig. 5.15). In contrast to ergosterol, the absence of a smooth α-face holds lanosterol's steroid ring system further from the DPPC acyl chains than the other two sterols.

One result of the closer packing of the lipid chains against the ergosterol ring is that the lipid chains become ordered, as reflected in increased order parameters (Fig. 5.5). This order is also reflected in the percentage of the acyl chain dihedral angles in the *gauche* conformation, which again follows the order ergosterol $<$ cholesterol $<$ lanosterol, as does the area per lipid. Thus, for ergosterol, the packing of the phospholipids is enhanced by reducing cavity volumes between the molecules. A consequence of the ordering is a thickening of the membrane (increased headgroup:headgroup distance). In contrast, the bulkiest sterol (lanosterol) induces the least effective packing among the three sterols and the weakest ordering effect on the chains.

The two additional methyl groups at carbon C_4 of lanosterol are very close to the hydroxyl group that is responsible for the amphipathic character of sterols. Their pres-

ence may weaken the ability of lanosterol to form hydrogen bonds to phospholipids, and may play a role in another property seen here, namely that the distance from the bilayer center follows the order ergosterol > cholesterol > lanosterol. Thus, lanosterol is located, on average, the closest to the bilayer center and ergosterol the closest to the bilayer:water interface. Among the consequences of this is the observation that, although all three sterols do have a hydration shell around their hydroxyl groups (and at T=309K cholesterol is almost as hydrated as ergosterol), lanosterol is the least hydrated. The relative distance from the bilayer center also explains the closer interaction of the ergosterol and cholesterol hydroxyl groups with the $sn2$ carbonyl group, than with that of $sn1$ and that this preference is not seen for lanosterol.

The center of a lipid bilayer is relatively disordered and less well packed. Thus, the observation that lanosterol is positioned closer to the center, together with the disordering effect of the rough α-face, mean that the lanosterol molecule has more room to move than the other two sterols, and consequently has a broader distribution of tilt angles relative to the membrane normal, with a significantly higher average tilt angle, which follows the order lanosterol > cholesterol > ergosterol.

BIBLIOGRAPHY

[1] BROOKS, B. R., BRUCCOLERI, R., OLAFSON, B. D., STATES, D. J., SWAMINATHAN, S., AND KARPLUS, M. CHARMM: A Program for Macromolecular Energy, Minimization and Dynamics Calculations. *J. Comp. Chem.*, 1983, **4**, 187–217.

[2] COURNIA, Z., SMITH, J. C., AND ULLMANN, G. M. A molecular mechanics force-field for biologically important sterols. *J. Comp. Chem.*, 2005, **26**, 1383–1399.

[3] DARDEN, T., YORK, D., AND PEDERSEN, L. Particle mesh Ewald: An N.log(N) method for Ewald sums in large systems. *J. Chem. Phys.*, 1993, **98**, 10089–10092.

[4] ANÉZO, C., DE VRIES, A. H., HÖLTJE, H.-D., TIELEMAN, D. P., AND MARRINK, S. J. Methodological issues in lipid bilayer simulations. *J. Chem. Phys.B*, 2003, **107**, 9424–9433.

[5] HOOVER, W. G. Canonical dynamics: Equilibrium phase-space distributions. *Phys. Rev. A*, 1985, **31**, 1695–1697.

[6] FELLER, S. E., ZHANG, Y., PASTOR, R. W., AND BROOKS, B. R. Constant pressure molecular dynamics simulation: The Langevin piston method. *J. Chem. Phys.*, 1995, **103**, 4613–4621.

[7] SHIEH, H. S., HOARD, L. G., AND NORDMAN, C. E. The structure of cholesterol. *Acta Cryst.*, 1981, **B37**, 1538–1543.

[8] LÉONARD, A., ESCRIVE, C., LAGUERRE, M., PEBAY-PEYROULA, E., NÉRI, W., POTT, T., KATSARAS, J., AND DUFOURC, E. Location of cholesterol in DMPC Membranes. A comparative study by neutron diffraction and molecular mechanics simulation. *Langmuir*, 2001, **17**, 2019–2030.

[9] ACCELRYS. Insight II. *San Diego, CA*, 2000.

[10] JORGENSEN, W. L., CHANDRASEKHAR, J., MADURA, J. D., IMPEY, R. W., AND KLEIN, M. L. Comparison of simple potential functions for simulating liquid water. *J. Chem. Phys.*, 1983, **79**, 926.

[11] SMONDYREV, A. M., AND BERKOWITZ, M. L. Structure of DPPC/Cholesterol bilayer at low and high cholesterol concentrations: molecular dynamics simulation. *Biophys. J.*, 1999, **77**, 2075–2089.

[12] HOFSÄSS, C., LINDAHL, E., AND EDHOLM, O. Molecular dynamics simulations of phospholipid bilayers with cholesterol. *Biophys. J.*, 2003, **84**, 2192–2206.

[13] PITMAN, M. C., SUITS, F., A. D. MACKERELL, J., AND FELLER, S. E. Molecular-Level Organization of Saturated and Polyunsaturated Fatty Acids in a Phosphatidylcholine Bilayer Containing Cholesterol. *Biochemistry*, 2004, **43**, 15318–15328.

[14] ROG, T., AND PASENKIEWICZ-GIERULA, M. Cholesterol effects on the phospatidylcholine bilayer nonpolar region: a molecular simulation study. *Biophys. J.*, 2001, **81**, 2190–2202.

[15] SANKARARAMAKRISHNAN, R., AND WEINSTEIN, H. Surface tension parameterization in molecular dynamics simulations of a phospholipid-bilayer membrane: calibration and effects. *J. Chem. Phys.B*, 2004, **108**, 11802–11811.

[16] NAGLE, J. F., AND TRISTRAM-NAGLE, S. Structure of lipid bilayers. *Biochim. Biophys. Acta*, 2000, **1469**, 159–195.

[17] DOULIEZ, J.-P., LÉONARD, A., AND DUFOURC, E.-J. Restatement of order parameters in biomembranes: calculation of C-C bond order parameters from C-D quadrupolar splittings. *Biophys. J.*, 1995, **68**, 1727–1739.

[18] DUFOURC, E. J., PARISH, E. J., CHITRAKORN, S., AND SMITH, I. C. P. On the relationship between C-C and C-D order parameters and its use for studying the conformation of lipid acyl chains in biomembranes. *Biochemistry*, 1984, **23**, 6062–6071.

[19] CZUB, J., AND M.BAGINSKI. Comparative molecular dynamics study of lipid membranes containing cholesterol and ergosterol. *Biophys. J.*, 2006, **90**, 2368–2382.

[20] ANDERSON, T. G., AND MCCONNELL, H. M. Condensed complexes and the calorimetry of cholesterol-phospholipid bilayers. *Biophys. J.*, 2001, **81**, 2774–2785.

[21] URBINA, J. A., PEKERAR, S., LE, H., PATTERSON, J., MONTEZ, B., AND OLDFIELD, E. Molecular order and dynamics of phosphatidylcholine bilayer membranes in the presence of cholesterol, ergosterol and lanosterol: a comparative study using ^{2}H-, ^{13}C- and 31P-NMR spectroscopy. *Biochim. Biophys. Acta*, 1995, **1238**, 163.

[22] SANKARAM, M. B., AND THOMPSON, T. E. Modulation of phospholipid acyl chain order by cholesterol. A solid state ^{2}H nuclear magnetic resonance study. *Biochemistry*, 1990, **29**, 10676–10684.

[23] HUSTER, D., SCHEIDT, H. A., ARNOLD, K., HERMANN, A., AND MUELLER, P. Desmosterol may replace cholesterol in lipid membranes. *Biophys. J.*, 2005, **88**, 1838–1844.

[24] HSUEH, Y.-W., GILBERT, K., TRANDUM, C., ZUCKERMANN, M., AND THEWALT, J. The effect of ergosterol on dipalmitoylphosphatidylcholine bilayers: A deuterium NMR and calorimetric study. *Biophys. J.*, 2005, **88**, 1799–1808.

[25] ENDRESS, E., BAYERL, S., PRECHTEL, K., MAIER, C., MERKEL, R., AND BAYERL, T. M. The effect of cholesterol, lanosterol, and ergosterol on lecithin bilayer mechanical properties at molecular and microscopic dimensions: A solid-state NMR and micropipet study. *Langmuir*, 2002, **18**, 3292–3299.

[26] HAUSER, H., PASCHER, I., PEARSON, R. H., AND SUNDELL, S. Preferred conformation and molecular packing of phosphatidylethanolamine and phospatidylcholine. *Biochim. Biophys. Acta*, 1981, **650**, 21–51.

[27] MENDELSOHN, R., AND SNYDER, R. G. *Infrared spectroscopic determination of conformational disorder and microphase separation in phospholipid acyl chains*. *In:* Biological Membranes: A Molecular Perspective from Computation and Experiment, Birkhäuser, Boston, 1996, pp. 145–174.

[28] CASAL, H. L., AND MCELHANEY, R. N. Quantitative determination of hydrocarbon chain conformational order in bilayers of saturated phosphatidylcholines of various chain lengths by Fourier transform infrared spectroscopy. *Biochemistry*, 1990, **29**, 5423–5427.

[29] MENDELSOHN, R., DAVIES, M. A., SCHUSTER, H. F., XU, Z., AND R.BITTMAN. CD2 rocking modes as quantitative infrared probes of one-, two-, and three-bond conformational disorder in dipalmitoylphosphatidylcholine and dipalmitoylphosphatidylcholine/cholesterol mixtures. *Biochemistry*, 1991, **30**, 8558–8563.

[30] SENAK, L., MOORE, D., AND MENDELSOHN, R. CH_2 wagging progressions as IR probes of slightly disordered phospholipid acyl chain states. *J. Chem. Phys.*, 1992, **96**, 2749–2754.

[31] HENRIKSEN, J., ROWAT, A. C., BRIEF, E., HSUEH, Y. W., THEWALT, J. L., ZUCKERMANN, M. J., AND IPSEN, J. H. Universal behavior of membranes with sterols. *Biophys. J.*, 2006, **90**, 1639–1649.

[32] PENCER, J., NIEH, M.-P., HARROUN, T. A., KRUEGER, S., ADAMS, C., AND KATSARAS, J. Bilayer thickness and thermal response of dimyristoylphospatidylcholine unilamellar vesicles containing cholesterol, ergosterol and lanosterol: A small-angle neutron scattering study. *Biochim. Biophys. Acta*, 2005, **1720**, 84–91.

[33] VIST, M. R., AND DAVIS, J. H. Phase equilibria of cholesterol/dipalmitoylphosphatidylcholine mixtures: ^{2}H nuclear magnetic resonance and differential scanning calorimetry. *Biochemistry*, 1990, **29**, 451–464.

[34] MIAO, L., NIELSEN, M., THEWALT, J., IPSEN, J., BLOOM, M., ZUCKERMANN, M. J., AND MOURITSEN, O. G. From lanosterol to cholesterol: structural evolution and differential effects on lipid bilayers. *Biophys. J.*, 2002, **82**, 1429–1444.

[35] IPSEN, J. H., MOURITSEN, O. G., AND BLOOM, M. Relationships between lipid membrane area, hydrophobic thickness, and acyl-chain orientational order. *Biophys. J.*, 1990, **57**, 405–412.

[36] CLARKE, J. A., HERON, A. J., SEDDON, J. M., AND LAW, R. V. The diversity of the liquid ordered phase (L_o) phase of phosphatidylcholine/cholesterol membranes: a variable temperature multinuclear solid-state NMR and X-Ray diffraction study. *Biophys. J.*, 2006, **90**, 2383–2393.

[37] CHIU, S. W., JACOBSSON, E., MASHL, R. J., AND SCOTT, H. L. Cholesterol-Induced Modifications in lipid bilayers:A Simulation Study. *Biophys. J.*, 2002, **83**, 1842–1853.

[38] PANDIT, S. A., VASUDEVAN, S., CHIU, S. W., MASHL, R. J., JACOBSSON, E., AND SCOTT, H. L. Sphingomyelin-Cholesterol Domains in Pholipid Membranes: Atomistic Simulation. *Biophys. J.*, 2004, **87**, 1092–1100.

[39] SHIEH, H. S., HOARD, L. G., AND NORDMAN, C. E. Crystal structure of anhydrous cholesterol. *Nature*, 1977, **267**, 287–289.

[40] CRAVEN, B. M. Pseudosymmetry in Cholesterol Monohydrate. *Acta Cryst.*, 1979, **B35**, 1123–1128.

[41] HSU, H.-Y., KAMPF, J. W., AND NORDMAN, C. E. Structure and Pseudosymmetry of Cholesterol at 310K. *Acta Cryst.*, 2002, **B58**, 260–264.

[42] PANDIT, S. A., BOSTICK, D., AND BERKOWITZ, M. L. Complexation of Phosphatidylcholine Lipids with Cholesterol. *Biophys. J.*, 2004, **86**, 1345–1356.

[43] NAGLE, J. F., ZHANG, R., TRISTRAM-NAGLE, S., SUN, W., PETRACHE, H. I., AND SUTER, R. M. X-ray structure determination of fully hydrated L alpha phase dipalmitoylphosphatidylcholine bilayers. *Biophys. J.*, 1996, **70**, 1419–1431.

[44] XU, X., AND LONDON, E. The effect of sterol structure on membrane lipid domains reveals how cholesterol can induce lipid domain formation. *Biochemistry*, 2000, **39**, 843–849.

[45] CHILD, P., AND KUKSIS, A. Critical role of ring structure in the differential uptake of cholesterol and plant sterols by membrane preparations in vitro. *J. Lipid Res.*, 1983, **24**, 1196–1209.

[46] WANG, J., MEGHA, K., AND LONDON, E. Relationship between sterol/steroid structure and participation in ordered lipid domains (lipid rafts): implications for lipid raft structure and function. *Biochemistry*, 2004, **43**, 1010–1018.

CHAPTER 6

INVESTIGATION OF STEROL DYNAMICS BY MD SIMULATIONS AND NEUTRON SCATTERING CALCULATIONS

Our understanding of membrane molecular dynamics has improved in recent years, both from the experimental as well as the theoretical viewpoint. New experiments have contributed to this, as well as the enormous improvement in the description of membranes using simulation methods. In the experimental field, spectroscopic methods (NMR, QENS, IR, fluorescence), micromechanical (micropipettes) and optical techniques (videomicroscopy) have provided new insights. In the field of high-frequency dynamics quasielastic neutron scattering (QENS) in the THz regime has been able to demonstrate the existence of collective membrane motions and dominant motional contributions were described in this timescale.[1] NMR relaxation measurements have elucidated small rotational motions of membrane components to be elucidated.[2, 3] Most theoretical studies have up to now concentrated on studying in detail structural features of membranes (as reviewed in Chapter 5) leaving their dynamics unexamined. However, recently, there has been a growing interest in studying the dynamical properties of membranes (such as lipid center-of-mass diffusion, rotational dynamics, chain and headgroup conformational changes, as well as membrane protein dynamics) and relating those to membrane function.[4–8]

In this chapter, sterol diffusion in the direction parallel and perpendicular to the membrane plane is analyzed and discussed up to a 4ns time scale. The sterol effect on the diffusion of DPPC is also discussed. A comparison of our MD results with experimental QENS results that probe motions on the same time scale is also presented.

6.1 OVERVIEW OF DYNAMIC PROCESSES IN MEMBRANES

As in most biomolecular assemblies, functionally relevant motions in membranes span a wide range of length and time scales.[9] Motions that have been detected experimentally include isomerisation of the hydrocarbon chains (10-100 ps), single lipid protrusions (10 ps to 1 ns), reorientation of the headgroups (1 ns), rotations of the lipid molecules about their long axes (10 ns), collective bilayer undulations (>10 ns), and local as well as long range diffusion in the plane of the bilayer (10 ps to 1 s). For a schematic representation of some of the dynamic processes occurring in the lipids see Figure 6.1.

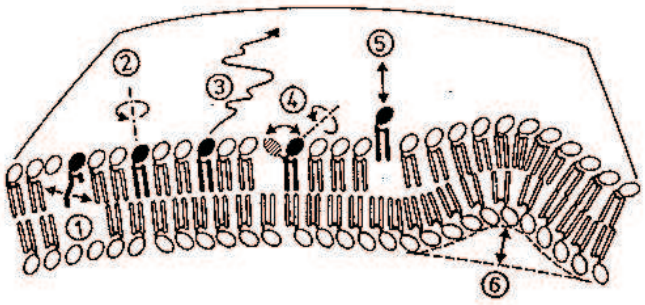

Figure 6.1: Schematic view of the most pertinent motional processes in lipid bilayers: (1) chain excitations (10^{-11}-10^{-11}s) (2) rotational diffusion (10^{-8}s) (3) local and long-range translational diffusion (10^{-11}-10^{0}s) (4) headgroup conformational dynamics (10^{-9}s) (5) single lipid protrusion (10^{-11}-10^{-9}s) (6) collective undulations ($>10^{-8}$s)

Some of these motions are presently accessible to MD simulations. However, detailed analyses of dynamics in membrane simulations have been relatively scarce compared to the structural analyses.[5, 7, 10–13]

6.2 DIFFUSION OF STEROLS IN THE MEMBRANE

The diffusion of cholesterol in membranes has been extensively studied with NMR spectroscopy[14–17] and MD simulations,[4, 18] with diffusion coefficients for cholesterol ranging between 5-30$\times 10^{-8}$ cm^2/s.[19] Diffusion measurements on ergosterol and lanosterol are very limited in the literature.[20–22]

The self-diffusion coefficient of a molecule can be calculated in the MD simulation from the mean square displacement (MSD) evolution in time. The MSD is defined as:

$$MSD(t) = \left\langle \Delta \mathbf{r}_i(t)^2 \right\rangle = \frac{1}{N_i} \sum_{i}^{N_i} \frac{1}{N_t} \sum_{t}^{N_t} (\mathbf{r}_i(t) - \mathbf{r}_i(0))^2. \tag{6.1}$$

In this equation, $\mathbf{r}_i(t) - \mathbf{r}_i(0)$ is the distance traveled by a molecule i over some time interval of length t. The squared magnitude of this vector is averaged over the molecules, N_i, in a system and also over all the possible time intervals, N_t, in the trajectory.

The mean square displacement can be decomposed in lateral ($x - y$ plane) and transversal (z-axis) components:

$$MSD_{lat}(t) = \frac{1}{N_i} \sum_{i}^{N_i} \frac{1}{N_t} \sum_{t}^{N_t} \left[(\mathbf{r}_{x_i}(t) - \mathbf{r}_{x_i}(0))^2 + (\mathbf{r}_{y_i}(t) - \mathbf{r}_{y_i}(0))^2 \right] \tag{6.2}$$

$$MSD_{tr}(t) = \frac{1}{N_i} \sum_{i}^{N_i} \frac{1}{N_t} \sum_{t}^{N_t} (\mathbf{r}_{z_i}(t) - \mathbf{r}_{z_i}(0))^2. \tag{6.3}$$

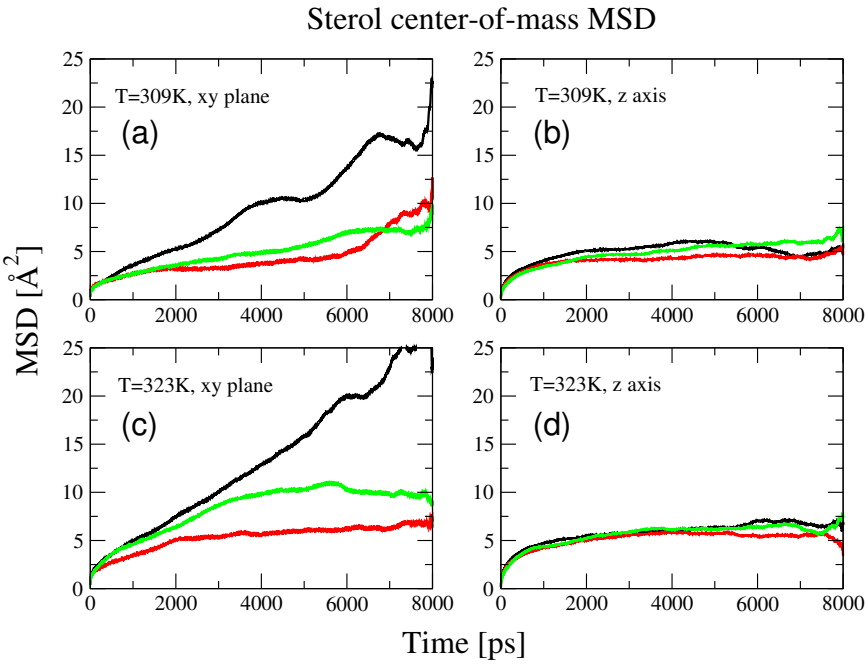

Figure 6.2: Mean square displacement curves for sterol center of mass, for (a) T=309K and xy plane, (b) T=309K and z plane (c) T=323K and xy plane and (d) T=323K and z plane. Cholesterol: black, ergosterol: red, lanosterol: green.

The limiting slope of $MSD(t)$, considered for time intervals sufficiently long for it to be in the linear regime, is related to the self-diffusion coefficient constant D:

$$2dD = \lim_{t \to \infty} \left\langle \Delta \mathbf{r}_i(t)^2 \right\rangle \tag{6.4}$$

where d is the dimensionality of the system.

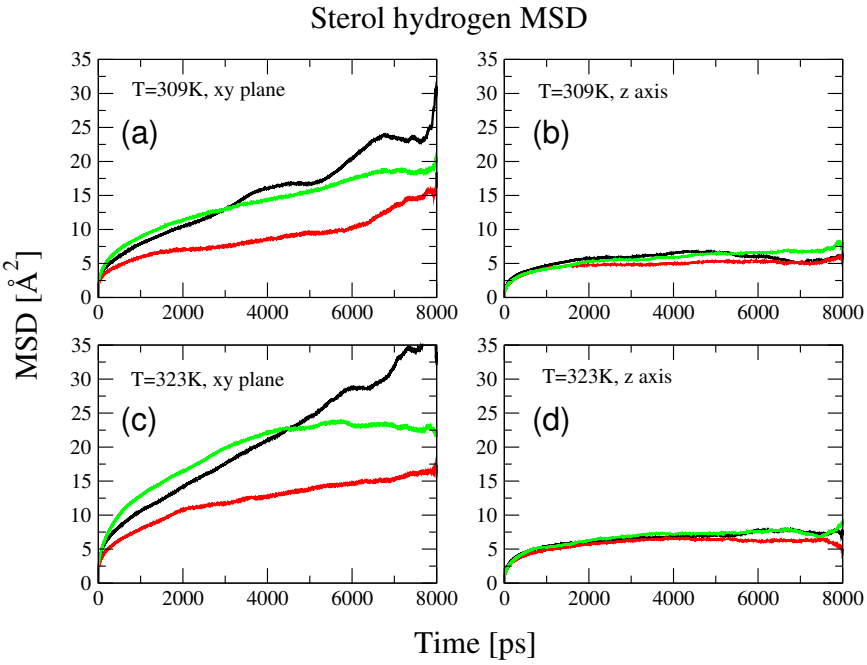

Figure 6.3: Mean square displacement curves for sterol hydrogens, for (a) T=309K and xy plane, (b) T=309K and z plane (c) T=323K and xy plane and (d) T=323K and z plane. Cholesterol: black, ergosterol: red, lanosterol: green.

In Figures 6.2 and 6.3 the mean-square displacements along the bilayer normal, $\langle \mathbf{r}_{tr}^2 \rangle$, and in the plane of membrane, $\langle \mathbf{r}_{lat}^2 \rangle$, are shown for the three different sterols in the DPPC membrane. Figure 6.2 shows the time evolution of the center-of-mass (COM) MSD for each sterol and Figure 6.3 the sterol hydrogens MSD. The MSD of DPPC in a sterol-containing membrane as well as in the pure DPPC systems was also measured (Fig. 6.4).

Here, to estimate D in the limit of large t, the slope of the MSD curve was calculated by fitting the linear regime between 1-4 ns. d was taken to be 2 when studying the diffusion in the plane of the membrane and 1 in the z-axis. The non-linear regime, which appears after 4ns, is due to poor statistics for long time intervals because of the limited simulation time. The standard deviation, σ is:

$$\sigma = \sqrt{\frac{1}{N_i}\sum_{i}^{N_i}\frac{1}{N_t}\sum_{t}^{N_t}(\mathbf{r}_i(t) - \langle \mathbf{r}_i(t) \rangle)}, \tag{6.5}$$

where N_i is the number of the molecules in the system and N_t is the number of the possible time intervals in the trajectory. Therefore, beyond 4ns the statistical errors become significant and this part is not taken into account into the diffusion coefficient calculation. The diffusion coefficients calculated from the MD simulation for each of the simulated systems are reported in Tables 6.1 and 6.2.

x(10^{-8}) cm^2/s	T [K]	MD Hydr. D_{lat}	MD Hydr. D_{tr}	MD COM D_{lat}	MD COM D_{tr}	$D_{lat}^{COM}/D_{tr}^{COM}$
chol	309	6.8*	2.3*	5.6	2.3	2.4
	323	8.8	2.1	6.8	2.1	3.2
erg	309	1.8	0.8	0.6	0.6	1
	323	3.5	2.7	1.6	2.5	0.6
lan	309	4.3	2.4	1.8	2.3	0.8
	323	7.8	3.5	4.8	3.2	1.5

Table 6.1: Diffusion coefficients for sterols from the MD simulation, see also Figs. 6.2 and 6.3. * For T=309K and the cholesterol:DPPC membrane, the diffusion coefficients have been calculated also from the neutron scattering calculations: D_{lat}=6.9 and D_{tr}=1.4 (see later in text).

x(10^{-8}) cm^2/s	T [K]	CHARMM D_{lat}	CHARMM D_{tr}
DPPC/chol	309	6.8	2.2
	323	6.3	1.7
DPPC/erg	309	1.0	0.7
	323	2.3	1.8
DPPC/lan	309	2.3	1.2
	323	4.4	1.6
DPPC	309	0.9	0.6
	323	15.6	4.1

Table 6.2: Diffusion coefficients for DPPC in the various simulation systems. (See Fig. 6.4.)

The most striking feature of the MSD results is that ergosterol diffuses the slowest in the lateral direction (see Table 6.1 and Fig. 6.2). The diffusion constant for ergosterol is by a factor of 4 smaller in comparison to cholesterol for 323K. Moreover, DPPC diffuses the slowest in an ergosterol-containing membrane (see Table 6.2 and Fig. 6.4). As discussed in Chapter 5, ergosterol results in the most condensed, stiffest and most ordered membrane. This condensation reflects not only in ergosterol inhibiting the DPPC chain conformational freedom (as shown in Section 5.2.2), but also ergosterol inhibits its long-range diffusion and thus the overall fluidity of the membrane. Cholesterol, on the other hand, has the fastest diffusion among the three sterols studied for both temperatures.

Another observation is the fact that cholesterol has a strong anisotropic center-of-mass motion favoring the lateral motion. The ratio D_{lat}/D_{tr} for cholesterol at 323K is 3.2, while 1.5 for lanosterol and 0.6 for ergosterol.

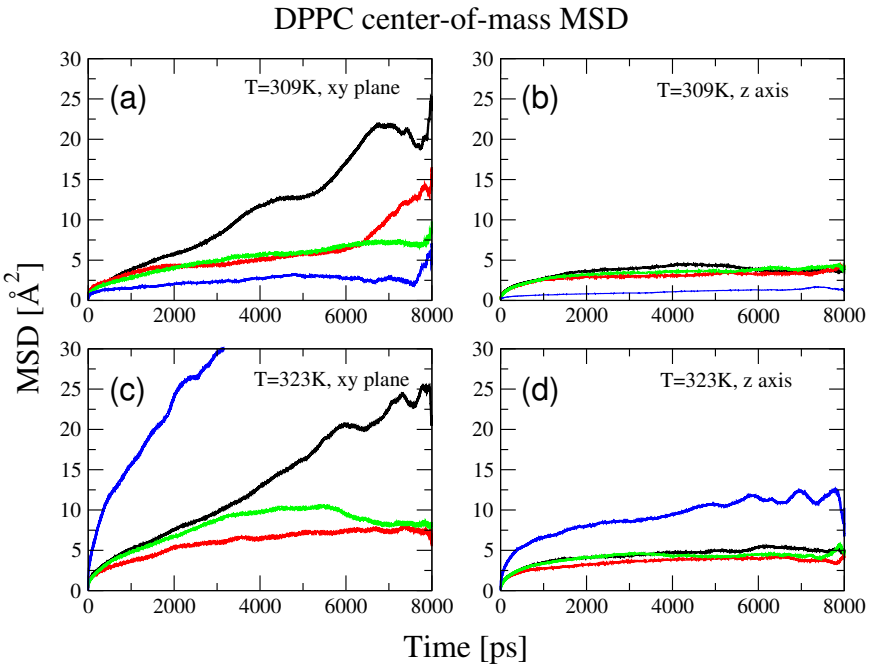

Figure 6.4: Mean square displacement curves for DPPC center of mass, for (a) T=309K and xy plane, (b) T=309K and z plane (c) T=323K and xy plane and (d) T=323K and z plane. Cholesterol: black, ergosterol: red, lanosterol: green, pure DPPC: blue.

The lateral and transverse diffusion coefficients of cholesterol (6.8 and 2.1 cm^2/s, respectively) and DPPC molecules (6.3 and 1.7 cm^2/s, respectively) are very similar. In the sterol-containing membranes, the fact that both components have the same diffusion coefficients indicates that most probably the translational diffusion is supported by some kind of a cooperative mechanism.

The diffusion of the phospholipid in the liquid phase is slowed down by a factor of 2 upon the addition of any sterol, as suggested by Ref. 14. In our simulation the self-diffusion constant decreases from a value of 15.6 cm^2/s for the pure DPPC to 6.3 cm^2/s in the cholesterol-containing membrane. On the other hand, addition of any sterol in a pure gel phospholipidic bilayer results in the increase of diffusion coefficient of DPPC. As described in Chapter 5, ergosterol optimizes the interactions with DPPC. This optimization leads to ergosterol and DPPC having very favorable interactions, which in turn, do not favor the free diffusion of the ergosterol:DPPC complex.

The lateral diffusion of cholesterol and DMPC was recently studied with pulsed field gradient NMR spectroscopy[14] and of cholesterol and lanosterol with NMR spectroscopy.[15] Ref. 14 shows that cholesterol and DMPC exhibit the same lateral diffusion coefficients (in the mixture) over 30-60°C, *i.e.*, in the liquid phase and that the addition of cholesterol to the phospholipid bilayer results in a decrease of the translational diffusion of the phospholipid. These results agree qualitatively very well with

x(10^{-8}) cm^2/s	T [K]	QENS[1] D_{lat}	QENS[1] D_{tr}	QENS[2] D_{lat}	QENS[2] D_{tr}
chol	309	17	5	24.6	13.5
	323	16	-	47.8	30.3
erg	309	-	-	9.5	3.5
	323	-	-	18.6	9.5
lan	309	-	-	30.5	17.9
	323	-	-	-	-

Table 6.3: Diffusion coefficients for sterols from quasielastic neutron scattering experiments (QENS[1] from Ref. 23 and QENS[2] from Ref. 19).

our simulation results.

The decrease of the lipid diffusion in the liquid phase upon addition of a sterol could be explained from the fact that the sterols have a condensing effect on the lipid packing. In a denser membrane, the conformational freedom of the lipid is restricted compared to that of the liquid phase.

6.3 QENS CALCULATIONS OF CHOLESTEROL-DPPC BILAYERS

The dynamics of cholesterol in the *lo* phase was also studied using quasi-elastic neutron scattering (QENS) at three different temperatures.[23] Furthermore, another QENS study comparing the different dynamics of cholesterol, ergosterol and lanosterol in a DPPC membrane was also performed.[19] The results showed a highly-anisotropic motion of cholesterol within the DPPC bilayer and suggested a higher-amplitude motion of cholesterol along the membrane normal than observed for ergosterol and lanosterol. The characteristic time scale of the QENS experiment, which is determined by the energy resolution of the instrument, lies in the ps-ns range, and is thus the timescale accessible to MD simulations. Therefore, MD is particularly useful for the interpretation of this QENS data.

Diffusion coefficients for sterol-containing membranes have also been measured by means of QENS experiments. In the neutron scattering experiment, to determine the dynamics of the sterols in the two relevant dimensions of the membrane (*i.e* parallel to the membrane normal (*z*-axis) and the membrane plane *x*-*y*), two orientations of the sample with respect to the neutron beam were used (see also Section 2.4.5.) At an orientation of 135° between the incident neutron beam and the plane of the sample, the momentum transfer is mainly directed parallel to the bilayer plane ($x - y$ plane).

In this case, the in-plane (lateral) motion of the sterol under study will dominate the incoherent scattering. On the other hand, at an orientation of 45° the momentum transfer is mainly parallel to the membrane normal, and thus the incoherent scattering is dominated by out-of plain motion of the sterol along the z-direction (membrane normal).[24, 25] Refs. 19, 23 due to an accidental exchange of notation concerning the neutron scattering vector triangle, the results reported for the in-plane motion were interpreted as results for the transverse direction and *vice versa*. Consequently, it suffices to exchange the reported directions in these two papers to obtain the correct results.

With quasielastic neutron scattering, one can gain information not only about the diffusional constants but also about the geometry of the sterol motions in the membrane. Up to the starting point of this project, sterol dynamics had been examined with QENS only for cholesterol, for which, interestingly, strong anisotropy[23] together with discrete rotation around its long axis[3] were found.

6.3.1 THE SAMPLING PROBLEM

In MD simulations one integrates the Newtonian equation of motion with a time step of 1 fs, which corresponds to the vibration of the carbon-hydrogen bond. It is therefore possible to store the atomic coordinates for all atoms every 1 fs. In practice, however, for long trajectories this is not possible due to the huge storage space that is required for such frequent saving of coordinates. Neutron scattering probes motions on timescales that are dictated by the resolution of the instrument. This means that for a resolution of 1μeV the timescales of the motions detected by the instrument will be faster or equal to 4ns. Therefore, the very fast motions also significantly contribute to the spectra measured. On these grounds, one needs to decide on the sampling interval of the trajectory, judging on what features of the spectra one needs to characterize. For example, if one wishes to study inelastic scattering (*i.e.* the vibrational part of the spectrum) with MD simulations, then the sampling of the trajectory has to be in time steps sufficiently small to allow for accurate description of these motions. Therefore, a compromise between the accuracy of the spectra and the sampling of the trajectory has to be made.

The quasielastic region of the neutron scattering spectra arises from diffusional motions. To investigate with which minimum sampling we are able to reproduce the diffusional motions we have performed neutron scattering calculations in different sampling intervals and compared the resulting spectra. The trajectory was saved every 0.05, 0.1, 0.2, 0.4, 0.5, 1, 2 and 10ps and the difference in the spectra and in the elastic

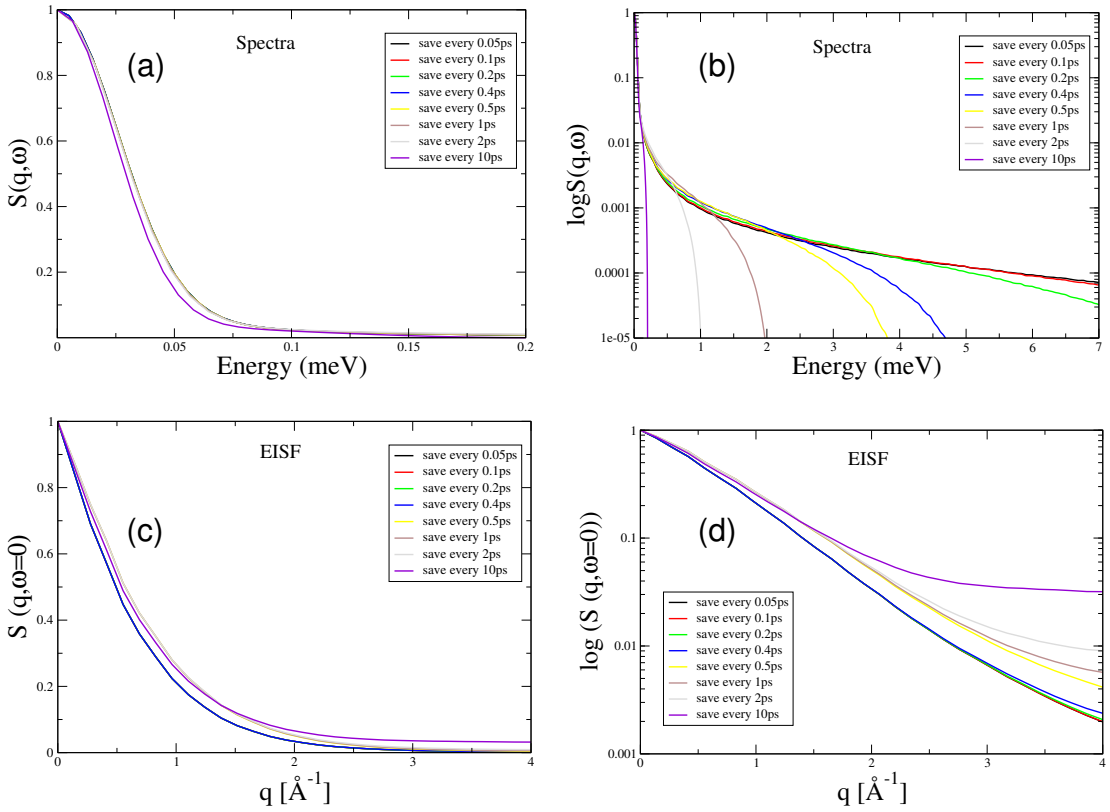

Figure 6.5: (a) and (b) Neutron scattering spectra for different sampling intervals. (c) and (d) elastic incoherent structure factor for different sampling intervals.

incoherent structure factor were monitored (see Fig. 6.5). If we consider that for 0.05 ps all features of the spectra are reproduced, then for a sampling of 0.2 ps we have good reproduction of the main features of both the structure factor and the EISF for the quasielastic region (*i.e.* for energy range smaller than 1meV). Therefore, sampling of 0.2ps intervals was chosen.

6.3.2 CALCULATION OF THE DYNAMIC STRUCTURE FACTOR

The dynamic structure factor was calculated from the MD trajectory and for the cholesterol-DPPC membrane and was directly compared to the neutron scattering spectra obtained in Ref. 19. The instruments used in these experiments were: (a) The IN5 time-of-flight spectrometer with an energy resolution of 14μeV and incident neutron wavelength λ=1.0nm. This energy resolution corresponds to a time scale of up to 300ps. (b) The IN10 backscattering spectrometer with an incident wavelength of 0.6271 nm and an energy resolution of 1μeV, which corresponds to a time scale of 4ns.

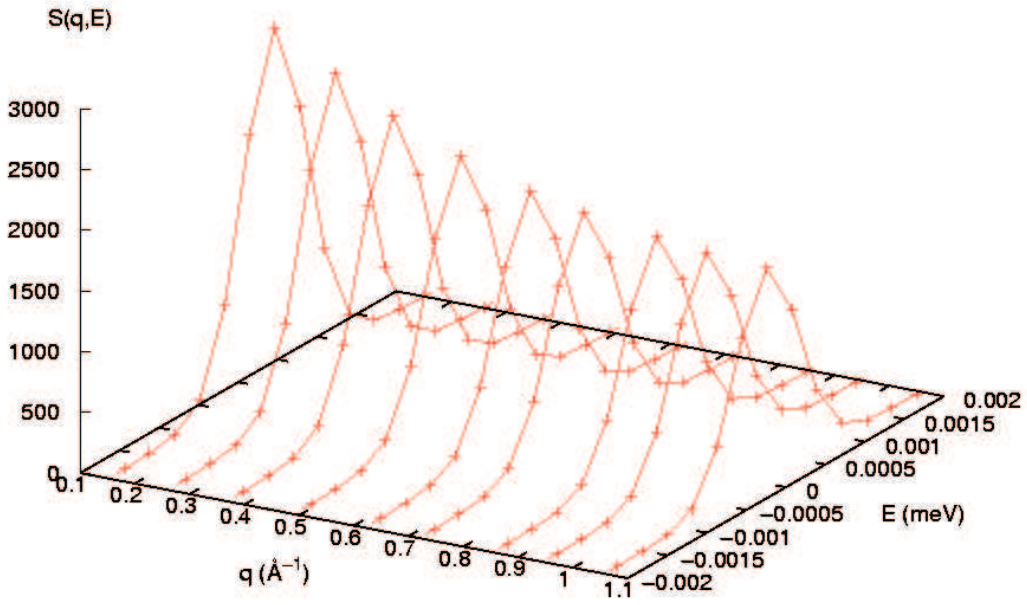

Figure 6.6: The dynamic structure factor calculated from the MD cholesterol-DPPC trajectory at T=309K for the IN5 instrumental resolution (14μeV) and for the 45° orientation. of energy and momentum transfer for the IN5

All the neutron scattering calculations have been performed with the program package nMoldyn.[26] For a meaningful comparison between experiment and MD, it is essential to compute spectra from the MD trajectory that are broadened by the resolution of the experiment. Moreover the data has to be reduced and analyzed by the same procedure as that used in the experimental data reduction.

In nMoldyn the input provided by the user are the atomic coordinates, the instrumental resolution and the **q** vectors so that the intermediate scattering function is calculated. In the case of isotropic media, such as powders, the **q** vectors are randomly distributed on a set of equidistant shells in order to achieve isotropic scattering. However, for oriented samples, the scattering is not isotropic and the momentum transfer **q** vectors have a specific orientation. Therefore, the intermediate scattering function needs to be calculated only for the required q_x, q_y, q_z components and not to be averaged as in the case of isotropic media. Using the detector angles used in the experimental setup and Eq. 2.70 the input vectors, **q**, were calculated with the procedure mentioned in Section 2.4.5. The membrane normal in the simulation was taken to coincide with the z-axis.

The dynamic structure factor was then calculated by Fourier transformation of the intermediate scattering function calculated from the MD trajectory. Example structure

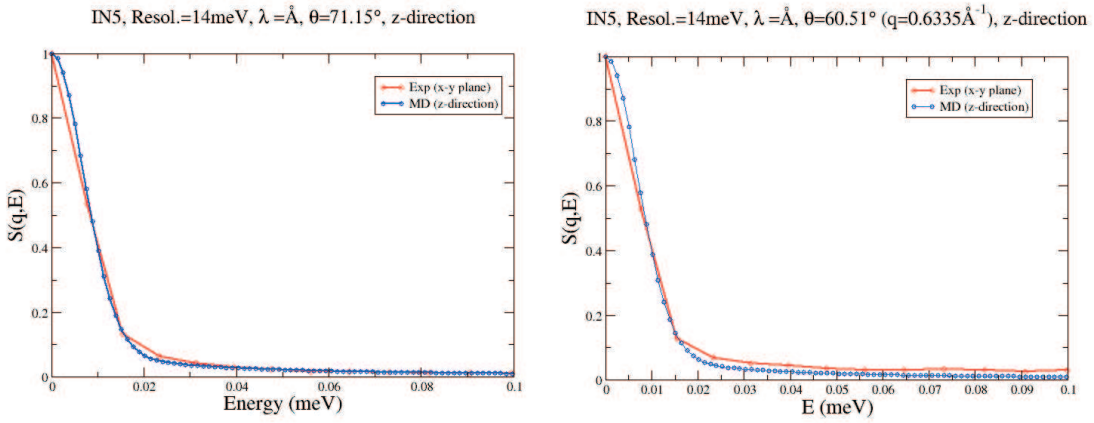

Figure 6.7: Comparison of experimental and simulation structure factors.

factors for the 45° orientation are plotted as a function of both the momentum transfer, **q**, and the energy transfer, E, in Figure 6.6.

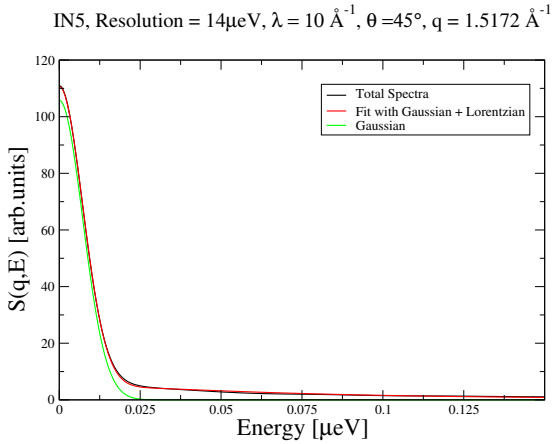

Figure 6.8: The dynamic structure factor calculated from the MD cholesterol-DPPC trajectory at T=309K for the IN5 instrumental resolution (14μeV) and for the 45° orientation fitted with one Gaussian and one Lorentzian function.

As a next step, to validate the dynamics of the MD model used in the simulations, we directly compared the dynamic structure factors, $S(\mathbf{q}, E)$, resulting from the cholesterol-DPPC MD trajectory for T=309K with the experimentally deduced ones. Two examples of such a comparison can be seen in Fig. 6.7 for the resolution of the IN5 spectrometer in ILL (14μeV). The comparison between the calculated and experimental spectra was very good in all cases.

6.3.3 EISF AND LONG-RANGE DIFFUSION CALCULATION

In a first step, the line shape parameters A_0, A_i and Γ_i were fitted to each spectrum separately according to Eq. 2.86. One Gaussian (which accounts for the elastic scat-

tering) and one Lorentzian function (which accounts for the quasielastic component) were thus fitted to calculate the EISF. An example fit can be seen in Fig. 6.8. Using Eq. 2.83, the EISF was then calculated from the ratio of the elastic and the quasielastic components of the spectra as modeled with the Gaussian and the Lorentzian functions. The calculated EISFs also agree well with those measured experimentally (shown in Fig. 6.9).

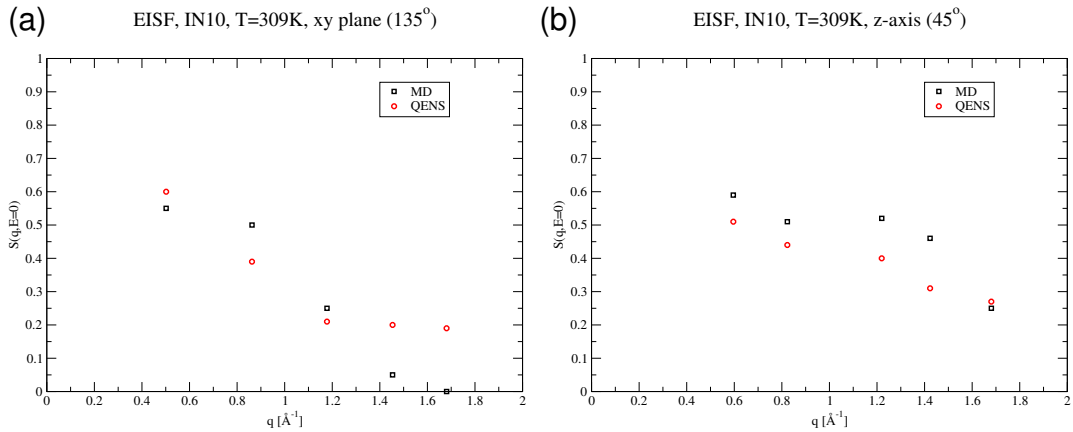

Figure 6.9: The elastic incoherent structure factor as calculated by MD simulations and in comparison with the experimental EISF. In red circles the QENS experimental results and in black squares the MD calculated ones.

The shape of the EISF functions presented in Fig. 6.9 can be fitted with different motional models for the z-axis motion (Fig. 6.9a) and for the $x-y$ plane motion (Fig. 6.9b). In Ref. 19, the out-of plane motion was considered to be a composite model consisting of jump motion over a mean jump distance d at a jump rate $1/\tau$, and a continuous rotational diffusion about the sterol long axis (*i.e.* z-axis).[24, 27] For the sterol motion along the membrane normal a model of two-site jump diffusion was employed.[19]

Comparing Figs. 6.9a and b, we can see that both the experimental as well as the calculated EISFs do not have the same shape for motions in and perpendicular to the plane of the bilayer, indicating that the motion is anisotropic. The MD EISF for in-plane motion decays significantly faster with q than that for the EISF from the bilayer normal, suggesting more mobility in the xy plane of the bilayer.

Since the QENS spectra at this energy resolution (4 ns time scale) are dominated by translational diffusion of the whole molecules the QENS spectral line widths $\Gamma(\mathbf{q})$ were analyzed in terms of long-range diffusion of the sterols. As mentioned above, the QENS spectra were fitted by a single Lorentzian line, as is typical for the case of Fickian diffusion.[24] For the full width at half maximum (FWHM) of the Lorentzian, $\Gamma(\mathbf{q})$, the Fickian theory predicts a linear dependence of $\Gamma(\mathbf{q})$ vs q^2 with the slope D

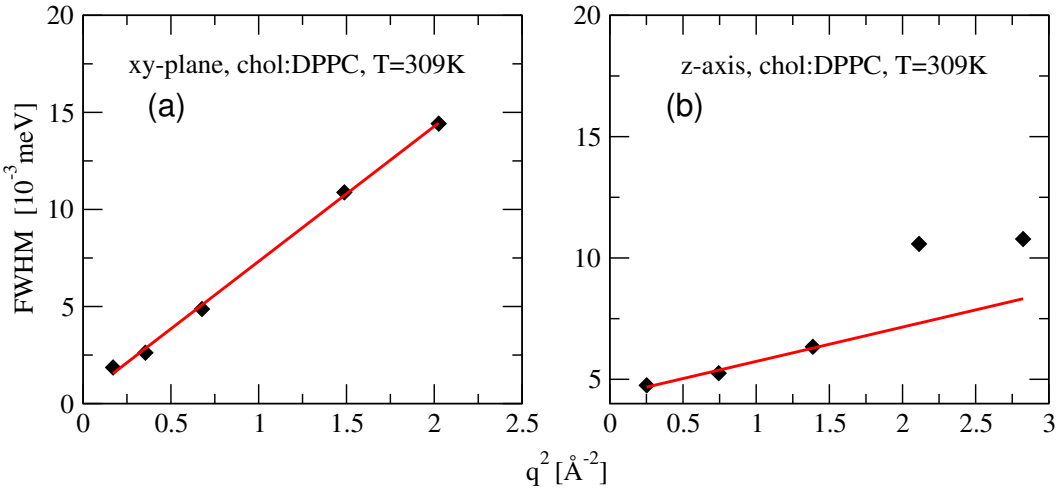

Figure 6.10: Quasielastic line width (FWHM) vs q^2 for the chol:DPPC bilayer and for T=309K. (a) xy-plane and (b) z-axis. The solid red lines represent straight-line fits of the continuous diffusion model to the values of small q. Black diamonds are the calculated results. The slope of the line corresponds to the long-range diffusion constant D.

in the limit of small q, *i.e.* large distances. In Figure 6.10 the region of small q is fitted to a straight line for the cholesterol:DPPC membrane at T=309K. The fit results to D_{lat}=6.9 and D_{tr}=1.4, which is remarkably close to the values derived directly from the MD for the MSD of the cholesterol hydrogens.

6.4 CONCLUSION

Sterol dynamics was investigated here using a combination of mean square displacement analysis and neutron scattering calculations. The diffusion in the plane of the membrane was found to be significantly different for each sterol, despite their very similar chemical structures. On the contrary, the diffusion of all three sterols in the membrane normal was similar. The diffusion constants for the cholesterol-DPPC system are within the experimentally-deduced range (5 - 30 $\times$ 10 $^{-8}$ cm^2/s). The diffusion of cholesterol in the $x-y$ plane of the membrane is significantly different than that in the z-axis, suggesting a strong motional anisotropy in favor of the in-plane motion.

In all cases, the ergosterol diffusion was found to be the slowest among the three sterols studied. The reason for the significant differences in the diffusion of the three sterols lies in their different chemical characteristics. Ergosterol, has a smooth α-face (as does cholesterol), but also two more double bonds than cholesterol, which make ergosterol the stiffest molecule among the three sterols studied. The result of the stiffness of ergosterol is that the ring packs closer to the lipid chains and orders them

significantly more than do the other two sterols. This closer packing in the ergosterol:DPPC system results also in decreased fluidity and flexibility in this membrane system.

At 323K the addition of any of the three sterols to the membrane slows down the lipid relative to the pure DPPC liquid phase. In contrast, at T=309K the sterols promote the diffusion of DPPC with respect to its diffusion in the gel state.

To validate the dynamics of the MD simulation we have calculated the dynamic structure factor from the cholesterol-DPPC simulation at 309K and directly compared it with the experimentally-derived one. The calculated structure factors agree well with the measured ones. Furthermore, we investigated the EISF for this system, which gives information on the geometry of the motions of the molecule under study. The different shape of the $x-y$ plane EISF as compared to the z-axis EISF again indicates a motional anisotropy, which was also observed in the QENS experiments.

Since the simulations reproduce not only the structural but also the dynamical information, the simulations can now be used to discuss the validity of the dynamic models used to fit the experimental EISF and/or to inspire new models for interpreting experimental data. In particular, the calculation of the EISF can be extended to the ergosterol and lanosterol systems. The shape of the EISF can subsequently be fitted with different motional models in order to investigate the anisotropy observed in the two dimensions of the membrane. Moreover, the dynamic structure factor from the simulations can be decomposed to different motional components (*i.e.* isolate rotational, translational and internal motion contributions). The calculation of the EISF from those components can help us fit different dynamical models to describe each of these contributions. Finally, any observed differences between the dynamics of the three sterols can be correlated to their different chemical characteristics, ultimately providing a complete picture of the sterol structure-function relationship in biomembranes.

BIBLIOGRAPHY

[1] KNIG, S., BAYERL, T. M., CODDENS, G., RICHTER, D., AND SACKMANN, E. Hydration dependence of chain dynamics and local diffusion in L-a DPPC multilayers studied by incoherent quasi-elastic neutron scattering. *Biophys. J.*, 1995, **68**, 1871–1880.

[2] DUFOURC, E. J., MAYER, C., STOHRER, J., ALTHOFF, G., AND KOTHE, G. Dynamics of Phosphate Head Groups in Biomembranes - Comprehensive Analysis Using Phosphorus-31 Nuclear Magnetic Resonance Lineshape and Relaxation Time Measurements. *Biophys. J.*, 1992, **61**, 42–57.

[3] BROWN, M. Anisotropic nuclear spin relaxation of cholesterol in phospholipid bilayers. *Mol. Phys.*, 1990, **71**, 903–908.

[4] DOXASTAKIS, M., SUM, A. K., AND DE PABLO, J. J. Modulating Membrane Properties: The Effect of Trehalose and Cholesterol on a Phospholipid Bilayer. *J. Phys. Chem. B*, 2005, **109**, 24173–24181.

[5] ESSMANN, U., AND BERKOWITZ, M. L. Dynamical Properties of Phospholipid Bilayers from Computer Simulation. *Biophys. J.*, 1999, **76**, 2081–2089.

[6] KASSON, P. M., KELLEY, N. W., SINGHAL, N., VRLJIC, M., BRUNGER, A., AND PANDE, V. S. Ensemble molecular dynamics yields submillisecond kinetics and intermediates of membrane fusion. *Proc. Natl. Acad. Sci. USA*, 2006, **103**, 11916–11921.

[7] HOGBERG, C. J., AND LYUBARTSEV, A. P. A molecular dynamics investigation of the influence of hydration and temperature on structural and dynamical properties of a dimyristoylphosphatidylcholine bilayer. *J. Phys. Chem. B*, 2006, **110**, 14326–14336.

[8] PATARGIAS, G., PJ, P. J. B., DEOL, S. S., AND SANSOM, M. S. Molecular dynamics simulations of GlpF in a micelle vs in a bilayer: conformational dynamics of a membrane protein as a function of environment. *J. Phys. Chem. B*, 2005, **109**, 575–582.

[9] KNIG, S., AND SACKMANN, E. . *Curr. Opin. Colloid Int. Sci.*, 1996, **1**, 78–82.

[10] TOBIAS, D. *Membrane Simulations. In:* Computational Biochemistry and Biophysics,, 2001, pp. 465–496.

[11] PITMAN, M. C., SUITS, F., A. D. MACKERELL, J., AND FELLER, S. E. Molecular-Level Organization of Saturated and Polyunsaturated Fatty Acids in a Phosphatidylcholine Bilayer Containing Cholesterol. *Biochemistry*, 2004, **43**, 15318–15328.

[12] TAREK, M., TOBIAS, D. J., CHEN, S.-H., AND KLEIN, M. L. Short Wavelength Collective Dynamics in Phospholipid Bilayers: a Molecular Dynamics Study. *Phys. Rev. Lett*, 2001, **87**, no.238101.

[13] PASTOR, R. W., VENABLE, R. M., AND FELLER, S. E. Lipid Bilayers, NMR Relaxation, and Computer Simulations. *Acc. Chem. Res.*, 2002, **35**, 438–446.

[14] ORÄDD, G., LINDBLOM, G., AND WESTERMAN, P. W. Lateral Diffusion of Cholesterol and Dimyristoylphosphatidylcholine in a Lipid Bilayer Measured by Pulsed Field Gradient NMR Spectroscopy. *Biophys. J.*, 2002, **83**, 2702–2704.

[15] A.SCHEIDT, H., HUSTER, D., AND GAWRISCH, K. Diffusion of Cholesterol and its Precursors in Lipid Membranes Studied by ^{1}H Pulsed Field Gradient Magic Angle Spinning NMR. *Biophys. J.*, 2005, **89**, 2504–2512.

[16] FILIPPOV, A., ORÄDD, G., AND LINDBLOM, G. The effect of cholesterol on the lateral diffusion of phospholipids in oriented bilayers. *Biophys. J.*, 2003, **84**, 3079–3086.

[17] ALMEIDA, P. F. F., VAZ, W. L. C., AND THOMPSON, T. E. Lateral diffusion in the liquid phases of dimyristoylphosphatidylcholine/cholesterol lipid bilayers: A free volume analysis. *Biochemistry*, 1992, **31**, 6739–6747.

[18] HOFSÄSS, C., LINDAHL, E., AND EDHOLM, O. Molecular dynamics simulations of phospholipid bilayers with cholesterol. *Biophys. J.*, 2003, **84**, 2192–2206.

[19] ENDRESS, E., HELLER, H., CASALTA, H., BROWN, M. F., AND BAYERL, T. M. Anisotropic motion and molecular dynamics of cholesterol, lanosterol and ergosterol in lecithin bilayers studied by quasi-elastic neutron scattering. *Biochemistry*, 2002, **41**, 13078.

[20] MARTINEZ, G. V., DYKSTRA, E. M., LOPE-PIEDRAFITA, S., AND BROWN, M. F. Lanosterol and cholesterol-induced variations in bilayer elasticity probed by H-2 NMR relaxation. *Langmuir*, 2004, **20**, 1043–1046.

[21] ENDRESS, E., BAYERL, S., PRECHTEL, K., MAIER, C., MERKEL, R., AND BAYERL, T. M. The effect of cholesterol, lanosterol, and ergosterol on lecithin bilayer mechanical properties at molecular and microscopic dimensions: A solid-state NMR and micropipet study. *Langmuir*, 2002, **18**, 3292–3299.

[22] CZUB, J., AND M.BAGINSKI. Comparative molecular dynamics study of lipid membranes containing cholesterol and ergosterol. *Biophys. J.*, 2006, **90**, 2368–2382.

[23] GLISS, C., RANDL, O., CASALTA, H., SACKMANN, E., ZORN, R., AND BAYERL, T. Anisotropic motion of cholesterol in oriented DPPC bilayers studies by quasielastic neutron scattering: the liquid-ordered phase. *Biophys. J.*, 1999, **77**, 331.

[24] BEE, M. *Quasielastic Neutron Scattering*. Adam Hilger, Bristol and Philadephia, 1988.

[25] FITTER, J., LECHNER, R. E., BÜLDT, G., AND DENCHER, N. A. Internal molecular motions of bacteriorhodopsin: Hydration-induced flexibility studied by quasielastic incoherent neutron-scattering using oriented purple membranes. *Proc. Natl. Acad. Sci. USA*, 1996, **93**, 7600–7605.

[26] KNELLER, G. R., KEINER, V., KNELLER, M., AND SCHILLER, M. nMOLDYN: A program package for a neutron scattering oriented analysis of molecular dynamics simulations. *Comp. Phys. Commun.*, 1995, **91**, 191–214.

[27] DIANOUX, A. J., VOLINO, F., AND HERVERT, H. Incoherent scattering law for neutron quasielastic scattering in liquid crystals. *Mol. Phys.*, 1975, **30**, 1181–1194.

CONCLUSIONS

A problem of longstanding interest in biological research has been to determine how cholesterol and other biologically-important sterols influence the structure and dynamics of lipid bilayers. Moreover, an intriguing question is to justify the evolutionary selection of cholesterol and its incorporation in mammalian cells. The present thesis aims at providing insights to those yet unanswered questions using the Molecular Dynamics simulation technique.

As a first step towards realistic sterol:membrane simulations, a new force field for cholesterol, ergosterol and lanosterol has been derived using an automated frequency matching method (AFMM). Molecular mechanics parameterization is a tedious but necessary task in the case of missing force field parameters. In this framework, a new program for molecular mechanics force field parametrization was developed, which can be readily used for parametrization of new molecules.[1, 2]

AFMM fits the molecular mechanics potential to both vibrational frequencies and eigenvector projections derived from quantum chemical calculations. The frequency-matching plots for the three molecules show good agreement between the CHARMM and quantum chemical normal modes. The parameter set is refined to reproduce the energy barrier for the rotation of the hydroxyl group around the carbon connected to the hydroxyl of each sterol. The cholesterol parameters were successfully tested in a MD simulation of the cholesterol crystal structure.[3, 4] The force field presented in this thesis is a general steroid force field that can be useful in simulation studies involving other sterols or steroids, such as the phytosterols sigmasterol and sitosterol and also many classes of steroids. The new parameter set has enabled us to subsequently perform sterol:membrane MD simulations.

Six MD simulations of DPPC membranes containing three different sterols (cholesterol, ergosterol or lanosterol) at a concentration of 40%mol. were performed. At 40%mol. cholesterol the membrane is found in the *lo* phase, which is the phase where lipid rafts are found. The simulations were performed at temperatures of 309K and 323K. Two additional control simulations of the gel and liquid DPPC phases were

also performed and compared to the sterol-containing membranes.

The second aim of the present thesis was to probe the differential effects of each sterol on the structure of the model membrane. Several molecular dynamics studies have been previously performed on pure bilayers.[5–14] These have generally been in good agreement with experiments, and the control simulations presented here (of DPPC in the gel phase at 309K and liquid phase at 323K) are also in good agreement with the existing experimental data, including the electron density profiles, and in particularly good agreement with the available NMR order parameters.

A number of structural properties of the simulated systems were also directly compared to experimental results for the sterol-containing membranes. Electron density profiles were compared to X-ray scattering data, order parameter profiles to NMR data and *trans-gauche* DPPC populations to IR spectroscopic results. In all cases there was very good agreement of our calculations with the experimental results. Subsequently, we have extended the calculation of structural properties to quantities that have not been yet determined experimentally, such as surface area per lipid, sterol tilt angles and radial distribution functions, in order to gain a more complete picture of the differential effects of each sterol on the membrane structure.

All three sterols are found to order and condense the lipids relative to the liquid phase, but to markedly different degrees. Ergosterol is enhancing the packing of the lipids with each other and has a higher condensing effect on the membrane than the other two sterols. Moreover, ergosterol induces a higher proportion of *trans* lipid conformers, a thicker membrane and higher lipid order parameters, and is aligned more closely with the membrane normal. Ergosterol also positions itself closer to the bilayer:water interface. In contrast, lanosterol orders, straightens and packs the lipids less well, and is less closely aligned with the membrane normal. Furthermore, lanosterol lies closer to the relatively-disordered membrane center than do the other sterols. The behaviour of cholesterol in all the above respects is intermediate between that of lanosterol and ergosterol. The above-mentioned effects suggest that the slight modifications of the sterol structure have a drastic effect on the membrane structural properties.

The next aim of the thesis was to investigate the sterol dynamics in the membrane. Sterol dynamics was investigated here using a combination of mean square displacement analysis and neutron scattering calculations. The diffusion in the plane of the membrane was found to be significantly different for each sterol. Ergosterol was found to diffuse the slowest and cholesterol the fastest among the three sterols studied. The diffusion constants for cholesterol in the $x - y$ plane of the membrane are significantly different if compared to those in the z-axis, suggesting a strong motional

anisotropy for this sterol in favor of the in-plane motion.

To validate the dynamics of the MD simulation the dynamic structure factor was calculated from the cholesterol-DPPC trajectory at 309K and was directly compared to the experimentally-derived one. The calculated structure factors agree very well with the measured ones. Furthermore, we investigated the EISF for this system, which gives information on the geometry of the motions of the molecule under study. The different shape of the $x - y$ plane EISF compared to the z-axis EISF also indicates a motional anisotropy, which was also observed in the QENS experiments. QENS gives us information on the average dynamic behavior of the molecules, and therefore a further analysis of the structure factor would include decomposition of the simulation-derived structure factor into motional components (rotational, translational, internal) and thus shed light on which particular parts of cholesterol provide the optimal physical properties of the membrane. Future prospects include modeling and understanding more complex systems (e.g. cholesterol, lipid and membrane proteins). The dynamical analysis of the membrane properties is still an ongoing project.

The origins of the different membrane behavior upon addition of different sterols are being discussed in this thesis with respect to their chemical differences. Lanosterol is the earliest intermediate in the cholesterol biosynthetic pathway, while cholesterol is the sterol "of choice" for mammalian plasma membranes. The structural modifications of lanosterol during the conversion to cholesterol in the biosynthetic pathway start with the complete demethylation of the lanosterol α-face (the methyl groups attached to C_{14} and to C_4 are removed). These three extra methyls of lanosterol (C_{28},C_{29},C_{30}) with respect to the other two sterols, protrude from its otherwise flat α-face and roughen its surface. In contrast, ergosterol has a smooth α-face (as does cholesterol), one double bond more than lanosterol and two more than cholesterol. The result of the smoothness of ergosterol is a closer packing of its ring to the lipid chains, which can be seen in the relevant radial distribution functions (Section 5.2.8). In contrast to ergosterol, the absence of a smooth α-face holds lanosterol's steroid ring system further from the DPPC acyl chains than the other two sterols, therefore not allowing optimal interaction of lanosterol with DPPC.

The explanation for the removal of the C_4 methyls of lanosterol might lie in the reduced hydrophilicity of the OH in lanosterol. C_4 methyls reduce the possibility of lanosterol being hydrated by water as shown in Section 5.2.8. Therefore, possibly to allow better interactions of the sterol with the polar moieties of the membrane (*i.e.* water and headgroups), the C_4 methyls were evolutionarily removed.

A question that also arises is why are the methyl substituents in the β-face conserved in membrane sterols while they are cleaved off from the α-face? One possible

explanation based on the results of this thesis is that nature needs only one smooth face for optimizing sterol-lipid interactions. Two smooth faces would probably make the membrane too stiff and could lead to complete immobilization of the lipid acyl chains. It is evident that the slightly stiffer ergosterol molecule has a significantly larger ordering and stiffening effect on the membrane, as well as a dramatic decrease of membrane dynamics. Therefore, a too smooth sterol structure might not be suitable for membranes, as a certain degree of flexibility must be ensured in order for membrane proteins and membrane-associated tasks to take place.

One of the major achievements of this thesis is that it may shed light on the mechanism of the promotion of lipid rafts (domains) in eukaryotic plasma membranes. It has been suggested that lipid raft/domain formation is dependent on the sterol component because it requires a structure that allows tight packing of lipids.[15] Here, we have described in detail the result of this tighter sterol:lipid packing on the structure of a model DPPC membrane. The induction of lipid order, lipid:lipid packing condensation, sterol tilt angles and sterol positioning relative to the membrane center may all play roles in raft formation. Fluorescence quenching and detergent-insolubility experiments have suggested that ergosterol is promoted significantly more domain formation than cholesterol[15] and that lanosterol is the weakest promoted of lipid rafts among the three sterols,[16, 17] consistent with the present relative ordering effects.

Cholesterol adopts a behaviour in between the other two sterols: not as disordering as lanosterol but not as stiffening and ordering as ergosterol. In this context, cholesterol seems to perfectly balance membrane rigidity, which is needed for large cells such as the eukaryotic cells, with membrane flexibility and fluidity, which allows the membrane to perform complex functions. The stronger ordering effect of cholesterol relative to lanosterol and its significantly faster dynamics among the three sterols studied, revealed in detail in the present simulations, may well be part of the reason why cholesterol has been evolutionarily preferred in higher-vertebrate plasma membranes.

BIBLIOGRAPHY

[1] VAIANA, A. C., COURNIA, Z., COSTESCU, I. B., AND SMITH, J. C. AFMM: A Molecular Mechanics Force-Field Vibrational Parametrization Program. *Computer Physics Communications*, 2005, **167**, 34–42.

[2] DE HATTEN, X., COURNIA, Z., SMITH, J., AND METZLER-NOLTE, N. Towards Synthetic Hydrogenase Mimicry: Force-Field Development and Molecular Dynamics Simulations of Novel Ferrocene-Bearing Peptides. *manuscript in preparation*, 2006.

[3] COURNIA, Z., SMITH, J. C., AND ULLMANN, G. M. A molecular mechanics force-field for biologically important sterols. *J. Comp. Chem.*, 2005, **26**, 1383–1399.

[4] COURNIA, Z., ULLMANN, G. M., AND SMITH, J. C. *Development and Validation of a Force-Feild for Biologically-Important Sterol in Biomembranes. In:* Lecture Series on Computer and Computational Sciences, Vol. 4, Brill Academic Publishers, Leiden, 2005, pp. 949–953.

[5] TIELEMAN, D. P., AND BERENDSEN, H. J. C. Molecular Dynamics simulation of a fully hydrated dipalmitoylphosphatidylcholine bilayer with different macroscopic boundary conditions and parameters. *J. Phys. Chem.*, 1996, **105**, 4871–4880.

[6] A. H. DE VRIES, S. YEFIMOV, A. E. M., AND MARRINK, S. J. Molecular structure of the lecithin ripple phase. *Proc. Natl. Acad. Sci. USA*, 2005, **102**, 5392–5396.

[7] A. H. DE VRIES, I. C., VAN GUNSTEREN, W. F., AND HÜNENBERGER, P. H. Molecular Dynamics Simulations of Phospholipid Bilayers: Influence of Artificial Periodicity, System Size and Simulation Time. *J. Phys. Chem. B*, 2005, **109**, 11643–11652.

[8] LINDAHL, E., AND EDHOLM, O. Mesoscopic undulations and thickness fluctuations in lipid bilayers from molecular dynamics simulations. *Biophys. J.*, 2000, **79**, 426–433.

[9] JENSEN, M. O., MOURITSEN, O. G., AND PETERS, G. H. Simulations of a membrane-anchored peptide: structure, dynamics, and influence on bilayer properties. *Biophys. J.*, 2004, **86**, 3556–3575.

[10] PASTOR, R. W., VENABLE, R. M., AND FELLER, S. E. Lipid Bilayers, NMR Relaxation, and Computer Simulations. *Acc. Chem. Res.*, 2002, **35**, 438–446.

[11] ESSMANN, U., AND BERKOWITZ, M. L. Dynamical Properties of Phospholipid Bilayers from Computer Simulation. *Biophys. J.*, 1999, **76**, 2081–2089.

[12] CHIU, S. W., JAKOBSSON, E., SUBRAMANIAM, S., AND SCOTT, H. L. Combined Monter Carlo and Molecular Dynamics Simulation of a fully hydrated Dioleyl and Palmitoyl-oleyl Phosphatidylcholine Lipid Bilayers. *Biophys. J.*, 1999, **77**, 2462–2469.

[13] PASENKIEWICZ-GIERULA, M., TAKAOKA, Y., MIYAGAWA, H., KITAMURA, K., AND KUSUMI, A. Hydrogen Bonding of water to Phosphatidylcholine in the Membrane as studied by a Molecular Dynamics Simulation: Location, Geometry and Lipid-Lipid Bridging via Hydrogen-Bonded Water. *J. Phys. Chem. A*, 1997, **101**, 3677–3691.

[14] TU, K., TOBIAS, D. J., AND KLEIN, M. L. Constant Pressure and Temperature Molecular Dynamics of a Fully Hydrated Liquid Crystal Phase Dipalmitoylphosphatidylcholine bilayer. *Biophys. J.*, 1995, **69**, 2558–2562.

[15] XU, X., BITTMAN, R., DUPORTAIL, G., HEISSLER, D., VILCHEZE, C., AND LONDON, E. Effect of the structure of natural sterols and sphingolipids on the formation of ordered sphingolipid/sterol domains (rafts). *J. Biol. Chem.*, 2001, **276**, 33540–33546.

[16] XU, X., AND LONDON, E. The effect of sterol structure on membrane lipid domains reveals how cholesterol can induce lipid domain formation. *Biochemistry*, 2000, **39**, 843–849.

[17] MIAO, L., NIELSEN, M., THEWALT, J., IPSEN, J., BLOOM, M., ZUCKERMANN, M. J., AND MOURITSEN, O. G. From lanosterol to cholesterol: structural evolution and differential effects on lipid bilayers. *Biophys. J.*, 2002, **82**, 1429–1444.

FUTURE PERSPECTIVES

This thesis has explored aspects of the complex interactions between sterols and phospholipids. Cholesterol and other biologically-important sterols have an important effect on the membrane physical properties (such as ordering, condensation, decrease of *gauche* defects). These effects are directly dictated by the sterol chemical structure and are important for the function that each sterol performs in different types of organisms. There remains, however, much to be investigated and understood.

It is known since a decade that cholesterol associates with saturated, high-melting lipids, such as DPPC and sphingomyelin, to create dynamic complexes in model membranes, so-called 'lipid rafts' that are found in a 'liquid-ordered' phase. Cholesterol thus promotes a phase separation in model membranes where cholesterol-rich and cholesterol-poor microdomains are formed. Lipid rafts, which are postulated to exist in mammalian plasma membranes, have been extensively researched in the past few years, because of their possible roles in regulating membrane function and signaling. Moreover, they are also thought to be implicated in the HIV, Alzheimer and prion diseases. The evidence for lipid rafts is still a very controversial issue, and their role in cellular signaling, trafficking, and structure has yet to be determined despite many experiments involving several different methods. Arguments against the existence of lipid rafts include the following: i) there should be a line tension between the liquid-disordered and liquid-ordered (*lo*) phase. Though this has been seen in model membranes, it has not been readily observed in cell systems, ii) the size of lipid rafts. This has been reported between 0.1 and 1000 nanometers so there seems to be no consensus, iii) the time scale of the existence of lipid rafts. If they do exist they may only occur on a time scale irrelevant to biological processes. iv) the entire membrane may exist in the *lo* phase. Advances in experimental as well as in computer simulation techniques (along with the increase in computer power) can help in this context to elucidate some questions.

Membranes are complex systems, including not only a variety of lipids, but also membrane-associated proteins. Certain proteins associated with cellular signaling pro-

cesses have been shown to associate with lipid rafts. Proteins that have shown association to the lipid rafts include glycosylphosphatidylinositol(GPI)-anchored proteins, doubly-acylated tyrosine kinases of the Src family, and transmembrane proteins. This association can at least be partially contributed to the acylated, saturated tails of both the tyrosine kinases and the GPI-anchored proteins, which matches the properties of sphingolipids more than the rest of the membrane. While these proteins tend to be continuously present in lipid rafts, there are others that associate with lipid rafts only when the protein is activated. Therefore, apart from cholesterol altering the bulk biophysical properties of the membrane, the possibility of cholesterol also modulating membrane protein function within lipid rafts is possible. Advances in the computational power definitely promise further investigation of simulation of more realistic membranes. Possible questions that arise are: In what time scale are the lipid rafts formed? Can we observe spontaneous lipid raft formation from a pool of saturated and unsaturated lipids in a membrane containing membrane proteins? Is cholesterol influencing the function of membrane proteins and in which way? Does cholesterol bind to specific sites of membrane enzymes so that a conformational change occurs?

If sterols interact directly with membrane proteins, then specific chemical structures would also be required to modulate protein activity. On the other hand, by modulating the content of cholesterol in the plasma membrane to have regions with low (fluid domains) and high (lipid rafts) cholesterol-content, the membrane can have less condensed and more condensed regions. In a less condensed region of the bilayer the proteins would then have the available space to perform the conformational changes required for their function . Membrane simulations involving a variety of lipids and/or membrane proteins could shed light on the role of lipid rafts in membranes.

Another intriguing question involves the mechanism of insertion of cholesterol in membranes. Very recently, the X-ray crystal structure of an oxysterol binding-related protein (ORP), the full-length yeast ORP Osh4, was solved. This class of proteins are conserved from yeast to humans and are implicated in the regulation of sterol homeostasis and signal transduction pathways. The transfer of sterol molecules and the mechanism through which this is achieved has been recently hypothesized upon. However, the specific interactions that might support this mechanism are still not known. Molecular Dynamics simulation is a useful tool with which we can understand membrane:protein interactions, as it can reveal the dynamic behavior of the static Xray structures. Open questions are the mechanism of cholesterol transport to the membrane, the differences between the protein sterol-bound form and the unbound form, the interactions of sterols in the binding site of the protein, the interactions of proteins with the lipid bilayer and the dynamics of the sterols in the

protein and of the dynamics of the protein itself.

These aspects just represent a 'next step' in the study of biomembranes viewed from the perspective of the present thesis. There are undoubtedly many more perspectives of membrane function that need to be addressed in the future than the few listed above. Research in this field needs the concerted efforts of biochemistry and biophysics. The final goal is to understand structure-function relationships that will pave the way to the understanding of life processes in biomolecular system. This thesis and many of the present efforts in Biophysical Chemistry are dedicated to this task.

APPENDIX I: MOLECULAR MECHANICS FORCE FIELD PARAMETERS FOR CHOLESTEROL, ERGOSTEROL AND LANOSTEROL

This appendix presents the new force field parameters optimized for the CHARMM force field with the AFMM method as described in this thesis.

Group	Atome Name	Atom Type	Charge	Group	Atome Name	Atom Type	Charge
Group 1	C_1	CTL2	-0.118	Group 2	C_2	CTL2	-0.162
	H_{C_1}	HAL2	0.059		H_{C_2}	HAL2	0.081
	H_{C_1}	HAL2	0.059		H_{C_2}	HAL2	0.081
Group 3	C_3	CTL1	-0.008	Group 4	C_5	CEL1	-0.092
	H_{C_3}	HAL1	0.180		C_6	CEL1	-0.083
	O	OHL	-0.566		H_{C_6}	HEL1	0.088
	H	HOL	0.394		C_{10}	CTL1	0.087
Group 5	C_4	CTL2	-0.200	Group 6	C_{12}	CTL2	0.036
	H_{C4}	HAL2	0.100		$H_{C_{12}}$	HAL2	-0.018
	H_{C4}	HAL2	0.100		$H_{C_{12}}$	HAL2	-0.018
Group 7	C_7	CTL2	-0.187	Group 8	C_9	CTL1	-0.159
	H_{C7}	HAL2	0.092		H_{C9}	HAL1	0.104
	H_{C7}	HAL2	0.103		C_{11}	CTL2	0.036
	C_8	CTL1	-0.190		H_{C11}	HAL2	0.012
	H_{C8}	HAL1	0.183		$H_{C_{11}}$	HAL2	0.007
Group 9	C_{14}	CTL1	-0.204	Group 10	C_{15}	CTL2	-0.134
	H_{C14}	HAL1	0.121		$H_{C_{15}}$	HAL3	0.067
	C_{13}	CTL1	0.083		$H_{C_{15}}$	HAL3	0.067
Group 11	C_{16}	CTL2	-0.108	Group 12	C_{22}	CTL2	0.042
	$H_{C_{16}}$	HAL2	0.054		$H_{C_{22}}$	HAL2	-0.021
	$H_{C_{16}}$	HAL2	0.054		$H_{C_{22}}$	HAL2	-0.021
Group 13	C_{20}	CTL1	-0.017	Group 14	C_{21}	CTL3	-0.144
	$H_{C_{20}}$	HAL1	0.029		$H_{C_{21}}$	HAL3	0.048
	C_{17}	CTL1	-0.075		$H_{C_{21}}$	HAL3	0.048
	$H_{C_{17}}$	HAL1	0.063		$H_{C_{21}}$	HAL3	0.048
Group 15	C_{18}	CTL3	-0.018	Group 16	C_{19}	CTL3	-0.144
	$H_{C_{18}}$	HAL3	0.006		$H_{C_{19}}$	HAL3	0.048
	$H_{C_{18}}$	HAL3	0.006		$H_{C_{19}}$	HAL3	0.048
	$H_{C_{18}}$	HAL3	0.006		$H_{C_{19}}$	HAL3	0.048
Group 17	C_{23}	CTL2	0.010	Group 18	C_{24}	CTL2	-0.014
	$H_{C_{23}}$	HAL2	-0.005		$H_{C_{24}}$	HAL2	0.007
	$H_{C_{23}}$	HAL2	-0.005		$H_{C_{24}}$	HAL2	0.007
Group 19	C_{26}	CTL3	0.033	Group 20	C_{27}	CTL3	0.054
	$H_{C_{26}}$	HAL3	-0.011		$H_{C_{27}}$	HAL3	-0.018
	$H_{C_{26}}$	HAL3	-0.011		$H_{C_{27}}$	HAL3	-0.018
	$H_{C_{26}}$	HAL3	-0.011		$H_{C_{27}}$	HAL3	-0.018
Group 21	C_{25}	CTL1	-0.007				
	$H_{C_{25}}$	HAL1	0.007				

Table I: Grouping, atom type assignments and partial atomic charges for cholesterol. Subscripts of the hydrogen atoms indicate to which carbon atoms the hydrogen atom are bonded.

Bonds	K_b $\left[\frac{kcal}{mol\mathring{A}^2}\right]$	$b_0[\mathring{A}]$
CEL1-CTL1	283.389	1.500
CAL1-CAL1	360.325	1.340
CAL1-CTL2	360.500	1.500
CAL1-CTL1	218.773	1.500
HEL1-CAL1	360.282	1.100
OHL-HOL	504.484	0.690

Table II: CHARMM27 bond parameters for cholesterol, ergosterol and lanosterol. Only parameters not already published are listed.

Angles	K_θ $\left[\frac{kcal}{molrad^2}\right]$	θ_0[deg]	K_{ub} $\left[\frac{kcal}{mol\mathring{A}^2}\right]$	s_0 [Å]
CEL1-CEL1-CTL1	36.346	123.0		
CTL2-CEL1-CTL1	54.051	116.0		
CTL1-CTL2-CEL1	23.072	111.0		
CTL2-CTL1-CEL1	27.856	108.0		
CEL1-CTL1-CTL3	72.030	112.2		
CEL1-CTL1-CTL1	57.137	110.0		
CTL3-CTL1-CTL3	41.205	110.0	11.16	2.561
CAL1-CAL1-CAL1	67.646	121.0		
CTL1-CAL1-CTL1	42.102	118.0		
CEL1-CTL1-HAL1	53.267	107.0		
CAL1-CTL1-HAL1	29.270	107.0		
CTL1-CEL1-HEL1	23.697	120.0		
CTL1-CAL1-HEL1	20.313	120.0		
HEL1-CAL1-CAL1	33.920	119.5		
CAL1-CAL1-CTL1	73.148	123.0		
CTL2-CAL1-CTL1	54.051	116.0		
CTL1-CTL2-CAL1	23.072	111.0		
CTL2-CTL1-CAL1	56.185	108.0		
CAL1-CTL1-CTL3	22.746	112.2		
CAL1-CTL1-CTL1	73.676	110.0		
CTL3-CEL1-CTL3	33.260	111.0		
OHL-CTL1-CTL1	63.985	112.0		

Table III: CHARMM27 angle parameters for cholesterol, ergosterol and lanosterol.

Improper Torsions	molecule	atoms	K_ψ $\left[\frac{kcal}{molrad^2}\right]$	ψ_0[deg]
CTL3-CTL1-CTL1-CEL1	cholesterol	C19-C9-C10-C5	2.218	-120.0
CTL3-CTL1-CTL1-CTL1	cholesterol	C18-C17-C13-C14	7.645	- 50.0
OHL-CTL2-CTL1-CTL2	cholesterol	O-C4-C3-C2	3.000	125.0
CEL1-CTL1-CEL1-CTL2	cholesterol	C6-C10-C5-C4	3.000	130.0
HAL1-CTL1-CTL1-CTL1	cholesterol	H11-C9-C8-C14	3.000	-120.0
CTL2-CTL1-CTL1-CTL1	cholesterol	C15-C13-C14-C8	3.000	130.0
CEL1-CTL2-CEL1-HEL1	cholesterol	C5-C6-C7-HE1	20.176	180.0
CTL1-CTL2-CTL1-CTL1	cholesterol	C20-C16-C17-C13	2.986	-130.0
CTL3-CTL2-CTL1-CTL1	cholesterol	C21-C22-C20-C17	3.000	125.0
CTL2-CEL1-CEL1-CTL1	cholesterol	C4-C6-C5-C10	60.599	180.0
OHL-CTL2-CTL1-CTL2	ergosterol	O-C4-C3-C2	3.000	125.0
CTL1-CTL2-CTL1-CTL1	ergosterol	C20-C16-C17-C13	2.986	-130.0
CAL1-CAL1-CAL1-CAL1	ergosterol	C5-C6-C7-C8	0.500	0.0
CAL1-CAL1-CAL1-HEL1	ergosterol	C5-C6-C7-HE1	2.345	180.0
CAL1-CAL1-CAL1-HEL1	ergosterol	C8-C7-C6-H15	2.345	180.0
HEL1-CEL1-CEL1-HEL1	ergosterol	H31-C22-C23-H32	5.044	180.0
OHL-CTL1-CTL1-CTL2	lanosterol	O-C4-C3-C2	3.220	150.0
CTL3-CTL1-CTL1-CTL1	lanosterol	C21-C22-C20-C17	3.000	125.0

Table IV: CHARMM27 improper torsion parameters for cholesterol, ergosterol and lanosterol.

Dihedral Angles	K_χ $\left[\frac{kcal}{mol}\right]$	n	χ_0[deg]	molecule
CTL2-CTL1-CEL1-CTL2	0.500	3	0.0	
CTL3-CTL1-CEL1-CTL2	0.500	3	0.0	
CTL1-CTL2-CEL1-CTL1	0.500	3	0.0	
CTL1-CTL1-CEL1-CTL2	0.500	3	0.0	
CTL1-CTL1-CEL1-CEL1	1.000	3	0.0	
CTL2-CTL1-CEL1-CEL1	1.000	3	0.0	
CTL3-CTL1-CEL1-CEL1	0.860	3	0.0	
CTL1-CTL2 CEL1-CEL1	0.247	3	0.0	
HAL2-CTL2-CEL1-CTL1	0.294	3	0.0	
CTL2-CTL1-OHL-HOL	0.23	3	0.0	c/e
HAL1-CTL1-OHL-HOL	0.23	3	0.0	c/e
HAL1-CTL1-OHL-HOL	1.3	1	180.0	c/e
CTL2-CEL1-CEL1-HEL1	1.063	2	180.0	
CTL1-CEL1-CEL1-HEL1	0.707	2	180.0	
HEL1-CEL1-CTL2-CTL1	0.422	3	0.0	
CTL1-CTL1-CEL1-CTL1	1.003	3	0.0	
HAL1-CTL1-CEL1-CTL1	0.099	3	0.0	
CTL1-CEL1-CTL1-CTL2	1.328	3	0.0	
HAL1-CTL1-CEL1-HEL1	0.130	3	0.0	
CTL1-CTL1-CEL1-HEL1	0.015	3	0.0	
CTL3-CTL1-CEL1-HEL1	0.037	3	0.0	
CEL1-CEL1-CTL1-HAL1	0.015	3	0.0	
HEL1-CAL1-CAL1-HEL1	1.969	2	180.0	
X-CAL1-CAL1-X	7.121	2	180.0	
X-CEL1-CEL1-X	9.750	2	180.0	e
X-CEL1-CEL1-X	0.130	1	180.0	e
CAL1-CAL1-CTL2-HAL2	0.030	3	0.0	
CTL2-CTL1-CAL1-CTL2	0.500	3	0.0	
CTL3-CTL1-CAL1-CTL2	0.500	3	0.0	
CTL1-CTL2-CAL1-CTL1	0.500	3	0.0	
CTL1-CTL1-CAL1-CTL2	0.500	3	0.0	
CTL1-CTL1-CAL1-CAL1	1.129	3	0.0	
CTL2-CTL1-CAL1-CAL1	0.945	3	0.0	
CTL3-CTL1-CAL1-CAL1	0.122	3	0.0	
CTL1-CTL2-CAL1-CAL1	0.247	3	0.0	
HAL2-CTL2-CAL1-CTL1	0.294	3	0.0	
CTL1-CAL1-CAL1-HEL1	0.707	2	180.0	
CTL1-CEL1-CEL1-HEL1	0.707	2	180.0	
HEL1-CEL1-CTL2-CTL1	0.422	3	0.0	
CTL1-CTL1-CAL1-CTL1	1.033	3	0.0	
HAL1-CTL1-CAL1-CTL1	0.1667	3	0.0	
CTL1-CAL1-CTL1-CTL2	1.4857	3	0.0	
HAL1-CTL1-CAL1-HEL1	0.130	3	0.0	
CTL3-CTL1-CAL1-HEL1	0.037	3	0.0	
CAL1-CAL1-CTL1-HAL1	0.015	3	0.0	
HOL-OHL-CTL1-CTL1	0.16	3	0.0	l
HOL-OHL-CTL1-CTL2	0.24	3	0.0	l
HAL1-CTL1-OHL-HOL	0.24	3	0.0	l
HAL1-CTL1-OHL-HOL	0.5	1	120.0	l
HAL1-CTL1-OHL-HOL	0.7	1	220.0	l
HAL1-CTL1-OHL-HOL	0.12	2	0.0	l
HAL1-CTL1-OHL-HOL	0.15	2	90.0	l
CTL2-CTL2-CEL1-CTL1	1.815	3	0.0	
HAL3-CTL3-CEL1-CTL3	0.155	3	0.0	
CTL2-CEL1-CTL1-HAL1	3.233	3	0.0	

Table V: CHARMM27 dihedral angle parameters for cholesterol, ergosterol and lanosterol. The last column indicates parameters which are common for the three molecules but may used only for the indicated molecule: cholesterol (c), ergosterol (e) and lanosterol (l).

Group	Atome Name	Atom Type	Charge	Group	Atome Name	Atom Type	Charge
Group 1	C_1	CTL2	-0.056	Group 2	C_2	CTL2	-0.174
	H_{C_1}	HAL2	0.028		H_{C_2}	HAL2	0.087
	H_{C_1}	HAL2	0.028		H_{C_2}	HAL2	0.087
Group 3	C_3	CTL1	0.133	Group 4	C_5	CAL1	-0.101
	H_{C_3}	HAL1	0.055		C_6	CAL1	-0.150
	O	OHL	-0.557		H_{C_6}	HEL1	0.092
	H	HOL	0.369		C_{10}	CTL1	0.159
Group 5	C_4	CTL2	-0.174	Group 6	C_{12}	CTL2	-0.022
	H_{C4}	HAL2	0.087		$H_{C_{12}}$	HAL2	0.011
	H_{C4}	HAL2	0.087		$H_{C_{12}}$	HAL2	0.011
Group 7	C_7	CAL1	-0.036	Group 8	C_{16}	CTL2	-0.142
	H_{C_7}	HEL1	0.078		$H_{C_{16}}$	HAL2	0.071
	C_8	CAL1	-0.042		$H_{C_{16}}$	HAL2	0.071
Group 9	C_{14}	CTL1	-0.264	Group 10	C_{15}	CTL2	-0.186
	H_{C14}	HAL1	0.147		$H_{C_{15}}$	HAL3	0.093
	C_{13}	CTL1	0.117		$H_{C_{15}}$	HAL3	0.093
Group 11	C_{20}	CTL1	-0.182	Group 12	C_{22}	CEL1	-0.113
	$H_{C_{20}}$	HAL1	0.131		$H_{C_{22}}$	HEL1	0.103
	C_{17}	CTL1	-0.034		C_{23}	CEL1	-0.091
	$H_{C_{17}}$	HAL1	0.085		$H_{C_{23}}$	HEL1	0.101
Group 13	C_{11}	CTL1	-0.072	Group 14	C_9	HAL2	-0.066
	$H_{C_{11}}$	HAL1	0.036		H_{C_9}	HAL2	0.066
	$H_{C_{11}}$	CTL2	0.036				
Group 15	C_{18}	CTL3	-0.174	Group 16	C_{19}	CTL3	-0.111
	$H_{C_{18}}$	HAL3	0.058		$H_{C_{19}}$	HAL3	0.037
	$H_{C_{18}}$	HAL3	0.058		$H_{C_{19}}$	HAL3	0.037
	$H_{C_{18}}$	HAL3	0.058		$H_{C_{19}}$	HAL3	0.037
Group 17	C_{25}	CTL1	-0.067	Group 18	C_{24}	CTL1	-0.067
	$H_{C_{25}}$	HAL1	0.067		$H_{C_{24}}$	HAL1	0.067
Group 19	C_{26}	CTL3	-0.069	Group 20	C_{27}	CTL3	-0.135
	$H_{C_{26}}$	HAL3	-0.023		$H_{C_{27}}$	HAL3	0.045
	$H_{C_{26}}$	HAL3	-0.023		$H_{C_{27}}$	HAL3	0.045
	$H_{C_{26}}$	HAL3	-0.023		$H_{C_{27}}$	HAL3	0.045
Group 21	C_{28}	CTL3	-0.069	Group 22	C_{21}	CTL3	-0.252
	$H_{C_{28}}$	HAL3	0.023		$H_{C_{21}}$	HAL3	0.084
	$H_{C_{28}}$	HAL3	0.023		$H_{C_{21}}$	HAL3	0.084
	$H_{C_{28}}$	HAL3	0.023		$H_{C_{21}}$	HAL3	0.084

Table VI: Grouping, atom type assignments and partial atomic charges for ergosterol. Subscripts of the hydrogen atoms indicate to which carbon atoms the hydrogen atom are bonded.

Group	Atome Name	Atom Type	Charge	Group	Atome Name	Atom Type	Charge
Group 1	C_1	CTL2	-0.148	Group 2	C_2	CTL2	-0.118
	H_{C_1}	HAL2	0.074		H_{C_2}	HAL2	0.059
	H_{C_1}	HAL2	0.074		H_{C_2}	HAL2	0.059
Group 3	C_3	CTL1	0.053	Group 4	C_4	CTL1	0.036
	H_{C_3}	HAL1	0.114		C_5	CTL1	-0.149
	O	OHL	-0.535		H_{C_5}	HAL1	0.113
	H	HOL	0.368				
Group 5	C_6	CTL2	-0.192	Group 6	C_7	CTL2	-0.082
	H_{C6}	HAL2	0.096		H_{C7}	HAL2	0.041
	H_{C6}	HAL2	0.096		H_{C7}	HAL2	0.041
Group 7	C_8	CEL1	0.096	Group 8	C_{11}	CTL3	-0.186
	C_9	CEL1	-0.082		$H_{C_{11}}$	HAL3	0.093
	C_{10}	CTL1	-0.014		$H_{C_{11}}$	HAL3	0.093
Group 9	C_{12}	CTL2	-0.096	Group 10	C_{13}	CTL1	0.018
	$H_{C_{12}}$	HAL2	0.048		C_{14}	CTL1	-0.018
	$H_{C_{12}}$	HAL2	0.048				
Group 11	C_{15}	CTL2	-0.110	Group 12	C_{16}	CTL2	-0.096
	$H_{C_{15}}$	HAL3	0.055		$H_{C_{16}}$	HAL2	0.048
	$H_{C_{15}}$	HAL3	0.055		$H_{C_{16}}$	HAL2	0.048
Group 13	C_{20}	CTL1	-0.154	Group 14	C_{21}	CTL3	-0.219
	$H_{C_{20}}$	HAL1	0.128		$H_{C_{21}}$	HAL3	0.073
	C_{17}	CTL1	-0.077		$H_{C_{21}}$	HAL3	0.073
	$H_{C_{17}}$	HAL1	0.103		$H_{C_{21}}$	HAL3	0.073
Group 15	C_{18}	CTL3	-0.165	Group 16	C_{19}	CTL3	-0.252
	$H_{C_{18}}$	HAL3	0.055		$H_{C_{19}}$	HAL3	0.084
	$H_{C_{18}}$	HAL3	0.055		$H_{C_{19}}$	HAL3	0.084
	$H_{C_{18}}$	HAL3	0.055		$H_{C_{19}}$	HAL3	0.084
Group 17	C_{22}	CTL2	-0.144	Group 18	C_{23}	CTL2	-0.102
	$H_{C_{22}}$	HAL2	0.072		$H_{C_{23}}$	HAL2	0.051
	$H_{C_{22}}$	HAL2	0.072		$H_{C_{23}}$	HAL2	0.051
Group 19	C_{24}	CEL1	-0.038	Group 20	C_{26}	CTL3	-0.309
	C_{25}	CEL1	-0.009		$H_{C_{26}}$	HAL3	0.103
	$H_{C_{25}}$	HEL1	0.047		$H_{C_{26}}$	HAL3	0.103
					$H_{C_{26}}$	HAL3	0.103
Group 21	C_{27}	CTL3	-0.195	Group 22	C_{28}	CTL3	-0.309
	$H_{C_{27}}$	HAL3	0.065		$H_{C_{28}}$	HAL3	0.103
	$H_{C_{27}}$	HAL3	0.065		$H_{C_{28}}$	HAL3	0.103
	$H_{C_{27}}$	HAL3	0.065		$H_{C_{28}}$	HAL3	0.103
Group 23	C_{29}	CTL3	-0.195	Group 24	C_{30}	CTL3	-0.123
	$H_{C_{29}}$	HAL3	0.065		$H_{C_{30}}$	HAL3	0.041
	$H_{C_{29}}$	HAL3	0.065		$H_{C_{30}}$	HAL3	0.041
	$H_{C_{29}}$	HAL3	0.065		$H_{C_{30}}$	HAL3	0.041

Table VII: Grouping, atom type assignments and partial atomic charges for lanosterol. Subscripts of the hydrogen atoms indicate to which carbon atoms the hydrogen atom are bonded.

Erklärung gemäß §8 (3) b) und c) der Promotionsordnung:

a) ich erkläre hiermit, dass ich die vorgelegte Dissertation selbst verfasst und mich keiner anderen als der von mir ausdrücklich bezeichneten Quellen und Hilfen bedient habe,

b) ich erkläre hiermit, dass ich an keiner anderen Stelle ein Prüfungsverfahren beantragt bzw. die Dissertation in dieser oder anderer Form bereits anderweitig als Prüfungsarbeit verwendet oder einer anderen Fakultät als Dissertation vorgelegt habe.

Zoe Cournia
Heidelberg, 28 September 2006